

# **BULGARIAN CHEMICAL COMMUNICATIONS**

**2020** Volume 52 / Special Issue F

Papers, presented on the 16<sup>th</sup> Workshop on Transport  
Phenomena in Two-Phase Flows, Sofia, September 15-17, 2020

*Journal of the Chemical Institutes  
of the Bulgarian Academy of Sciences  
and of the Union of Chemists in Bulgaria*



## Introduction in the chemical engineering processes modeling

Chr. Boyadjiev

*Institute of Chemical Engineering, Bulgarian Academy of Sciences, Bulgaria*

Received: July 25, 2020; Accepted: August 03, 2020

In the paper is presented a theoretical analysis of the methods for chemical engineering processes modeling. The methods for modeling specific processes may be different, but in all cases they must bring the mathematical description closer to the real process by using appropriate experimental data. These methods are presented in the cases of co-current absorption column without packings, counter-current absorption column with random packings and modeling of processes with unknown mechanism.

### PRELUDE

The main problems in the chemical industry (biotechnology, heat energy) are the optimal design of new devices and the optimal control of active processes, i.e. minimization of the investment and operating costs. These problems are solved by chemical engineering with modeling methods [1]. The creation of the mathematical model begins with the formulation of the physical model of the complex process, i.e. the definition of the simple processes that make it up and the interactions between them. The second step is to define simple processes that have mathematical descriptions (equivalent mathematical operators). The other simple processes are introduced into the mathematical model through quantitative information obtained from experimental data, which brings the mathematical model as close as possible to the real process. The experiment brings mathematics closer to physics (reality).

The optimal design and control in the chemical industry is uniquely related to processes rates, so all mathematical descriptions of processes are linked to algorithms to determine these rates, i.e. processes kinetics.

### *Industrial Processes Kinetics*

The industrial systems consist of separate phases (gas, liquid, solid) in the industrial apparatuses volumes. They are in thermodynamic equilibrium when the velocities, temperatures and concentrations of substances in the individual parts or points of the phases are equal.

The processes in the chemical industry (biotechnology, heat energy) are a result of the deviation of the systems from their thermodynamic equilibrium [2]. One system is not in a thermodynamic equilibrium when the velocities, concentrations of the components (substances) and

the temperatures at the individual points in the phase volumes are different. These differences are the result of reactions, i.e. of processes that create or consume substance and (or) heat. As a result, the industrial processes kinetics is equivalent to the reactions kinetics [3].

The presented analysis shows that processes in the chemical industry are result of reactions that occur in the phase volume (homogeneous) or on the boundary between two phases (heterogeneous). Homogeneous reactions are generally chemical, while heterogeneous reactions are chemical, catalytic, physical and chemical adsorption, interphase mass transfer in gas-liquid and liquid-liquid systems (on the interphase surface the substance disappears from one phase and occurs in the other phase). The rates of these processes are determined by the reaction kinetics [3], which lies at the basis of modeling in chemical engineering, and solving the basic problems in the chemical industry (biotechnology, heat energy).

### *Modeling*

The basics of modeling in chemical engineering, as part of human knowledge and science, are related to the combination of intuition and logic that has different forms in individual sciences [4]. In mathematics the intuition is the axiom (unconditional statements that cannot be proven), while the logic is the theorem (the logical consequences of the axiom), but logic prevails over intuition. In the natural sciences (physics, chemistry, biology), the "axioms" (principles, postulates, laws) are not always unconditional, but logic prevails over intuition too.

The processes in chemical engineering take place in the industrial apparatuses, where gas, liquid and solid phases move together or alone.

---

\* To whom all correspondence should be sent:  
E-mail: chr.boyadjiev@gmail.com

They are described by variables which are extensive or intensive. In the case of merging of two identical systems, the extensive variables are doubled, but the intensive variables are retained.

In the chemical industry (biotechnology, heat energy), processes take place in moving phases (gas, liquid, solid). Reactions (reaction processes) lead to different concentrations (and temperatures) in the phase volumes and the phase boundaries. As a result, hydrodynamic processes, diffusion mass transfer and heat conduction are joined to the reaction processes. Under these conditions there are various forms of mass transfer (heat transfer) that are convective (as a result of phase movements) and diffusion (as a result of concentration (temperature) gradients in the phases).

Convective mass transfer (heat transfer) can be laminar or turbulent (as a result of large-scale turbulent pulsations). Diffusion mass transfer (heat transfer) can be molecular or turbulent (as a result of small-scale turbulent pulsations).

Mathematical models of industrial apparatuses aim at determining the concentration of substances (flow temperatures) in the phases. They have different degrees of approximation – thermodynamic, hydrodynamic and Boltzmann's approximations.

#### *Thermodynamic Approximation*

The processes in chemical engineering are the result of a deviation from the thermodynamic equilibrium between two-phase volumes or the volume and phase boundaries of one phase and represent the pursuit of systems to achieve thermodynamic equilibrium [2]. They are irreversible processes and their kinetics use mathematical structures derived from Onsager's principle of linearity. According to him, the average values of the derivatives at the time of the extensive variables depend linearly on the mean deviations of the conjugated intensive variables from their equilibrium states. The principle is valid close to equilibrium, and the Onsager's linearity coefficients are kinetic constants. When the process is done away from equilibrium (high-intensity processes) kinetic constants become kinetic complexes, depending on the corresponding intensive variables. The thermodynamic approximation models cover the entire volume of the phase or part of it.

#### *Hydrodynamic Approximations*

The hydrodynamic level uses the approximations of the mechanics of continua, where the mathematical point is equivalent to an elementary physical volume, which is sufficiently

small with respect to the apparatus volume, but at the same time sufficiently large with respect to the intermolecular volumes in the medium. In this level the molecules are not visible, as is done in the next level of detail of Boltzmann.

The models of the hydrodynamic approximations can be created on the basis of the mass (heat) transfer theory, whose models are created by the models of the hydrodynamics, diffusion, thermal diffusion and reaction kinetics, using the logical structures of three main "axioms", related with the impulse, mass and heat transfer:

1. The postulate of Stokes for the linear relationship between the stress and deformation rate, which is the basis of the Newtonian fluid dynamics models;
2. The first law of Fick for the linear relationship between the mass flow and the concentration gradient, which is the basis of the linear theory of the mass transfer;
3. The first law of Fourier for the linear relationship between the heat flux and the temperature gradient, which is the basis of the linear theories of the heat transfer.

These are the laws of the impulse, mass and energy transfer.

#### *Boltzmann's Approximation*

In Boltzmann's kinetic theory of the ideal gas, the hydrodynamic "axioms" are three "theorems" that derive from the axiom of the "elastic shock" (in a shock between two molecules the direction and the velocity of the movement change, but the sum of their kinetic energies is retained, i.e. there is no loss of kinetic energy) and the rate coefficients are theoretically determined by the average velocity and the average free run of the molecules.

#### *Mechanism of Influence of Reaction Kinetics*

The mathematical model of an engineering chemical process is a mass (heat) balance in the phase's volumes, where the mathematical operators are mathematical descriptions of the composite processes, and the relationship between them (differential equations) corresponds to the mechanism of the complex process. The boundary conditions of the differential equations are formulated at the interphase boundaries. For this purpose, the knowledge of the mathematical descriptions of the velocity distribution in the phases and the interphase boundaries is necessary.

Industrial processes are a set of physical and chemical reactions, hydrodynamic, diffusion and thermal processes that take place in the industrial

apparatus volume. The problems in compiling the models of the kinetics of industrial apparatuses arise from the need for information about the interaction between the individual processes in the complex process (its mechanism) and a mathematical description of the geometry of the industrial apparatus volume.

For the most part, industrial cases do not have the above information, which requires simplification of the models and introduction of some effects through experimentally determined parameters. As examples will be considered a co-current absorption column without packings and a counter-current absorption column with random packings.

#### Co-current Absorption Column without Packings

In the absorption columns without packings, the velocity distributions in the gas and liquid phases and the interfacial limits are unknown, i.e. the differential equations (mass balances in the phases) and their boundary conditions at the interphase boundaries (velocity of the interphase mass

transfer) cannot be formulated. These problems are overcome by creating of convection-diffusion and average-concentration models [5, 6]. In the convection-diffusion model the velocity of the interphase mass transfer is replaced by volume physical reaction and experimentally determinable parameter. In this model, the velocities are unknown, so it can only be used for qualitative analysis. From it the average-concentration models are obtained, by model averaging along the cross section of the column. The obtained average-concentration model involves average velocities and concentrations, and the velocity distributions in the phase volumes are introduced with experimentally determined parameters.

#### Convection-diffusion model

In the stationary case, the convection-diffusion model [3, 4] of the co-current chemical absorption process, with a pseudo-first-order chemical reaction in the liquid phase, in cylindrical coordinate system  $(r, z)$  [m], has the form:

$$u_j \frac{\partial c_j}{\partial z} + v_j \frac{\partial c_j}{\partial r} = D_j \left( \frac{\partial^2 c_j}{\partial z^2} + \frac{1}{r} \frac{\partial c_j}{\partial r} + \frac{\partial^2 c_j}{\partial r^2} \right) + (-1)^{(2-j)} k (c_1 - \chi c_2) - (j-1) k_0 c_2;$$

$$r = 0, \quad \frac{\partial c_j}{\partial r} \equiv 0; \quad r = r_0, \quad c_j = (j-1) c_1^0 \chi^{-1}; \quad j = 1, 2; \quad (1)$$

$$z = 0, \quad c_1 \equiv c_1^0, \quad c_2 \equiv 0, \quad u_1^0 c_1^0 \equiv u_1 c_1^0 - D_1 \left( \frac{\partial c_1}{\partial z} \right)_{z=0}, \quad \left( \frac{\partial c_2}{\partial z} \right)_{z=0} = 0.$$

$$\frac{\partial u_j}{\partial z} + \frac{\partial v_j}{\partial r} + \frac{v_j}{r} = 0; \quad (2)$$

$$r = r_0, \quad v_j(r_0, z) = 0; \quad z = 0, \quad u_j = u_j(r, 0); \quad j = 1, 2.$$

In (1, 2)  $u_j = u_j(r, z)$ ,  $v_j = v_j(r, z)$  and  $c_j = c_j(r, z)$  are the axial and radial velocity components and transferred substance concentrations in the gas ( $j=1$ ) and liquid ( $j=2$ ) phases,  $D_j$  are the diffusivities in the phases,  $u_j^0$  and  $c_j^0$  are the inlet velocities and the concentrations in the phases,  $k$  is the interphase mass transfer rate coefficient,  $\chi$  - the Henry's number,  $k_0$  - the chemical reaction rate constant. The concentrations of the transferred substance in the phases are presented as kg-mol of the transferred substance in 1 m<sup>3</sup> of the phase volume. The inlet velocities  $u_j^0$  ( $j=1,2$ ) of the gas and

liquid phases are equal to the average velocities  $\bar{u}_j$  ( $j=1,2$ ) of the phases in the column.

On the column wall the velocity components are zero ( $r = r_0, u_j = v_j \equiv 0, j = 1, 2$ ), i.e. there is no convective mass transfer. At the surface of the column, the motionless gas phase substance is absorbed into the motionless liquid phase. As a result, the concentration of the absorbent substance in the gas on the wall decreases to zero and its concentration in the liquid increases maximally (until thermodynamic equilibrium is reached), i.e.  $r = r_0, c_1 = 0, c_2 = c_1^0 \chi^{-1}$ .

In the physical absorption, the interphase mass transfer between gas and liquid phases is a surface physical reaction. In (1) this reaction is presented as a volume reaction and its rate

$Q = (-1)^{(2-j)} k(c_1 - \chi c_2)$ ,  $j = 1, 2$  participates in the mass balances in the gas and liquid phases.

*Average-concentration model*

The averaging of the convection-diffusion model [5, 6] along the cross section of the column leads to the average-concentration model:

$$\begin{aligned} \alpha_j(z) \bar{u}_j \frac{d\bar{c}_j}{dz} + [\beta_j(z) + \varepsilon \gamma_j(z)] \bar{u}_j \bar{c}_j &= \\ = D_j \frac{d^2 \bar{c}_j}{dz^2} + (-1)^{(2-j)} k(\bar{c}_1 - \chi \bar{c}_2) - (j-1) k_0 \bar{c}_2; & \quad (3) \\ z = 0, \quad \bar{c}_j(0) \equiv (2-j) c_j^0, \quad \frac{d\bar{c}_j}{dz} \equiv 0; \quad j = 1, 2, \end{aligned}$$

where

$$\alpha_j(z) = 1 + a_{j1}z + a_{j2}z^2, \quad \beta_j(z) = 1 + b_{j1}z + b_{j2}z^2, \quad \gamma_j(z) = 1 + g_{j1}z + g_{j2}z^2, \quad j = 1, 2, \quad (5)$$

where the values of  $a_{j1}, a_{j2}, b_{j1}, b_{j2}, g_{j1}, g_{j2}, j = 1, 2$  can be obtained using experimental data for the average concentration at the column end:

$$\bar{c}_{jm}(l), \quad j = 1, 2, \quad m = 1, \dots, 10. \quad (6)$$

Introducing (5) into (3) leads to

$$\begin{aligned} (1 + a_{j1}z + a_{j2}z^2) \bar{u}_j \frac{d\bar{c}_j}{dz} + [(1 + b_{j1}z + b_{j2}z^2) + \varepsilon(1 + g_{j1}z + g_{j2}z^2)] \bar{u}_j \bar{c}_j &= \\ = D_j \frac{d^2 \bar{c}_j}{dz^2} + (-1)^{(2-j)} k(\bar{c}_1 - \chi \bar{c}_2) - (j-1) k_0 \bar{c}_2; & \quad (7) \\ z = 0, \quad \bar{c}_j(0) \equiv (2-j) c_j^0, \quad \frac{d\bar{c}_j}{dz} \equiv 0; \quad j = 1, 2, \end{aligned}$$

where the unknown parameters values  $P(k, a_{j1}, a_{j2}, b_{j1}, b_{j2}, g_{j1}, g_{j2}, j = 1, 2)$  must be obtained, using experimental data, by the minimization of the of the least-squares function  $Q$  with respect to  $P$ :

$$Q(P) = \sum_{m=1}^{10} [\bar{c}_1(l, P) - \bar{c}_{1m}(l)]^2 + \sum_{m=1}^{10} [\bar{c}_2(l, P) - \bar{c}_{2m}(l)]^2, \quad (8)$$

where  $\bar{c}_1(l, P), \bar{c}_2(l, P)$  are solutions of the average-concentration model (7).

The presented approach is used for modeling of chemical, absorption, adsorption and catalytic processes in column apparatuses without packings [5, 6].

*Counter-current Absorption Column with Random Packings*

Counter-current absorption columns with random packings are characterized by the presence of a layer of liquid that flows along the wall of the column and practically does not participate in the absorption process and reduces the working volume of the column. The created hydrodynamic situation does not allow the approach to be used in the modeling of columns without packings.

*Fluid flow along the column wall*

The liquid flow on the surface of the random packings and when it reaches the column wall most

$$\alpha_j(z) = \frac{2}{r_0^2} \int_0^{r_0} r \frac{u_j c_j}{\bar{u}_j \bar{c}_j} dr, \quad \beta_j(z) = \frac{2}{r_0^2} \int_0^{r_0} r \frac{u_j}{\bar{u}_j \bar{c}_j} \frac{\partial c_j}{\partial z} dr, \quad (4)$$

$$\gamma_j(z) = \frac{2}{r_0^2} \int_0^{r_0} r \frac{v_j}{\varepsilon \bar{u}_j \bar{c}_j} \frac{\partial c_j}{\partial r} dr, \quad \varepsilon = \frac{r_0}{l}.$$

The functions  $\alpha_j(z), \beta_j(z), \gamma_j(z), j = 1, 2$  can to be presented as the following approximations:

of it flows on this surface and cannot return to the column volume due to the small contact surface between the wall surface and the random packings. The thickness of the flowing layer of liquid increases and conditions are created for the return of liquid from the layer to the packings and further the two effects are equalized. In this way, the layer of liquid reaches a constant maximum thickness, with which it moves to the end of the column. The amount of liquid entering the flowing layer leads to a reduction in the amount of liquid in the volume of the column, i.e. to the radial non-uniformity of the axial component of the liquid velocity in the column and to the reduction of the mass transfer rate in the liquid phase. In addition, this layer is not involved in the absorption process.

The effect of liquid flowing on the column wall is the result only of the geometric shape of the random packings and thus determines the rate of absorption of slightly soluble gases, which reaches a maximum value at maximum packings surface

per unit volume of the column and minimum thickness of the flowing layer of liquid.

#### Problems with random packings in the columns

In the case of modeling the hydrodynamics in the gas and liquid phases in columns with random packings, the following problems arise:

1. The flow rate of the liquid flowing on the surface of the random packings [ $\text{m}^3 \cdot \text{s}^{-1}$ ] and the retention of the liquid on this surface are unknown;
2. The flow rate of the liquid flowing on the column wall [ $\text{m}^3 \cdot \text{s}^{-1}$ ] and the retention of the liquid on this surface are unknown;
3. The hydrodynamic resistance of the random packings on the gas phase is unknown.

Theoretical analysis [7] shows that this problem can be overcome in the presence of experimental data on the flow rate of the liquid flowing along the column wall, at different packings heights and on the packing pressure drop, during the movement of the gas phase. This requires the creation of a hydrodynamic model in which the liquid and the gas move in separate channels and interact on the surface of the flowing layer. The introduction of experimentally determined quantities into the model brings it as close as possible to the real process.

#### Experimental data

The wall flow thickness in columns with random packing changes smoothly from 0 to a constant maximal value  $\delta_{\max}$  and can be expressed by an approximation function  $\delta(z)$ :

$$\delta(z) = \frac{z}{a+bz}, \quad \delta(0) = 0, \quad \delta(\infty) = \frac{1}{b} = \delta_{\max}, \quad (9)$$

where  $z$  is the axial coordinate. The parameters ( $a$ ,  $b$ ) is possible to be determined from experimental data for the flow rate of the wall flow  $Q_{WF}$  at various packing heights  $l$  in the column -  $Q_{WF}(z)$ ,  $z = l_i$ ,  $i = 1, \dots, n$ . The available experimental data can be described by the following approximation:

$$Q_{WF}(z) = \frac{z}{k_1 + k_2 z}. \quad (10)$$

From (10) is possible to determine the flow rate  $Q(z)$  of the wall flow per unit periphery of the column ( $2\pi r_0$ ).

$$Q(z) = \frac{Q_{WF}(z)}{2\pi r_0} = \frac{z}{m_1 + m_2 z}, \quad m_1 = 2\pi r_0 k_1, \quad m_2 = 2\pi r_0 k_2, \quad (11)$$

where  $r_0$  is the column radius.

#### Phase volume parts in the column volume

The volumes of the solid, gas, and liquid phases per unit volume of the column can be represented as:

$$\varepsilon_j, \quad j = 0, 1, 2, \quad \varepsilon_0 + \varepsilon_1 + \varepsilon_2 = 1, \quad (12)$$

where the indices  $j = 0, 1, 2$  corresponds to solid, gas, and liquid phases.

As a result of the liquid flow on the column wall, the liquid phase is divided into two parts:

$$\varepsilon_2 = \varepsilon_{21}(z) + \varepsilon_{22}(z), \quad (13)$$

where  $\varepsilon_{22}(z)$  is the fraction of the liquid flowing along the wall.

The gas and liquid flow rates  $Q_G, Q_L, Q_{WF}$  [ $\text{m}^3 \cdot \text{s}^{-1}$ ] permit to obtain the gas-liquid and liquid-liquid ratios in the column volume:

$$\bar{\varepsilon}_1 = \frac{Q_G}{Q_G + Q_L}, \quad \bar{\varepsilon}_2 = \frac{Q_L}{Q_G + Q_L}, \quad \bar{\varepsilon}_{21} = \frac{Q_L - Q_{WF}}{Q_L}, \quad \bar{\varepsilon}_{22} = \frac{Q_{WF}}{Q_L} \quad (14)$$

and gas and liquid hold-up in the packing:

$$\varepsilon_1 = \frac{\bar{\varepsilon}_1}{1 - \varepsilon_0}, \quad \varepsilon_2 = \frac{\bar{\varepsilon}_2}{1 - \varepsilon_0}, \quad \varepsilon_{21} = \frac{\bar{\varepsilon}_{21}}{\varepsilon_2}, \quad \varepsilon_{22} = \frac{\bar{\varepsilon}_{22}}{\varepsilon_2}. \quad (15)$$

The parameters  $\varepsilon_1, \varepsilon_2$  denote the volume fraction, as well as the cross-section fraction of the gas and liquid in the packing and are used to determine their inlet average velocities:

$$u_z^0 = \frac{Q_G}{\varepsilon_1 \pi r_0^2}, \quad v_z^0 = \frac{Q_L}{\varepsilon_2 \pi r_0^2}, \quad (16)$$

where  $u_z^0, v_z^0$  are the average velocities in the void cross-section of the gas and liquid phase at the inlet of the packing bed,  $Q_G, Q_L$  - gas and liquid inlet flow rates.

#### Pressure drop of random packings columns

The hydraulic resistance of the fillings  $H$ , i.e. the pressure drop through a layer of random packings with a thickness of 1 meter, at a given gas velocity:

$$H = \frac{p^0 - p(0, z_0)}{z_0}, \quad (17)$$

is determined from experimental data on the pressure difference at both ends  $p^0 - p(0, z_0)$  of the random packings height  $z_0$ .

The obtained results permit a physical model to be used, where the gas and the liquid move in parts of the column volume and through parts of the column cross section ( $\varepsilon_1, \varepsilon_{21}, \varepsilon_{22}$ ) and contact on a

cylindrical surface with variable radius  $R_0(z) = r_0 - \delta(z)$ .

*Hydrodynamics of the liquid phase in the column volume*

The flows in the column are axially symmetrical and the model of the hydrodynamics of the liquid phase in the volume of the column will be presented in a cylindrical coordinate system  $(r, z)$ , where  $r$  and  $z$  are the radial and axial coordinates. In the packings columns the pressure is constant during the movement of liquid under the action of weight. In this case the axial and radial components of the velocity  $v_z$  and  $v_r$  satisfy the Navier and Stokes equations:

$$v_z \frac{\partial v_z}{\partial z} + v_r \frac{\partial v_z}{\partial r} = \nu \left( \frac{\partial^2 v_z}{\partial z^2} + \frac{\partial^2 v_z}{\partial r^2} + \frac{1}{r} \frac{\partial v_z}{\partial r} \right) + g, \quad (18)$$

$$v_z \frac{\partial v_r}{\partial z} + v_r \frac{\partial v_r}{\partial r} = \nu \left( \frac{\partial^2 v_r}{\partial z^2} + \frac{\partial^2 v_r}{\partial r^2} + \frac{1}{r} \frac{\partial v_r}{\partial r} - \frac{v_r}{r^2} \right).$$

The inlet boundary conditions are:

$$z = 0, \quad v_z = v_z^0, \quad \frac{\partial v_z}{\partial z} = 0, \quad v_r = 0, \quad \frac{\partial v_r}{\partial z} = 0. \quad (19)$$

The boundary conditions along the axis of the column are:

$$r = 0, \quad \frac{\partial v_z}{\partial r} = 0, \quad \frac{\partial v_r}{\partial r} = 0. \quad (20)$$

The effect of the flow of liquid on the wall of the column must be taken into account when  $r = R_0(z) = r_0 - \delta(z)$ , where the amount of liquid which enters the wall of the column through the

$$v_z \frac{\partial v_z}{\partial z} + v_r \frac{\partial v_z}{\partial r} = \nu \left( \frac{\partial^2 v_z}{\partial z^2} + \frac{\partial^2 v_z}{\partial r^2} + \frac{1}{r} \frac{\partial v_z}{\partial r} \right) + g,$$

$$v_z \frac{\partial v_r}{\partial z} + v_r \frac{\partial v_r}{\partial r} = \nu \left( \frac{\partial^2 v_r}{\partial z^2} + \frac{\partial^2 v_r}{\partial r^2} + \frac{1}{r} \frac{\partial v_r}{\partial r} - \frac{v_r}{r^2} \right);$$

$$z = 0, \quad v_z = v_z^0, \quad \frac{\partial v_z}{\partial z} = 0, \quad v_r = 0, \quad \frac{\partial v_r}{\partial z} = 0;$$

$$r = 0, \quad \frac{\partial v_z}{\partial r} = 0, \quad \frac{\partial v_r}{\partial r} = 0; \quad r = r_0 - \delta(z), \quad v_z = v_0(z), \quad v_r = \frac{r_0 v_0(z)}{r_0 - \delta(z)} \frac{d\delta}{dz};$$

$$\delta(z) = \frac{z}{a + bz}, \quad \frac{d\delta}{dz} = \frac{a}{(a + bz)^2}, \quad v_0(z) = \frac{z}{\alpha + \beta z}. \quad (25)$$

*Liquid layer hydrodynamics*

The wall flow in the column is described by the equations:

surface  $2\pi R_0 dz$  by the radial velocity component  $v_r$ , i.e.  $2\pi R_0 v_r dz$  must be equal to the volume of the liquid layer obtained on the wall of the column  $2\pi r_0 v_0 d\delta$ , where  $v_0 = v_0(z)$  is the surface velocity of the liquid layer:

$$2\pi R_0 v_r(R_0, z) dz = 2\pi r_0 v_0(z) d\delta. \quad (21)$$

As a result

$$r = R_0 = r_0 - \delta(z), \quad v_r(R_0, z) = \frac{r_0 v_0(z)}{r_0 - \delta(z)} \frac{d\delta}{dz}, \quad \frac{d\delta}{dz} = \frac{a}{(a + bz)^2}. \quad (22)$$

The axial component of the liquid velocity  $v_z$  at the boundary  $r = r_0 - \delta(z)$  must be equal to the surface velocity of the film flowing down the column wall  $v_0(z)$ :

$$r = r_0 - \delta(z) = r_0 - \frac{z}{a + bz}, \quad v_z = v_0(z), \quad (23)$$

where the surface velocity changes smoothly from 0 to a constant maximal value and can be expressed by an approximation function:

$$v_0(z) = \frac{z}{\alpha + \beta z}. \quad (24)$$

The parameters  $(a, b, \alpha, \beta)$  in the approximation functions (9, 24) must be obtained using experimental data.

Finally, the hydrodynamic model of the liquid phase in column volume can be written as:

$$\begin{aligned} w_z \frac{\partial w_z}{\partial z} + w_r \frac{\partial w_z}{\partial r} &= v \left( \frac{\partial^2 w_z}{\partial z^2} + \frac{\partial^2 w_z}{\partial r^2} + \frac{1}{r} \frac{\partial w_z}{\partial r} \right) + g, \\ w_z \frac{\partial w_r}{\partial z} + w_r \frac{\partial w_r}{\partial r} &= v \left( \frac{\partial^2 w_r}{\partial z^2} + \frac{\partial^2 w_r}{\partial r^2} + \frac{1}{r} \frac{\partial w_r}{\partial r} - \frac{w_r}{r^2} \right); \end{aligned} \quad (26)$$

$$z = 0, \quad w_z = 0, \quad \frac{\partial w_z}{\partial z} = 0, \quad w_r = 0, \quad \frac{\partial w_r}{\partial z} = 0;$$

$$r = r_0, \quad w_z = 0, \quad w_r = 0; \quad r = r_0 - \delta(z), \quad w_z = v_0(z), \quad w_r = v_r = \frac{r_0 v_0(z)}{r_0 - \delta(z)} \frac{d\delta}{dz};$$

$$\delta(z) = \frac{z}{a+bz}, \quad \frac{d\delta}{dz} = \frac{a}{(a+bz)^2}, \quad v_0(z) = \frac{z}{\alpha + \beta z}.$$

#### Parameters identification

The comparison of (25) and (26) shows that there is a common boundary condition at an unknown boundary  $\delta(z)$ :

$$r = r_0 - \delta(z), \quad w_z = v_z = v_0(z), \quad (27)$$

where the surface velocity of the wall flow  $v_0(z)$  is unknown too.

The flow rate of the liquid flowing on the wall, per unit of column circumference  $Q(z)$  in (11), which has passed from the bulk of the liquid in the column, depends on the functions  $\delta(z), v_0(z)$  and must be determined by the equations:

$$Q(z) = \frac{z}{m_1 + m_2 z} = \int_{r_0 - \delta(z)}^{r_0} w_z dr = \int_0^{r_0 - \delta(z)} [v_z^0 - v_z] dr, \quad v_z^0 = \frac{Q_L}{\varepsilon_2 \pi l_0^2}, \quad (28)$$

i.e. the flow rate of the wall flow is equal to the difference in the flow rates of the liquid in the bulk of the column in presence and absence of a wall flow. The conditions (28) and the solution of the system of equations (25, 26) permit to obtain the parameters  $(a, b, \alpha, \beta)$ , using a suitable algorithm [7].

#### Gas phase hydrodynamics

The hydrodynamics of the gas phase will be represented in a cylindrical coordinate system  $(r, z_0), z_0 = l - z$ , where the axial coordinate is directed back to the axial coordinate of the liquid phase. The movement of the gas is the result of the pressure gradient along the height of the column (hydraulic resistance), which depends on the packings and is determined experimentally. The axial  $u_z$  and radial  $u_r$  components of velocity in the gas phase and pressure (per unit volume)  $p$  satisfy the Navier-Stokes equations:

$$\begin{aligned} u_z \frac{\partial u_z}{\partial z_0} + u_r \frac{\partial u_z}{\partial r} &= -\frac{1}{\rho} \frac{\partial p}{\partial z_0} + v \left( \frac{\partial^2 u_z}{\partial z_0^2} + \frac{\partial^2 u_z}{\partial r^2} + \frac{1}{r} \frac{\partial u_z}{\partial r} \right), \\ u_z \frac{\partial u_r}{\partial z_0} + u_r \frac{\partial u_r}{\partial r} &= -\frac{1}{\rho} \frac{\partial p}{\partial r} + v \left( \frac{\partial^2 u_r}{\partial z_0^2} + \frac{\partial^2 u_r}{\partial r^2} + \frac{1}{r} \frac{\partial u_r}{\partial r} - \frac{u_r}{r^2} \right), \\ \frac{\partial u_z}{\partial z_0} + \frac{\partial u_r}{\partial r} + \frac{u_r}{r} &= 0; \\ z_0 = 0, \quad u_z = u_z^0, \quad \frac{\partial u_z}{\partial z_0} = 0, \quad u_r = 0, \quad \frac{\partial u_r}{\partial z_0} = 0, \quad p = p^0; \\ r = 0, \quad \frac{\partial u_z}{\partial r} = 0, \quad \frac{\partial u_r}{\partial r} = 0, \quad p = p(0, z); \\ r = r_0 - \frac{l - z_0}{a + b(l - z_0)}, \quad u_z = -v_0(l - z_0), \quad u_r = 0. \end{aligned} \quad (29)$$

The pressure in the gas phase  $p(r, z_0)$  can be presented in (29) as

$$\frac{\partial p}{\partial r} = 0, \quad \frac{\partial p}{\partial z_0} = H = \frac{p^0 - p(0, z_0)}{z_0}, \quad (30)$$

where  $H$  is the packing pressure drop, i.e. the pressure drop through a packing layer of a thickness of 1 meter at a given gas velocity.

#### Modeling of Processes with Unknown Mechanism

There are complex processes whose mechanism is unknown. A typical example of this are the complex chemical reactions, the rate of which depends on the concentrations of several substances, but the simple chemical reactions and the relationships between them are unknown.

The kinetics of processes with an unknown mechanism can be modeled on the basis of the axiom, according to which "The mathematical structure of the quantitative description of real processes does not depend on the measuring system of the quantities involved in them". On the basis of this axiom, Guchmann's theorem can be proved [8] – "If the mathematical structure is invariant with respect to similar transformations, it can be presented as power functions complex", i.e. „Mathematical structure of the quantitative

description of real systems can be presented as power functions complex“, because the mathematical structure which is invariant with respect to similar transformations is a mathematical structure of real processes which does not depend on the measuring system.

The kinetics of the chemical engineering processes depends on a set of variables. If the velocity of these processes is denoted by  $y$  and the values of these variables are  $x_1, \dots, x_n$ , the equation of the kinetic model will have the form:

$$y = f(x_1, \dots, x_n). \quad (31)$$

This function is a mathematical structure that is retained when changed the measurement system of the variable, i.e. this mathematical structure is invariant with respect to similar transformations [7]:

$$\bar{x}_i = k_i x_i, \quad i = 1, \dots, n, \quad (32)$$

i.e.  $f$  is a homogeneous function:

$$ky = f(k_1 x_1, \dots, k_n x_n) = \phi(k_1, \dots, k_n) \cdot f(x_1, \dots, x_n), \quad k = \phi(k_1, \dots, k_n). \quad (33)$$

A short recording of (33) is:

$$f[\bar{x}_i] = \phi[k_i] f[x_i]. \quad (34)$$

The problem consists in finding a function  $f$  that satisfies equation (34). A differentiation of equation (34) concerning  $k_i$  leads to:

$$\frac{\partial f[\bar{x}_i]}{\partial k_i} = \frac{\partial \phi}{\partial k_i} f(x_i). \quad (35)$$

On the other hand

$$\frac{\partial f[\bar{x}_i]}{\partial k_i} = \frac{\partial f[\bar{x}_i]}{\partial \bar{x}_1} \frac{\partial \bar{x}_1}{\partial k_i} = \frac{\partial f[\bar{x}_i]}{\partial \bar{x}_1} x_1. \quad (36)$$

From (35, 36) follows

$$\frac{\partial f[\bar{x}_i]}{\partial \bar{x}_1} x_1 = \alpha_1 f[x_i], \quad (37)$$

where

$$\alpha_1 = \left( \frac{\partial \phi}{\partial k_1} \right)_{k_i=1}. \quad (38)$$

The equation (37) is valid for different values of  $k_i$  including  $k_i = 1$  ( $i = 1, \dots, n$ ). As a result

$\bar{x}_i = x_i, i = 1, \dots, n$  and from (37) follows

$$\frac{1}{f} \frac{\partial f}{\partial x_1} = \frac{\alpha_1}{x_1}, \quad (39)$$

i.e.

$$f = c_1 x_1^{\alpha_1}. \quad (40)$$

When the above operations are repeated for  $x_2, \dots, x_n$ , the homogenous function  $f$  assumes the form:

$$f = k x_1^{\alpha_1}, \dots, x_n^{\alpha_n}, \quad (41),$$

i.e. the function  $f$  is homogenous if it represents a power functions complex and as a result is invariant with respect to similarity (metric) transformations. The parameters  $k, a_1, \dots, a_n$  are determined by experimental data of the industrial process velocity.

The power functions complex (41) is used in the similarity criterion models equation in the similarity theory [7], where  $x_i, i = 1, \dots, n$  are similarity criteria. The information about the process mechanism permits to obtain dimensionless combinations of the model parameters (similarity criteria) which represent the ratio of the efficiency of two processes, for example [1]:

$$Fo = \frac{Dl}{u^0 r_0^2}, \quad Da = \frac{kl}{u^0}, \quad (42)$$

are the Fourier and Damkohler numbers and represent the ratio of the efficiency of the convective and diffusion mass transfer (Fo) and convective mass transfer and chemical reaction rate (Da). In (42)  $D$  is diffusivity,  $r_0, l$  - linear characteristic scales,  $u^0$  - velocity characteristic scale.

The power functions complex (41) is used by the dimension analysis [1], but the dimension criteria do not represent the ratio of the efficiency of two processes, because the method is used in absence of the processes mechanism information.

## CONCLUSIONS

In the paper is presented a theoretical analysis of the methods for chemical engineering processes modeling. The methods for modeling specific processes may be different, but in all cases they must bring the mathematical description closer to the real process by using appropriate experimental data.

The role of the kinetics of industrial apparatuses for solving the problems of optimal design and control is analyzed. The thermodynamic, hydrodynamic and Boltzmann approximations for the mathematical description of the kinetics of industrial apparatuses are described.

They are presented for the cases of co-current absorption column without packings, counter-current absorption column with random packings and modeling of processes with unknown mechanism.

**Acknowledgements:** This work is supported by the Project of Fundamental Scientific Research 19-58-18004, conducted by RFBR and the National Science Fund of Bulgaria under contract No KP 06 RUSIA-3 from 27 Sep. 2019, “Modeling, simulation and experimental investigations of the interphase

*mass transfer and separation in distillation, absorption, adsorption and catalytic processes in industrial column apparatuses”.*

#### REFERENCES

1. Chr. Boyadjiev, Theoretical Chemical Engineering. Modeling and simulation, Springer-Verlag, Berlin Heidelberg, 2010.
2. J. Keizer, Statistical Thermodynamics of Nonequilibrium Processes, Springer-Verlag, New York, 1987.
3. Chr. Boyadjiev, Reaction kinetics in chemical engineering, *Bulgarian Chemical Communications*, 50(Special Issue-K), 112 (2018).
4. Chr. Boyadjiev, Some Thoughts on Logic and Intuition in Science and Chemical Engineering, I, **1**, №6, 2014, p. 1.
5. Chr. Boyadjiev, M. Doichinova, B. Boyadjiev, P. Popova-Krumova, Modeling of Column Apparatus Processes, Springer-Verlag, Berlin Heidelberg, 2016.
6. Chr. Boyadjiev, M. Doichinova, B. Boyadjiev, P. Popova-Krumova, Modeling of Column Apparatus Processes (Second edn.), Springer-Verlag, Berlin Heidelberg, 2018.
7. B. Boyadjiev, Chr. Boyadjiev, D. Dzhonova, A. N. Pavlenko, On the Hydrodynamics of Gas and Liquid Counter-Current Flows in Packed Columns, Private communication.
8. А. А. Гухман, Введение в теорию подобия, Изд. „Высшая школа“, Москва (1973) (А. А. Gukhman, Introduction to the theory of similarity, „Higher School“, Moscow, 1973).

## Boilers modernization due to energy-ecological improvement technology of burning

M. Z. Abdulin, O. A. Siryi\*, O. M. Tkachenko, A. A. Kunyk

National Technical University of Ukraine "Igor Sikorsky Kyiv Politechnic Institute", Kyiv, Ukraine

Received: August 02, 2020; Accepted: August 10, 2020

According to the practice of burning gaseous fuels in energetic and industrial installations, one of the most important elements of the boiler-furnace process is the burner device (BD). The main processes taking place in a BD are hydrodynamic phenomena in the working channel that determine the efficiency of burning organic fuels due to such working stages: mixing fuel and oxidizer, ignition, stabilization of ignition torch and fuel burn up. These processes based on the phenomenon of heat and mass transfer and chemical interaction of burning components determine the ecological impact of the studied processes.

This paper is devoted to the energy-ecological evaluation of industrial-scale plants equipped with Jet-niche technology of burning (JNT). Today modernized are dozens of gas burning objects such as: steam and water boilers, industrial furnaces, dryers and heaters of steel ladles in metallurgy, cement mills and melting furnaces in industry. The main issue is to determine the influence of vitiated air to the emission characteristics of gas-powered equipment in a wide capacity range. At the nominal operating conditions a 2.5 fold reduction of nitrogen oxide concentrations up to 25...35 ppm was achieved at 12% volumetric gas recirculation. Thus, a reduction of  $NO_x$  emissions in the range of 3.4-4.8% per 1% of the recirculation gases was achieved. The effect was increased with the power set. The results are presented for steam water boiler units with a capacity of 6.5-50 gcal.

**Keywords:** jet-niche technology, gaseous fuel, hot-water boiler, nitrogen oxides

### INTRODUCTION

Diatomic molecular nitrogen ( $N_2$ ) is a relatively inert gas that makes up about 79% of the ambient air we breathe. The chemical element nitrogen ( $N$ ), as a single atom, can be reactive and have different ionization levels from one to five. Thus, nitrogen can form several different oxides. In general, nitrogen oxides ( $NO_x$ ) are a family of seven compounds. Nitrogen oxides take second place after sulfur dioxide among the elements that increase acid precipitation. Nitrogen oxides also impair visibility and play a significant role in the formation of photochemical smog [1].

It is known that there are different mechanisms of formation of nitrogen oxides during fuel combustion: thermal, fuel and fast. The proportion of fast nitrogen oxides is negligible and increases for fuel with a higher molecular weight. The proportion of thermal nitrogen oxides decreases. The content of thermal nitrogen oxides in gaseous fuels reaches more than 80% of the total emissions.

The nature of  $NO_x$  formation has not been thoroughly studied, the behavior of oxides is often ambiguous and theoretically unpredictable. The basis of  $NO_x$  are thermal oxides of nitrogen.

Reduction in the intensity of  $NO_x$  emissions can be achieved in two ways. The first one is associated with the direct improvement of the combustion process (so-called technological methods), and the second is achieved by purification of exhaust gases.

### LITERATURE REVIEW

There are many technological factors that affect the level of nitrogen oxides emissions in a gas burning unit., such as the level of excess air, current load of unit, flue gas recirculation, afterburning, water or steam supply to the combustion zone, redistribution of fuel and air through the burner channels, redistribution of fuel and air on the burner tiers, switching off part of the burners, regulation of the intensity of swirling (for swirling type burning devices (BD)), use of a micro torch combustion mechanism (multi burner furnaces of power boilers and combustion chambers gas-turbine units) [2-10].

Application of catalytic combustion technologies belongs to the second method of denitrification of flue gases. It is divided into selective catalytic and selective non-catalytic removal of nitrogen oxides [11-13].

The efficiency of reducing emissions depends on the technology of fuel combustion. The base canonical principles of  $NO_x$  minimization are: preliminary mixture formation, stage combustion and direct-flow aerodynamic scheme of oxidant flow. The Jet-niche combustion technology (JNT) meets all the canonical principles [14]. The main features of the technology are as follows: rational distribution of fuel in the oxidant stream; stable

\* To whom all correspondence should be sent:  
E-mail: [osiryi@gmail.com](mailto:osiryi@gmail.com)

regulated structure of fuel, oxidant and combustion products; self-regulation of the fuel mixture in the flame stabilization zone. The main element of JNT burners is a jet-niche system (Fig. 1) [15].

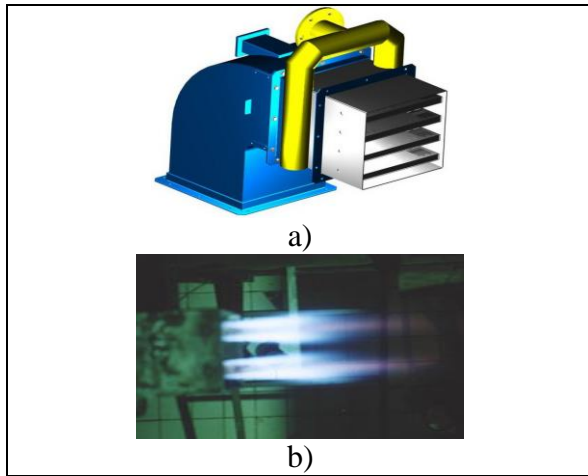


**Fig. 1.** Jet-niche fuel combustion technology: burner (a), open gas torch (b),

A significant experience of energy-ecological modernization of boiler equipment with a capacity of 0.5...125 MW has been gained on the basis of JNT.

The "National Emissions Reduction Plan for Large Combustion Plants" is valid in Ukraine [16]. The plan is designed for gradual implementation until 2032 inclusive. According to the plan, the implementation of primary technological measures is considered on the first stage, and the technologies based on the process of deoxidation of nitrogen oxides – on the second stage.

In particular, the aim of this research is defining the role of primary technological methods of nitrogen oxides reduction on boilers equipped with JNT type BD.

## RESULTS AND DISCUSSION

The emission performance of boiler equipment is significantly influenced by the main process variables: the excess air factor in the unit furnace ( $\alpha_f$ ) and the productivity of the boiler ( $D_0$ ) (Fig. 2).

The normalized indicators of nitrogen oxides  $NO_x^{norm}$  are practically important for the process of forecasting emission characteristics. They are determined in the absence of main operational influences at  $\alpha_f=1.0$ . The maximum value of the nitric oxide concentration  $NO_x^{max}$  is reached at certain values of the critical excess air  $\alpha_{cr} = \alpha_f$ .

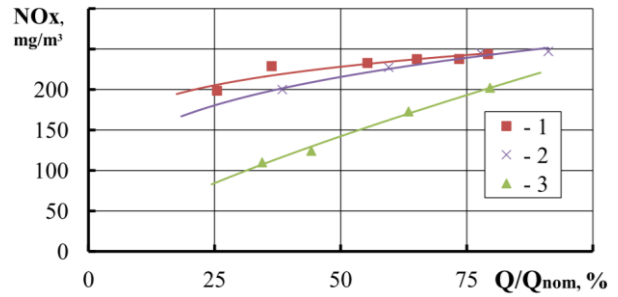


**Fig. 2.** Dependence of nitrogen oxides concentration on the main technological parameters on a boiler equipment with JNT: 1 – KVGM-20, 2 – KVG-7.56, 3 – TVG-8

The value of the critical excess air factor  $\alpha_{cr1} > 1.0$  (hereinafter  $\alpha_{cr}$ ) is a determining parameter during the industrial adjustment of boiler equipment. In fact, a further reduction of excess air on the burners in the direction of  $\alpha \rightarrow 1.0$  leads to a decrease in the concentration of nitrogen oxides at simultaneously with an excessive increase in chemical fuel underburning. There is a second critical point of ecological indicators  $\alpha_{cr2}$  ( $\alpha_{cr2} > \alpha_{cr1}$ ). It corresponds to the minimum concentrations of carbon monoxide and is closer to the stoichiometric mixture implemented in burners [17].

Using the data of [17] and the results of industrial implementation of JNT, the emission parameters of the modernized equipment are presented in the Table below.

The parameter  $\alpha_{cr}$  takes a fairly wide range of values 1.14-1.45, which is explained by the peculiarities of the studied equipment and its actual condition at the time of modernization. For instance, this parameter is close to 1.5 for boilers converted from solid fuel combustion to natural gas (NIISTU-5), but it is in the range of values  $\alpha_{cr} = 1.14-1.2$  for gas-fired boilers. The difference is determined by the peculiarities of the process of heat removal from the torch in the furnace space and the quantity of the air inflow. Intensification of these processes leads to an increase in the parameter  $\alpha_{cr}$ . The reverse trend of the  $\alpha_{cr}$  displacement closer to stoichiometry is related to the improval of mixing processes in the burners of boiler equipment. The results show the correlation between normalized and maximum concentrations of nitrogen oxides ( $\overline{NO}_x = NO_x^{norm} / NO_x^{max}$ ). Thus, for boiler equipment with a heat power from 6.5 to 50 Gcal, the ratio is in the range of 0.63-0.81, the exception is a specific equipment, represented by small-sized water heaters of the contact type KVN and converted solid fuel boilers NIISTU.

**Table.** Emission indicators of low and medium capacity boiler units at rated load (N = 100%), degree of furnace waterwall ( $\psi = 0.55-0.8$ ), and volumetric heat load of units  $q_v = 0.3-0.35 \text{ MW/m}^3$  (KVN-2.9 –  $q_v = 3.0 \text{ MW/m}^3$ ).

Boiler type	Thermal power, $\alpha_{cr}$	$\alpha_{cr}$	$NO_x^{max}$			$NO_x^{norm}$		$NO_x^{norm}/NO_x^{max}$
			Measured value	experiment is reduced	Calculation	Experiment	Calculation	
NIISTU-5	0.5	1.45	130	69.89	73.50	66	61	0.95
KVN-2.9	2.9	1.2	80	66.67	133.3	88	101	1.32
KVG-7.56/6.5	7.56	1.15	250	178.6	172.7	112	131	0.63
DKVR-10	9.2	1.17	280	200.0	186.2	161	142	0.81
KVGM-20	23.2	1.14	295	268.2	234.2	194	171	0.72
PTVM-50	58.2	1.17	350	304.4	296.7	209	219	0.69

For comparison, the technologies with swirling-type burners according to the experimental data of [17] have an average value of 0.78 with a deviation from the average value for different types of boiler equipment not more than 7%. The average value of the parameter for JNT is lower by 8% compared to swirling-type burners, due to a more advanced process of mixing and combustion, which is confirmed by the results of gas analysis of combustion products. As a result, there is no chemical underburning in the regimes corresponding to  $NO_x^{norm}$  due to higher levels of maximum temperatures, which in turn increases the emission of nitrogen oxides. The  $NO_x$  concentrations increase with increasing heat output of boilers ( $D_0$ ).

If we take the achieved level of nitrogen oxide emissions as a result of heat transfer by radiation from the torch to the waterwall tubes of the boiler ( $Q_{rad} = q_{rad} \cdot F_{tub}$ , where  $q_{rad}$  is the radiative heat flux,  $F_{tub}$  is the waterwall surface of the boiler furnace) the part of this heat-sink in relation to the heat-sink of the torch ( $Q_{heat} = q_v \cdot V_f$ ,  $q_v$  – furnace volumetric heat load,  $V_f$  – furnace volume), will be determined by the dimensions of the boiler.

The scale of the linear size of the furnace can be taken equal to  $L = V_f^{1/3}$ , then the ratio of heat fluxes will be simplified as follows:  $Q_{rad}/Q_{heat} = F_{tub}/V_f \approx 1/L$ . It can be assumed that the productivity of the boiler is proportional to the furnace volume ( $D_0 \sim L^3$ ), then ( $D_0 \sim L^3$ ),  $Q_{rad}/Q_{heat} \sim D_0^{-1/3}$ . As a result, there is a decrease in the flux of heat-sink from the torch with increasing dimensions of the boiler. Thus, the effective temperature of the torch increases and the levels of emissions of toxic nitrogen oxides rise too.

Forecasting of the emission properties for low power boilers ( $D_0 < 10 \text{ Gcal}$ ) can be done by the equation:

$$NO_x^{max} = a \cdot D_0^n \quad (1)$$

where  $a$  and  $n$  are selected individually for a certain type of equipment.

Forecasting of the emission properties for mean power boilers ( $11 < D_0 < 120 \text{ Gcal}$ ) is convenient to execute by equation:

$$NO_x^{max} = a \cdot D_0 / (b + c \cdot D_0), \quad (2)$$

where:  $a, b, c$  – empirical coefficients.

Thus, the calculated values of the maximum  $NO_x^{max}$  in Table 1 were obtained by equation (1) at:  $a = 100$ ,  $n = 0.27$  (for boilers KVG-7.56/6.5 and DKVR-10);  $a = 92$ ,  $n = 0.266$  (NIISTU-5);  $a = 50$ ,  $n = 0.27$  (KVN-2.9);  $a = 1000$ ,  $b = 30$ ;  $c = 2.77$  (KVG-20 and PTVM-50).

For determining the normalized value of  $NO_x^{norm}$  concentrations, it is advisable to apply the dependence (1), the values of the coefficients are as follows:  $a = 76$ ,  $n = 0.27$ .

The comparison of experimental and calculated values (Table 1) confirms a sufficient level of their coincidence. The data deviations can be explained by measurement errors and also by a number of unaccounted factors, such as: the life cycle of the facility, the design features of the combustion chamber, etc. The following formula is usable for determining the maximum value of  $NO_x$  concentrations on practice:

$$NO_x^{max} = K_d \cdot K_D \quad (3)$$

where  $K_d$  is the discrete influence parameter,  $K_D = a \cdot D_0^n$  – productivity parameter.

It is possible to get the characteristics of combustion solid and liquid fuels in a similar way. If the boiler productivity  $D_0$  is determined by the scale effect, then the influence of the load ( $N = (D/D_0) \cdot 100\%$ ) can be considered as the  $NO_x \sim q_v^{0.5}$ . In case if there is a correlation between the forcing of the furnace  $q_v$  and the boiler load, the corresponding emission characteristic is represented as a power dependence of the form:

$$NO_x = a \cdot (N/100)^n = a \cdot (D/D_0)^n \quad (4)$$

The coefficient  $a$  reflects the level of nitrogen oxides concentration at a nominal boiler load, taking into account the interaction of excess air factor and other discrete factors (burner type, fuel type, layout and number of switched burners, combustion chamber design features, etc.).

The results of technology implementation for natural gas combustion during depletion of air by combustion products on a boiler 9.2 MW are shown in fig. 3. The scheme is a self-recirculation and implemented on the water boilers with JNT burners type. 12-14% introduction of exhaust gases in the furnace space with blasting air reducing the content of nitric oxide in the combustion products almost 2.5 times. The emission reduction was achieved in the range of 2.8... 7.8% per 1% of recirculation gases.

The effect of suppression of  $NO_x$  concentration decreases due to increasing percentage of dilution of air with gases (Fig. 4).

The vitiated air with combustion products in a volume of more than 12% significantly reduces the suppression of  $NO_x$  emissions (oxygen content in the blast air less then 19%). In addition, increasing the percentage of recycling increases the emission of carbon monoxide  $CO$  (fig. 5).

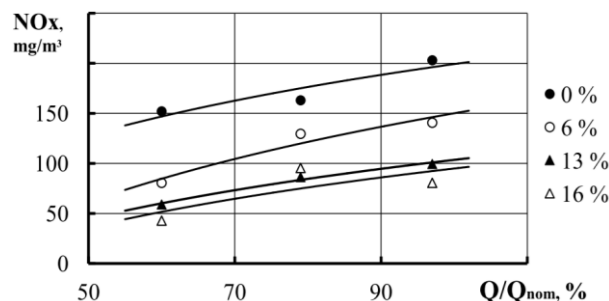


Fig. 3. Influence of boiler heat load and volume of recirculation gases for boiler DKVR-10 on  $NO_x$  concentration.

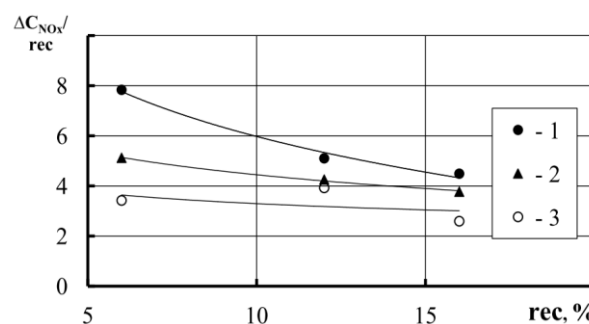


Fig. 4. Dependence of the nitrogen oxides concentration reduction on the volume of recirculation gases for boiler DKVR-10 when the heat load changes: 1 –  $N=60\%$ , 2 –  $N=97\%$ , 3 –  $N=79\%$ .

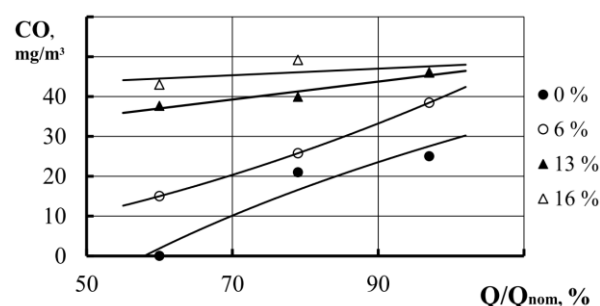


Fig. 5. Influence of boiler heat load and volume of recirculation gases for boiler DKVR-10 on carbon monoxide  $CO$  concentration.

The total  $NO_x$  concentration was reduced to 50...100  $mg/m^3$  (on some type units DKVR-10 a decrease in concentrations below 50  $mg/m^3$  was achieved). According to the gas analysis results, the maximum volume of recirculation gases do not lead to exceed the maximum allowable norms of carbon monoxide ( $C_{CO} < 90 mg/m^3$ ).

The stage of preparation for combustion and the high efficiency of mixture formation create the

necessary conditions for the organization of efficient microdiffusion combustion of the fuel mixture. The process of oxygen depletion of air is effectively regulated and limits the chemical underburning. The main factor is the high quality of the fuel mixture homogenization. The process of mixture preparing consist of two consistent stages. The blast air is ballasted with exhaust gases in the first stage and then gaseous fuel is mixed with the vitiated air in the second stage. Thus, unexcessive increase in  $C_{CO}$  or specific equipment features in terms of reducing the efficiency are limiting factors of volume of recirculation gases.

The boiler efficiency is directly dependent of the load. The most economical modes of operation for both units are at partial loads (Fig. 6).

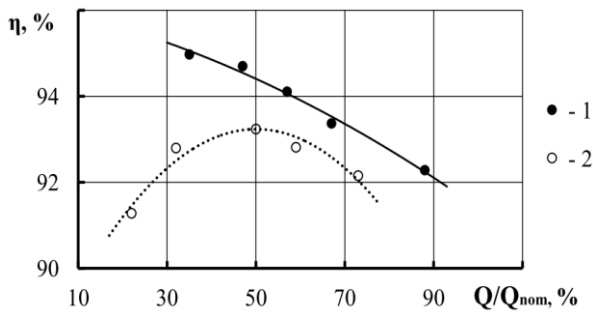


**Fig. 6.** Influence of boiler heat load on the efficiency of boiler units with exhaust gas recirculation for boilers: 1 – PTVM-50, 2 – KVGM-20.

The KVGM-20 characteristic has an extremum approximately on 50% of nominal loading whereas PTVM-50 characteristic monotonically decreases simultaneously with power increase. The maximum efficiency will be obtained in partial modes. It should be noted that equipment operates on the lowered loads on the main part of the heating period. Reliable forecasting method of  $NO_x$  emissions for medium and high capacity boilers due to the presence of various discrete effects is considered the ratio of the form:

$$NO_x = NO_x^{\max} K_N K_\alpha = K_d K_D K_N K_\alpha \quad (5)$$

It is hard to obtain emission characteristics in "pure" form for high-performance boilers due to the existence of different influences (recirculation, staged combustion, different layout and number of switched-on burners). For predicting the emission characteristics of a powerful boiler equipment, it is convenient to use the method of influences compensation in the form:

$$NO_x = NO_x^{\text{norm}} \prod_{i=1}^n K_i, \quad (6)$$

where  $K_i$  – corresponding emission parameter of nitrogen oxides impact.

For the PTVM-50 boiler as influential factors on the emission indicators are considered the following:

$$K_\alpha = \alpha^{5.5}; K_N = (D/D_0)^{1.15}; K_\delta = \exp[-0,257\Delta\bar{h}_\delta],$$

where  $\Delta\bar{h}_\delta$  – relative air supply bypassing the burners (does not apply to JNT burners);  $K_{\Delta V} = \exp[-0,2\Delta\bar{V}]$ ,  $\Delta\bar{V}$  – specific distribution of gas in tiers (evenly for JNT burners);  $K_r = \exp[-0,05r]$ ,  $r$  – degree of recirculation, %. Proposed coefficients taking into account the normalized value  $NO_x^{\text{norm}}$  are shown in Fig. 7

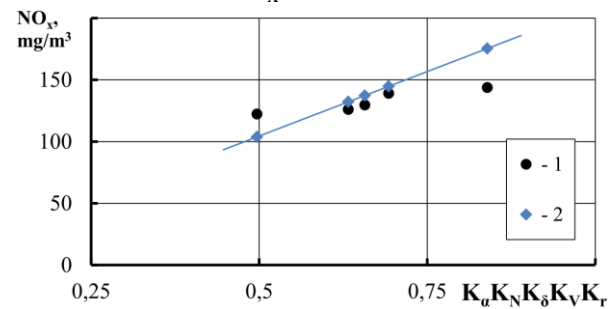


**Fig. 7.** Graphic interpretation of the influence of the compensation method for the PTVM-50 boiler – 1, prediction – 2.

## CONCLUSIONS

1. The versatile high-efficiency technology of fuel combustion was widely introduced. Today, a wide range of gas-consuming energy equipments has been modernized, including: boilers, furnaces, dryers, metallurgical facilities, etc. The possibilities of nitrogen oxides reduction by primary technological methods were identified. The first necessary step in the implementation of environmental standards is the recycling of combustion products into the furnace volume.

2. Efficiency of nitrogen oxides reduction by flue gases depends on the current power of the unit and the amount of ballasting oxidant. The percentage reduction of nitrogen oxides by one percent of recirculation gases is the value of  $C_{NO_x} = 2...8\%$ . The greatest value was achieved at partial loads when ballasting the air with gases by no more than 5-7% by volume. The introduction of ballast gases more than 12...14% significantly reduces the efficiency of the denitrification process for boilers with a thermal capacity less than 10 MW. The recirculation scheme was implemented on hot water boilers with a capacity of 0.5-56 MW on the basis of jet-niche technology. JNT shows by 1/3 higher efficiency of the recirculation scheme compared to swirling-type combustion systems due

to high-quality mixing processes. The actual concentration of nitrogen oxides does not exceed  $100 \text{ mg/m}^3$  (except for boiler PTVM -100).

3. Local emission characteristics of  $\text{NO}_x$  dependences on operational factors are purely individual. Characteristics are continuous and are determined by the indicator  $K_i = \varphi(f_i)$ . The influences compensation method can serve as a reliable tool for assessing the ecological performance in case of the presence of a sufficient amount of experimental data on the heat engineering setup of boiler equipment.

4. There are also discrete influences such as: type of boiler, design of furnace, type of fuel, layout of burners in the furnace, etc. The total parameter of influence could be more or less than 1.0.

5. The procedure of constructing a generalized ecological characteristic should be done by dependence (6). The normalized concentration of nitrogen oxides  $\text{NO}_x^{\text{norm}}$  is an objective criterion of ecological safety.

#### REFERENCES

1. Clean technology center, Nitrogen oxides ( $\text{NO}_x$ ), why and how they are controlled, EPA-456/F-99-006R. 1999. INTERNET / World Wide Web home page, <http://www.epa.gov/ttn/catc>.
2. J. Ma, Y. Hou, L. Shuyuan, W. Shang, *Carbon Resources Conversion*, **1** (1), 86 (2018).
3. A. M. Elbazab, H. A. Moneibb, K. M. Shebilb, W. L. Roberts, *Renewable Energy*, **138**, 303 (2019).
4. N. Frederick, R. K. Agrawal, P. E. Wood, S. C. Wood, Induced flue gas recirculation for  $\text{NO}_x$  control: Application on boilers and process heaters. Energy Texas Industries Press. R. 03 ETEC, 2004, p. 24.
5. S. G. Kobzar, A. A. Halatov, *Thermal Engineering*, **31** (4), 5 (2009).
6. V. R. Kotler, *Thermal Engineering*, **8**, 73 (2003).
7. M. Dutka, M. Ditaranto, T. Lovas, *Energies*, **8**, 3606 (2015).
8. R. Navrodska, N. Fialko, G. Presich, G. Gnedash, S. Alioshko, Sv. Shevcuk, E3S Web of Conferences, 100, 2019.
9. M. J. Landman, M. A. F. Derksen, J. B. W. Kok, *Combustion Science and Technology*, Pittsburgh, USA, **17**, 2006, p. 623.
10. D. Zhao, H. Yamashita, K. Kitagawa, N. Arai, T. Furuhashi, *Combustion and Flame*, **130**, 352 (2002).
11. T. Blejchař, J. Konvička, B. Heide, R. Malý, M. Maier, EPJ Web of Conferences, EFM, 2017, 2018.
12. J. L. Byeong, K. Ho-Chul, O. J. Jin, S. M. Young, *MDPI Catalysts*, **7**, 325 (2017).
13. R. Wang, X. Wu, Z. Chunlei, L. Xiaojian, D. Yali, *MDPI Catalysts*, **7**, 61 (2017).
14. M. Z. Abdulin, V. N. Petrenko, The Crimea, 2009, p. 28.
15. M. Z. Abdulin, O. A. Siryi, *Scientific Journal of Riga Technical University. Series: Power and Electrical Engineering*, **32**, 12 (2014).
16. <https://zakon.rada.gov.ua/laws/show/796-2017-%D1%80>
17. G. M. Lyubchik, *Energy: Economics, Technology, Ecology*, **1**, 48 (2002).

## Convective type models of chemical processes in column apparatuses

B. Boyadjiev, Chr. Boyadjiev\*

*Institute of Chemical Engineering, Bulgarian Academy of Sciences,  
1113 Sofia, Acad. St. Angelov str., bl.103, Bulgaria*

Received: August 1, 2020; Accepted: August 10, 2020

A new approach for the chemical processes modeling in column apparatuses is presented in industrial column apparatuses. An exact approach for solutions of the equations in the convective type models is used. The use of experimental data for the average concentration at the column end, for a concrete process and column, permits to obtain the model parameters related with the radial non-uniformity of the velocity. These parameter values permit to use the average-concentration model for modeling of chemical processes with different reaction rates.

## INTRODUCTION

The modeling and simulation of the chemical processes in column apparatuses is possible, using the new approach [1-3] on the basis of the physical approximations of the mechanics of continua, where the mathematical point (in the phase volume or on the surface between the phases) is equivalent to a small (elementary) physical volume, which is sufficiently small with respect to the apparatus volume, but at the same time sufficiently large with respect to the intermolecular volumes in the medium. On this base convection-diffusion and average-concentration type models are presented.

The convection-diffusion type models permit the qualitative analysis of the processes. These models are the base of the average-concentration models which allow a quantitative analysis of the chemical processes in column apparatuses [4].

In the case of the chemical reactions in industrial column apparatuses the effects of the

radial component of velocity and the axial diffusion transfer are not negligible and must be taken into account in the convection-diffusion and average-concentration type models [6]. The use of the perturbations method [4, 5] permits to obtain approximation solutions of the model equations. In this paper an exact approach for solutions of the equations in the convective type models of industrial chemical processes in column apparatuses will be presented.

*Convection-Diffusion Model*

A theoretical analysis of the effect of the radial velocity components and the axial diffusion transfer in industrial column chemical reactors will be presented in the case, when the radial velocity component is not equal to zero for pseudo-first order chemical reactions. In the stationary case, the convection-diffusion model [3, 4] has the form:

$$u \frac{\partial c}{\partial z} + v \frac{\partial c}{\partial r} = D \left( \frac{\partial^2 c}{\partial z^2} + \frac{1}{r} \frac{\partial c}{\partial r} + \frac{\partial^2 c}{\partial r^2} \right) - kc; \quad (1)$$

$$r = 0, \quad \frac{\partial c}{\partial r} \equiv 0; \quad r = r_0, \quad \frac{\partial c}{\partial r} \equiv 0; \quad z = 0, \quad c \equiv c^0, \quad u^0 c^0 \equiv u c^0 - D \frac{\partial c}{\partial z}.$$

$$\frac{\partial u}{\partial z} + \frac{\partial v}{\partial r} + \frac{v}{r} = 0; \quad r = r_0, \quad v(r_0, z) \equiv 0, \quad z = 0, \quad u = u(r, 0). \quad (2)$$

In (1, 2)  $c(r, z)$ ,  $D$ , are the concentrations [kg·mol·m<sup>-3</sup>] and the diffusivities [m<sup>2</sup>·s<sup>-1</sup>] of the reagents in the fluid,  $u(r, z)$  and  $v(r, z)$  - the axial and radial velocity components [m·s<sup>-1</sup>],  $(r, z)$  - the

radial and axial coordinates [m],  $k$  - chemical reaction rate constant,  $u^0, c^0$  - input ( $z=0$ ) velocity and concentrations.

The theoretical analysis of the model (1, 2) will be made using the generalized variables [1]:

\* To whom all correspondence should be sent:

E-mail: [boyadjiev.boyan@gmail.com](mailto:boyadjiev.boyan@gmail.com)

$$r = r_0 R, \quad z = lZ, \quad \varepsilon = \frac{r_0}{l}, \quad c(r, z) = c(r_0 R, lZ) = c^0 C(R, Z), \quad (3)$$

$$u(r, z) = u(r_0 R, lZ) = u^0 U(R, Z), \quad v(r, z) = v(r_0 R, lZ) = u^0 \varepsilon V(R, Z).$$

As a result, from (1-3) it may be obtained:

$$U \frac{\partial C}{\partial Z} + V \frac{\partial C}{\partial R} = \text{Fo} \left( \varepsilon^2 \frac{\partial^2 C}{\partial Z^2} + \frac{1}{R} \frac{\partial C}{\partial R} + \frac{\partial^2 C}{\partial R^2} \right) - \text{Da} C; \quad (4)$$

$$R = 0, \quad \frac{\partial C}{\partial R} \equiv 0; \quad R = 1, \quad \frac{\partial C}{\partial R} \equiv 0; \quad Z = 0, \quad C \equiv 1, \quad 1 \equiv U - \varepsilon^2 \text{Fo} \frac{\partial C}{\partial Z}.$$

$$\frac{\partial U}{\partial Z} + \frac{\partial V}{\partial R} + \frac{V}{R} = 0; \quad R = 1, \quad V(1, Z) \equiv 0; \quad Z = 0, \quad U = U(R, 0). \quad (5)$$

In (5) are used the parameters:

$$\text{Fo} = \frac{D_i l}{u^0 r_0^2}, \quad \text{Da} = \frac{kl}{u^0}, \quad (6)$$

where Fo and Da are the Fourier and Damkohler numbers, respectively. In industrial conditions the parameters  $\text{Fo} < 10^{-2}$  are small and the model (4) has a convective form:

$$U \frac{\partial C}{\partial Z} + V \frac{\partial C}{\partial R} = -\text{Da} C; \quad (7)$$

$$Z = 0, \quad C \equiv 1; \quad R = 1, \quad \frac{\partial C}{\partial R} \equiv 0.$$

#### Axial and Radial Velocity Components

The theoretical analysis of the change in the radial non-uniformity of the axial velocity component (effect of the radial velocity component) in a column can be made by an appropriate hydrodynamic model, where the average velocity at the cross section of the column is a constant (inlet average axial velocity component), while the radial non-uniformity of the axial velocity component decreases along the column height and as a result a radial velocity component is initiated. In generalized variables (3) the model can be used:

$$U = (2 - 0.4Z) - 2(1 - 0.4Z)R^2, \quad V = 0.2(R - R^3), \quad (8)$$

where the velocity components satisfy equation (5). The velocity components (8) are presented on Figs. 1, 2.

Eq. (7) is solved using the Method of Lines [6], by discretizing it in respect to  $R_i = i/n$ ,  $i = 0, \dots, n$ , with 3 points central finite difference scheme, thus transforming it from partial differential equation to a system of ordinary differential equations in respect to Z:

The problem (9) is stiff, that's why it is solved using MATLAB variable-step, variable-order solver ode15s, using second order backward

differentiation formulas (BDF, also known as Gear's method).

$$\begin{aligned} U(R_0, Z) \frac{dC_0}{dZ} &= -\text{Da} C_0; \\ U(R_i, Z) \frac{dC_i}{dZ} &= -V(R_i) \frac{C_{i+1} - C_{i-1}}{R_{i+1} - R_{i-1}} - \text{Da} C_i; \\ U(R_n, Z) \frac{dC_n}{dZ} &= -\text{Da} C_n; \\ Z = 0, \quad C_0 &\equiv 1, \quad C_i \equiv 1, \quad C_n \equiv 1; \quad i = 1, \dots, n-1. \end{aligned} \quad (9)$$

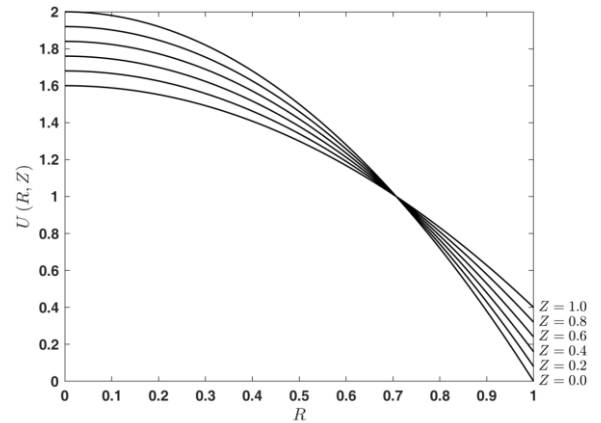


Fig. 1. Axial velocity component  $U(R, Z)$  for different  $Z = 0, 0.2, 0.4, 0.6, 0.8, 1.0$ .

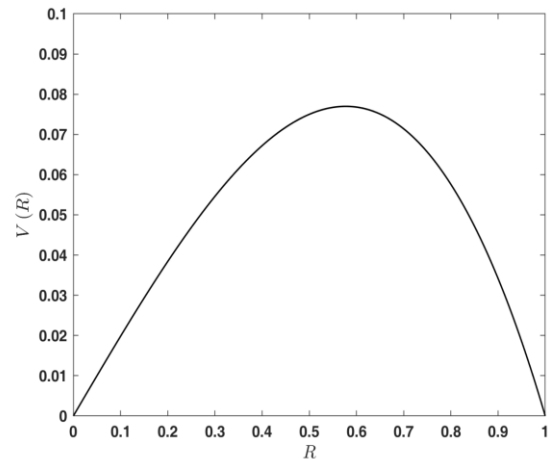
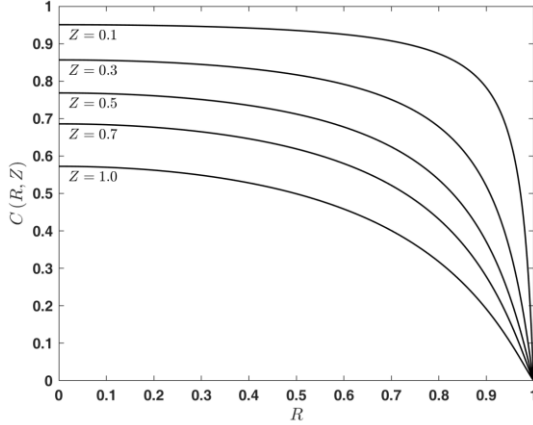


Fig. 2. Radial velocity component  $V(R)$ .

The solutions of (7) in the case  $Da=1$  are presented on Fig. 3.



**Fig. 3.** Concentration distributions  $C(R,Z)$  for different  $Z = 0.1, 0.3, 0.5, 0.7, 1.0$ .

#### Average-Concentration Model

The functions  $u(r,z), v(r,z), c(r,z)$  in (1) can be presented with the help of the average values of the velocity and concentration at the column cross-sectional area [1-3]:

$$z = lZ, \quad r = r_0R, \quad \bar{c}(z) = c^0 \bar{C}(Z), \quad \bar{C}(Z) = 2 \int_0^1 RC(R,Z) dR,$$

$$\tilde{c}(r,z) = \frac{c(r,z)}{\bar{c}(z)} = \frac{C(R,Z)}{\bar{C}(Z)} = \tilde{C}(R,Z), \quad \alpha(z) = A(Z) = 2 \int_0^1 RU(R,Z) \tilde{C}(R,Z) dR, \quad (14)$$

$$\beta(z) = \beta(lZ) = B(Z) = 2 \int_0^1 RU(R,Z) \frac{\partial \tilde{C}}{\partial Z} dR, \quad \gamma(z) = \gamma(lZ) = G(Z) = 2 \int_0^1 RV(R) \frac{\partial \tilde{C}}{\partial R} dR$$

and as a result:

$$A(Z) \frac{d\bar{C}}{dZ} + [B(Z) + G(Z)] \bar{C} = \varepsilon^2 Fo \frac{d^2 \bar{C}}{dZ^2} - Da \bar{C}; \quad (15)$$

$$Z = 0, \quad \bar{C} = 1, \quad \frac{d\bar{C}}{dZ} = 0.$$

In industrial conditions  $Fo < 10^{-2}$  and the model (15) has the convective form:

$$A(Z) \frac{d\bar{C}}{dZ} + [B(Z) + G(Z)] \bar{C} = -Da \bar{C}; \quad (16)$$

$$Z = 0, \quad \bar{C} = 1.$$

The solution of (7) and (14) permits to obtain the average concentrations (“theoretical” values)  $\bar{C}(Z_n)$  and functions  $A(Z_n), B(Z_n), G(Z_n)$ ,  $Z_n = 0.1(n+1)$ ,  $n = 0, 1, \dots, 9$ , which are presented (points) on Figs. 4, 5.

$$\bar{u} = \frac{2}{r_0^2} \int_0^{r_0} ru(r) dr, \quad \bar{c}(z) = \frac{2}{r_0^2} \int_0^{r_0} rc(r,z) dr, \quad (10)$$

i.e.

$$u(r,z) = \bar{u}U(R,Z), \quad v(r,z) = \varepsilon \bar{u}V(R), \quad c(r,z) = \bar{c}(z) \tilde{c}(r,z). \quad (11)$$

As a result, the following is obtained [3]:

$$\alpha(z) \bar{u} \frac{d\bar{c}}{dz} + [\beta(z) + \varepsilon \gamma(z)] \bar{u} \bar{c}_i = D \frac{d^2 \bar{c}}{dz^2} - k \bar{c}; \quad (12)$$

$$z = 0, \quad \bar{c} \equiv c^0, \quad \frac{d\bar{c}}{dz} \equiv 0,$$

where

$$\alpha(z) = \frac{2}{r_0^2} \int_0^{r_0} rU \tilde{c} dr, \quad \beta(z) = \frac{2}{r_0^2} \int_0^{r_0} rU \frac{\partial \tilde{c}}{\partial z} dr, \quad \gamma(z) = \frac{2}{r_0^2} \int_0^{r_0} rV \frac{\partial \tilde{c}}{\partial r} dr,$$

$$\tilde{c}(r,z) = \tilde{C}(R,Z), \quad U = U(R,Z), \quad V = V(R). \quad (13)$$

The theoretical analysis of the model (12) will be made using the following generalized variables and functions:

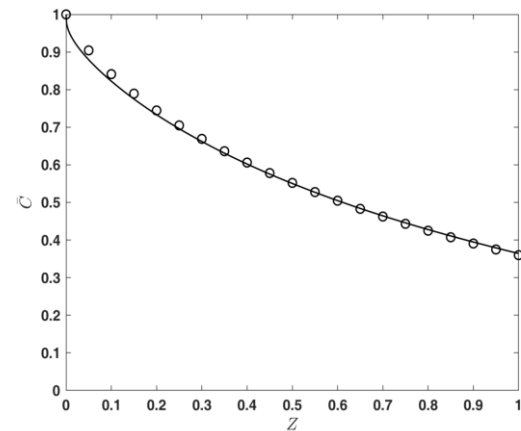


**Fig. 4.** Average concentrations  $\bar{C}(Z)$ : “theoretical” values  $\bar{C}(Z_n)$ ,  $Z_n = 0.1(n+1)$ ,  $n = 0, 1, \dots, 9$  (points); solution of (18) (lines)

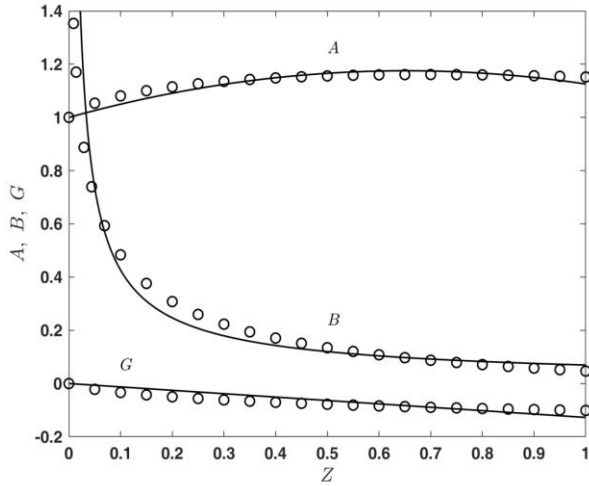


**Fig. 5.** Functions  $A(Z_n)$ ,  $B(Z_n)$ ,  $G(Z_n)$ ,  $Z_n = 0.1(n+1)$ ,  $n = 0, 1, \dots, 9$  (points) and their quadratic and linear approximations (17) (lines).

From Fig. 5 is seen, that the functions  $A(Z)$ ,  $B(Z)$ ,  $G(Z)$  can be presented as the following approximations:

$$A(Z) = 1 + a_1 Z + a_2 Z^2, \quad B(Z) = b_1 Z^{b_2}, \quad G(Z) = gZ. \quad (17)$$

As a result, the model (16) has the form:

$$\left(1 + a_1 Z + a_2 Z^2\right) \frac{d\bar{C}}{dZ} + (b_1 Z^{b_2} + gZ) \bar{C} = -Da \bar{C}; \quad (18)$$

$Z = 0, \quad \bar{C} = 1,$

where the parameters  $P(a_1, a_2, b_1, b_2, g)$  must be obtained using experimental data.

#### Parameters Identification

The value of the function  $\bar{C}(1)$  obtained from (7) and (14) permits to obtain the artificial experimental data  $\bar{C}_{\text{exp}}^m(1)$  for the column end ( $Z = 1$ ):

$$\bar{C}_{\text{exp}}^m(1) = (0.95 + 0.1B_m) \bar{C}(1), \quad m = 1, \dots, 10, \quad (19)$$

where  $0 \leq B_m \leq 1, m = 0, 1, \dots, 10$  are obtained by a generator of random numbers.

The obtained artificial experimental data (19) can be used for the illustration of the parameters  $P$  identification in the average concentrations model (18) by the minimization of the least-squares function:

$$Q(P) = \sum_{m=1}^{10} [\bar{C}(1, P) - \bar{C}_{\text{exp}}^m(1)]^2, \quad (20)$$

where the values of  $\bar{C}(1, P)$  are obtained after the solution of (17) for  $Z = 1$ .

The obtained (“experimental”) parameter values (Table 1) are used for the solution of (18) and the results (lines) are compared with the average

“theoretical” concentration values  $\bar{C}(Z_n)$ ,  $Z_n = 0.1(n+1)$ ,  $n = 0, 1, \dots, 9$  (points) on Fig. 4.

**Table 1.** Parameters  $P(a_1, a_2, b_1, b_2, g)$ .

Parameters	“Theoretical” values	“Experimental” values
$a_1$	0.5373	0.5850
$a_2$	-0.4118	-0.4226
$b_1$	0.0695	0.0697
$b_2$	-0.7878	-0.6726
$g$	-0.1274	-0.1361

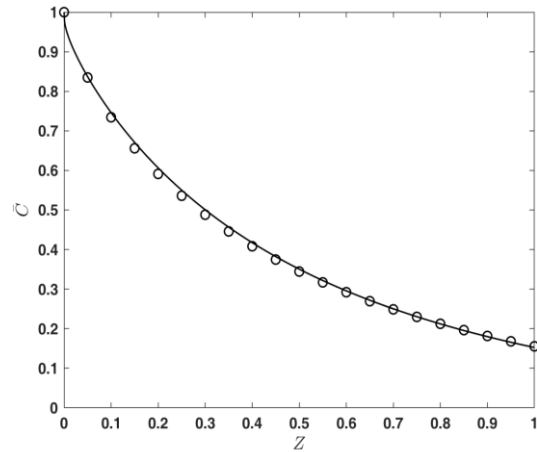


**Fig. 6.** Average concentrations  $\bar{C}(Z)$  for  $Da = 2$ : “theoretical” values  $\bar{C}(Z_n)$ ,  $Z_n = 0.1(n+1)$ ,  $n = 0, 1, \dots, 9$  (points); solution of (18) (lines).

#### Effect of the Chemical Reaction Rate

The effect of the chemical reaction rate will be obtained in the case when  $Da = 2$  in the models (7) and (18). The solution of (7) and (14) permits to obtain the theoretical values of the average concentration (points), which are compared (Fig. 6) with the solution of the average-concentration model equation (18), where the obtained experimental parameters values (Table 1) are used.

#### CONCLUSIONS

A new approach for the chemical processes modeling in column apparatuses, is presented in industrial column apparatuses. An exact approach for solutions of the equations in the convective type models is used. The use of experimental data, for the average concentration at the column end, for a concrete process and column, permits to obtain the model parameters related to the radial non-uniformity of the velocity. These parameter values permit to use the average-concentration model for modeling of chemical processes with different reaction rates.

#### NOTATIONS

- $c(r, z)$  – concentration [kg·mol·m<sup>-3</sup>]  
 $D$  – diffusivity [m<sup>2</sup>·s<sup>-1</sup>]  
 $u(r, z)$  – axial velocity component [m·s<sup>-1</sup>]  
 $v(r, z)$  – radial velocity component [m·s<sup>-1</sup>]  
 $(r, z)$  – radial and axial coordinates [m]  
 $k$  – chemical reaction rate constant [s<sup>-1</sup>]  
 $Fo$  – Fourier number  
 $Da$  – Damkohler number

**Acknowledgements:** *this work is supported by the project of fundamental scientific research 19-58-18004, conducted by RFBR and the National Science Fund of Bulgaria under contract no KP 06 RUSIA-3 from 27 Sep. 2019, “Modeling, simulation and experimental investigations of the interphase mass transfer and separation in distillation, absorption, adsorption and catalytic processes in industrial column apparatuses”.*

#### REFERENCES

1. Chr. Boyadjiev, Theoretical Chemical Engineering. Modeling and Simulation, Springer-Verlag, Berlin Heidelberg, 2010.
2. Chr. Boyadjiev, M. Doichinova, B. Boyadjiev, P. Popova-Krumova, Modeling of Column Apparatus Processes, Springer-Verlag, Berlin Heidelberg, 2016.
3. Chr. Boyadjiev, M. Doichinova, B. Boyadjiev, P. Popova-Krumova, Modeling of Column Apparatus Processes (Second edn.), Springer-Verlag, Berlin Heidelberg, 2018.
4. B. Boyadjiev, Chr. Boyadjiev, *Bulg. Chem. Commun.*, **49** (3), 706 (2017).
5. Chr. Boyadjiev, B. Boyadjiev, *Bulg. Chem. Commun.*, **50**, Special Issue K, 7 (2018).
6. W. E. Schiesser, The Numerical Method of Lines, Academic Press, San Diego, 1991.

## Computer modeling of plate heat exchanger for heat utilization from exhaust gases of drying process

P. O. Kapustenko<sup>1</sup>, L. L. Tovazhnyansky<sup>1</sup>, O. P. Arsenyeva<sup>2</sup>, S. K. Kusakov<sup>3</sup>, V. V. Zorenko<sup>3</sup>, O. Y. Fedorenko<sup>1</sup>

<sup>1</sup>National Technical University, Kharkiv Polytechnic Institute, Dept. ITPA, CRMGET, Kharkiv, Ukraine

<sup>2</sup>O. M. Beketov Kharkiv National University, Kharkiv, Ukraine

<sup>3</sup>AO Spivdruzhnist-T LLC, Kharkiv, Ukraine

Received: August 02, 2020 Accepted: August 10, 2020

Based on the mathematical model published in a previous paper for the models of PHE channels corrugated field, a mathematical model of the thermal and hydraulic performance of PHE assembled from commercially produced plates is developed. It accounts for processes at the main corrugated field and also in PHE collectors and channels distribution zones. The results of mathematical modeling are compared with data obtained on a pilot unit for utilization of waste heat from gases coming after tobacco drying. The PHE type TS-6MFG produced by AlfaLaval is tested. The content of the air in the coming air-steam mixture was 10 % at a temperature of 140 °C. The comparison of modeling results and tests data showed good accuracy of prediction. It allowed recommending the obtained correlations and developed mathematical model for the design of plate heat exchangers in applications with heat utilization from exhaust gases after drying processes in the industry.

**Keywords:** Plate heat exchanger, condensation, noncondensing gas, heat and mass transfer, mathematical model, pressure loss.

### INTRODUCTION

Many process technologies require cooling of the gaseous streams, which involves phase change when the working fluids are cooled to the temperatures below the saturation point. It exceeds the heat load of the heat transfer equipment as the latent heat of condensable components is also involved. The process of gaseous stream cooling can be single phase, a process of one component condensation or a process of gaseous mixture condensation, containing condensable and non-condensable components. The presence of condensable vapor in the gas can increase the efficiency of the process, namely in boilers it can lead to 10-12 % raise of condensation of flue gas [1], in ventilation systems it ensures an increased amount of recovered heat [2]. On the other side of the concentration range the content of 0.5 % of non-condensable gas (NCG) in water vapor can lead to a decrease of heat transfer coefficient down to 50% [3]. The vapor condensation from its mixture was studied by many researchers and revealed its importance for refrigeration systems [4], CO<sub>2</sub> and H<sub>2</sub>O separation [5], utilisation of heat from flue gases [6] and exhaust gases of combustion engines [7] and others.

The present requirements for higher energy efficiency stipulated the application of more advanced compact heat exchangers with enhanced

heat transfer for heat recuperation.

A plate heat exchanger (PHE) corresponds to these requirements in a number of industrial applications. Its construction and operation are sufficiently well described in the literature [8]. PHE has a number of advantages over conventional shell-and-tube heat exchangers. It has smaller size and inventory volume, lower cost, lower fouling, flexible design, access for mechanical surface cleaning, and small temperature approach of streams, down to 1 °C. The heat transfer enhancement allows them to have a smaller heat transfer surface area for the same working conditions. Such features render economically favorable solutions in a number of applications in industry, as, e.g. in CO<sub>2</sub> post-combustion capture plants [9], for heat utilization from exhaust gases [10].

The correct selection of a PHE for specific duty necessitates accounting of all factors influencing its performance, including the construction features of a heat exchanger. The PHE consists of corrugated plates, which as assembled in a pack are forming channels of intricate geometry (see Fig. 1) that promote high levels of turbulence in flows of heat exchanging streams stipulating heat and mass transfer enhancement.

For the accurate design of the PHE used for the condensation of vapor from its mixture with a noncondensing gas, all important factors affecting its performance should be accounted for.

\* To whom all correspondence should be sent:

E-mail: [sodrut@gmail.com](mailto:sodrut@gmail.com)

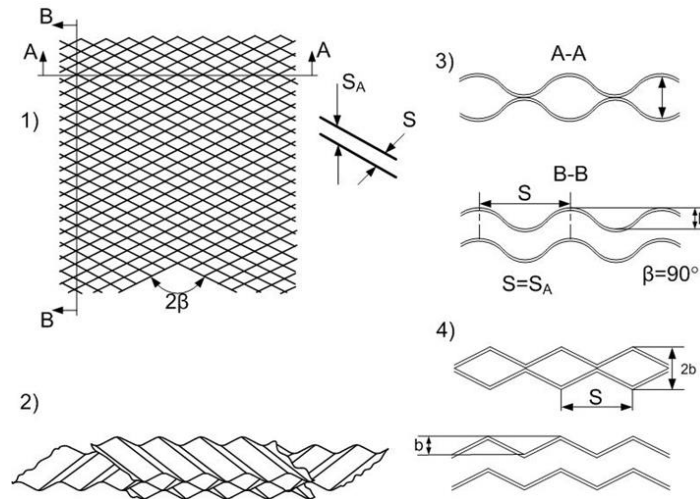


**Fig. 1.** Scheme of PHE channel corrugated field with various form of plates corrugations: 1, 2 – two neighbor plates intersection; 3 – channels cross-section with sinusoidal corrugations; 4 – channels cross-section with triangular corrugations.

The study of condensation processes in pipes [3] showed that the physical properties of gas and vapor, their concentrations, as well as the geometry of channels and process behavior along the heat transfer surface influence the process intensity. The design of PHEs for cooling a gaseous mixture needs the estimation of heat and mass transfer coefficients and pressure losses in channels, what consists of the following calculations: (1) film heat transfer coefficients at the cooling side, (2) thermal resistance in the condensate film, (3) mass and heat transfer in the vapor-gas mixture and (4) pressure losses in a two-phase flow of gases and liquid.

To calculate the film heat transfer coefficients at the cooling side and the thermal resistance in a condensate film, heat and mass transfer in the condensing flow, the pressure loss in a two-phase flow, the single-phase correlations are needed. The studies of heat transfer and pressure drop in complex criss-cross channels of PHEs are still under investigation and are reported, e.g. for specific plate types [11], or generalized correlations for different corrugations geometries [12], influence of different plate zones on pressure losses in channels for commercial plates [13, 14].

To calculate the heat transfer coefficient in the condensate film, the relations for pure vapor condensation are used. The condensation mechanism is clearly described in [15]. A study of steam condensing in PHE channels is presented in [16]. A review of researches on condensation in PHE channels is given in [17]. For shear driven condensate film flow, the equation based on a homogeneous-dispersed model in the main flow and condensate film flow on the walls is proposed in [18]. The process of heat and mass transport in the gas phase can be estimated by the correlations

for the single-phase applying the heat and mass transfer analogy, as analyzed in [19]. Its experimental validation for a small mass flux is reported in [20].

The estimation of pressure losses in a two-phase flow is crucial for the design of PHEs used for condensation. The designed value of pressure drop in PHE unit determines the condensation process in the channels by interacting the driving forces of heat and mass transfer along the plate length due to the vapor equilibrium. Some empirical correlations for condensation for the range of experimental conditions regarding pressure loss for the whole channel length are given in [21]. In [22] the map of different flow regimes for a two-phase flow in PHE channels is presented. The accuracy of pressure loss estimation in a -phase flow depends on how the model corresponds to the experimental conditions.

The state-of-the-art research analysis shows the gap between the data available in literature for laboratory researches and modeling of heat and mass transfer and hydraulic resistance during condensation of gas-vapor mixtures and their validation in industrial conditions, especially for PHE channels of intricate geometry.

In the present paper, a mathematical model proposed in [23] for the models of criss-cross channels is further developed for the thermal design of PHE with commercial plates used for the condensation process. It gives the possibility to determine the process parameters along the channel length and to confirm the accuracy of correlations for pressure losses. The case study of tobacco drying process with application of PHE for condensation of exhaust gases for waste heat utilization is presented.

Model of PHE for Condensation of Gas-Vapor Mixture

The mathematical model of a PHE for condensation based on experimental data, presented in [24] was further improved for the use with commercially produced plates. The main difference of commercially produced plates for PHEs from considered experimental models consists in the design features for flow distribution along the channel and between them. The streams are coming into the PHE via connections and are distributed between the channels by collectors organized in the assembled PHE by an arrangement of gaskets around portholes of plates, the flow is distributed from portholes to the main corrugated field by distribution zones as shown in Fig. 2. In the proposed model, the maldistribution of flow between the channels is not accounted for, and the flow rates in all channels are assumed as equal.

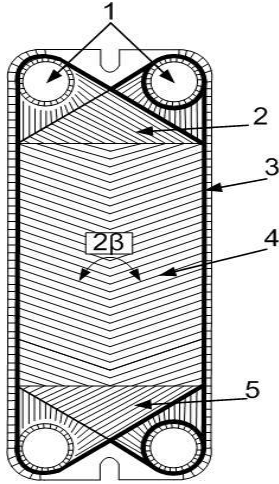


Fig. 2. Schematic drawing of a PHE plate: 1 – heat carrier inlet and outlet; 2,5 – zones for flow distribution; 3 – rubber gasket; 4 – main corrugated field.

It is assumed that the heat and mass transfer processes in all PHE channels are described by correlations and equations determined for the main corrugated field of the channels area. Therefore, the mathematical model presented in paper [24] for criss-cross flow channels with specific geometry is valid also for a PHE with commercial plates having the same corrugation geometry. Another feature difference is the introduction of a more accurate method accounting for the influence on mass transfer of transverse mass flux presented in paper [23] as follows:

The parameter  $\Psi_D$  is introduced as the correction factor:

$$\beta_D = (D_D / d_e) \cdot \Psi_D \cdot Sh_0 \quad (1)$$

Here  $D_D$  is the mass diffusivity  $m^2/s$ ;  $\beta_D$  is the mass transfer coefficient,  $m/s$ ;  $Sh_0$  is the Sherwood

number calculated by heat and mass transfer analogy:

$$Sh_0 = \frac{\beta_{D0} \cdot d_e}{D_D} = 0.065 \cdot Re^{0.7} \cdot \left( \frac{\psi \cdot \zeta}{F_x} \right)^{3/7} \cdot Sc^{0.4} \quad (2)$$

where  $Sc = \mu / (\rho D_D)$  is the Schmidt number;  $F_x$  is area enlargement factor;  $Re$  is the Reynolds number calculated with the channel equivalent diameter.

For accounting the effect of transverse mass flux and the variation of air-stream mixture density from flow core to liquid film surface, the correction coefficient is calculated according to the following equation:

$$\Psi_D = \frac{\ln(1 + B_m)}{B_m} \cdot 4 \cdot \left( 1 + \sqrt{\frac{\rho_{mx}}{\rho_{mx-f}}} \right)^{-2} \quad (3)$$

where  $\rho_{mx}$  and  $\rho_{mx-f}$  are the densities of the gas-vapor mixture at the main flow and at condensate film surface, respectively,  $kg/m^3$ ;  $B_m$  is mass transfer driving force:

$$B_m = \frac{m_v - m_{v-f}}{m_{v-f} - 1} \quad (4)$$

Here  $m_v$  and  $m_{v-f}$  are mass fractions of vapor in the flow core and on the surface of the liquid film. The calculations of pressure during the gas-vapor condensation process at the channels main corrugated field is performed with the mathematical model described in [23] that is validated for the experimental models of PHE channel corrugated field as follows.

The total pressure loss in two-phase flow  $P_{mx}$  (the first term is for friction losses, the second term is for the acceleration due to change of velocity, and the third term is for geometrical elevation):

$$\frac{dP_{mx}}{dx} = \frac{dP_{TP}}{dx} - \frac{d}{dx} \left( \frac{\rho_{mx} \cdot W_{mx}^2}{2} \right) - \frac{d}{dx} \left( \frac{\rho_{mx} \cdot g \cdot x}{2} \right) \quad (5)$$

where  $\rho_{mx}$  is density of gaseous mixture,  $kg/m^3$ ;  $W_{mx}$  is flow velocity of gaseous mixture,  $m/s$ ;  $x$  is longitudinal coordinate,  $m$ ;  $g$  is gravity force,  $m^2/s$ ;  $P_{mx}$  is the pressure of condensing flow,  $Pa$ ;  $dP_{TP}/dx$  is pressure loss due to friction (including form drag) in two-phase flow,  $Pa$ .

For calculation of the pressure losses in condensing two phase flow at PHE channel the combination of two approaches was used. The first one for separate flow of phases is based on Lockhart-Martinelli parameters in the following form:

$$X_{LM} = \sqrt{\frac{dP_L \cdot \phi_L}{dP_G \cdot \phi_G}}; \quad \Phi_G = \sqrt{\frac{dP_{TP}}{dP_G}}; \quad \Phi_L = \sqrt{\frac{dP_{TP}}{dP_L}}; \quad (6)$$

Here  $dP_L$  and  $dP_G$  are pressure losses of liquid and gas flowing alone in the channel calculated by correlation for single-phase flow,  $Pa$ :

$$dP = \frac{1}{2} \zeta \cdot \rho \cdot W^2 \cdot \frac{dx}{d_e} \quad (7)$$

where  $W$  is the velocity of single-phase flow in a channel, m/s;  $d_e$  is channel equivalent diameter, m;  $\zeta$  is friction factor coefficient;  $\phi_L$  and  $\phi_G$  are the share of friction losses in total pressure losses for liquid and gas flowing in channel alone, respectively.

The second approach for pressure loss calculation is based on dispersed-annular flow model and the correlation proposed in the paper by Boyko and Kruzhilin for two phase condensing flow in tubes [25]:

$$dP_{TP} = dP_{OL} \cdot \left[ 1 + x_{TP} \cdot \left( \frac{\rho_L}{\rho_{mx}} - 1 \right) \right] \quad (8)$$

Here  $dP_{OL}$  is pressure loss in single-phase flow of liquid determined on a total flow rate of two-phase flow, Pa;  $\rho_L$  is density of liquid, kg/m<sup>3</sup>;  $x_{TP}$  is gas phase mass share in two-phase mixture.

As the application of these approaches separately for all channel length give significantly different and not accurate results for varied types of corrugation, in [23] the improved correlation was proposed, which can account both models of flow structure.

For the channel parts close to the entrance of gas-vapor mixture, where Reynolds numbers calculated for liquid only flowing in channel  $Re_L \leq 125$  the following Equation is applied:

$$\Phi_G^2 = 1 + 255 \cdot X_{LM} + X_{LM}^2 \quad (9)$$

For all other channels equation (10) combining both approaches and also accounting for the influence of surface tension forces is used:

$$dP_{TP} = dP_L \cdot \sqrt{1 + x_{TP} \cdot \left( \frac{\rho_L}{\rho_{mx}} - 1 \right)} \cdot \left( 1 + \frac{7.3 \cdot We^{-0.24}}{X_{LM}} + \frac{0.03}{X_{LM}^2} \right) \quad (10)$$

Here the Weber number is determined as:

$$We = \frac{\rho_{mx} \cdot W_{mx}^2 \cdot d_e}{\sigma} \quad (11)$$

where  $\sigma$  is the surface tension of the liquid, N/m.

The driving forces of heat and mass transfer processes during the condensation of a gas-vapor mixture are influenced by the pressure of the condensing stream due to the pressure effect on vapor partial pressure and saturation temperature. The thermal design of a PHE should take into account the change of pressure at the inlet parts of the PHE and inter-plate channels. The pressure losses at collector inlet, the inlet port and inlet distribution zones can be calculated according to the approach given in [14] for a single-phase flow

in a PHE. Here the assumption that the friction pressure loss in a single-phase flow is the same at ports and collectors at the inlet and at the outlet is taken. The recovery of pressure due to the difference of velocities in the collector and in channels must also be considered. When coming to the PHE, where the gas-vapor mixture contains no liquid phase, the pressure loss at the entrance can be calculated as for a single-phase flow. Then the change of pressure at the PHE channel entrance, before the gas-vapor mixture is entering the main corrugated field is calculated according to:

$$\Delta P_{mx.in} = \zeta_{DZin} \cdot \frac{\rho_{mx.in} \cdot W_{mx.in}^2}{2} + 0.65 \cdot \frac{\rho_{mx.in} \cdot W_{pc.in}^2}{2} + \frac{\rho_{mx.in}}{2} \cdot (W_{mx.in}^2 - W_{pc.in}^2) \quad (12)$$

where  $W_{pc.in}$  is the velocity of flow in entrance ports, m/s;  $W_{mx.in}$  is the velocity of the gas-vapor mixture at the entrance of the main corrugated field, m/s;  $\rho_{mx.in}$  is the density of the incoming gas-vapor mixture, kg/m<sup>3</sup>.

For accounting the local pressure losses, the pressure at the entrance to the main corrugated field  $P_{mx.cfl}$  is determined by subtraction of pressure drop at the channel entrance from pressure  $P_{mx.in}$  at the PHE inlet:

$$P_{mx.cfl} = P_{mx.in} - \Delta P_{mx.in} \quad (13)$$

The total pressure drop in the PHE also includes the pressure loss in the exit distribution zone, port and collector. These pressure drops are determined as local hydraulic resistances calculated on the condensed liquid velocity with a correction factor  $(dP_{TP}/dP_L)_{out}$ , calculated for the closest to the exit section of a channel as follows:

$$\Delta P_{mx.out} = \left( \zeta_{DZout} \cdot \frac{\rho_{L.out} \cdot W_{L.out}^2}{2} + 0.65 \cdot \frac{\rho_{L.out} \cdot W_{Lpc.out}^2}{2} \right) \times \left( \frac{dP_{TP}}{dP_L} \right)_{out} \quad (14)$$

In eq. (14)  $W_{L.out}$  is the velocity calculated for a liquid phase moving alone at the channel exit, m/s;  $W_{Lpc.out}$  is the velocity calculated for a liquid phase moving alone in channel exit port, m/s;  $\rho_{L.out}$  is the density of outgoing liquid phase, kg/m<sup>3</sup>.

The values of the coefficients of local hydraulic resistance at inlet and outlet distribution zones,  $\zeta_{DZin}$  and  $\zeta_{DZout}$  are taken equal to 38, in accordance with data from [14] for a single-phase flow in a PHE with commercial plates. The total pressure drop of a condensing gas-vapor mixture in a PHE by accounting for velocity change at the channel exit is:

$$\Delta P_{mx.PHE} = \Delta P_{mx.in} + \int_0^{L_{pl}} \left( \frac{dP_{TP}}{dx} \right) \cdot dx + \Delta P_{mx.out} + \frac{\rho_{mx.out}}{2} \cdot (W_{pc.out}^2 - W_{mx.out}^2) \quad (15)$$

where  $W_{mx.out}$  is gas-vapor mixture velocity at the channel exit, m/s;  $W_{Lpc.out}$  is gas-vapor mixture

velocity in channel exit port, m/s;  $\rho_{mx.out}$  is the density of the outgoing gas-vapor mixture, kg/m<sup>3</sup>;  $x$  is the distance from gas-vapor mixture entrance to channel, m.

For the thermal design of a PHE, mathematical modeling of heat and mass transfer is performed by the equations of the one-dimensional mathematical model proposed in [23]. The heat and mass transfer correlations are taken according to geometrical parameters of corrugations on the main corrugated field with heat transfer area of one plate equal to its total heat transfer area. The calculations were performed for the PHE installed in the industry as is reported in the following case study to check the model validity.

#### *Industrial PHE Test*

The use of a PHE for utilization of waste heat from exhaust gases after the drying process at an operating tobacco factory was reported in [10]. At the existing drying plant crushed raw tobacco with a moisture content of about 22.5 % is fed to a drying tunnel, to which superheated steam at a temperature of 180 °C is supplied. In this tunnel, the water inside the tobacco particles boils up, increasing the volume of the particle and partly evaporates to the mainstream. After being kept in the tunnel for about 6–7 s the tobacco particles are separated by precipitation in the cyclone. Tobacco is discharged from the cyclone with a rotary discharger leaving it with 14.5 % moisture content. The remaining steam-air mixture is circulating in the drying circuit, passing through a heat exchanger to maintain the required temperature.

Part of the steam-air mixture containing part of injected steam and steam evaporated from tobacco is discharged into the atmosphere through the adjusting valve. The flow rate of the outgoing part of the steam-air mixture varies from 0.264 to

0.306 kg/s, and its temperature is 140 °C. It is about 15–19 % of the circulating stream. These exhaust gases are used to heat up an ethylene glycol solution circulating in the heating system of factory workshops and administrative building. PHE AlfaLaval production type TS6M-FG is used for this purpose. The parameters of the PHE and its plates are presented in Table 1.

The measurements of process parameters at the inlet and outlet of the tested PHE were performed during the operation of the drying unit. The results of measurements for four test runs are presented in Table 2. The results of process modeling with the presented mathematical model are also given. The calculations were performed for the measured values of stream flow rates and their parameters at the inlet of the PHE. The calculated outlet temperatures and pressures of the steam-air mixture are also presented in Table 2.

The calculated distribution of process parameters along the length of the PHE channel is presented in Fig. 3 for the conditions of test #2. At the sections of the channel close to the inlet of the steam-air mixture, up to about 0.25 of the relative channel length ( $x/L_{pl}$ ), there is a steep decrease of gaseous mixture temperature. In this zone, the steam-air mixture is overheated above its saturation temperature.

The cooling of the gaseous mixture in this zone is happening mostly by convection heat transfer from the flow bulk to the channel wall with some condensation at the wall, which temperature is lower than the steam saturation temperature. After the saturation temperature is reached the rate of temperature change decreases and after the equilibrium conditions, it increases again towards the channel exit with increasing air content in the mixture.

**Table 1.** Main characteristics of the tested PHE TS6M-FG

Parameter	Value
Total number of plates $N$	50
Heat transfer area of PHE $F_{PHE}$ , m <sup>2</sup>	4.80
Heat transfer area of one plate $F_{pl}$ , m <sup>2</sup>	0.0850
Channel cross section area, m <sup>2</sup>	0.001080
Plate length $L_{pl}$ , m	0.270
Plate width $W_{pl}$ , m	0.276
Area enlargement factor $F_x$ , m/m	1.140
Corrugation pitch $S$ , mm	14.0
Corrugation height $b$ , mm	3.90
Corrugation angle to plate vertical axis $\beta$ , degrees	60

**Table 2.** Process parameters

Process parameter	Test #1	Test #2	Test #3	Test #4
Steam-air: flow rate, kg/s	0.2640	0.2780	0.2920	0.3060
inlet temperature, °C	140.0	140.0	140.0	140.0
inlet pressure, Pa	132,000	132,000	131,000	130,000
outlet temperature (measured), °C	76.1	79.1	79.6	81.5
outlet temperature (calculated), °C	75.7	77.9	80.1	82.08
error in outlet temperature), °C	-0.4	-1.2	+0.5	+0.58
pressure drop (measured), Pa	10.10	10.40	12.00	14.40
pressure drop (calculated), Pa	10.21	11.19	12.32	13.51
error in pressure drop, %	+1.1	+7.6	+2.7	-6.2
Cooling media: flow rate, kg/s	7.80	7.80	7.80	7.80
inlet temperature, °C	50.0	50.0	50.0	50.0
outlet temperature (measured), °C	68.0	69.0	69.3	69.5
outlet temperature (calculated), °C	67.41	68.21	68.91	69.61
Total heat load: measured, W	75,23	79,41	80,64	81,50
calculated, W	72,710	76,07	78,97	81,92
Error in heat load, %	-3.3	-4.2	-2.1	+0.5

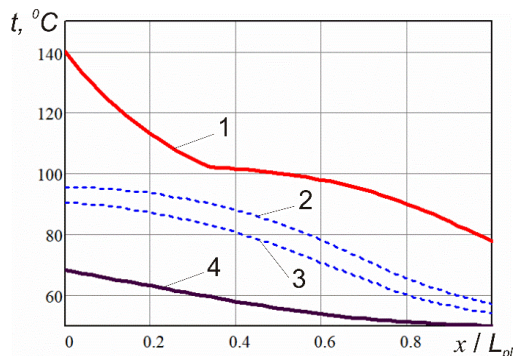


**Fig. 3.** Distribution of temperatures  $t$  along PHE channels relative distance from the entrance of gas-vapor mixture ( $x/L_{pi}$ ) in test #2: 1 – steam-air mixture; 2 – condensate film surface; 3 – wall; 4 – cooling media

The calculated temperature at the channel exit is lower than its measured value by 1.2 °C; in the other three test runs (see Table 2) this difference is not higher than this value. The difference between the calculated and experimental values of the heat load is less than 4.2 %. This accuracy of thermal modeling of steam-air mixture condensation in the PHE assembled with commercially manufactured plates. The accuracy of predicting the pressure drop is also not exceeding 7.6 %. It is acceptable for practical engineering applications.

## CONCLUSIONS

The mathematical model of a PHE accounting for the pressure losses in commercially produced plates is developed and approved for the condensation process using the steam-air gaseous mixture with steam partial condensation as a working fluid. The model validation was performed for the design of the commercially produced PHE installed for heat utilization from exhaust gases coming after the process of tobacco drying at an operating factory. The analysis of modeling results revealed a considerable change of process parameters along the length of PHE channels starting with the cooling of the superheated gaseous mixture at about 1/3 of the PHE surface followed by condensation of steam from a saturated mixture. The developed mathematical model can be used for the design of PHEs in the processes of waste heat utilization from the gaseous stream in different industrial applications and widen the use of PHEs in such conditions

## REFERENCES

1. H. Satyavada, S. Baldi, *Energy*, **142**: 121 (2018).
2. S. Gendebien, S. Bertagnolio, V. Lemort, *Energy and Buildings*, **62**, 176 (2013).
3. J. Huang, J. Zhang, L. Wang, *Applied Thermal Engineering*, **89**, 469 (2015).

4. A. Charef, et al., *Heat and Mass Transfer*, **54**(4), 1085 (2018).
5. M. Ge, et al., *Experimental Thermal and Fluid Science*, **75**, 147 (2016).
6. I. Zeynali Famileh, J. Abolfazli Esfahani, *International Journal of Heat and Mass Transfer*, **108**, 1466 (2017).
7. K. K. Srinivasan, P. J. Mago, S. R. Krishnan, *Energy*, **35**(6), 2387 (2010).
8. J.J. Klemes, et al., *Compact Heat Exchangers for Energy Transfer Intensification: Low Grade Heat and Fouling Mitigation*, CRC Press, 2015, p.3 54.
9. O.Y. Perevertaylenko, et al., *Energy*, vol. page (2015).
10. O.P. Arsenyeva, et al., *Frontiers of Chemical Science and Engineering*, **10**(1), 131 (2016).
11. B. Kumar, A. Soni, S. N. Singh, *Experimental Thermal and Fluid Science*, **91**, 126 (2018).
12. P. Kapustenko, O. Arsenyeva, O. Dolgonosova. in *PRES'11: 14th Conference on Process Integration, Modelling and Optimisation for Energy Saving and Pollution Reduction*, Firenze, Italy, Chemical Engineering Transactions, 2011.
13. S. Gusew, R. Stuke, *International Journal of Chemical Engineering*, **2019**, 3693657 (2019).
14. O. Arsenyeva, et al., *Energy*, **57**, 201 (2013).
15. V.P. Carey, *Liquid-Vapor Phase-Change Phenomena: An Introduction to the Thermophysics of Vaporization and Condensation Processes in Heat Transfer Equipment*, Third edn., CRC Press, 2020:
16. S. Hu, X. Ma, W. Zhou, *Applied Thermal Engineering*, **113**, 1047 (2017).
17. R. Eldeeb, V. Aute, R. Radermacher, *International Journal of Refrigeration*, **65**, 12 (2016).
18. L. Tovazhnyansky, et al., *Applied Thermal Engineering*, **31**(13), 2146 (2011).
19. W. Ambrosini, et al., *Nuclear Engineering and Design*, **236**(9), 1013 (2006).
20. K. S. Kulkarni, et al., *International Journal of Heat and Mass Transfer*, **113**, 84 (2017).
21. S. B. Al-Shammari, D. R. Webb, P. Heggs, *Desalination*, **169**(2), 151 (2004).
22. X. Tao, M. P. Nuijten, C. A. Infante Ferreira, *International Journal of Refrigeration*, **85**, 489 (2018).
23. P. O. Kapustenko, et al., *Energy*, **201**, 117661 (2020).
24. L. Tovazhnyansky, et al., *Bulg. Chem. Commun.*, **50**, 76 (2018).
25. L. D. Boyko, G. N. Kruzhilin, *International Journal of Heat and Mass Transfer*, **10**(3), 361 (1967).

## Dynamic hold-up of modern high-performance packings

Sv. Ts. Nakov, D. B. Dzhonova-Atanasova\*, E. N. Razkazova-Velkova

*Institute of Chemical Engineering, Bulgarian Academy of Sciences,  
Acad. G. Bonchev St., Bl. 103, 1113 Sofia, Bulgaria*

Received: July 30, 2020; Accepted: August 03, 2020

Metal Raschig Super-Ring (RSR) and Intalox Metal Tower Packing (IMTP) are modern high-performance packings that combine efficient mass transfer, large interfacial surface area and regular phase distribution over the cross section of the column apparatus. This work presents and summarizes original experimental data of the dynamic hold-up of 4 IMTP sizes and 7 RSR sizes. Dimensionless criterion equations are proposed for both types of packings to calculate their dynamic hold-up for regimes below the loading point. The average arithmetic error of the IMTP equation is 7.5% and of the RRS equation is 4.6%. The proposed equations not only take into account the geometry of the packings, but also the effect of the dumping of the packing in the column.

**Keywords:** Packed columns; Random packings; Dynamic hold-up of the packing; Experiments.

### INTRODUCTION

Packed columns are the most commonly used apparatuses for CO<sub>2</sub> capturing from the flue gases of power plants by absorption technology. A common way to increase their efficiency is to replace existing traditional packings with new, modern highly efficient packings, designed specifically for this purpose. High-performance random latest-generation packings with a special lamellar geometry, such as Raschig Super-Ring (RSR) [1] and Intalox Metal Tower Packing (IMTP) [2], have the potential to increase unit productivity at lower operating expenses, while reducing capital costs.

RSR and IMTP are modern packings that combine efficient mass transfer, large interfacial surface area and uniform phase distribution over the cross section of the apparatus [3]. Both types of packing, due to their open structure, are characterized by the ability to operate at high loads with low pressure drop at the same time [4, 5]. It should be noted that the hydrodynamic optimization of the RSR geometry [1] results in up to 15% higher effective surface area in comparison to IMTP at equal specific surface area.

Dynamic hold-up is an essential packing characteristic in the overall hydrodynamic characterization of a type of packing. This is the amount of fluid retained in the packed bed in the operating mode that runs down after stopping the liquid input. For industrial column apparatuses, the dynamic hold-up is practically equal to the total one, due to the small amount of the static hold-up [6, 7]. In addition to the fact that the hold-up is the volume in which the slow chemical reactions (if

any), accompanying the absorption process take place, knowledge of this parameter is necessary for the strength analysis of the packing support grid, as well as for the sizing of the collecting reservoir of the column.

There is no universal methodology for calculating this performance characteristic of the packings. A widely used approach [8] accepts that the free volume for the liquid flow can be treated as many parallel channels, with the same specific geometrical surface area as that of the packing. Some authors, on the basis of experimental data from lab-scale columns, proposed semi-empirical equations with individual constants for each type and size of a packing. Another approach was proposed in [9] for structured packing. The experiments were carried out in a miniaturized set-up (several and single packing sheet), where the thickness of the liquid film over a plate with smooth surface and surface with the microstructure of the packing was studied. The total dynamic hold-up was determined by a geometrical scale-up model. The employment of CFD models also gives good possibilities for determining the dynamic hold-up of the packings. For example, in [10] a two-phase Eulerian CFD model was proposed, based on the porous media concept for simulation of the gas-liquid flow through packed beds. A very good agreement of the calculation results with the experimental data was reported there, especially for low liquid and gas loads.

The aim of the present study is, on the basis of own experimental data obtained in a semi-industrial column, to propose more precise equations for the dynamic hold-up of high-performance IMTP and metal RSR.

These equations take into account such very important values as specific surface area and void

\* To whom all correspondence should be sent:

E-mail: [d.dzhonova@gmail.com](mailto:d.dzhonova@gmail.com)

fraction, and represent the influence of the packing construction and dimensions, as well as the dumping of the packing in the column.

EXPERIMENTAL DETAILS

Figs. 1 and 2 are photographs of individual elements of the two types of packings, and Table 1 and Table 2 show the geometric characteristics of the packings examined [4, 5]. As it can be seen from the tables, experiments were carried out with 11 packing modifications, 4 IMTP and 7 RSR, differing in size and specific geometric characteristics. The geometric characteristic for IMTP packing  $s$  denotes the minimum width of lamellas 2 in their narrowest part, Fig. 1. For the RSR packings  $h_s$  denotes the lamella width, and  $h$  - the height of the packing element, Fig. 2. The nominal diameter  $d_n$  for both types of packings is the diameter of the inscribed circle in the packing element. All other geometric characteristics are defined as averages, obtained from triplicate redumpings of the packing in a single column section.

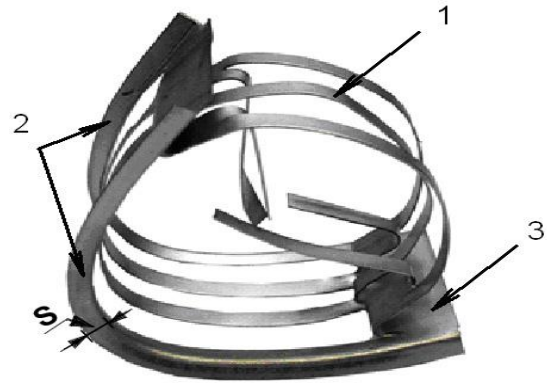


Fig. 1. IMTP packing element. 1- narrow lamellas, 2- lamellas, bent at 90°, 3- wide lamellas.

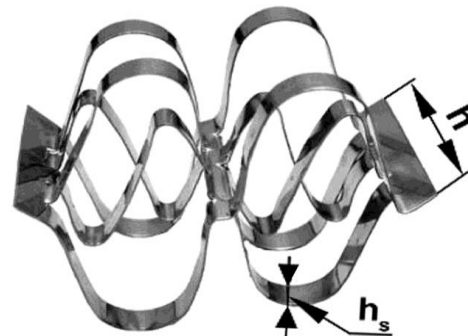


Fig. 2. RSR packing element

Table 1. Geometrical characteristics of the investigated types of IMTP packing

Name	Surface area $a$ $m^2/m^3$	Free volume $\varepsilon$ %	Size of lamellas 2 shown in Fig. 1 $s$ mm	Nominal diameter $d_n$ mm	Hydraulic diameter $d_h$ mm
IMTP 25	242.8	97.1	2.0	18.6	16.0
IMTP 40	171.6	96.7	3.1	26.5	22.5
IMTP 50	107.1	97.8	4.1	37.5	36.5
IMTP 70	66.1	98.5	4.1	61.0	59.6

Table 2. Geometrical characteristics of the investigated metal RSR packing

Name	Surface area $a$ $m^2/m^3$	Free volume $\varepsilon$ %	Element height $h$ mm	Number of strips $n$	Strip width $h_s$ mm	Nominal diameter $d_n$ mm	Hydraulic diameter $d_h$ mm
Raschig Super-Ring No. 0.5	236.2	96.5	15	4	3.8	21	16.3
Raschig Super-Ring No. 0.6	180.5	97.5	20	6	3.3	27	21.6
Raschig Super-Ring No. 0.7	175.9	97.7	20	5	4.0	34	22.2
Raschig Super-Ring No.1	155.5	98.0	25	6	4.2	34	25.2
Raschig Super-Ring No. 1.5	105.8	97.9	30	5	6.0	48	37.0
Raschig Super-Ring No. 2	100.6	98.0	38	6	6.3	50	39.0
Raschig Super-Ring No. 3	74.9	98.0	50	6	8.3	65	52.3

The experimental results were obtained in a column with a diameter of 470 mm with water as a liquid phase in the absence of a gas flow. A detailed description of the scheme is presented in [3]. The liquid load ranged from 10 to 200 m<sup>3</sup>/(m<sup>2</sup>h). The height of the packing layer was 2400 mm. The liquid distributor provided 920 drip points per square meter.

The packing hold-up was obtained by the method of measuring the difference in the liquid level in a level tank in the presence and absence of liquid irrigation [7]. The following procedure was applied. Prior to each series of experiments, the liquid was fed in the column at maximum liquid superficial velocity to ensure that the packing elements were completely wetted. The irrigation was then interrupted, and after a certain time to allow the liquid from the column to drain into the tank, the necessary liquid load was applied. After stabilizing the flow (the level of the liquid in the measuring tank was stationary), the liquid feed was stopped and after the liquid had drained the difference in the level of the tank was recorded. Having in mind the semi-industrial size of the column, the end effects (the volume of drops and trickles under and over the packing layer) were neglected because of insignificance. The dynamic hold-up was calculated as the liquid volume per unit volume of the packed bed.

Figs. 3 and 4 present the experimental results obtained for the dynamic hold-up of the studied packings as a function of the liquid load. The lines obtained are similar to those already established for well-known random packings. In both figures, it can be seen that an increase in the liquid load leads to an increase in the packing hold-up. Packings characterized by smaller geometric dimensions retain larger amount of liquid.

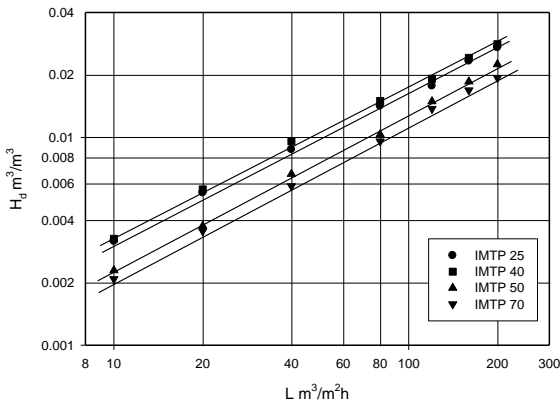


**Fig. 3.** Dynamic hold-up of IMTP packings related to the liquid superficial velocity in the absence of gas flow

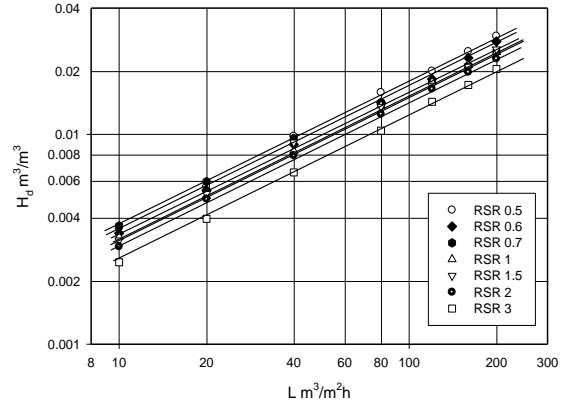


**Fig. 4.** Dynamic hold-up of RSR packings related to the liquid superficial velocity in the absence of gas flow

### DATA CORRELATION

The analytical approach accepted in describing the obtained data is based on the multichannel flow in the packing layer [6, 8]. In [8], it is shown how the specific surface characteristics of the different packing types are taken into consideration by the introduced hydraulic surface area, and for each type and size of a packing a constant obtained from experiments in laboratory conditions is proposed.

In the present study, two criterion equations for the two different packing types are derived, taking into account their specific geometric characteristics.

The dynamic hold-up below the loading point is determined in the absence of a gas phase and can be represented as a function of the liquid load and their geometric characteristics as:

For IMTP:

$$H_d = f [Fr_L (s/d_n)] \quad (1)$$

For RSR:

$$H_d = f [Fr_L (h.a)] \quad (2)$$

where:  $Fr_L = \frac{L^2 a}{g}$  - Froude number for the liquid

phase;  $L$  - liquid phase superficial velocity, m/s;

$d_h = \frac{4\varepsilon}{a}$  - the packing hydraulic diameter, m;  $\varepsilon$  is

the packing void fraction, m<sup>3</sup>/m<sup>3</sup>;  $a$  - packing specific surface area, m<sup>2</sup>/m<sup>3</sup>;  $s$  - minimal width of lamellas 2, Fig. 1, m; and  $h$  - packing height, Fig. 2, m.

Applying dimensional analysis and processing by regression analysis the experimental data for the packing dynamic hold-up below the loading point, the following expressions were obtained:

For IMTP:

$$H_d = 0.067 Fr_L^{0.35} \left( \frac{s}{d_n} \right)^{-0.03} \quad (3)$$

The mean arithmetic error of Eq. (3) is 7.5%.

The precision of the obtained experimental constants at 95% statistical reliability is given below:

$$0.067 \pm 0.0013;$$

$$0.35 \pm 0.0145;$$

$$-0.03 \pm 0.0087.$$

For RSR:

$$H_d = 0.12Fr_L^{0.329}(h.a)^{-0.4} \quad (4)$$

The mean arithmetic error of Eq. (4) is 4.6%.

The precision of the obtained experimental constants at 95% statistical reliability is given below:

$$0.12 \pm 0.0174;$$

$$0.329 \pm 0.0062;$$

$$-0.4 \pm 0.1057.$$

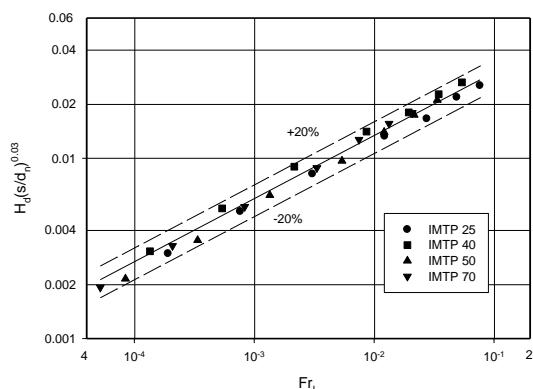


Fig. 5. Comparison of experimental data for IMTP packing with the results calculated by Eq. (3).

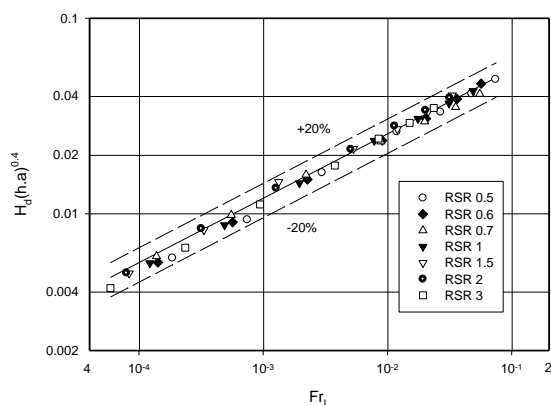


Fig. 6. Comparison of experimental data for RSR packing with the results calculated by the respective Eq. (4)

Figs. 5 and 6 present a comparison of the experimental data with the equations thus obtained. From both figures it can be seen that the proposed equations describe the experimental results adequately in the whole wide range of experimental

liquid loads. An important advantage of these equations is that the resulting constants in them are derived for a packing type, describing all of the packing sizes. Moreover, they are obtained on the basis of experiments in a semi-industrial installation and also take into consideration the dumping of the packing in the column.

## CONCLUSION

An experimental study was conducted to determine the dynamic hold-up of two types of advanced metal high performance packings, IMTP and RSR, in a semi-industrial installation. A total of 11 packing modifications, IMTP - 4 and RSR - 7, were studied, differing in size and geometric characteristics. More precise equations for prediction were proposed for both packing types for the dynamic hold-up below the loading point. They fit the experimental results with accuracy acceptable for practical use and can be successfully applied for design and correct constructive sizing of industrial apparatuses.

**Acknowledgement:** This work was supported by the Bulgarian Ministry of Education and Science under the National Research Programme “Low-carbon energy for transport and domestic use (EPLUS)” (approved by DCM No. 577/17.08.2018 and Grant Agreement DOI-214/28.11.2018), by the National Science Fund of Bulgaria, contract KP 06 RUSIA-3/27.09.2019 and by the Russian Foundation for Basic Research contract # 19-58-18004.

## REFERENCES

1. M. Schultes, *Trans. IChemE*, **81**, Part A, 48 (2003).
2. IMTP High Performance Packing, Bulletin KGIMTP-2. Rev. 3-2010, Koch-Glitsch, LP, 2010.
3. N. Kolev, Sv. Nakov, L. Ljutzkanov, D. Kolev, *Chem. Eng. Process.*, **45**, 429 (2006).
4. Sv. Nakov, D. Dzhonova-Atanasova, N. Kolev, *Bulg. Chem. Commun.*, **44**, 283 (2012).
5. D. Dzhonova-Atanasova, Sv. Nakov, E. Razkazova-Velkova, N. Kolev, *Bulg. Chem. Commun.*, **47**, 793, (2015).
6. R. Billet, *Packed Towers in Processing and Environmental Technology*, Weinheim, 1995.
7. N. Kolev, *Packed bed columns for absorption, desorption, rectification and direct heat transfer*, Elsevier, 2006.
8. R. Billet, M. Schultes, *Trans. IChemE*, **77**, Part A, 498 (1999).
9. H. Leuner, M. Hapke, J. Saher, M. Grünwald, J. Repke, *Chem. Eng. Trans.*, **69**, 781 (2018).
10. A. Arnab, R. Shantanau, K. D. P. Nigam, *Chem. Eng. Sci.*, **62**, 587 (2007).

## Impact analysis of a transient temperature field on the service life of the high pressure rotor of K-1000-60/3000 turbine

T. V. Nikulenkova\*, A. G. Nikulenkov

*National Technical University of Ukraine "Igor Sikorsky" Kyiv Polytechnic Institute, Kyiv, Ukraine*

Received: July 30, 2020; Accepted: August 03, 2020

Ensuring continued operation of NPP turbines envisages carrying out a set of works to assess the technical conditions of the turbine to detect and analyze damages, defects, identify causes and mechanisms for their occurrence and possible development. Further, the residual service life is assessed and recommendations in aging management are developed to ensure robust and safe operation of the turbine beyond the design period.

It is well-known that increasing the installed capacity of a power unit requires modernization of the flow section of the turbine high pressure cylinder, which, accordingly, will affect the service life of the rotor of the high-pressure cylinder. Therefore, one of the purposes of this paper is to investigate the impact on the service life of the high-pressure cylinder rotor of a typical high-speed turbine K-1000-60/3000. The residual life assessment of power equipment would require determining viability and damage of its base metal. Typical degradation mechanisms of steam turbine equipment include long-term strength reduction and low cycle fatigue accumulation. Intensity of their impact is determined by a numerical examination of equipment thermal (TS) and stress strain states (SSS) for standard operation modes. To perform a numerical examination of the stress strain state would require solving a thermal conductivity boundary problem in quasi-stationary (for normal operation modes) and nonstationary modes (for transients). It is convenient to solve such problems of mathematical physics through discretization of the calculation object using the finite element method.

**Keywords:** steam turbine, service life, stress strain states, high-pressure cylinder, rotor, initial and boundary conditions, CFD-codes, turbine K-1000-60/3000

### INTRODUCTION

With extended operation of power plant equipment, the definition of its service life has changed. After the fleet life is reached, an in-depth diagnostic is carried out for specific nodes of the electric power installation, including:

- analysis of its operating conditions;
- measurement of the actual component geometry;
- examination of steel structure, its properties and accumulated damage;
- non-destructive testing and calculated estimate of stress state and residual service life of components.

Based on the results of performed studies an individual residual service life is established for a specific component of the power equipment.

The decision-making algorithm regarding capability and conditions for equipment operation throughout the individual service life can be described as follows:

- assessment of actual operating conditions for the entire period of component use;
- conducting repeated strength analysis based on the refined operation data;
- defectoscopy (visual inspection, ultrasonic testing, X-ray examination, magnetic particle testing,

lab examinations of steel samples);

- assessment of the expired service life and forecasting further operation after defining equipment conditions.

This approach allows combining calculation methods, results of steel examination and samples tests, which complement each other.

### LITERATURE REVIEW

An important task of the power sector is to ensure maintaining electricity production at the attained level until new generating capacities are commissioned. That is why lifetime extension of operating power units is one of the most efficient ways of ensuring return on investments in the power sector.

The U.S.A. developed a Plant Life Extension Programme for TPPs and NPPs way back in the 1980s. Implementation of the programme at thermal power units is 10 times cheaper than building a new unit.

Since the 1980s and until the present day a range of scientific and research studies have been conducted with relevant operating experience accumulated which allowed a twofold increase of the service life of steam turbines. The approaches have been elaborated for service life extension of

\* To whom all correspondence should be sent:

E-mail: [tetyana.nikulenkova@gmail.com](mailto:tetyana.nikulenkova@gmail.com)

equipment being in different stages of its life expiration.

In previous times, when performing calculated estimates of the service life of steam turbines authors of the methodology guidelines for assessment of individual life of steam turbines [1, 2] did not take into account the engineering changes in power equipment components formed during the entire previous period of steam turbine operation, specifically repair and renewal changes of rotor structure.

Later, the National Technical University of Ukraine "Igor Sikorsky Kyiv Polytechnic Institute" conducted a number of scientific and research studies. These studies were devoted to the development of a methodology for calculated assessment of a low cycle fatigue of the steel of high-temperature casings and rotors of K-200-130 steam turbines using ANSYS and COsikoSMOS. These software suits allow building a diagnostic system for the stress strain state (SSS) of steam turbines [3, 4]. A comprehensive approach was proposed to extending operation of steam turbines while maintaining the required safety level.

A similar approach is used by specialists from different countries of the world – conducting a calculation analysis while taking maximum account of research results and then defining the most stressed components of plant power equipment. Thereafter, these components are checked using instrumentation monitoring methods [5, 6].

Nowadays, particularly relevant are scientific and technical, as well as economic studies aimed at justifying the capability and economic feasibility of NPP operation beyond its design life as an alternative to decommissioning. Economic expediency of certain actions is evaluated based on operation track record and considering equipment repairs and replacements important for safety. This should properly reflect the present requirements and recommendations.

When forecasting service life of NPP units the decisive factors are ageing processes undergoing in equipment materials and limiting its life. The main mechanisms defining degradation of steel properties of NPPs are considered to be: radiation embrittlement of RPV steels, fatigue damages affected by thermal fatigue and mechanical loadings, primary water stress corrosion cracking, thermal ageing, corrosion.

The estimates obtained by different authors vary from 15 to 40 % of the cost of a new power plant. It is a rather significant element of costs, even if considering it at minimum.

## RESULTS AND DISCUSSION

Approaching the end of the established life of an NPP equipment poses a number of challenges to nuclear industry:

- to increase the installed capacity while maintaining the required safety level of operating power units using the built-in engineered margins of operating units along with the ever increasing pace of science and technology development, and taking due account of international practice;

- to carry out a range of works and upgrades to ensure operation of power units beyond their design life while maintaining the required safety level.

The range of works to be carried out when assessing the service life of the critical elements of the turbine is comprised of several phases.

In the first phase, the 3-D analogues of the turbine machine elements were built based on the results of the technical audit and conclusions of the visual inspection, when different types of damages are localized in the geometrical model of a turbine element in the form of steel samples of different shape. Such approach allows to bring the calculation model of the steam turbine element close to real conditions after continuous operation.

The next phase is to calculate initial and boundary conditions (using CFD-codes or critical equations as specified in [7, 8]) and determine a nonstationary temperature field in the solid critical element for further calculation of thermal load.

It starts with solving the non-stationary thermal conductivity equation and assigning boundary conditions for heat transfer on the surfaces of the rotor based on 2-D and 3-D geometrical models. The non-stationary thermal conductivity equations are given below:

$$\text{div}[\lambda(T) \text{grad}(T)] = c(T) \gamma(T) dT/dt \quad (1)$$

where  $\lambda$  – coefficient of thermal conductivity,  $c$  – specific heat capacity,  $\gamma$  – specific weight, which are functions of temperature and coordinates under initial conditions  $T_0 = T(x, y, z, 0) = f_0(x, y, z)$ .

The third phase involves using the ANSYS package to determine the stress strain state of the high pressure cylinder rotor considering its complex spatial geometry, damages over the period of operation, and repair and renewal changes of the design geometry [9-12].

The outcome is calculations of equivalent elastic strain, von Mises equivalent strain, principal stresses, taking into account the effect of the centrifugal forces, temperature and steam pressure loads during start-up of the K-1000/60-3000 turbine from cold (CS), warm (WS) and hot states (HS).

1. Equivalent elastic strain shall be calculated by the formula:

$$\epsilon_e = (1/1 + \nu') (1/2 [(\epsilon_1 - \epsilon_2)^2 + (\epsilon_2 - \epsilon_3)^2 + (\epsilon_3 - \epsilon_1)^2])^{1/2} \quad (2)$$

where  $\nu'$  – the effective Poisson's ratio defined as: i) the Poisson's ratio at the relevant temperature of the considered body for elastic and thermal deformations; ii) 0.5 for plastic deformations.

2. Von Mises equivalent strain shall be calculated by the formula:

$$\sigma_e = [((\sigma_1 - \sigma_2)^2 + (\sigma_2 - \sigma_3)^2 + (\sigma_3 - \sigma_1)^2) / 2]^{1/2} \quad (3)$$

### 3. Principal stresses

It is well-known from the theory of elasticity that an infinitely small volume of material in the arbitrary point of the solid body and inside it can be rotated so that there remain only normal stresses, and all shear stresses are equal to zero. The three remaining normal stresses are called principal stresses (see Fig. 1).

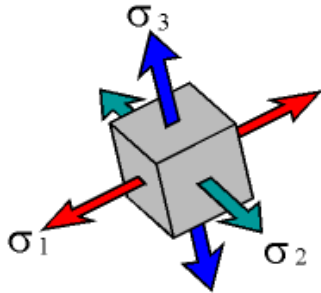


Fig. 1. Principal stresses

Principal stresses are always arranged as follows:  $\sigma_1 > \sigma_2 > \sigma_3$ , where  $\sigma_1$  – maximum principal stress,  $\sigma_2$  – middle principal stress,  $\sigma_3$  – minimum principal stress.

To calculate transient temperature fields for CS, WS and HS the boundary conditions were determined for temperature distribution in the rotor ( $t=f(x,y)$  at the time  $\tau=0$ ). The boundary conditions are presented in Figs. 2-4.

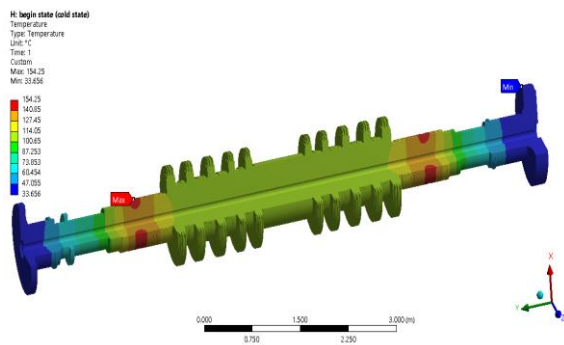


Fig. 2. Initial temperature distribution in the rotor during cold start-up

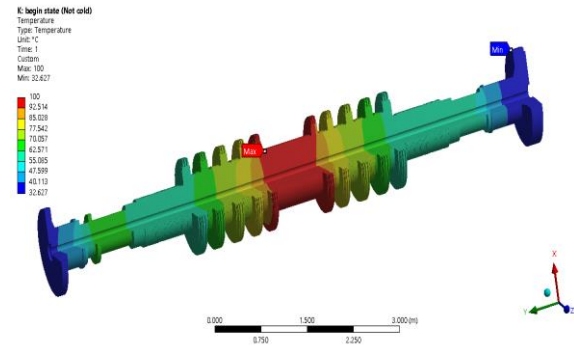


Fig. 3. Initial temperature distribution in the rotor during warm start-up.

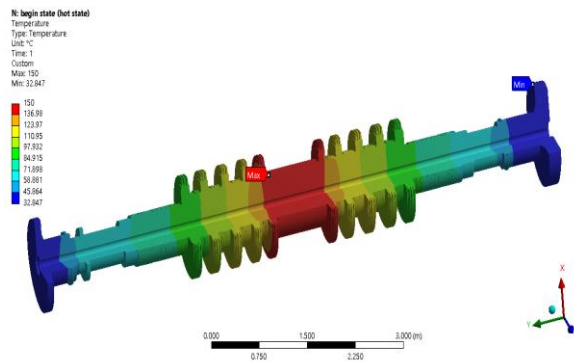


Fig. 4. Initial temperature distribution in the rotor during hot start-up

The calculations determine principal stresses and intensity of stresses over the entire life corresponding to start-up and stationary operating conditions in all division points of high temperature elements of the stream turbine.

The results of stress and deformation calculations under cold start-up of the K-1000/60-3000 turbine are provided below.

Figs. 5-8 show the change of maximum stress (equivalent (von-Mises) stress, principal stress) during the cold start-up.

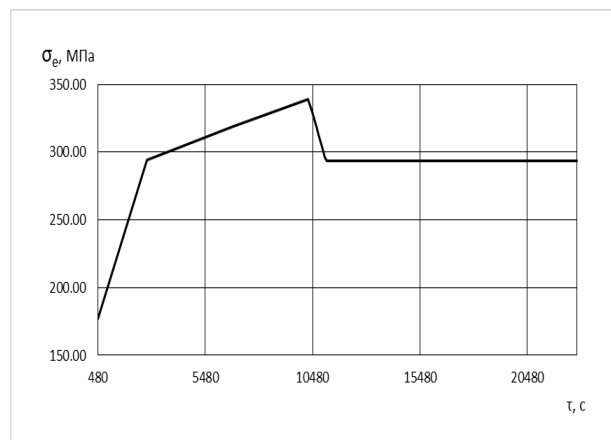
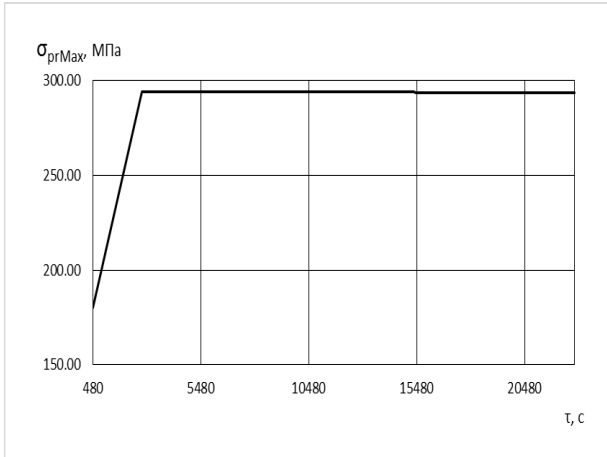


Fig. 5. Time change of maximum equivalent stress (von Mises) during cold start-up

The maximum equivalent stress is 338.9 MPa reached at 10260 s. The stress peak shifts from end seals (during warming-up of the turbine due to steam directed onto seals) to the first stage disk and further to the coupling when reaching nominal conditions.



**Fig. 6.** Time change of the maximum value of maximum principal stress during cold start-up.

The maximum value of the maximum principal stress is 294.16 MPa reached at 2760 s.

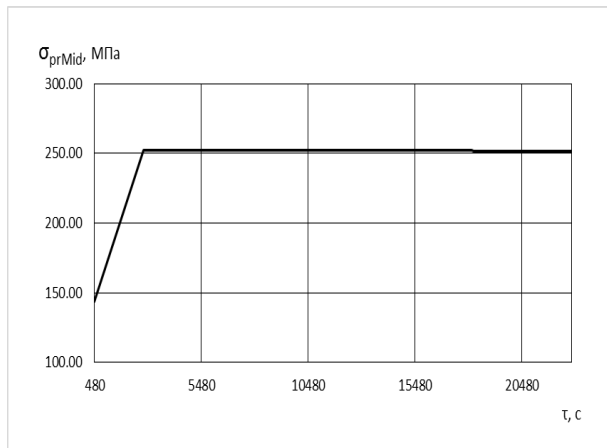


**Fig. 7.** Time change of the maximum value of middle principal stress during cold start-up.

The maximum value of middle principle stress is 252.05 MPa reached at 2760 s.

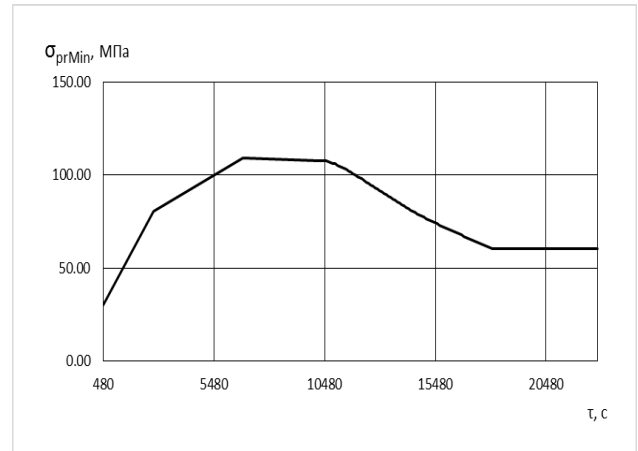
The maximum value of minimum principal stress is 109.09 MPa reached at 6780 s.

Fig. 9 illustrates the time change of maximum equivalent elastic strain during cold start-up.

As it can be seen from Fig. 9, the maximum equivalent elastic strain is 1.76E-03 m/m reached at 10260 s.

Figs. 10, 11 show the stress strain state of the K-1000/60-3000 steam turbine at the starting point (480 s) and at the end of the calculation (22740 s). According to the presented calculations the maximum stress is 338.9 MPa reached at 10260 s.

The stress peak shifts from end seals to the first stage disk and further to the coupling when reaching nominal conditions.



**Fig. 8.** Time change of the maximum value of minimum principal stress during cold start-up.

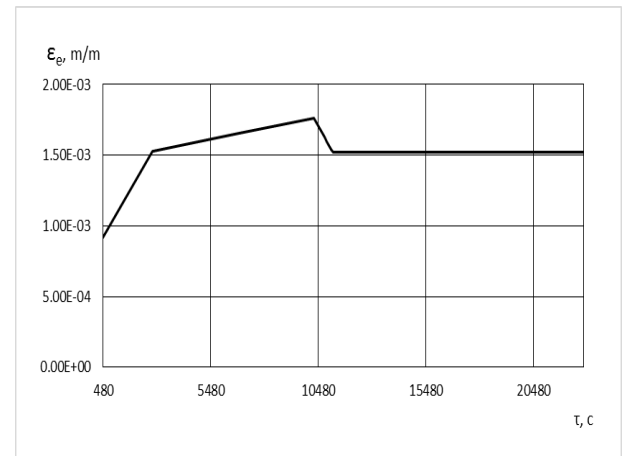


**Fig. 9.** Time change of maximum equivalent elastic strain during cold start-up.

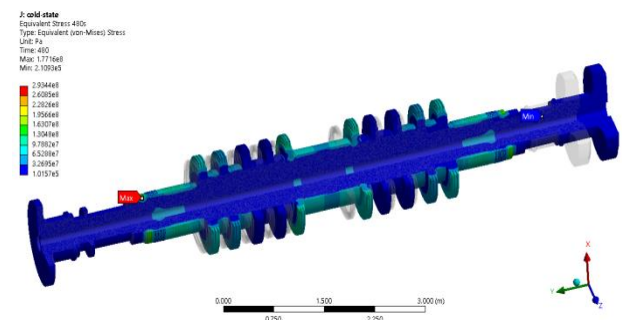


**Fig. 10.** Stress strain state of the K-1000/60-3000 steam turbine at the starting point (480 s).

The calculation results of the stress strain state of the high-temperature elements of the steam turbine obtained using ANSYS in different spatial settings (2-D and 3-D) were compare between each

other and with the results obtained by other authors [13].

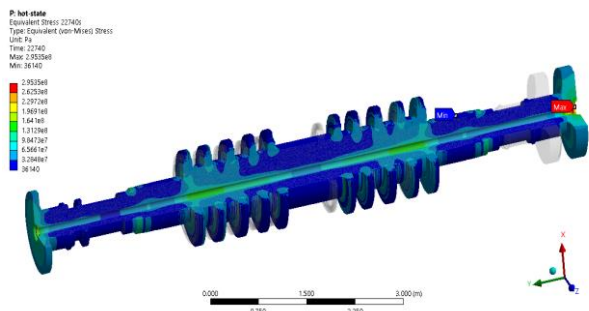


**Fig. 11.** Stress strain state of the K-1000/60-3000 steam turbine at the end of the calculation (22740 s)

The final phase implies a development of a methodological approach to the calculation of the low cycle fatigue with account of changes in the stress strain state of the K-1000/60-3000 turbine elements for optimization of strength margins by number of cycles and deformations [14-17].

The described methodology was used to develop a software for numerical analysis of the residual service life of steam turbines used at thermal and nuclear power plants.

The individual residual service life is defined as the time margin of potential operation of equipment after inspecting its technical conditions (or repair) during which all its main technical, operation and safety indicators shall meet the requirements of scientific and technical documentation.

The individual residual service life should be evaluated in three main phases:

- evaluation of turbine's technical conditions by controlling parameters with conclusions;
- evaluation of turbine's technical conditions by strength parameters with conclusions;
- evaluation of the residual service life of a turbine by life parameters with conclusions.

The possibility of forecasting the residual service life is ensured under the conditions as follows:

- parameters defining technical conditions of the equipment are known;
- criteria of the boundary conditions of the equipment are known;
- there is possibility of periodical and continuous inspection of technical condition parameters.

## CONCLUSIONS

1. The set of works to estimate the service life of the critical elements of the K-1000/60-3000 turbine was described in phases.

2. The calculations were made for equivalent elastic strain, von Mises equivalent strain, principal stresses, taking into account the effect of the centrifugal forces, temperature and steam pressure loads during start-up of the K-1000/60-3000 turbine from cold, warm and hot states.

3. The maximum stress was calculated as 338.9 MPa reached at 10260 s during cold start-up of the K-1000/60-3000 steam turbine.

4. The maximum equivalent elastic strain was calculated as 1.76E-03 m/m reached at 10260 s during cold start-up of the K-1000/60-3000 steam turbine.

## REFERENCES

1. M. Shulzhenko, P. Hontarovskiy, Yu. Matiukhin, I. Melezhyk, O. Pozhydaiev, Regulatory document SOU-N MEV 0.1-21677681-52:2011: approved by the Ministry of Energy and Coal Mining of Ukraine: effective as of 07.07.11, Kyiv: MECM of Ukraine, 2011.
2. Y. Matsevityi, N. Shulzhenko, V. Goloshapov et al. Increasing energy efficiency of turbine set performance of TPP and CHPP through modernization, reconstruction and improvement of their operation modes. K., Scient. Idea, 2008.
3. O. Chernousenko, Y. Shtefan, D. Rindyuk, D. Tretiak, *Energy and Electrification*, **3**, 42, (2008).
4. Y. Pismennyi, O. Chernousenko, Y. Shtefan, D. Rindyuk, D. Tretiak, *Bulletin of the National Technical University "KhPI", Machine Building..* **52**, 188 (2008).
5. H. Matsumoto, *IEEE Transactions of Power Apparatus and Systems*, **101** (8), 2504 (1982).
6. E. Tsunoda, *Toshiba Review*, **40**(9), 783 (1985).
7. T. Nikulenkova, A. Nikulenkov, *The 16th International Conference of Young Scientists on Energy Issues*, **VII**, 267 (2019).
8. O. Chernousenko, A. Nikulenkov, T. Nikulenkova, L. Butovskiy, I. Bednarska, *Bulletin of the National Technical University "KhPI"*, **12** (1288), 51 (2018) doi: 10.20998/2078-774X.2019.03.01.
9. V. Peshko, O. Chernousenko, T. Nikulenkova, A. Nikulenkov, *Propulsion and Power Research*, **5**(4), 302 (2016), doi: 10.1016/j.jprr.2016.11.008.
10. A. Nikulenkov, D. Samoilenko, T. Nikulenkova, *Nuclear and Radiation Safety*, **4**(80), 9 (2018), doi: 10.32918/nrs.2018.4(80).02.
11. O. Chernousenko, D. Rindyuk, V. Peshko, *The Problems of General Energy*, **2**(53), 65 (2018), doi: 10.15407/pge2018.02.065.
12. O. Chernousenko, D. Rindyuk, V. Peshko, *Eastern-European Journal of Enterprise Technologies*, **5**(8-89), 39 (2017), 17doi: 10.15587/1729-4061.2017.112284.
13. O. Chernousenko, D. Sc. Thesis, Turbine machines and turbine sets, X, 2009.
14. O. Chernousenko, D. Rindyuk, V. Peshko, *Power Engineering: Economics, Technique, Ecology*, **3**,

*T. V. Nikulenkova, A. G. Nikulenkov: Impact analysis of a transient temperature field on the service life of...*

- 135 (2018), doi: 0.20535/1813-5420.3.2018.163981.
15. O. Chernousenko, D. Rindyuk, V. Peshko, V. Goryazhenko, *Eastern-European Journal of Enterprise Technologies*, **2**(1-92), 51 (2018), doi:10.15587/1729-4061.2018.126042
16. O. Chernousenko, D. Rindyuk, V. Peshko, *Bulletin of the National Technical University "KhPI"*, **3** (1328), 4 (2019), doi: 10.20998/2078-774X.2019.03.01.
17. O. Chernousenko, V. Peshko, *Journal of Mechanical Engineering*, **4**(22), 41 (2019), doi: 10.15407/pmach2019.04.041.

## Large-scale maldistributions of local flow parameters at distillation on a structured packing

A. N. Pavlenko<sup>1</sup>, V. E. Zhukov<sup>1</sup>, E. Yu. Slesareva<sup>1\*</sup>, Chr. Boyadjiev<sup>2</sup>, B. Boyadjiev<sup>2</sup>,  
D. Dzhonova-Atanasova<sup>2</sup>, P. Popova-Krumova<sup>2</sup>

<sup>1</sup>*Kutateladze Institute of Thermophysics, Siberian Branch of the Russian Academy of Sciences, Novosibirsk*

<sup>2</sup>*Institute of Chemical Engineering, Bulgarian Academy of Sciences, Bulgaria*

Received: July 26, 2020; Accepted: August 03, 2020

The results of research and operation of industrial distillation columns with the most widely used regular packing have shown that the separation efficiency with increasing diameter can significantly decrease due to formation of large-scale nonuniformity of liquid flows, as well as concentrations along the column section, which significantly affects the performance and purity of the finished product. The experiments were carried out on a large-scale experimental setup, designed to study the integral and local characteristics of mixture separation by distillation on a structured packing. To simulate the process of separation of liquefied air, a mixture of R114/R21 freons was used. The separation of mixture was studied on a structured package Mellapak 350.Y with a diameter of 0.9 m and height of 2100 mm. We studied the efficiency of mixture separation, dynamics of formation of large-scale temperature field non-uniformity over the column cross-section during mixture separation, and distribution of the density of local liquid flow rates at the packing outlet. The experiments were carried out at a pressure of 0.3 MPa and initial concentration of the R114 / R21 mixture of 12%. The conducted experimental studies showed that large-scale temperature maldistribution over the cross-section and height of the distillation column is formed. The conditions leading to formation of this nonuniformity are considered. The obtained experimental data will be used in the development of new approaches for numerical simulation of mass transfer and mixture separation efficiency in distillation columns with structured packing in the framework of a joint project.

**Keywords:** distillation columns, structured packing, numerical simulation, large-scale nonuniformity

### INTRODUCTION

Distillation columns are widely used to separate two- and multicomponent mixtures in the chemical industry [1-4]. Mixtures are separated during heat and mass transfer under conditions of countercurrent motion of vapor and liquid phases using contact devices of various types [5, 6]. In accordance with the laws of thermodynamic vapor-liquid equilibrium, the vapor phase is enriched with low-boiling and the liquid phase is enriched with high-boiling components. The main requirement for contact devices is to ensure uniform distribution of the liquid film and countercurrent vapor flow over the column cross-section, as well as the maximum development of the liquid-vapor contact surface with a minimum pressure drop on the contact devices. Therefore, contact devices determine to a large extent the total efficiency of the separation process. The heat and mass transfer plates, all kinds of filling elements, as well as regular structured packing are used as contact devices [7]. Moreover, the columns with a structured packing have higher efficiency, wide range of stable operation, relatively low cost and simplicity of design, as well as low hydraulic resistance [8]. Currently, the diameter of widely used industrial distillation

columns with regular packing can reach 7 m or more. However, the efficiency of mixture separation with increasing diameter can be significantly reduced. One of the reasons for this is the formation of large-scale maldistribution of liquid and vapor flows, as well as both phase concentrations over the column cross-section, which significantly affects the productivity and purity of the finished product.

The experimental results on the formation dynamics of large-scale temperature field maldistribution over the cross-section and height of a distillation column with a regular packing under conditions of negative stratification of the countercurrent vapor flow are presented in this paper.

### EXPERIMENTAL

The experiments were carried out at a large-scale research setup [9], made to study hydrodynamics and heat and mass transfer in large-scale separation columns during distillation on structured packing. Separation of liquefied air to obtain pure cryogenic products (oxygen, nitrogen, argon, etc.) is a very significant aspect of industrial distillation. However, the studies in large-scale cryogenic columns are extremely complex and expensive.

\* To whom all correspondence should be sent:

E-mail: styuardessa@yandex.ru

Therefore, it is justified to use modeling mixtures for a comprehensive study of the processes of hydrodynamics and heat and mass transfer on large-scale elements of complex geometry composing the packing of modern columns. To perform the studies, we used a mixture of freon R114/R21, selected to simulate the process of liquefied air separation. The mixture was separated on a structured Mellapak 350.Y packing with a diameter of 0.9 m and height of 2100 mm (10 layers of the packing with a height of 210 mm) under conditions of full reflux. The mixture poured into the bottom of the column (bottom space) evaporated, vapor passed through a structured packing and turned into the liquid phase in the condenser completely. The packing was irrigated by the jets from a liquid distributor located in the column head. The circulation pump fed liquid from the condenser to the distributor, in the bottom of which there were 83 holes with installed nozzles for packing irrigation. The flow rate of irrigating liquid changed within 0.8 – 2.0 l/s. To study the dynamics of formation of large-scale temperature field non-

uniformity during mixture separation, the miniature temperature sensors were installed in layers No. 2, 5, and 8, counting from the lower layer, in three layers of the packing cross-section. In each cross-section, 16 sensors were installed on the upper edge of the layer. To study the distribution of local liquid flow density over the packing of a distillation column, a flow meter with a diameter of the receiving collector of 28 mm was used. The flow meter was mounted on a two-coordinate device located directly below the bottom layer of the structured packing.

## RESULTS AND DISCUSSION

The experiments were carried out at a pressure of 0.3 MPa and initial concentration of the R114/R21 mixture of 12%. The vapor velocity, averaged over the column cross-section, was 0.15 – 0.3 m/s (F-factor 0.63 – 1.26 (Pa)<sup>0.5</sup>). The data on temperature changes in the middle cross-section of the packing in the process of column transition to the stationary regime of mixture separation are shown in Fig. 1.

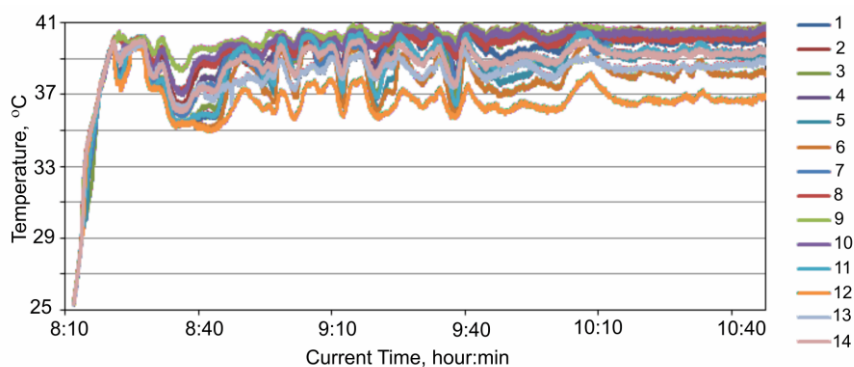


**Fig. 1.** The temperature change in the middle cross-section of the packing in the process of column transition to the stationary regime. F-factor = 0.63 (Pa)<sup>0.5</sup>; liquid flow rate = 0.85 l/s.

As it can be seen in the diagram that at the initial stage, the temperature field over the packing cross-section is quite uniform. In the process of mixture separation, when the temperature in the packing cross-section is about 39-40°C, the readings of thermometers within one packing cross-section start stratifying substantially. Within one and a half hour, the operating parameters of the column become stable, and the column enters the stationary operation regime. The diagram shows that in the process of establishing a stationary regime, the temperature field in the column cross-section undergoes significant changes, but in general the character of non-uniformity is kept. In the stationary regime of column operation, the

temperature field in the column cross-section remains almost unchanged. The diagrams of spatial distribution of the temperature field in the middle (Fig. 2a) and lower (Fig. 2b) cross-sections of the column are presented in Fig. 2.

This diagram illustrates the large-scale temperature maldistribution formed in the packing cross-section. The volatile component of the mixture (R114) has a higher density than the high-boiling component (R21). As a result, during mixture separation in the upper part of the column, the vapor density in the upward flow becomes higher than its density in the lower part of the column. Negative stratification of the vapor density in the upward flow is formed.

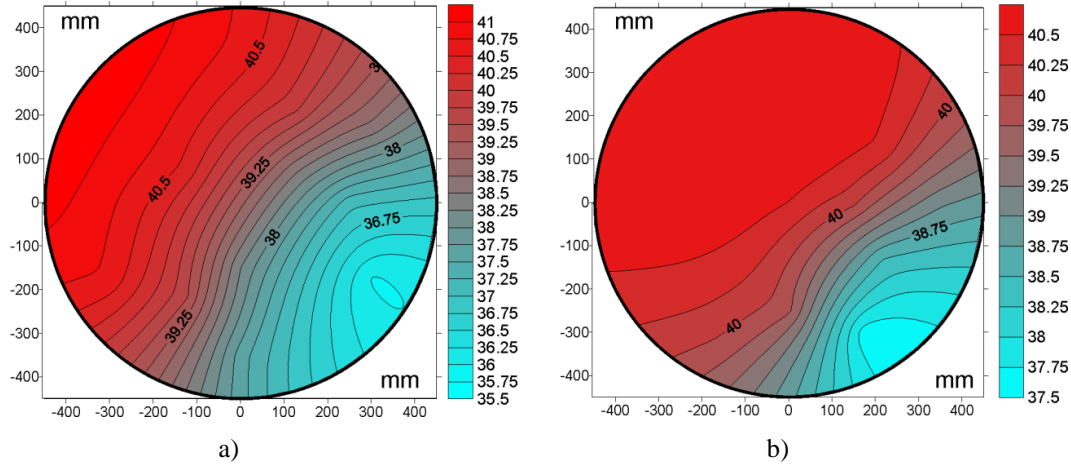


**Fig. 2.** Diagram of spatial distribution of the temperature fields in the column cross-sections: a) middle cross-section, layer 5; b) lower cross-section, layer 2. F-factor = 0.63 (Pa)<sup>0.5</sup>; liquid flow rate = 0.85 l/s.

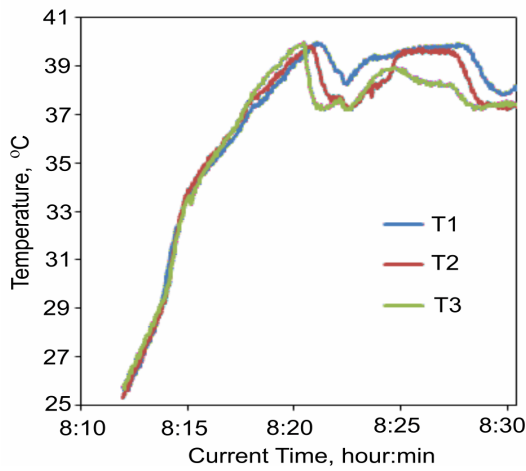


**Fig. 3.** Temperature changes in different packing layers during stabilization of column operation. T1 – layer 2, T2 – layer 5, T3 – layer 8. F-factor = 0.63 (Pa)<sup>0.5</sup>; liquid flow rate = 0.85 l/s.

As a result, when reaching the critical values of the vapor density gradient, a loss of stability of the uniform countercurrent flows can occur and a large-scale maldistribution of the local parameters of mixture over the column cross-section may form. The scale of the perturbing effect, which can lead to a loss of stability in the upward vapor flow and formation of a large-scale maldistribution of local flow parameters in the column cross-section, is estimated in [10]. As it can be seen in the diagram, when a temperature close to 40°C is reached, a rapid decrease in temperature to 37°C is observed in the upper part of the packing (T3 thermometer). Relative to the top part of the packing (T3), the temperature drop in the middle part (T2) is delayed for 30 s. At the packing bottom (T1), the temperature drop is delayed for 72 s. The perturbation spread along the packing height at a velocity of 0.015 - 0.021 m/s. At that, the average

velocity of the vapor flow over the column cross-section was 0.15 m/s.

Such a low velocity of perturbation propagation may indicate in favor of another formation mechanism of large-scale non-uniformity. It is observed in the packed columns that a significant portion of liquid flows down the column wall (up to ~ 8% or more of the total flow rate in the column, [11]), but not along the elements of the structured packing. Hydrodynamics of a two-phase mixture in a structured packing (a falling liquid film in contact with an upward vapor flow) depends significantly on the stress tensor [12], i.e., the tangential components of the stress tensors in two phases should be equal at the phase boundary:

$$\mu_G \frac{\partial u_G}{\partial y} = \mu_L \frac{\partial u_L}{\partial y}, \quad (1)$$

where  $u_G, u_L, \mu_G, \mu_L$  are velocities and viscosities in the vapor and liquid phases, and the coordinate is directed along the normal to the interface. It can be derived from (1):

$$\frac{\mu_G \bar{u}_G}{\mu_L \bar{u}_L} \frac{\partial U_G}{\partial y} = \frac{\partial U_L}{\partial y}, \quad (2)$$

where  $\bar{u}_G, \bar{u}_L, U_G, U_L$  are average and dimensionless velocities in the vapor and liquid phases. For the industrial columns, the ratios of values in (2) are of the following order:

$$\frac{\mu_G}{\mu_L} \sim 10^{-4}, \frac{\bar{u}_G}{\bar{u}_L} \sim 10, \frac{\mu_G \bar{u}_G}{\mu_L \bar{u}_L} \sim 10^{-3}, \quad (3)$$

i.e., under these conditions (below the loading regime, which develops at higher vapor velocities), the motion of the vapor phase does not significantly affect the motion of the liquid phase, but the liquid film flow affects the motion of the vapor phase.

When modeling hydrodynamic and heat and mass transfer processes during distillation in packed columns, a problem arises because of the need to take into account the presence of flowing liquid on the column wall, when there is a main flow of liquid in the volume of the structured packing and a significant liquid flow on the column wall. There are a number of design solutions that help to reduce the probability of liquid flow on the wall and increase the probability of liquid return from the wall to the nozzle (the character of initial irrigation, specific channel shapes, the presence of wipers and distance spacers), but these measures cannot eliminate the liquid flow on the column wall completely.

Liquid flows over the packing surface, and when it reaches the column wall, its most part flows on this surface since this part of liquid cannot return completely to the structured packing due to the limited contact surface between the column wall and the packing. With an increase in the thickness of the flowing liquid film, conditions for more intensive reverse flow of liquid from the wall to the volume of the packing are created, when these two reciprocal processes can be equalized (strictly speaking, these two processes depend on a gap between the column wall and the structured packing, features of connection and arrangement of sheets in the structured packing, molar flow rates of liquid and vapor, geometry and material of the used wipers and clips fixing the packing, number of packing layers in the column, etc.). In the process of such repeated mutual liquid flows between the packing and the column wall, the liquid film can ultimately reach its constant maximum thickness with which it flows down the column bottom. The amount of liquid entering the film flowing down the column wall causes a decrease in the total amount of liquid in the volume of the structured packing. Thus, the considered factor of the transverse liquid flow creates a significant radial non-uniformity of the axial component of liquid velocity (and non-uniform distribution of the local vapor flow over the packing cross-section, respectively) in the column and finally, can significantly reduce the mass transfer intensity in the liquid and vapor phases and, as a result, efficiency of mixture separation.

The surface of the falling liquid film is the interface between the vapor and liquid phases. For large values of the liquid film thickness (and the average velocity in it, respectively), the velocity of the vapor phase at the interface with the falling liquid can be directed downward, i.e., against the velocity of the bulk of the vapor phase. As a result,

the direction of velocity in the vapor phase in a local zone near the boundary of liquid flowing along the column wall can change; as a consequence, this can lead to creation of a large-scale circulation zone. Thus, if the conditions of assembly and installation of the structured packing in the distillation column create the possibility of organizing a significant liquid flow on the column wall, this can lead to the presence of a large-scale zone of vapor circulation, which is observed in the performed experiments.

The diagram of distribution of the local density of liquid flow from the structured packing, averaged over the azimuthal coordinate, along the column radius is shown in Fig. 4.

As it can be seen in the diagram, a slight decrease in the density of liquid flow from the packing center to its edges is observed along the column cross-section.

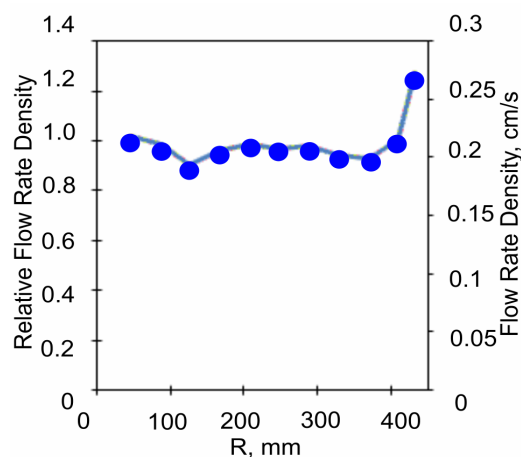


**Fig. 4.** The diagram of distribution of the local flow density of liquid from the structured packing, averaged over the azimuthal coordinate, along the column radius.  $F$ -factor =  $1.27 \text{ (Pa)}^{0.5}$ ; liquid flow rate =  $1.4 \text{ l/s}$ .

However, when approaching the packing periphery, we can see a fairly significant increase in the density of liquid flow rate to approximately  $\sim 1.25$  of the average density of the liquid flow rate in the structured packing. The diagram of distribution of the local liquid flow density in an annular cross-section, bounded by a radius  $417 < R < 445 \text{ mm}$ , is shown in Fig. 5. The average density of the liquid flow rate at the outlet of the nozzle is  $0.22 \text{ cm/s}$ .

According to the diagram, the distribution of the liquid flow density at the packing periphery is substantially uneven. The density of the liquid flow is mainly in the range from  $0.15$  to  $0.4 \text{ cm/s}$ . The areas of increased flow rate density are observed with a periodicity of  $90^\circ$ . With rotation at such an angle, the layers in the column packing alternate. There is no direct correlation of the position of

large-scale areas of the maximum and minimum temperatures with the flow density at the packing periphery, but this periodicity of the liquid flow density may be the initiator of a large-scale convective process.

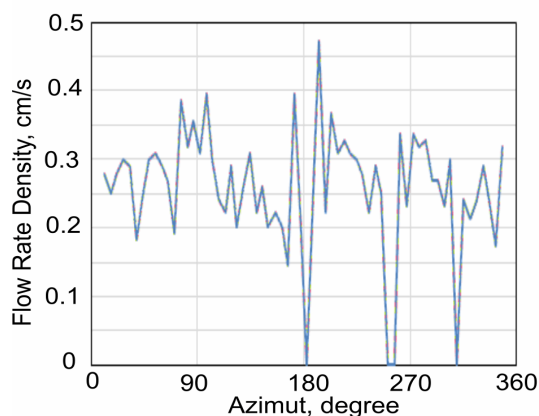


**Fig. 5.** The diagram of distribution of the local liquid flow density in a near-wall annular cross-section, bounded by a radius  $417 < R < 445$  mm. F-factor = 1.27 (Pa)<sup>0.5</sup>; liquid flow rate = 1.4 l/s.

#### CONCLUSIONS

Experimental studies have shown that in the distillation column of a 0.9-m diameter a large-scale temperature maldistribution is formed over the cross-section and height of the column. The velocity of maldistribution propagation along the column height is 0.015 - 0.021 m/s at a countercurrent vapor flow velocity of 0.15 m/s.

At the outlet of the structured packing, a decrease in the local density of liquid flow from the packing center to its edges is observed over the column cross-section. However, when approaching the packing periphery then, a significant increase is observed in the density of the liquid flow rate to approximately ~ 1.25 of the average density of the liquid flow rate in the structured packing.

The results of processing the obtained array of experimental data will serve as the basis for the construction and verification of models aimed at developing methods for calculating the efficiency

of mixture separation during distillation on the structured packing in industrial columns, allowing the quantitative consideration of the scale factor influence associated with large-scale maldistribution of local parameters of liquid and vapor flows.

**Acknowledgements:** This study was carried out at the Kutateladze Institute of Thermophysics, Siberian Branch of the Russian Academy of Sciences under the grant of the Russian Foundation for Basic Research no. 19-58-18004-Bulgaria\_a. with the support of the National Science Fund of Bulgaria, contract No KP 06 RUSIA-3/27.09.2019.

#### REFERENCES

1. J. Fang, X. Cheng, Z. Li, H. Li, C. Li, *Chin. J. Chem. Eng.*, **27** (6), 1272 (2019).
2. M. Markowski, K. Urbaniec, *Proc. Syst. Eng.: Energy Systems Eng.*, **5**, 301 (2008).
3. M. Elhelw, A. Abdurrahman, A. Alsanousie, A. Attia, *Alexandria Eng. J.*, **59** (2), 613 (2020).
4. J. Fang, Zh. Li, G. Huang, H. Li, Ch. Li, *Ind. Eng. Chem. Res.*, **59** (4), 1668 (2020).
5. S. K. Churakova. *Bashkir Chem. J.*, **18** (2), 39 (2011).
6. V. Bessoua, D. Rouzineau, M. Prévost, F. Abbé, Ch. Dumont, J. - P. Maumus, M. Meyer, *Chem. Eng. Science*, **65** (16), 4855 (2010).
7. R. Battisti, R.A.F. Machado, C. Marangoni, *Chem. Eng. & Proc. – Process Intens.*, **150** (2020).
8. A. R. Muzafarova, E. A. Emelyanycheva, *University of Technology Herald*, **19** (2), 63 (2016).
9. A. N. Pavlenko, V. E. Zhukov, N. I. Pecherkin, V. Yu. Chekhovich, O. A. Volodin, A. Shilkin, C. Grossmann, *AIChE*, **60** (2), 690 (2014)
10. A. N. Pavlenko, V. E. Zhukov, N. I. Pecherkin, E. Yu. Slesareva, *JET*, (2), 1 (2020).
11. A. N. Pavlenko, N. I. Pecherkin, V. Yu. Chekhovich, V. E. Zhukov, A. F. Serov, A. D. Nazarov, S. Sunder, P. Houghton, *JET*, **13** (1), 1 (2005).
12. Chr. Boyadjiev, *Theoretical Chemical Engineering. Modeling and simulation*, Springer-Verlag, Berlin Heidelberg, 2010, p. 594.

## The influence of heat transfer on the energy efficiency in thin film evaporators

V. G. Rifert, P. A. Barabash, V. P. Boianivskiy\*, V. V. Sereda, A. S. Solomakha

*National Technical University of Ukraine "Igor Sikorsky Kyiv Polytechnic Institute"*

Received: July 26, 2020; Accepted: August 10, 2020

Today desalination of seawater provides world water production of 24.5 million m<sup>3</sup> per day. Some of the most common ways of desalinating are multi-effect distillation (MED) and multi-effect distillation with thermal (MED+TVC) and mechanical vapour compressors (MED+MVC). The key issues of this technology are the pollutant emissions into the atmosphere and the high energy consumption. A significant part of energy is consumed in evaporators, in which steam condenses in horizontal tubes at low pressures (from 7 to 50 kPa), and the evaporation of seawater occurs on the outer surface of the tubes. Such heat exchangers provide production of desalinated water from 0.5 to 500 m<sup>3</sup> per hour at a condensation temperature of water steam ranging from 40 to 80 °C and are made of tubes with a diameter of 10 to 50 mm. The operating efficiency of the evaporators depends on the pressure loss (temperature difference between evaporation and condensation) and heat transfer in these devices. Heat transfer, in its turn, depends on the intensity of the evaporation processes in the falling film and the condensation inside the tubes. The present paper aims to analyse the effect of heat transfer during evaporation and condensation on the temperature difference and pressure loss in horizontal tube evaporators.

**Keywords:** desalination, evaporation, multi-effect distillation (MED), film condensation, heat transfer, thin film evaporator

### INTRODUCTION

Thin film evaporators are widely used in desalination, food processing, petrochemical, and other fields because of their high heat transfer efficiency, small temperature difference, and small amount of liquid injection [1-4]. To reduce energy consumption in these systems, several methods are used: multi-effect distillation (MED), multi-effect distillation with thermal vapour compressor (MED+TVC) and multi-effect distillation with mechanical vapour compressor (MED+MVC).

Fig. 1 shows a principal scheme of a multi-effect MED [1]. Each effect consists of preheater, demister and thin film evaporator. The last effect is followed by the end condenser. Saturated steam with a temperature below 80°C is fed to the evaporator of the first effect. Steam is the primary source of the thermal energy that drives the entire distillation process. At the outlet of the end condenser, seawater is divided into two streams: feedwater, which is fed to the first effect, passing through the preheater of each effect, and cooling seawater, which is discharged back into the sea. Preheating of sea water reduces the energy needs of the distillation process due to partial condensation of the total steam flow.

Feed water after preheating is sprayed on the tubular beam of the first effect, where it partially evaporates due to the heat released during condensation.

The unevaporated salt solution remains at the bottom of the effect and forms feed water for the next effect. The vapour produced, considered free of salts, passes through a demister in order to retain the brine droplets, and is directed to a preheater where part of it condenses. The rest of the steam is fed to the evaporator of the second effect at the lower pressure and temperature than in the first effect. In the second effect, the feed water, which is a salt solution, is subjected to an instantaneous evaporation process and forms additional steam. The distillate obtained from preheater and thin film evaporator is collected in a flash box. This process is repeated sequentially in each effect up to the last one.

In MED systems, the efficiency factor (COP) is almost proportional to the number of effects  $n$ . In MED+ MVC systems, the main energy costs consist of the isothermal operation of the centrifugal vapour compressor [5]:

$$W = \frac{\frac{k}{k-1} p_1 v_1 \left[ \left( \frac{p_2}{p_1} \right)^{\frac{k-1}{k}} - 1 \right]}{\eta_c} = \frac{h_2 - h_1}{\eta_c}, \quad (1)$$

where  $W$  – compressor work, J/kg;  $p_1$  – input compressor pressure, Pa;  $p_2$  – output compressor pressure, Pa;  $v_1$  – specific volume of steam at compressor inlet, m<sup>3</sup>/kg;  $k$  – isentropic constant

\* To whom all correspondence should be sent:

E-mail: [volodya.81.vs@gmail.com](mailto:volodya.81.vs@gmail.com)



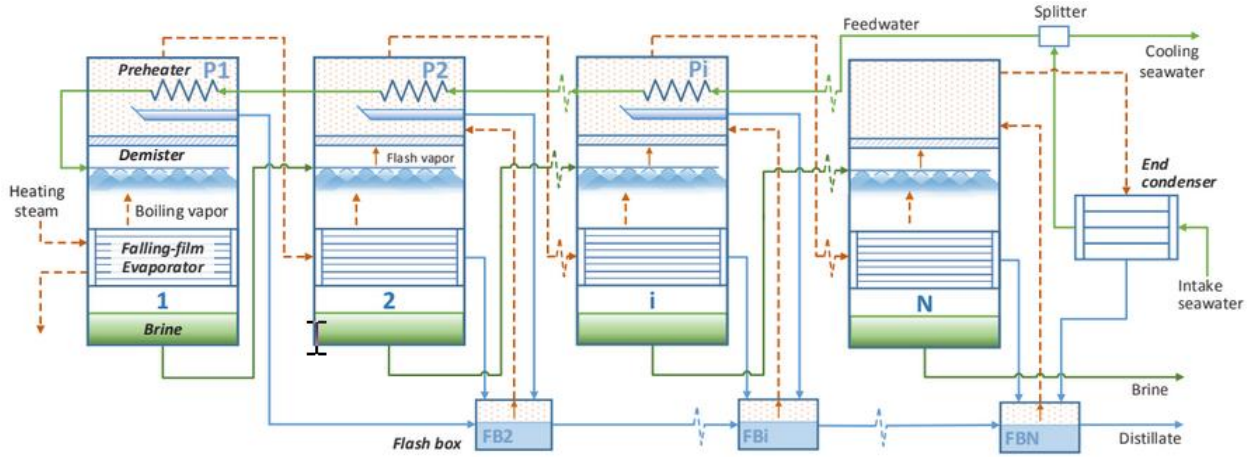


Fig. 1. Principal scheme of a multi-effect distillation system [1].

( $k=C_p/C_v=1.3$  – for steam);  $h_2$  – specific enthalpy of compressor exit, J/kg;  $h_1$  – specific enthalpy of compressor inlet, J/kg;  $\eta_c$  – isentropic efficiency of compressor ( $\eta_c=0.85$ ).

The energy losses of MED+TVC systems have been calculated assuming that it will have an overall thermal efficiency of 0.75, as suggested in [6]. The ejector efficiency can be expressed in terms of entrainment ratio by using the relationship:

$$\eta_e = (ER + 1) \frac{h_4 - h_3}{h_1 - h_2}, \quad (2)$$

where  $ER$  – entrainment ratio, (kg/h vapour taken from evaporator and compressed by ejector) / (kg/h driving stream);  $h_1$  – enthalpy of high pressure steam, J/kg;  $h_2$  – enthalpy of steam after isentropic expansion in nozzle to pressure of entrained vapour, J/kg;  $h_3$  – enthalpy of mixture at start of compression in diffuser section, J/kg;  $h_4$  – enthalpy of mixture after isentropic compression to discharge pressure, J/kg.

Thus, the efficiency of all the 3 distillation systems (MED, MED+MVC and MED+TVC) depends on the number of effects and the pressure difference in the first effect  $p_1$  and the last one  $p_n$ . For MED+TVC systems, the efficiency also depends on the pressure in the effect from which the steam enters the compressor.

The article analyses the factors influencing the pressure loss in the effects of the above-described installations and the overall pressure difference in the distillation systems. The methods for calculating heat transfer during evaporation in the falling film on the outer surface of horizontal tubes and during condensation inside these tubes are presented. The need to improve the methods of heat transfer calculation in thin film evaporators is substantiated.

## FACTORS INFLUENCING PRESSURE LOSS

The hydraulic resistance in heat exchangers with convective two-phase processes involves pressure loss during heat transfer (during condensation or evaporation) and pressure loss in the connecting pipelines. Vacuum distillation also results in pressure loss due to non-condensing gases. In the process of concentration of heat-sensitive liquids, the temperature difference increases due to an increase in temperature depression caused by the pressure loss in the apparatus.

When designing multi-effect distillation of heat-sensitive liquids, it is necessary to know the permissible evaporation temperature to avoid precipitation when the solubility limit of any salt is reached. The lower temperature limit in a multi-effect distillation system is determined by the ambient temperature to allow condensation in the last effect of the installation.

With qualified design, the values of the above-described pressure losses and temperature differences in the distillation system can be minimized. Reducing pressure loss will reduce the temperature difference in one effect and, accordingly, increase the number of effects and energy efficiency of thin film evaporators.

### Heat transfer components

Overall heat transfer coefficient (HTC) in thin film evaporators is determined by the formula:

$$U = \left( 1/h_{con} + 1/h_{evap} + \delta_w/k_w + \sum_{i=1}^n R_i \right)^{-1} \quad (3)$$

where  $h_{con}$  – HTC during condensation of water vapour inside horizontal tubes with a diameter of 10 to 50 mm and a length of 1 to 16 m;  $h_{evap}$  – HTC upon evaporation of a film of liquid flowing down the rows of horizontal tubes. Large desalination plants can have more than 10 rows;  $\delta_w$ ,  $k_w$  – tube

wall thickness and its thermal conductivity, respectively. In thermal desalination plants,  $\delta_w = 0.5\text{-}2$  mm and  $k_w = 60\text{-}100$  W/(m·K). With these values, the thermal resistance of the tube wall can be neglected. In the absence of salt deposits and other contaminants on the surface of the tubes ( $\sum_{i=1}^n R_i = 0$ ), the main thermal resistance in thin film evaporators can be calculated by the formula:

$$R = 1/h_{con} + 1/h_{evap}. \quad (4)$$

*Heat transfer efficiencies during evaporation of a liquid film flowing down horizontal tubes*

Calculation methods for HTC's during liquid evaporation on a smooth tube and on tubes with enhanced surface are given in [7-9]. Ribatski and Jacobi [7] analysed the studies of heat transfer during the evaporation of various liquids before 2005. The authors of [7] provided 16 formulae for calculating  $h_{evap}$ . In the thesis [8], analysis of 144 works was performed, 22 of which were published from 2005 to 2013. In addition to the formulae from [7], Bustamante [8] gave another 31 formulae for calculating  $h_{evap}$ .

Table 1 shows the formulae from [7, 8], which were obtained by evaporation of water vapour on a smooth tube. In these dependencies, the numerical values of the degrees under the criteria  $Re_f$  and  $Pr_l$  change from 0.06 to 0.85. Accordingly, the values of  $h_{evap}$  will be 1.5-10 times different.

Large discrepancies (more than three times) in the calculation of  $h_{evap}$  for various dependencies are also noted in [8, 9].

Rifert et al. [10-12] experimentally substantiated the model of heat transfer during evaporation and heating of a liquid film. This model is based on the analogy of the evaporation process with convective heat transfer at the initial thermal section of the development of velocity and temperature profiles in the laminar boundary layer [13].

Raising of the rate of average heat transfer with increasing mass flow rate noted by some investigators is caused by an increase in the initial thermal region length and by a decrease in the developing boundary layer thickness at all angular locations ( $\varphi$  coordinates) along the tube perimeter, but not by the transition to a turbulent regime at stable flow and heat transfer.

A comparison of  $h_{\varphi}=f(\varphi)$  obtained for a gravity-falling film with that for a cross liquid flow shows that the heat transfer processes are analogous for both cases [14]. Hence, the experimentally determined values of the average HTC's in a liquid

film were processed according to the system of dimensionless numbers accepted for heat transfer in a cross flow. The empirical dependence obtained:

$$Nu_{evap} = 0.295 Re_f^{0.63} Pr_l^{0.36} \quad (5)$$

$$\text{where } Re_d = w_0 d / \nu_l \quad (6)$$

$w_0$  – average film velocity, m/s

$$w_0 = (w_l^2 + 2gl_z)^{0.5} \quad (7)$$

$l_z$  – distance between the tubes, m;  $w_l$  – film velocity during liquid separation:

$$w_l = 0.52(g\nu_l)^{0.33} Re_f^{0.66} \text{ if } Re_f \leq 220 \quad (8)$$

$$w_l = 1.55(g\nu_l)^{0.33} Re_f^{0.462} \text{ if } Re_f > 220 \quad (9)$$

$$Re_f = G / (\pi d \mu_l). \quad (10)$$

Justification of Eqs. (8)-(10) is given in [15].

Equation 5 is almost the same as applied for calculation of heat transfer for cross flow over the in-line tube bundles and appropriately generalizes not only our test data, but also those of other investigators for film heating, cooling and evaporation [10]. In [11-12], it is proved that eq. (5) summarizes with sufficient accuracy (the discrepancy does not exceed 10%) the experimental data on heating and evaporation in a film of liquid flowing down horizontal tubes (single and in a bundle of tubes).

*Heat transfer coefficients during condensation inside horizontal tubes*

In thin film evaporators, condensation of heating steam occurs inside the tubes with a diameter from 10 to 50 mm and a length from 1 to 16 m. In MED systems, there can be from 2 to 10 effects. To prevent salt deposits, the steam temperature in the first effect should not exceed 80° C. The temperature in the last effect should not be lower than 30° C due to the limit for coolant temperature. Thus, the temperature difference in one effect can reach 3-10° C.

To determine  $h_{con}$ , a number of studies make use of dependencies given in Table 2. Calculations of  $h_{con}$  in different works give the values ranging from 4 kW/(m<sup>2</sup>·K) to 15 kW/(m<sup>2</sup>·K) [9]. If we take into account the possibility of heat transfer enhancement from evaporation by means of profiling tubes by 1.5-2 times [12, 14, 22, 24], then the values  $h_{evap}$  and  $h_{con}$  will be almost the same. The values  $h_{evap}$  and  $h_{con}$ , according to our calculations, will affect the value of overall heat transfer coefficient within 7-15%. It will lead to an increase in heat transfer area and capital costs (cost of tubes).

**Table 1.** Formulae for determining HTC during liquid film evaporation

Study	Correlation	Study	Correlation
Mitrovic (1986) [16]	$Nu_{evap} = \frac{0.0137 Re_f^{0.349} Pr_l^{0.5} (s/d)^{0.158}}{1 + \exp(-0.0032 Re_f^{1.32})}$	Putilin <i>et al.</i> (1996) [22]	$Nu_{evap} = 0.295 Re_f^{0.63} Pr_l^{0.36}$
Rogers and Goindi (1989) [17]	$Nu_{evap} = 0.063 Re_f^{0.466} Ar^{2/9} Pr_l^{1/3} (\sin \theta / P(\theta))^{1/3}$	Liu and Zhu (2005) [23]	$Nu_{evap} = 0.2116 Re_f^{0.29} Pr_l^{0.515} Ar^{-0.39}$
Parken <i>et al.</i> (1990) [18]	$Nu_{evap} = 0.042 Re_f^{0.15} Pr_l^{0.53}$	Li <i>et al.</i> (2011a) [24]	$Nu_{evap} = 7.426 Re_f^{-0.679} Bo^{-0.235}$
Rogers <i>et al.</i> (1995) [19]	$Nu_{evap} = 0.2071 Re_f^{0.24} Pr_l^{0.66} Ar^{-0.111}$	Li <i>et al.</i> (2011b) [25]	$Nu_{evap} = 182.1 Re_f^{-1.56}$
Hu and Jacobi (1996) [21]	$Nu_{evap} = 0.113 Re_f^{0.85} Pr_l^{0.85} Ar^{-0.27} (s/d)^{0.04}$	Wang <i>et al.</i> (2013) [26]	$Nu_{evap} = 1.57 Re_f^{0.49} Pr_l^{0.4} Ar^{-0.23} (s/d)^{0.45}$
Nomenclature: $Ar$ – Archimedes number; $Bo$ – Bond number; $d$ – outer diameter, m; $Nu_{evap}$ – Nusselt number ( $= h_{evap} d / k_l$ ); $Pr_l$ – liquid Prandtl number; $Re_f$ – film Reynolds number; $s$ – tube spacing, m.			

Calculations of the process of condensation of water vapour inside the tubes with a diameter of 10 to 50 mm and a length of 1 to 16 m at  $t_s=40-90$  °C and heat flows from 15 to 40 kW/(m<sup>2</sup>·K) demonstrate that at the tube inlet, the steam velocity can reach 100–150 m/s. Under such conditions, the steam velocity has a significant effect on heat transfer. On most surface of the tube, there will be an annular and intermediate (asymmetric) phase flow regime and the  $h_{con}$  values will differ from the HTCs in a stratified regime (see fig. 2).

The features of the film vapour condensation inside tubes (horizontal and vertical) are considered in reviews [30, 31], descriptions of new methods for calculating heat transfer during condensation are given in [34-38].

In [31-38], it is discussed that the area of condensation of the moving vapour in case of laminar condensate flow is not sufficiently studied experimentally, but this regime with  $Re_l < 200$  is characteristic of steam condensation in horizontal film evaporators.

#### EXPERIMENTAL RESEARCH

The detailed description of the experimental apparatus and method of heat transfer investigation during film condensation of moving vapour inside horizontal tube can be found in Rifert's previous publication [34]. The installation enables measuring circumferential local heat transfer coefficients by the “thickness wall” method. Using the “thickness wall” method allowed investigating the influence of the circumferential heat flux on the local values of the heat transfer coefficients. The research of water vapour condensation was performed at low pressures ( $t_s = 46-70$  °C) in the middle of a smooth

tube  $d = 18$  mm with the following parameters:  $G = 3-52$  kg/(m<sup>2</sup>s),  $x = 0.94-0.1$ ,  $q = 70-240$  kW/m<sup>2</sup>,  $Re_f=12-1500$ .

The flow pattern map of Rifert *et al.* [36, 37] was used to determine the limits of phase flow regimes. According to this regime map, the limits of the flow regimes are determined by the following dependencies:

$$\text{at } \tau_f / \tau_g > 10 \text{ – annular flow} \quad (11)$$

$$\text{at } 1 \leq \tau_f / \tau_g \leq 10 \text{ – intermediate flow} \quad (12)$$

$$\text{at } \tau_f / \tau_g < 1 \text{ – stratified flow} \quad (13)$$

where values of the shear stress  $\tau_f$  and the gravitational force  $\tau_g$  are calculated in such a way:

$$\tau_f = C_f \rho_v w_v^2 / 2 \quad (14)$$

$$\tau_g = \rho_l g \delta. \quad (15)$$

Fig. 2 demonstrates the regime map for all the experimental data obtained. It shows that the data correspond to annular, intermediate and stratified phase flows.

Compare the experimental values of HTC with the calculations according to the formulae from Table 2. The results are shown in Fig. 3. It is obvious that the obtained experimental data significantly (more than 100%) diverge from the calculated data.

Fig. 4 shows a comparison of the overall HTC calculated by the formula (3) for different values of  $h_{con}$ . In this case, the values of  $h_{evap}$  for each option were calculated by the formula (5), while the values of  $h_{con}$  – by the formulae from Table 2.

The statistical comparison is summarized in Table 3. It contains the mean absolute deviation  $e_A$ , the average deviation  $e_R$ , and the standard deviation,  $\sigma_N$ , given in Eqs. (16)–(18), respectively, along with the percentage of predicted points lying within  $\pm 10\%$  error bars.

$$e_A = 1/n \sum 100 |(h_{calc} - h_{exp}) / h_{exp}| \quad (16)$$

$$e_R = 1/n \sum 100 [(h_{calc} - h_{exp}) / h_{exp}] \quad (17)$$

$$\sigma_N = \left[ 1/(n-1) \sum (e - e_R)^2 \right]^{0.5} \quad (18)$$

where  $e = 100 [(h_{calc} - h_{exp}) / h_{exp}]$ ;  $n$  – number of calculation points. Fig. 4 and Table 3 show that the overall HTC values calculated using different formulae to determine  $h_{con}$  differ significantly. The

calculation by the Nusselt formula appears to be the closest to the experimental data.

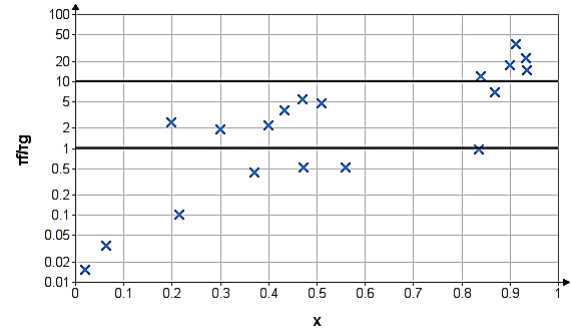


Fig. 2. Determining the phase flow regime

Table 2. Formulae for calculating HTCs in case of water vapour condensation

Authors, year	Heat transfer correlation
Nusselt [27] (1916)	$h_{con} = 0.728 \left[ \frac{k_l^3 \rho_l (\rho_l - \rho_v) g h_{lv}}{\mu_l d \Delta T} \right]^{0.25}$
Boyko [28] (1966)	$h_{con} = 0.024 \text{Re}_l^{0.8} \text{Pr}_l^{0.43} (1 + x(\rho_l/\rho_v - 1))^{0.5} \lambda_l / d$
Traviss [29] (1998)	$h_{con} = Nu \lambda_l / d,$ $Nu = F_{X,tt} \text{Pr}_l \text{Re}_l^{0.9} / F_2 \text{ if } F_{X,tt} \leq 1; Nu = F_{X,tt} \text{Pr}_l \text{Re}_l^{0.9} / F_2 \text{ if } F_{X,tt} < 1$ <i>Equations for calculation of <math>F_{X,tt}</math> and <math>F_2</math> are given in [29]</i>
Shen [30] (2017)	$h_{con} = \theta h_{top} + (2\pi - \theta) h_{bot}$ $h_{bot} = 0.033 \text{Re}_l^{0.8} \text{Pr}_l^{0.33} (k_l / d) \left[ 1 + \left( \frac{\rho_l}{\rho_v} \right)^{0.5} \left( \frac{x}{1-x} \right) \right]^{0.8},$ $h_{top} = \frac{0.02 \text{Re}_{vo}^{0.318}}{1 + 1.11 X_u^{0.755}} \left[ \frac{\rho_l (\rho_l - \rho_v) g h_{lv} k_l^3}{d \mu_l \Delta T} \right]^{0.25}$

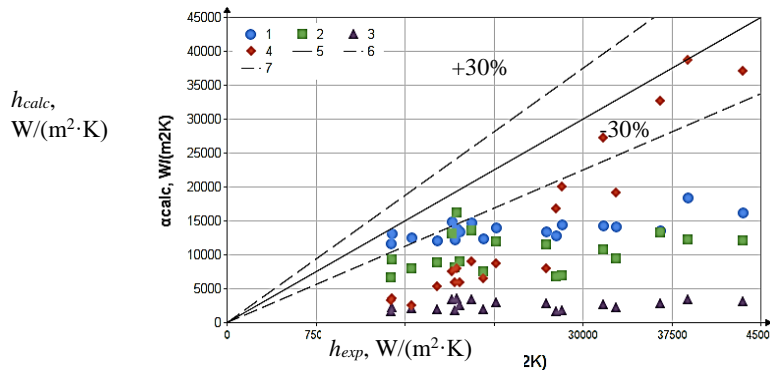


Fig. 3. Comparison of the obtained experimental data with correlations: 1 – Nusselt (1916) [27], 2 – Boyko (1966) [28], 3 – Shen (2017) [30], 4 – Traviss (1998) [29]

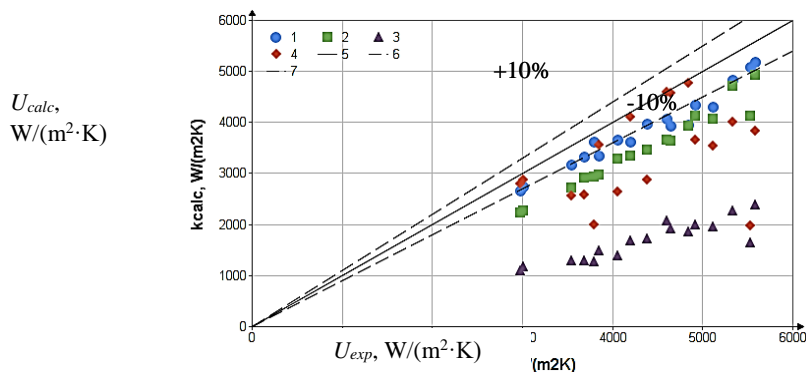


Fig. 4. Comparison of the overall HTC: 1 – Nusselt (1916) [27], 2 – Boyko (1966) [28], 3 – Shen (2017) [30], 4 – Traviss (1998) [29]

Table 3. Statistical comparison of the suggested method with the experimental data (in %)

Statistical comparison	$e_A$	$e_R$	$\sigma_N$	Percentage of predicted points lying within $\pm 10\%$ error bars
Nusselt [27]	10.8	-10.8	3.7	47
Boyko [28]	19.6	-19.6	5.0	5
Traviss [29]	24.6	-24.6	19.4	37
Shen [30]	62.1	-62.1	4.2	0

The studies of Rifert *et al.* [12, 14, 22] suggest various methods for heat transfer enhancement during liquid film evaporation. The analysis of these works leads to the conclusion that the most effective method of intensification in thin film evaporators is the longitudinal finning. This method allows increasing heat transfer by 60-80%, i.e. obtaining  $h_{evap} = 10-15 \text{ kW}/(\text{m}^2 \text{ K})$ . In this case, the accuracy of measuring the values of  $h_{con}$  according to the above calculation method will increase the heat transfer by 15-20%.

### CONCLUSIONS

The actual values of HTCs during steam condensation at low pressure significantly differ from those calculated by the formulae of Nusselt [27], Boyko [28], Shen [30] and Traviss [29] (error more than 100%). The inaccuracy in determining  $h_{con}$  leads to a change in the values of the overall heat transfer coefficients in the range of 7-15%, and, accordingly, the surface area of heat transfer. The use of various methods of heat transfer enhancement during liquid film evaporation allows the increase of not only  $h_{evap}$ , but also of overall heat transfer coefficients by 15-20%. In carrying out further experimental studies, it is necessary to study the process of steam condensation in the conditions of steam velocity influence on heat transfer and at the regime parameters characteristic of thin film evaporators. Such research will allow

improving thermal calculation of film evaporators and increasing their energy efficiency.

### REFERENCES

1. B. Ortega-Delgado, L. García-Rodríguez, D.-C. Alarcón-Padilla, *Desalination and Water Treatment*, **97**, 94 (2017).
2. M. L. Elsayed, O. Mesalhy, R. H. Mohammed, L. C. Chow, *Appl. Therm. Eng.* **137**, 475 (2018).
3. P. Cyklis, *Applied Thermal Engineering*, **123**, 1365 (2017).
4. Q. Zhang, X. Zhang, C. Yin et al., *International Journal of Refrigeration*, **113**, 80 (2020).
5. M. R. Lubis, M. T. Holtzaple, *Aceb International Journal of Science and Technology*, **1** (1) 1 2012.
6. O. A. Hamed, A. M. Zamamiri, S. Aly, N. Lior, *Energy Conversion and Management*, **37**(4), 379 (1996).
7. G. Ribatski, A. M. Jacobi, *International Journal of Refrigeration*, **28**, 635 (2005).
8. J. G. Bustamante, Falling-film evaporation over horizontal rectangular tubes, PhD Thesis, School of Mechanical Engineering, Georgia, 2014, p. 254.
9. J. Uche, J. Artal, L. Serra, *Desalination*, **152**, 195 (2002).
10. V. G. Rifert, B. V. Andreev, Boiling and Condensation, Riga, 1981, p. 24.
11. V. G. Rifert, Yu. V. Putilin, V. L. Podbereznyi, *Journal of Engineering Physics*, **54**(5), 490 (1988).
12. V. G. Rifert, Yu. V. Putilin, V. L. Podbereznyi, *Journal of Enhanced Heat Transfer*, **8**(2), 91 (2001).
13. A. Zakauskas, V. Makaryavichus, A. Shlancauskas, Heat transfer on the tubes band during cross liquid flow. Mintis., Vilnius, 1972.

14. Yu. V. Putilin, V. L. Podberezniy, V. G. Rifert, Proceedings of the 7th International Symposium on Fresh Water from the Sea, Amsterdam, vol. 1, 1980, p. 241.
15. V. Rifert, *Thermal Engineering*, **31**(11), 626. (1984).
16. J. Mitrovic, Eighth International Heat Transfer Conference, San Francisco, 1986, p. 1949.
17. J. T. Rogers, S. S. Goindi, *The Canadian Journal of Chemical Engineering*, **67**, 560 (1989).
18. W. H. Parken, L. S. Fletcher, V. Sernas et al., *J. Heat Transfer*, **112**, 744 (1990).
19. J. T. Rogers, S. S. G
20. oindi, M. Lamari, National Heat Transfer Conference, Portland, 1995, p. 3.
21. X. Hu, A. M Jacobi, *J. Heat Transfer*, **118**, 626 (1996b).
22. J. V. Putilin, V. L. Podberezny, V. G. Rifert, *Desalination*, **105**, 165 (1996).
23. Z.-H. Liu, Q.-Z. Zhu, *Chemical Engineering Communications*, **192**, 1334 (2005).
24. W. Li, X.-Y. Wu, Z. Luo et al., *Int. J. Heat Mass Transfer*, **54**, 2990 (2011a).
25. W. Li, X.-Y. Wu, Z. Luo et al., *Int. J. Heat Mass Transfer*, **54**, 1986 (2011b).
26. X. F. Wang, P. S. Hrnjak, S. Elbel, et al., *Journal of Heat Transfer*, **135**(7), 1 (2013).
27. W. Nusselt, *Zeitschrift VDI*, **60**, 541, 568 (1916).
28. L. D. Boyko, Heat Transfer in the Elements of Power Plants, (in Russian), 1966, p. 197.
29. D. P. Traviss, A. B. Baron, W. M. Rohsenow, Report No. DSR-72591-74, Massachusetts Institute of Technology, Cambridge, MA, 1971, p. 105.
30. S. Shen, Y. Wang, D. Yuan, *International Journal of Heat and Mass Transfer*, **114**, 816 (2017).
31. V. G. Rifert, V. V. Sereda, *Scientific journal "Thermal Science"*, **19**(5), 1769 (2015).
32. V. G. Rifert, V. V. Sereda, A.S. Solomakha, *Heat and Mass Transfer*, **55** (11), 3041 (2019).
33. Yu. E. Nikolaenko, E. S. Alekseik, D. V. Kozak, T. Yu. Nikolaienko, *Thermal Science and Engineering Progress*, **8**, 418 (2018).
34. V. G. Rifert, V. V. Sereda, P. A. Barabash, V. V. Gorin, *Thermal Science*, **21**(3), 1479 (2017).
35. V. G. Rifert, V. V. Sereda, P. A. Barabash et al., *Heat and Mass Transfer*. Vol. page (2020).
36. V. G. Rifert, V. V. Sereda, P. A. Barabash et al., *Energetika*, **64** (3), 146 (2018).
37. V. G. Rifert, V. V. Sereda, P. A. Barabash et al., *Bulg. Chem. Commun.*, **50** (K), 58 (2018).
38. V. G. Rifert, V. V. Gorin, V. V. Sereda et al., *Journal of Engineering Physics and Thermophysics*, **92**, 797 (2019).

## Pool boiling of refrigerant on a flat modified surface

A. N. Pavlenko, V. E. Zhukov, E. Yu. Slesareva\*

*Kutateladze Institute of Thermophysics, Siberian Branch of the Russian Academy of Sciences, Novosibirsk*

Received: June 30, 2020; Accepted: August 08, 2020

Improving the efficiency, reliability and energy intensity of heat exchangers is an urgent task in various fields of industry. One of the ways to increase the heat transfer efficiency and the critical heat flux is to modify the heat transfer surface. In our research, surface modification was carried out using 3D printing. This paper presents the results of a study of heat transfer on modified and unmodified surfaces during boiling under conditions of free convection. The working liquid is freon R21. The experiments were carried out at two working sections made of LS59 brass. The experimental blocks were in the form of cylinders with a diameter of 20 mm. Heat was released at one end of the cylindrical section and transferred to liquid from the opposite end of horizontal orientation. Thermometers were installed along the length of the cylinder, which measure the temperature distribution along the cylinder from the heat source to the heat transfer surface. According to thermometers, the temperature of the heat-transfer surface and the density of the heat flux through this surface were determined. In one section, the heat transfer surface was polished; in another section, a 0.5 mm thick coating of spherical copper granules with a diameter of 50  $\mu\text{m}$  was applied to the heating surface using a 3D printer. Heat transfer under the conditions of single-phase convection and pool boiling of liquid R21 freon on the saturation line before the boiling crisis was studied. The studies were carried out in the pressure range of 0.18 - 0.21 MPa.

**Keywords:** pool boiling, heat transfer coefficient, modified heat-transfer surface, vaporization sites, refrigerant

### INTRODUCTION

Heat exchangers are the devices designed to transfer heat from one coolant to another or to the environment. This is one of the most common devices for all types of power plants and engines. The efficiency and reliability of heat exchangers are of great importance for various industries, including intensively developing microelectronics, therefore, much attention is paid to promising developments for their improvement all over the world. Improvement of heat exchange equipment should make it possible to reduce the consumption of expensive materials for newly created heat exchangers, reduce their dimensions, facilitate the layout as a whole, and significantly increase their efficiency. One of the ways to increase the heat transfer efficiency and critical heat flux is to modify the heat-transfer surface using various technologies [1-6]. One of the latest technologies for modifying a heat-transfer surface is the technology of applying various structures *via* 3D printing [7, 8]. To obtain comparatively generalized experimental data on heat transfer characteristics and dynamics of crisis phenomena on various types of heat-transfer surfaces modified by 3D printing, the authors of this paper are performing a number of experimental studies. This paper presents investigation results about heat transfer intensity on horizontal smooth and 3D-modified heat-transfer surfaces at pool boiling R21.

### EXPERIMENTAL SETUP AND TECHNIQUES

The experiments were carried out using a setup, whose schematic diagram is shown in Fig. 1.

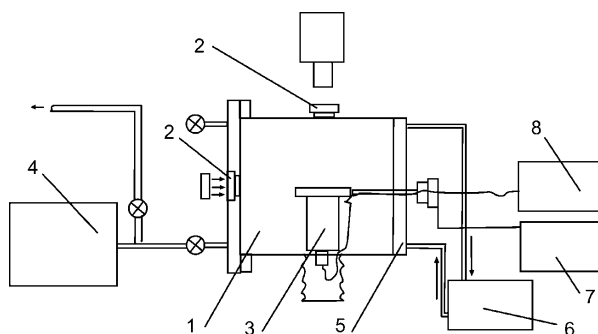


**Fig. 1.** Scheme of experimental setup. 1 – working vessel; 2 – windows; 3 – working section unit; 4 – filling tank; 5 – heat exchanger; 6 – thermostat; 7 – DC source; 8 – ADC.

The setup is a sealed cylindrical vessel (1) with a diameter of 250 mm and height of 250 mm. The vessel is equipped with glass windows (2) with a diameter of 60 mm for observation and photo-video recording of the processes on the heat-transfer surface of the working section (3). To fill the vessel with freon and evacuate freon from the vessel, a filling tank (4) with a system of overflow and vacuum pumping channels is used. A 50-W LED assembly is used to illuminate the object during photo and video shooting. The vessel is designed to operate at pressures of up to 0.4 MPa.

The pressure in the vessel is maintained at a predetermined level by a heat exchanger (5), where

\* To whom all correspondence should be sent:  
E-mail: styuardessa@yandex.ru

a refrigerant circulates, whose temperature is set by a thermostat (6). The working section is heated by a direct-current source (7). Silicon diodes with high temporal stability, acceptable linearity of calibration in the temperature range of 0–150°C, and higher sensitivity than that of platinum thermometers and thermocouples are used to measure the temperatures in the working volume and temperature distribution over the working section. The temperature sensors were individually calibrated using a Thermo Haake DC30 thermostat with temperature measurement accuracy of 0.1°C and temperature maintaining accuracy of  $\pm 0.02^\circ\text{C}$ . The calibration was carried out in the temperature range of 20 - 110°C. The voltage drop on the thermometers is measured by a 24-bit 16-channel ADC LTR114 (8).

The working section is made in the form of a sealed cylindrical stainless steel block (Fig. 2).

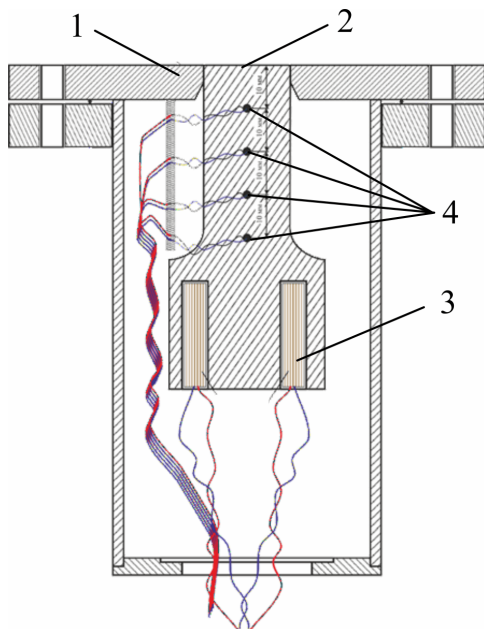


**Fig. 2.** Scheme of the working section. 1 – section cover; 2 – heat-transfer surface; 3 – heating element; 4 – thermocouples.

The round cover of section (1) is made of fiberglass with a thickness of 8 mm. In the center of the cover there is a hole with a diameter of 20 mm. A 70 mm long cylindrical rod made of LS-59-1 brass is installed in this hole. The end face of this rod (2) is the studied heat-transfer surface and it is installed at the same level with the section cover. The heat is generated by the heating elements (3) mounted on the opposite end of the cylinder. At a distance of 10, 20, 30, and 40 mm from the heat-transfer surface, the holes with a diameter of 1.3 mm are made in the cylinder, where the thermometers (4) are installed. The wires from the section are brought out through a sealed glass

connector; the space inside the section is filled with a basalt heat insulator.

Two series of experiments were carried out at the working section. In the first series, the heat-transfer surface was smooth, in the second series, it was modified using 3D printing. Porous strips 0.5 mm thick and 4 mm wide, made on a 3D printer from copper granules with a diameter of 50  $\mu\text{m}$ , were fixed on the heat-transfer surface by spot soldering. In soldering spots, conical holes with dimensions of 0.2 mm at the point of contact were formed. The photos of heat-transfer surfaces used in the first and second series of experiments are presented in Fig. 3.

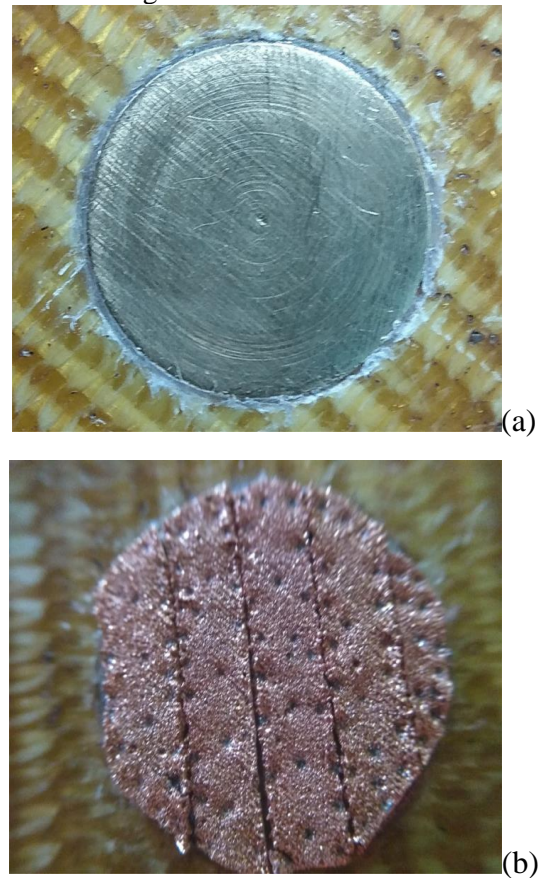


**Fig. 3.** Heat-transfer surface. a) heat-transfer surface in the first experimental series; b) modified heat-transfer surface in the second series of experiments.

## RESULTS AND DISCUSSION

The experiments were carried out under the conditions of a high volume at a pressure of 0.18 - 0.21 MPa, which corresponds to the equilibrium freon R21 temperatures of 25 - 30°C. The heat flux density increased from minimum to maximum, then decreased.

The dependence of the heat transfer coefficient ( $\alpha$ ) on the heat flux density ( $q$ ) for horizontally oriented surfaces is shown in Fig. 4.

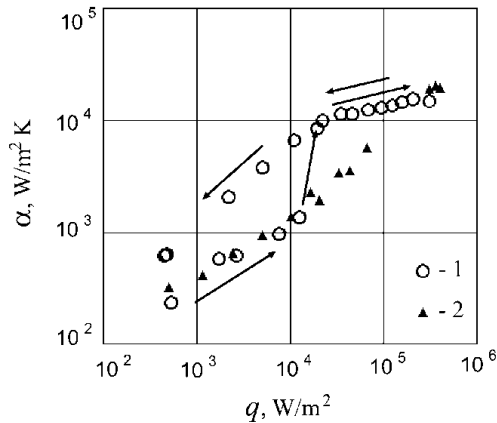


**Fig. 4.** Heat transfer coefficient ( $\alpha$ ) vs. heat flux density ( $q$ ) for horizontal surfaces.  $P = 0.18 - 0.21$  MPa. 1 – modified heat-transfer surface; 2 – unmodified heat-transfer surface.

At low heat flux densities  $q < 3000$  W/m<sup>2</sup> on a smooth and modified heat-transfer surface, vaporization is observed only from microcracks in the sealing layer of the brass cylinder joint with the fiberglass cover of the working section. There is no vaporization at the studied heat-transfer surface; the heat transfer process is carried out by a convective mechanism. On a smooth heat-transfer surface, activation of vaporization sites occurs gradually with an increase in the heat flux density in the range of  $3000 < q < 9000$  W/m<sup>2</sup>. In this range, the vaporization sites extend to the entire heat-transfer surface. With a further increase in the heat flux density, additional vaporization sites are activated and vapor generation at the existing sites becomes more intensive. With decreasing heat flux density, the heat transfer coefficient for a smooth surface without coating is almost unchanged for the same  $q$  values. On a modified heat-transfer surface, the presence of active vaporization sites is not observed up to the heat flux density  $q = 12300$  W/m<sup>2</sup>, inclusive. In this range of heat flux density, the heat transfer coefficients on smooth and modified surfaces almost coincide. An increase in the heat flux density to  $q = 19000$  W/m<sup>2</sup> leads to an abrupt activation of vaporization sites throughout the modified heat-transfer surface. At that, the heat transfer coefficient on a modified heat-transfer surface (8700 W/m<sup>2</sup>K) increases more than 4 times relative to the heat transfer coefficients on a smooth heat-transfer surface (1960 - 2200 W/m<sup>2</sup>K). As it can be seen from the figure, with a decrease in the heat flux density on the modified heat-transfer surface, the vaporization sites remain active up to the minimum values of the heat flux density. The value of the heat transfer coefficient in this case is 3–4 times higher than the value  $\alpha$  measured at the corresponding  $q$  values on a smooth heat-transfer

surface and on a modified heat-transfer surface with inactive vaporization sites.

In the range of  $22000 < q < 210000$  W/m<sup>2</sup>, the heat transfer coefficient for the modified heat-transfer surface increases from 10000 to 15900 W/m<sup>2</sup>K. In this range of heat loads, the difference in the rate of heat transfer between the modified and unmodified heat-transfer surfaces decreases and it is almost absent in the pre-crisis region ( $q > 300000$  W/m<sup>2</sup>).

## CONCLUSIONS

A technology for modifying the heat-transfer surface using a porous coating made on a 3D printer was developed. The coating with a thickness of 0.5 mm is made of copper granules with a diameter of 50  $\mu$ m.

The heat transfer coefficient was measured on a smooth unmodified heat-transfer surface and on a modified heat-transfer surface in the range of heat flux density from 500 to 400000 W/m<sup>2</sup>. Unlike a smooth surface without a coating, pronounced hysteresis of the heat transfer coefficient was observed on the modified heat-transfer surface for different directions of the change in the heat load. In the range of small and medium values of the heat flux density under the conditions of activated vaporization sites, the heat transfer rate at boiling on a modified heat transfer surface was up to 4 times higher than the heat transfer intensity on a smooth heat transfer surface. In the pre-crisis region, the heat transfer rate at nucleate boiling on both heat-transfer surfaces was almost the same.

**Acknowledgements:** This study was carried out at the Kutateladze Institute of Thermophysics, Siberian Branch of the Russian Academy of Sciences under the grant of the Russian Science Foundation no. 19–19–00180.

## REFERENCES

1. Y. Lv, M.Y. Liu, L.F. Hui, A.N. Pavlenko, A.S. Surtaev, V.S. Serdyukov, *J. Eng. Therm.*, **28**, 163 (2019).
2. S. Kim, A. Girard, S. Jun, J. Lee, S. M. You, *Int. J. Heat Mass Transf.*, **118**, 802 (2018).
3. D. Attinger, C. Frankiewicz, A. R. Betz, T. M. Schutzius, R. Ganguly, A. Das, C. J. Kim, C. M. Megaridis, *MRS Energy Sustainability*, **1**, 1 (2014).
4. J. P. McHale, S. V. Garimella, *Int. J. Multiphase Flow*, **36**, 249 (2010).
5. H. Hu, C. Xu, Y. Zhao, K. J. Ziegler, J. N. Chung, *Scientific Reports*, **7**, 1 (2017).
6. A. N. Pavlenko. *J. of Phys.: Conf. Ser.*, **1359**, 012001 (2019).
7. J. Dilag, T. Chen, S. Li, S. A. Bateman, *Additive Manufacturing*, **27**, (2019).
8. V. P. Bessmeltsev, A. N. Pavlenko, V. I. Zhukov. *Optoelectronics, Instrumentation and Data Processing*, **55** (6), 554 (2019).

# Integrated absorption-adsorption process for waste-free decontamination of gases from sulfur dioxide. Part 1. Choice of ion-exchange resin and adsorption and desorption parameters

S. Stefanov\*, E. Razkazova-Velkova

*Institute of Chemical Engineering, Bulgarian Academy of Sciences, Acad. G. Bonchev str, bldg. 103, 1113 Sofia, Bulgaria*

Received: July 26, 2020; Accepted: August 03, 2020

One of the most hazardous atmospheric air pollutants is sulfur dioxide. Its main anthropogenic source is the burning of fossil fuels with high sulfur content. A waste-free new technology is proposed for decontamination of sulfur dioxide-containing gases that uses its absorption by water, followed by adsorption by ion-exchange resin, subsequent desorption and further processing of the contaminant. As a first step for detailed investigation of the technology a screening for the appropriate resin is conducted. Seven different ion exchange resins and a zeolite are presented in this study. After the initial evaluation Dowex<sup>®</sup> 66 is selected as the most promising one and further experiments regarding adsorption and desorption times, as well as variation of the concentration of desorbing agent, are performed. Lastly, consecutive adsorption/desorption is conducted to determine the number of cycles the resin can operate at peak performance.

**Keywords:** Ion-exchange resin, adsorption, desorption, sulfur dioxide

## INTRODUCTION

Many technologies for gases purification from SO<sub>2</sub> are known [1,2]. A wide class of methods uses alkaline absorbents [3-8]. The products obtained from the absorption process in most cases have to be subjected to additional oxidation that increases the expenses for the whole process [9-11]. The final products - sulfates (Na<sub>2</sub>SO<sub>4</sub> and CaSO<sub>4</sub>) have limited practical application and they present a problem for their disposal.

There are few articles dedicated to the adsorption of gaseous sulfur dioxide by ion-exchange resins and zeolites [12-14]. Information for adsorption of sulfurous acid by ion-exchange resins wasn't found.

For the gas purification from SO<sub>2</sub>, a practically waste-free technology should be used. In view of the above, we propose a new absorption-adsorption approach for flue gas SO<sub>2</sub> decontamination by direct water absorption, followed by adsorption by ion-exchange resin and subsequent desorption from the resin by dilute ammonia solution. The resultant solution, treated appropriately, can be used as precursor in the chemical industry. The proposed absorption-adsorption method includes absorption of SO<sub>2</sub> in water with the simultaneous adsorption of the SO<sub>2</sub> from the water solution by ion-exchange resin. The adsorbent desorption is accomplished with a solution of NH<sub>3</sub>, followed by decomposition of the resulting (NH<sub>4</sub>)<sub>2</sub>SO<sub>3</sub> with HNO<sub>3</sub>. The products of the processes are pure - gaseous SO<sub>2</sub> and aqueous solution of NH<sub>4</sub>NO<sub>3</sub>.

Sulfur dioxide has application in the chemical industry, and NH<sub>4</sub>NO<sub>3</sub> is also a commercially viable product - nitrogen fertilizer.

## MATERIALS AND METHODS

### *Ion-exchange resins choice*

The ion-exchange resins used in this study are all commercially available and were chosen based on their size, functional groups and mechanism of adsorption. Sulfurous acid with concentration of  $1.6 \pm 0.2 \text{ g l}^{-1}$  was used to simulate the water-adsorption process of SO<sub>2</sub> flue gas decontamination. This concentration is consistent with the maximum concentration of sulfur dioxide in the flue gases [12] and Henry's law.

### *Adsorption of contaminant*

The initial screening of the resins was conducted by mixing a set amount of resin (1-5 g) and 100 ml of sulfurous acid in a closed flask. The mixture was stirred for a fixed time and at a constant rate (400 rpm). In order to evaluate the time needed for adsorption experiments were carried out varying the stirring time (0 - 60 min). After the stirring the mixture was left to settle, the aqueous phase was removed and the remaining sulfurous acid analyzed, while the loaded ion-exchange resin proceeded for desorption.

### *Desorption of contaminant*

Desorption of sulfurous acid was performed by adding 50 ml of aqueous solution of NH<sub>3</sub> to the ion-exchange resin.

\* To whom all correspondence should be sent:

E-mail: [s.stefanov@iche.bas.bg](mailto:s.stefanov@iche.bas.bg)

The mixture was stirred for a fixed time at a constant rate (400 rpm). In order to evaluate the time needed for desorption experiments were carried out varying the stirring time (0 - 60 min). Afterwards, the mixture was left to settle, the aqueous phase was removed and the solution analyzed. The amount of NH<sub>3</sub> used was chosen to be in great excess (2.5 % v/v) or near (0.8 % v/v) the stoichiometric amount needed for the complete desorption of the initial amount of sulfurous acid. The volume used was half that of the initial sulfurous acid in order to achieve additional increase of the acid concentration, which in turn will ease further processing of the contaminant.

The concentrations of sulfurous acid before and after the absorption and after regeneration were determined iodometrically.

### Ion-exchange resin cycle life

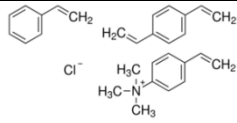
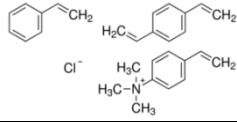
In order to determine the viability of the ion-exchange resin for continuous use 10 adsorption/desorption cycles were performed on the same resin sample, according to the above methodology. Due to a gradual decrease in the performance of the resin 5 additional cycles were performed with a “water rinsing” step between the end of the desorption and before the next adsorption. This “rinsing” step constituted of removing the desorption solution, adding 50 ml of distilled water and stirring at constant rate (400 rpm) for 60 min.

## RESULTS AND DISCUSSION

### Screening for the appropriate resin

For this study seven ion-exchange resins were chosen as appropriate, taking into account the resin particle size, the functional groups present, as well as their mechanism of adsorption.

**Table 1.** Ion-exchange resins characteristics

Resin trade name	pH range	Composition of the resin	Resin size	Resin application	Sign
Zeolite	0-14	(SiO <sub>2</sub> ) <sub>x</sub> (Al <sub>2</sub> O <sub>3</sub> ) <sub>y</sub>	2.2 – 4 mm	Zeolite is a naturally occurring volcanic rock used for its ability to bind with ammonias	Zeolite
Dowex <sup>®</sup> 1×8 Chloride form	1-14		20-50 mesh	Dowex <sup>®</sup> 1×8 is a strongly basic anion exchange resin which is used as an absorbent in solid phase extraction	Dowex ①
Dowex <sup>®</sup> 1×8 Chloride form	1-14		200-400 mesh	Dowex <sup>®</sup> 1×8 is a strongly basic anion exchange resin which is used as an absorbent in solid phase extraction	Dowex ②
AmberLite <sup>®</sup> FPA66 (formerly Dowex <sup>®</sup> 66) free base	0-14	Styrene-divinylbenzene (macroporous) matrix active group	50-125 mesh	Weakly basic anion exchange resin for deashing and mixed bed polishing of high fructose corn syrups.	Dowex ③
Ionac SR 7	1-14	Crosslinked polystyrene matrix; quaternary amine functional group	24-28 mesh	Very high selectivity for nitrate ions; selective removal of nitrates	IonacSR7
AmberLite <sup>™</sup> FPX66	0-14	Macroreticular aromatic polymer	24-28 mesh	Non-functionalized, adsorbent resin	Amberlite ①
Amberlite <sup>®</sup> XAD7HP	0-14	Matrix: acrylic	20-60 mesh	Nonionic macroreticular resin that adsorbs and releases ionic species through hydrophobic and polar interactions; usually used under isocratic conditions.	Amberlite ②
Amberlite <sup>®</sup> I RA-96 free base	0-7	Styrene-divinylbenzene (macroporous) matrix active group	20-27 mesh	Weakly basic anion exchange resin, useful for deionization, chromate recovery, formaldehyde deacidification, ammonium nitrate removal and recovery.	Amberlite ③

Additionally, a zeolite was also tested as it is proven that zeolites have the capacity to adsorb contaminants [14]. A list of the resins and some of their characteristics are presented in Table 1. The adsorption capacity of each resin was investigated separately and all experiments were performed in triplets, except one for the zeolite. Each experiment was performed as described above and consisted of mixing a fresh sample ( $5 \pm 0.1$  g) of ion-exchange resin and 100 ml of sulfurous acid ( $C_{H_2SO_3} = 1.6 \pm 0.2 \text{ g.l}^{-1}$ ), stirred for 60 min for the adsorption step and 50 ml of 2.5 % v/v aqueous  $NH_3$ , stirred for 30 min for the desorption step. Results are presented in Table 2, Fig. 1a) (adsorption) and 1b) (desorption).

The experiments showed that the zeolite sample was too brittle and was reduced to dust during the adsorption step. Moreover, no sulfurous acid was recovered, so a decision was made to eliminate it from further testing.

Of the rest of the samples all showed over 75 % adsorption of the contaminant, except for Amberlite 1 and Amberlite 2, which performed poorly and adsorbed only about 20 %.

For the desorption of the acid none of the ion-exchange resins showed consistent results over 60%. We attribute some of these lower results to oxidation of the sulfite to sulfate ions due to the prolonged time of the experiment. A note should be made that the presented percent of desorption is a ratio of adsorbed to desorbed sulfurous acid.

As can be seen from the figure Dowex 2, Dowex 3 and Amberlite 3 adsorb all the quantity of the acid. This is not the case with the regeneration. Only Dowex 3 shows about 60% desorption of the initial quantity of the acid and this is the reason why further experiments were carried with this ion-exchange resin.

#### Determination of the time for adsorption and desorption

The next step was to examine the influence of the adsorption and desorption time on the selected ion-exchange resin (Dowex 3). In order to achieve this goal, the time for adsorption and desorption was varied between 0 and 60 min. The results are presented in Fig. 2 (Fig. 2a) for adsorption and Fig. 2b) for regeneration).

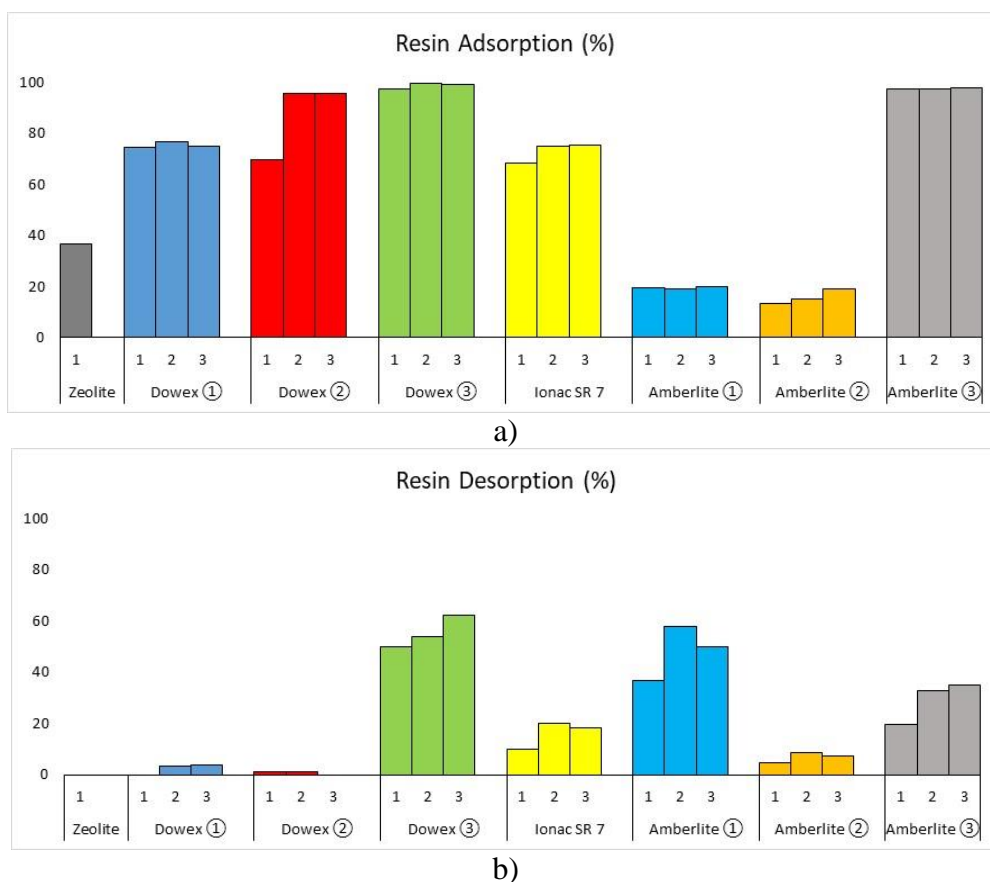
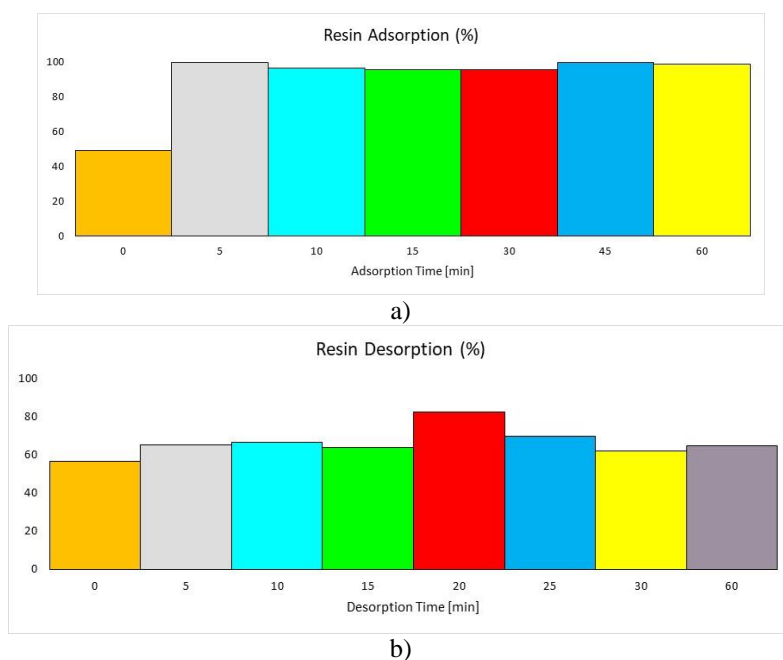


Fig. 1. Adsorption-desorption capacity of the resins investigated.

**Table 2.** Ion-exchange resin experimental results

Resin	Exp. №	Mass (g)	C <sub>H<sub>2</sub>SO<sub>3</sub></sub> (g.l <sup>-1</sup> )	C <sub>Ads H<sub>2</sub>SO<sub>3</sub></sub> (g.l <sup>-1</sup> )	Adsorbed %	C <sub>Des H<sub>2</sub>SO<sub>3</sub></sub> (g.l <sup>-1</sup> )	Desorbed %
Zeolite	1	5.0030	1.6851	0.6199	36.79	0.0000	0.00
Dowex ①	1	5.0033	1.6851	1.2546	74.45	0.0000	0.00
	2	5.0032	1.6789	1.2915	76.92	0.0807	3.12
	3	5.0032	1.6789	1.2591	74.99	0.0968	3.84
Dowex ②	1	5.0057	1.8401	1.2808	69.61	0.0242	0.95
	2	5.0049	1.4854	1.4209	95.65	0.0320	1.13
	3	5.0018	1.4854	1.4209	95.65	0.0000	0.00
Dowex ③	1	5.0779	1.6531	1.6144	97.66	1.6195	50.16
	2	5.0010	1.6789	1.6757	99.81	1.8081	53.95
	3	5.0032	1.6789	1.6628	99.04	2.0664	62.14
Ionac SR 7	1	5.0013	1.8401	1.2620	68.58	0.2558	10.14
	2	5.0017	1.6379	1.2320	75.22	0.4945	20.07
	3	5.0007	1.6379	1.2361	75.47	0.4572	18.49
Amberlite ①	1	5.0057	1.8040	0.3514	19.48	0.2583	36.76
	2	5.0040	1.7240	0.3292	19.10	0.3809	57.85
	3	5.0051	1.7240	0.3452	20.02	0.3456	50.06
Amberlite ②	1	5.0087	1.8040	0.2382	13.20	0.0225	4.73
	2	5.0106	1.7240	0.2647	15.35	0.0467	8.83
	3	5.0110	1.7240	0.3292	19.10	0.0467	7.10
Amberlite ③	1	5.0796	1.6531	1.6144	97.66	0.6355	19.68
	2	5.0052	1.6379	1.5974	97.52	1.0525	32.94
	3	5.0025	1.6379	1.6022	97.82	1.1283	35.21

Experimental conditions: V<sub>H<sub>2</sub>SO<sub>3</sub></sub> = 0.1 L, T<sub>ads</sub> = 60 min; V<sub>NH<sub>3</sub></sub> = 0.05 L, T<sub>des</sub> = 30 min.



**Fig. 2.** Dependence of the adsorption and desorption on time.

The figures show that the adsorption process is practically independent of time while maximum desorption is achieved at the 20<sup>th</sup> minute mark. The results for the regeneration exceed those in Fig. 1 (reaching more than 70%) probably because the prolonged time of desorption in the initial experiments results in higher oxidation of the sulfites to sulfates. So the conditions for further experiments were set at five min for adsorption and twenty min for desorption.

#### Determination of the capacity of the resin

Experiments with different quantity of resin (1, 2, 3, 4 and 5 g) were conducted next. The results are given in Fig. 3.

Figure 3 shows that the whole quantity of acid is adsorbed by about 4 g of resin. The results are sufficiently repeatable and will be used for further mathematical modeling of the proposed technology.

#### Ion-exchange resin cycle life

*Determination of the concentration of ammonia used.* In order to test the effect of ammonia concentration on the desorption cycles experiments with 2.5 % v/v and 0.8 % v/v ammonia were performed. The results are presented in Fig. 4.

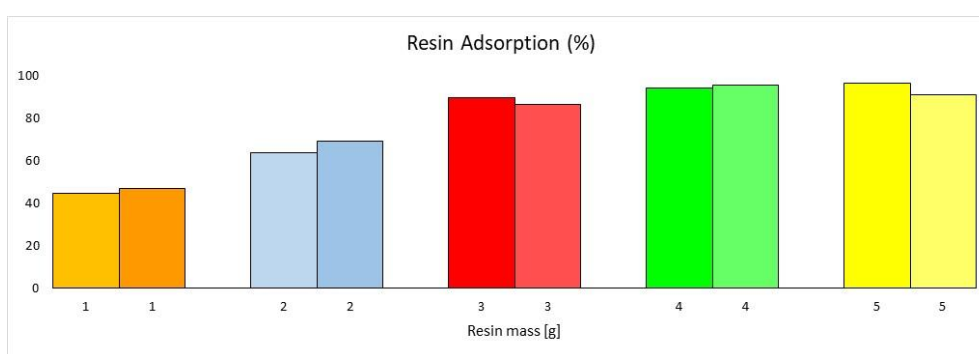
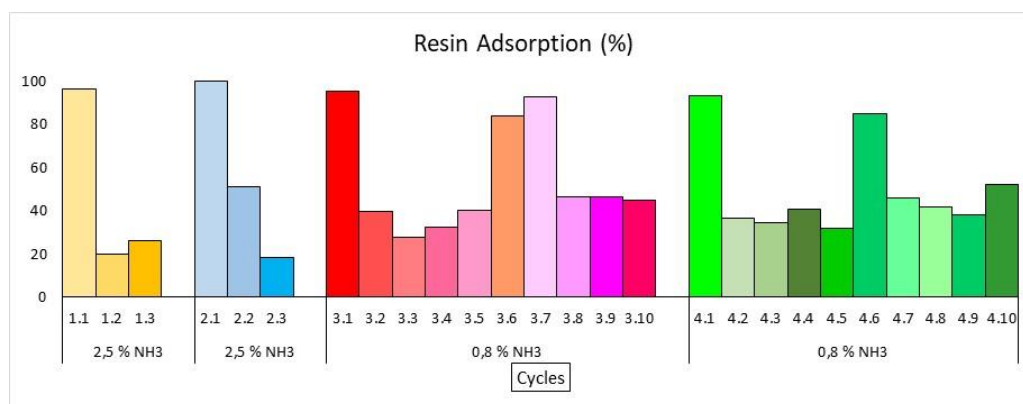
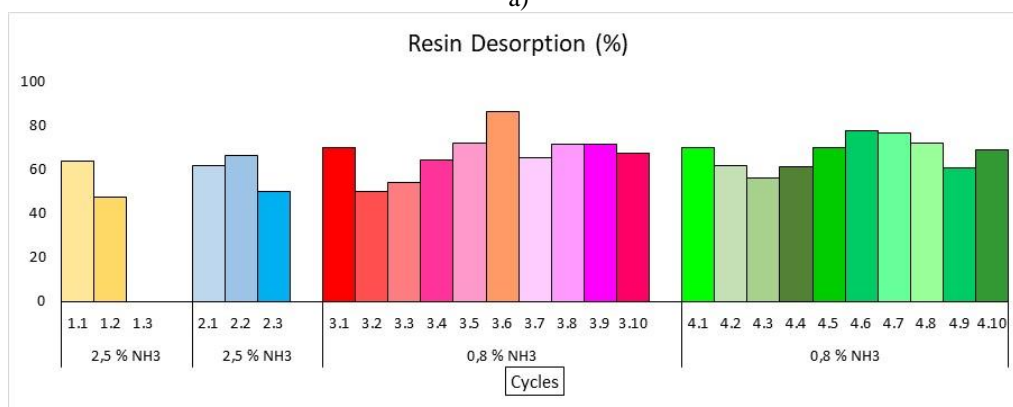


Fig. 3. Capacity of the resin



a)



b)

Fig. 4. Cycles for multiple use of one and the same resin sample. Comparison of the regeneration with 2.5 % v/v and 0.8 % v/v NH<sub>3</sub>

As can be seen the adsorption capacity (amount of adsorbed sulfurous acid) of the resin rapidly decreases with every cycle. Taking into account this decrease with every cycle the desorption capacity (amount of desorbed acid relative to the amount adsorbed) expressed as percent, seemingly remains stable, but actually the amount desorbed decreases with each cycle as well.

An interesting conclusion can be made by comparing the experiments with 2.5 % v/v and 0.8 % v/v NH<sub>3</sub> - the adsorption of each consecutive cycle declines much more rapidly when using the solution with higher ammonia concentration. We attribute this to irreversible chemical reactions between the desorbent and the ion-exchange resin which is avoided in the case of the lower concentration used. Hence, we decided to continue further experiments with 0.8 % v/v NH<sub>3</sub> used as desorbent. Another hypothesis for the steady

decrease in the adsorption capacity of the resin is that some of the products remain on the active sites of the resin after the desorption cycle. In an effort to bring the resin in its initial state we performed a conditioning with distilled water, as explained in “Materials and methods”, between the fourth and fifth cycle (between 3.4 - 3.5 and 4.3 - 4.5 from Fig. 4.). As the figure shows this conditioning regenerated the ion-exchange resin to performance comparable to the first cycle of use that gradually declined over the next cycles. These results inclined us to perform another set of experiments to further examine this “rinsing” method. The results are presented in Fig. 5.

Sulfates and a small quantity of sulfites are proved qualitatively in the conditioning water by addition of BaSO<sub>4</sub>. This coincides with the hypothesis that some of the sulfites are oxidized to sulfates and remain in the resin as larger ions.

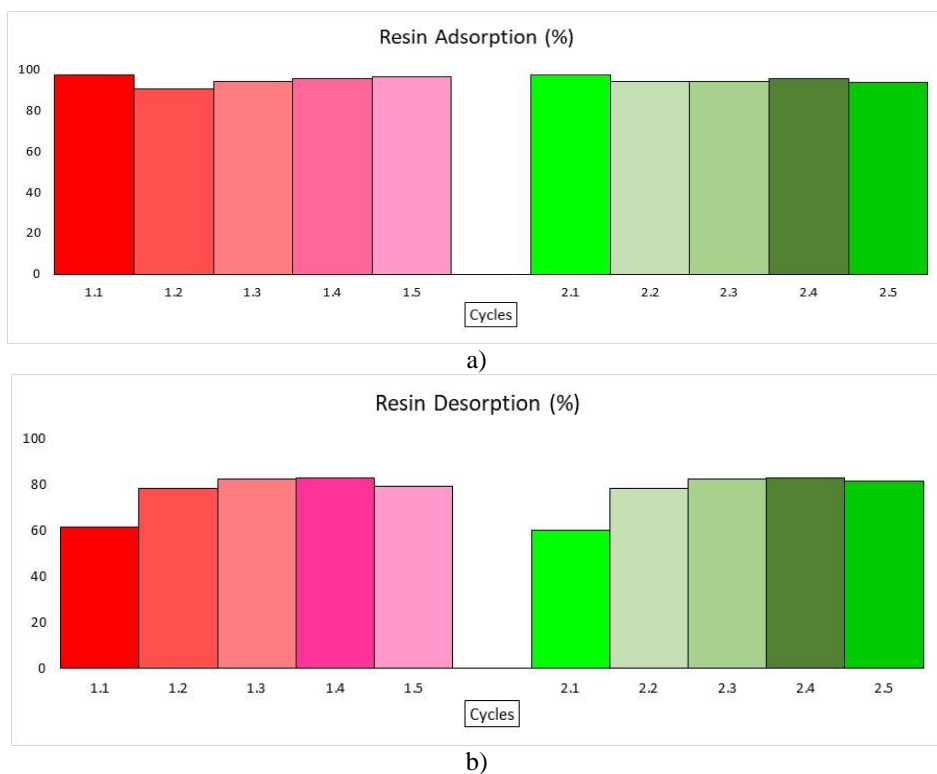


Fig. 5. Ion-exchange resin cycle life with conditioning

*Ion-exchange resin cycle life with conditioning*

As can be seen from the figures, the conditioning with distilled water after each desorption drastically improves the performance of the resin to the point that there is no noticeable decrease in both adsorption and desorption capacity after 5 consecutive cycles. This supports our hypothesis that some of the products with bigger molecules (sulfates) are not removed from the surface of the ion-exchange resin and “rinsing” it

with water removes most, if not all, of said products. This relatively simple (technologically) process substantially increases the cycles the ion-exchange resin can be used, thus improving the overall efficiency of the whole process being investigated as the ion-exchange resin itself is usually a large portion of the maintenance cost.

Detailed information about the cycles is presented in Table 3.

**Table 3.** Ion-exchange resin cycle life experimental results

Exp. set	Exp. №	Mass (g)	C <sub>H<sub>2</sub>SO<sub>3</sub></sub> (g.l <sup>-1</sup> )	C <sub>Ads H<sub>2</sub>SO<sub>3</sub></sub> (g.l <sup>-1</sup> )	Adsorbed %	C <sub>Des H<sub>2</sub>SO<sub>3</sub></sub> (g.l <sup>-1</sup> )	Desorbed %
①	1.1	5.0891	1.6331	1.5860	97.12	1.9471	61.39
	1.2	5.0891	1.6174	1.4604	90.29	2.2926	78.49
	1.3	5.0891	1.6174	1.5232	94.17	2.5125	82.47
	1.4	5.0891	1.7273	1.6488	95.45	2.7323	82.86
	1.5	5.0891	1.7273	1.6645	96.36	2.6381	79.25
②	2.1	5.1150	1.6331	1.5860	97.12	1.9032	60.00
	2.2	5.1150	1.6174	1.5232	94.17	2.3869	78.35
	2.3	5.1150	1.6174	1.5233	94.18	2.5120	82.45
	2.4	5.1150	1.7273	1.6488	95.45	2.7402	83.10
	2.5	5.1150	1.7273	1.6174	93.64	2.6381	81.55

Experimental conditions: V<sub>H<sub>2</sub>SO<sub>3</sub></sub> = 0.1 L, T<sub>ads</sub> = 5 min; V<sub>NH<sub>3</sub></sub> = 0.05 L, T<sub>des</sub> = 20 min, V<sub>H<sub>2</sub>O rinsing</sub> = 0.05 L, T<sub>rins</sub> = 60 min.

### CONCLUSIONS

The ion-exchange resin Dowex® 66 was chosen out of eight candidates for the novel technology being investigated in this study. Important technological parameters such as quantity of the resin for nearly total adsorption of the sulfurous acid (4 g of resin adsorb 0.1517 g of acid, 96% of total), time for adsorption (5 min) and desorption (20 min), concentration of the desorbing NH<sub>3</sub> (0.8 % v/v) were determined. Additionally, it was found that the conditioning of the resin with water can prolong its cycle life substantially (insignificant (< 2%) decrease after 5 cycles).

These parameters can be used for further scaling, implementation and investigation of the new technology for waste-free decontamination of gases from sulfur dioxide.

**Acknowledgement:** This work has received funding from the National Research Fund project No KII-06-H37/11/ 06.12.2019 "Integrated absorption-adsorption process for waste free decontamination of gases from sulfur dioxide".

### REFERENCES

1. A. Khol, R. Nielsen, Gas Purification, Fifth edition, Gulf Publishing Company, Huston Texas, 1997, p. 479.
2. K. B. Schnelle, Jr., C. A. Brown, Air Pollution Control Technology Handbook, CRS Press, LLC, 2002, p. 264.
3. Y. Niu, C. Li, J. Shen, X. Wei, *J. Clean. Prod.*, **171**, 506 (2018).
4. S.-B. Jeona, J.-H. Choa, M.-K. Kanga, S.-S. Lee, B.-j. Kima, K.-J. Oh, *J. Taiwan Inst. Chem. Eng.*, **81**, 175 (2017).
5. F. Shi, K. Li, D. Ying, J. Jia, N. Yan, X. Zhang, *Chem. Eng. J.*, **399** 125658 (2020);
6. D. Dzhonova-Atanasova, E. Razkazova-Velkova, L. Ljutzkanov, N. Kolev, D. Kolev, *J. Chem. Technol. Metall.*, **48** (5), 457 (2013).
7. N. N. Kolev, L. A. Ljutzkanov, D. N. Kolev, D. B. Dzhonova-Atanasova, E. N. Razkazova-Velkova, *J. Int. Sci. Publ.: Mater. Methods Technol.*, **5**, 375 (2011).
8. J. B. W. Frandsen, S. Kiil, J. E. Johnsson, *Chem. Eng. Sci.*, **56**, 3275 (2001).
9. R. de P. V. de Castro, J. L. de Medeiros, O. de Q. F. Araújo, M. de A. Cruz, G. T. Ribeiro, V. R. de Oliveira, *Energy Convers. Manag.*, **143**, 173 (2017).
10. D. Graves, J. J. Smith, L. Chen, A. Kreinberg, B. Wallace, R. White, *J. Environ. Manage.*, **201**, 357 (2017).
11. H. Fu, J. Huang, L. Yin, J. Yu, W. Lou, G. Jiang, *Fuel*, **203**, 445 (2017).
12. Kh. Boyadzhiev, L. Pantofchieva, I. Khristov, *Theor. Found. Chem. Eng.*, **34** (2), 141 (2000).
13. T.-W. Chen, N. G. Pinto, *React. Polym.*, **14**, 151 (1991).
14. T. Kopaq, E. Kaymak, M. Kopac, *Chem. Eng. Commun.*, **164** (1), 99 (1997).

## Autostabilization of propagation velocity of a self-sustaining evaporation front

V. E. Zhukov\*, E. Yu. Slesareva, A. Yu. Sakhnov

*Kutateladze Institute of Thermophysics, Siberian Branch of the Russian Academy of Sciences, Novosibirsk, Russia*

Received: August 02, 2020; Accepted: August 10, 2020

A self-sustaining evaporation front propagates along the heat-transfer surface within the thickness of the metastable thermal layer due to the heat stored in this layer. Under conditions of quasi-stationary heat release at a constant wall temperature, the front propagates at a constant velocity. With stepwise heat release, when the temperature of the heat-transfer wall increases with time, the researchers observed an increase in the velocity of evaporation front propagation. The dynamics of propagation of the evaporation front with a significant temperature gradient along a surface has not been previously studied. This paper presents the results of an experimental study of the dynamics of propagation of a self-sustaining evaporation front over a flat wedge-shaped surface with stepwise heat release. The dynamics of heating of the wedge-shaped surface and the temperature profile of the adjacent thermal layer, where a self-sustaining evaporation front propagates, were calculated. The measured spatial velocity of front propagation was compared with the calculated rate of heat-transfer wall heating. The experiments were carried out at pool boiling of freon R21 at ambient temperature. The working section in the form of an isosceles trapezoid with bases of 12 and 24 mm and height of 50 mm was made of stainless steel 0.2 mm thick. The experiments were carried out at a pressure of 0.18 MPa. The experiments showed that under the conditions of a significant temperature gradient of the heater surface, at the first stage the velocity of front propagation increases and at the second stage it correlates with the heating rate of the heat-transfer surface; thus, the velocity of evaporation front propagation is stabilized.

**Keywords:** pool boiling, self-sustaining evaporation front, evaporation rate, hydrodynamic stability

### INTRODUCTION

At pool boiling, the heat transfer coefficient increases with increasing heat flux density; therefore, the heat exchanger works most efficiently at high heat flux densities. However, the energy intensity of devices is limited by the heat transfer crisis of the first kind [1, 2]. Therefore, significantly less intense regimes are chosen for safe operation of heat exchangers. Nevertheless, the development of crisis phenomena at thermal loads much smaller than the magnitude of heat transfer crisis of the first kind is possible with substantially unsteady regimes of device operation [3]. Unsteady heat release into a single-phase liquid leads to formation of an overheated thermal layer with high metastability near the heat-transfer surface. The vapor bubble formed under such conditions starts growing; the interface of the growing vapor bubble loses stability, and starts propagating along the heat-transfer surface. A self-sustaining evaporation front propagates along the heat-transfer surface within the thickness of a metastable thermal layer due to the heat accumulated in this layer [4, 5]. Under conditions of quasi-stationary heat release at a constant wall temperature, the front propagates at a constant velocity [6–8]. With stepwise heat release, when the temperature of the heat-transfer wall increases with time, the researchers observed an increase in the propagation velocity of the

evaporation front [9, 10].

The dynamics of evaporation front propagation over a surface with a significant temperature gradient along the heat-transfer surface has not been previously studied. This paper presents the experimental results on the dynamics of propagation of a self-sustaining evaporation front over a flat wedge-shaped surface with stepwise heat release.

### EXPERIMENTAL

The experiments were carried out under the conditions of a large volume at an experimental setup described in [10]. A stainless steel cylindrical vessel with a diameter of 240 mm and depth of 225 mm is equipped with four windows designed to take the videos of the process and illuminate the research object. The working section is made of 0.2 mm thick stainless steel in the shape of an isosceles trapezoid. The bases of the trapezoid are 12 and 24 mm; the height is 50 mm. The video was shot with a high-speed Phantom video camera at a speed of 25,000 frames per second. To achieve stepwise heat release, a DC source Gorn-K 12/600 was used. The electric current density was linearly varied along the length of the trapezoidal working section, and the density of volumetric heat release in the plate was changed with the current density. As a result, a substantial temperature gradient was formed along the working section and in the thermal layer

\* To whom all correspondence should be sent:

E-mail: zhukov@itp.nsc.ru

adjacent to the heat-transfer surface. A self-sustaining evaporation front propagated under the conditions of that gradient.

## RESULTS AND DISCUSSION

The experiments were carried out using freon R21 at a pressure of 0.18 MPa, which corresponded to the ambient temperature of 24°C. The magnitude of current passing through the wedge-shaped working section was 420 A. The current was supplied in the form of a rectangular pulse of controlled duration. The maximum pulse duration was 32 ms. Over such a period of time, free convection does not have time to develop and formation of the temperature field in the working section and thermal layer of the adjacent liquid is determined by the laws of heat conduction. A numerical calculation of the temperature field for these conditions was performed using the equations of unsteady heat conduction. The diagram for calculating the temperature field of the working section is shown in Fig. 1.

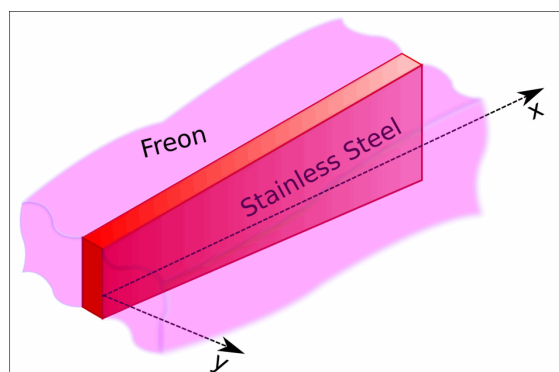


**Fig. 1.** Scheme for calculating the temperature field of the working section.

The diagram of distribution of heat-transfer surface overheating relative to the temperature of liquid saturation along the working section is shown in Fig. 2 at various points of time from the beginning of the stepwise heat release. This calculation was made for the condition of phase transition absence. In reality, at overheating by 30-40 K, single vaporization sites are activated on the heat-transfer surface; they start growing, and the interface loses stability under the conditions of high metastability of the surrounding thermal layer, and the evaporation front starts propagating. Nevertheless, before the front, the single-phase thermal layer and the heat-transfer wall have the temperatures corresponding to those calculated by the equations of unsteady heat conduction.

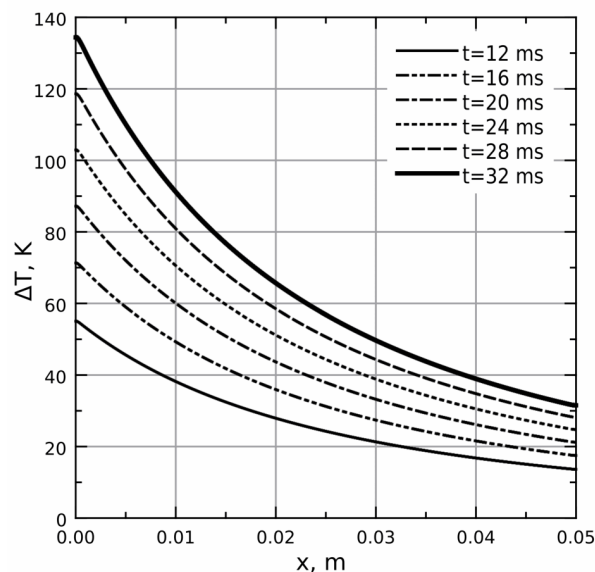


**Fig. 2.** Overheating of the heat-transfer surface relative to the temperature of liquid saturation. The saturation temperature is 24°C.

The video fragments of evaporation front propagation at various points of time from the beginning of heat release are shown in Fig. 3.

As it can be seen in the video frames, at 10 ms from the beginning of heat release there is a single vaporization site in a narrow part of the working section. At 15 ms, the vaporization sites and initial formation of the evaporation front are observed at several sites of the narrow edge. At 20 ms, the formed self-sustaining evaporation front spreads subsequently in a single line along the working section.

The diagram of a change in the coordinate of the leading point of evaporation front is shown in Fig. 4 depending on time from the moment of heat release beginning. The diagram also shows the lines of change in the coordinates of the calculated isotherms of the heat-transfer surface. As it can be seen in the diagram, the coordinate of the interface on the time interval of 10 - 15 ms from heat release beginning stays most unchanged. In the video, we see the growth of a bubble. For the next 5-6 ms, interface propagation with an increasing velocity is observed. Moreover, in the process of moving, the leading point of the front at each step is in the region of a higher temperature, which leads to acceleration of the leading point. At a time interval of 22-32 ms, an almost linear change in the coordinate of the leading point of the evaporation front is observed with time, which indicates moving at a constant velocity.

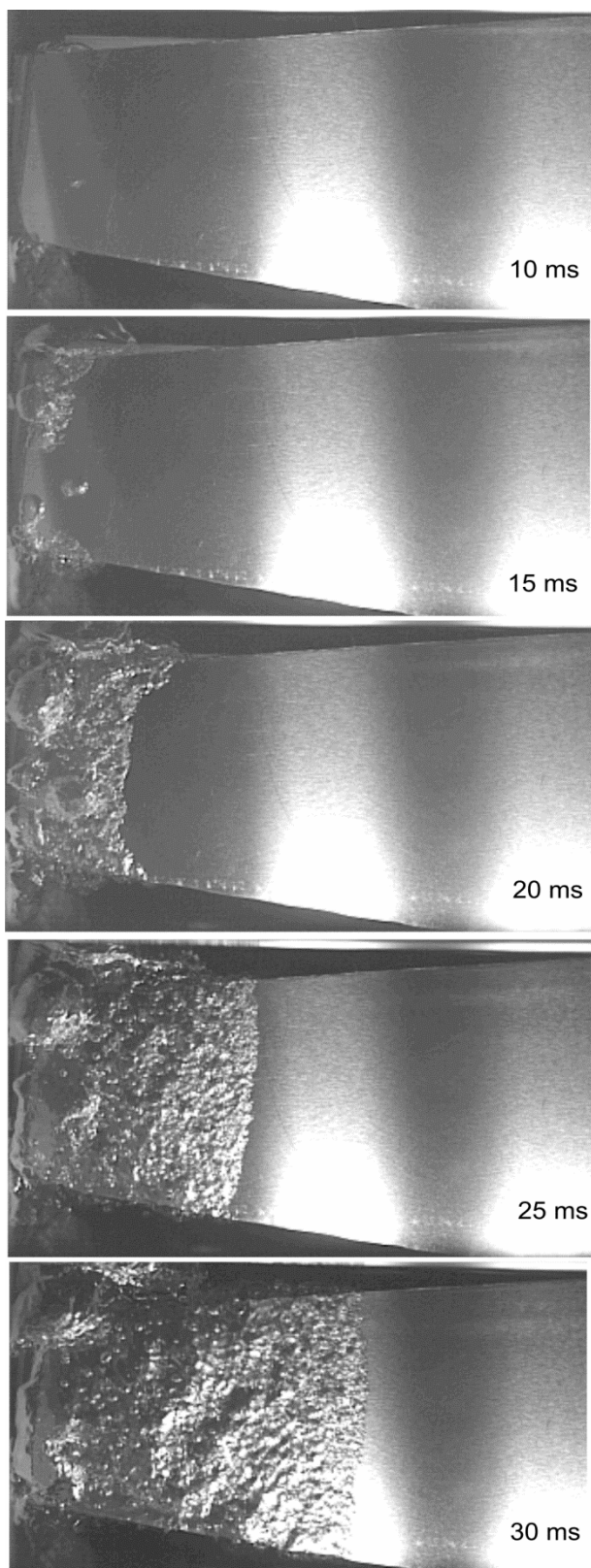


**Fig. 3.** Fragments of a video of evaporation front propagation. The time from the beginning of heat release is shown in the frames.

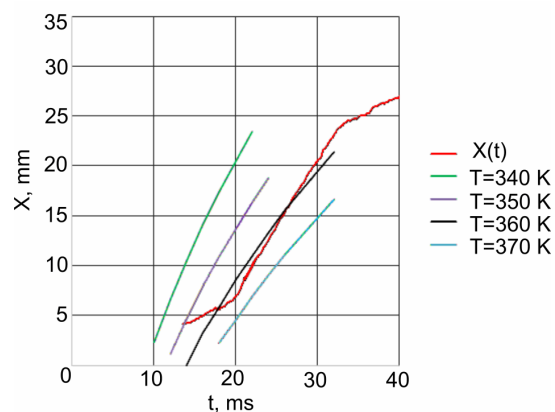


**Fig. 4.** Changes in the coordinates of the leading point of the evaporation front and calculated isotherms of the heat-transfer surface depending on the time from the moment of heat release beginning.

The diagram shows that the leading point of the front moves almost simultaneously with the isotherm ( $T = 360$  K) corresponding to a temperature head of 63 K. Advancing the isotherm by the leading point leads to the contact of the interface with the region of less metastability, which leads to a slowdown of the front. Thus, autostabilization of propagation velocity of the self-sustaining evaporation front occurs. At a time interval of 22 - 32 ms, the leading point of the front moves to a distance of 12.9 mm, which corresponds to a velocity of 1.29 m/s. Therefore, at a temperature head of 63 K, the velocity of evaporation front propagation is 1.29 m/s.

### CONCLUSIONS

The experimental studies showed that a self-sustaining evaporation front forms in the region of maximum overheating of the heat-transfer surface at a temperature head of 40-50 K with respect to the saturation temperature. The evaporation front formed in the region of maximum overheating propagates with acceleration in the direction of the temperature gradient along the heat-transfer surface until an equilibrium state is reached between the velocity of spatial displacement and the rate of metastable layer heating. Further front propagation occurs at a constant average velocity caused by the velocity of the corresponding isotherm of the heat-transfer surface.

**Acknowledgement:** The work was carried out at the IT SB RAS within the project of the Federal Program for Basic Research of the State Academy of Sciences for 2013-2020 (theme III.18.2.3, AAAA-A17-117030310025-3, AAAA-A17-117030310010-9).

REFERENCES

1. M. M. Kovetskaya, *Promyshlennaya Teplotekhnika*, **31** (5), 50 (2009).
2. I. Leontiev, V. V. Olimpiev, *High Temperature*, **45** (6), 844 (2007).
3. A. N. Pavlenko, V. Yu. Chekhovich, *Russ. J. Eng. Therm.*, **1** (1), 73 (1991).
4. P. A. Pavlov, V. E. Vinogradov, *High Temperature*, **48** (5), 683 (2010).
5. O. V. Sharypov, *Tech. Phys. Lett.*, **43** (4), 383 (2017).
6. B. P. Avksentyuk, V. V. Ovchinnikov, *Therm. Aeromech.*, **15** (2), 267 (2008).
7. S. P. Aktershev, V. V. Ovchinnikov, *J. Appl. Mech. Tech. Phys.*, **49** (2), 47 (2008).
8. S. P. Aktershev, V. V. Ovchinnikov, *J. Eng. Therm.*, **20** (1), 77 (2011).
9. A. N. Pavlenko, E. A. Tairov, V. E. Zhukov, A. A. Levin, M. I. Moiseev, *J. Eng. Therm.*, **23** (3), 173 (2014).
10. A. N. Pavlenko, V. E. Zhukov, A. N. Tsoi, E. A. Tairov, A. A. Levin, *J. Eng. Therm.*, **20** (4), 380 (2011).

## Approaches to mass transfer modeling in micro-channels inside gel

B. G. Pokusaev<sup>1</sup>, A. V. Vyazmin<sup>2\*</sup>, D. A. Nekrasov<sup>1</sup>, N. S. Zakharov<sup>1</sup>, D. P. Khramtsov<sup>2</sup>,  
N. V. Shumova<sup>2</sup>

<sup>1</sup>Department of Chemistry and Biotechnology, Moscow Polytechnic University, 107023, Moscow, Russia;

<sup>2</sup>Department of Chemical Engineering, MIREA – Russian Technological University, 119454, Moscow, Russia

Received: July 31, 2020; Accepted: August 10, 2020

The aim of the work is to find ways of effective cultivation of living microorganisms in the gel volume by designing a specific structure of internal channels, when the delivery of nutrients to the gel volume is carried out by the convective-diffusion mechanism. The nutrients penetration depth into the gel under microorganisms stable living conditions is estimated. The possibility of forming time-stable linear channels in the gel volume has been experimentally established. The possibility of their usage for convective nutrient supply to the volume was tested. The regularities of the nutrients diffusion from the channels into the gel volume with immobilized cells are established.

**Keywords:** gel, immobilized cells, microchannels, diffusion-convection mass transfer

### INTRODUCTION

The current state of society can be characterized as the period of the fourth technological revolution. One of its features is the use of additive 3D technologies [1]. In regenerative medicine this technology is commonly referred to as 3D bioprinting. Its goal is to create artificial human organs from stem cells using additive methods [2]. Like any new technology, bioprinting requires new materials that have a whole set of specific biochemical and technological properties. One of the promising materials for these purposes is gel [3, 4]. The network of capillaries in gels can be used to supply nutrients and oxygen to the cells and remove the products of their metabolism. In additive 3D printing the suitable peculiarity of these media is the specific rheological characteristics, which permits, when applied under high stress conditions, these materials to have features similar to liquids [5].

The future potential of gels applications puts them among some of the most promising materials for 3D printing technologies, particularly for forming objects with complex geometric shapes where gel can be used as a bioink [6]. Gels can be used for tissue building and serve as a framework for cells growth [7]. For example, gels can be applied for vascular tissue formation [8]. Such vascular structure can be initially formed with a bioresorbable gel with immobilized cells and after solidification serve as a framework for cells growth which will be subsequently resorbed after vascular tissue is formed in the gel [9]. In particular, it is possible to apply to this 3D bioprinting technology the possibility of predicting and controlling the

thermophysical characteristics that affect the mass transfer characteristics of the gel-based matrix [10].

The task of creating a tissue structure is complicated due to presence of living cells in the forming gel sample. In this regard, it is necessary to provide conditions suitable for the vital activity of cells. For this reason, it is absolutely essential to supply nutrients and oxygen to the cells, which can be implemented by forming artificial channels inside the gel, which are similar to the structure of blood capillaries in the organs [11-13]. To study this process, it is convenient that there is a formal analogy between the transfer of nutrients in gels and filtration with the formation of deposits in the pores [14].

Since gels can be produced from different chemical components, the question of choosing the right gel for tissue growth is of high importance. Moreover, it is important to know the thermophysical properties of gels [15, 16]. As minimum, such gels must solve two purposes: be a medium for cells immobilization and be able to be extruded *via* a 3D printer [17]. Hence, gels must melt and solidify in normal conditions. Pure agarose gels [18] and complicated gels with bioresorbable additives [19, 20] are considered as promising materials for 3D bioprinting.

Previously was shown the possibility of forming stable microchannel structures inside the gel, capable of transferring liquid to gel volume [21, 22]. Similar channels were produced in order to form a pattern for a vascular tissue [23]. The complexity of the problem requires the development of a model of the movement of a liquid through the capillaries in

\* To whom all correspondence should be sent:  
E-mail: av1958@list.ru

the gel structure, which will significantly reduce the time of research. This approach will allow to test the effectiveness of different configurations of the channels in the gel. Due to the irregularity, the problem of modeling the gel structure is nontrivial. There is also an open question about the optimal structure of the channels inside the gel, providing the effective mode of supply of nutrients to living organisms immobilized in the gel.

## EXPERIMENTAL

### Materials, Methods and Approaches

The mass transfer study in gels, including those with internal channels and living microorganisms, was carried out on model systems. For primary studies of the mass transfer the individual properties inherent to various living cells and gels are not of fundamental importance. At the present research stage, it is important to understand the fundamental mass transfer laws during bulk microorganism's cultivation in gels with artificial microchannels.

Pure gels based on agarose "Chemapol" and gels with the addition of yeast culture with a nutritious bouillon were used as model systems. The weight concentration of agarose in gels varied in the range of 0.6-1.5 %. Such gels are optically transparent, which makes it possible to conduct mass transfer studies using non-contact optical methods without disturbing the metabolism conditions.

The yeast culture *Pichia polymorpha* Y-314 was selected as a model microorganism, since its cells size is close to that of human somatic cells. The culture is viable if glucose is used as the only source of carbon. The yeast concentration was controlled by measuring the optical permittivity at a wavelength of 540 nm.

To visualize mass transfer processes and measure the diffusion rate, a 1.0 % aqueous solution of fuchsin was used, which is sometimes added to nutrient media. Aqueous solutions of fuchsin have a purple-red color and high-contrast against the gel background.

Optical methods of spectrometry and visualization with computer image processing were used to measure the mass transfer rate. Fig. 1 shows the experimental setup scheme used for the experiments [21]. The equipment consists of two working sections. Section 1 is designed to study mass transfer by scanning the test gel samples along the cuvette height. Section 2 is designed to study mass transfer in layered gel samples with flow microchannels.

A two-beam spectrophotometer UV-1280 manufactured by Shimadzu (7) was used for

spectrometric measurements. The technical characteristics of the equipment provide measurements of light transmission and absorption spectra at several wavelengths in the range of 190 - 1100 nm in automatic mode. A special system was installed in the working area to measure the gel sample position in space (3, 5, 6).

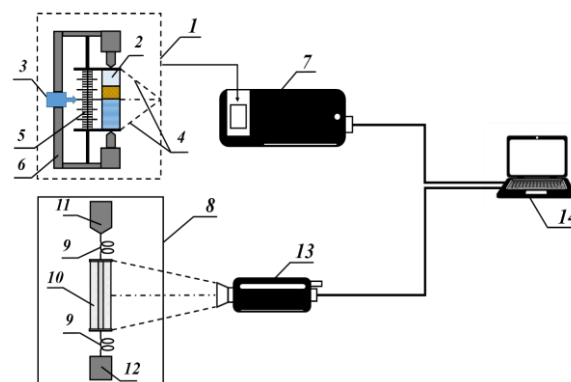


**Figure 1.** Scheme of the experimental setup: 1 - working area 1: 2 - optical cell with gel, 3 - level indicator, 4 - working area of scanning, 5 - scale of height measurement, 6 - cell holder, 7 - Shimadzu spectrophotometer, 8 - working area 2: 9 - pipeline system with control valve, 10 - optical cell with gel with channels, 11 - tank with nutrient medium, 12 - collection tank, 13 - camera, 14 - computer

To visualize mass transfer in gels with artificial microchannels, an automatic high-resolution photo recorder was used. A cuvette with a gel having channels (10) is placed in the working area, connected to a pipeline, through which the colored liquid from the container (11) enters the channel. The flow rate of the colored liquid is regulated by a valve on the pipeline (9). The colored liquid flows after the channel into a measuring container (12) with a graduated scale. Using a stopwatch, the average flow liquid rate that has passed through the channel is monitored. A photo-recording device (13) writes the diffusion front propagation in the gel, then the photos are processed on a computer (14) using the method [22] to calculate the diffusion coefficient value for mass transfer from the channel to the gel.

The method of forming artificial channels in the gel is the following: a metal wire is placed in an experimental cuvette which is filled with a gel forming agarose solution at a temperature not lower than 40°C (above the gel formation temperature). After lowering the temperature below the gel formation temperature and stabilizing the gel, the wire is removed. However, a time-stable channel of the required diameter and shape remains in the gel.

Using the described method, straight-flowing and branched channels with a thickness of 1.5 mm

to 0.3 mm were formed in agarose gels with different agarose concentrations. After removing the wire, the channels are filled with dispersion moisture, which is replaced by an aqueous solution of fuchsin. In the experimental setup described above, a flow of an aqueous solution of fuchsin with a flow rate of up to  $2 \times 10^{-10} \text{ m}^3/\text{s}$  takes place through direct channels.

## RESULTS AND DISCUSSION

In traditional deep cells cultivation in the gel volume, the transfer of nutrients and oxygen to the cells is carried out through the external boundary in a diffusive regime. Diffusion processes in gels are slow; their rate decreases as the dispersed phase concentration increases and may be by an order of magnitude lower than for a pure dispersion medium. As a result, the microorganisms' growth rate in the gel volume is limited by the supply rate of substances necessary for their immobilization. Internal artificial channels allow to partially take off these restrictions by reducing the path necessary for the nutrients penetration into the volume and the medium convective movement inside the channel.

Comparable experiments were performed to measure nutrients mass flow rate in the gel volume through the external boundary and internal artificial microchannels. For this purpose, temporal dynamics measurements of filling with fuchsin (transported substance) of the experimental cuvette test volume with the gel for both methods of mass transfer were performed. Further, it is assumed, that the fuchsin concentration in the gel is proportional to the transmitted light absorption intensity.

The experiment was carried out on the equipment described above and consisted in determining the absorption intensity of light at a 540 nm wavelength in two agarose gel samples with a 0.6% weight agarose concentration. In one sample, fuchsin was poured onto the upper gel boundary and transferred by diffusion into the bulk. In the other sample, fuchsin was fed into a single central channel 0.8 mm in diameter. The integral light absorption intensity was measured over the entire width of the experimental cell equal to 10 mm to a 10 mm depth from the upper surface with a 1 mm step. The measurements were carried out at different time intervals after the fuchsin was poured.

Data on the fuchsin diffusion temporal dynamics into the gel bulk from the upper surface as the relative light absorption intensity  $D$  depending on the penetration depth  $l$  at different times are shown in Fig. 2. The experimental results fully correspond to the mass transfer theoretical concepts described

by the exact solution of the non-stationary diffusion equation for a semi-infinite space under the third boundary value problem conditions [24]. Analysis of the experimental dependences form shows that there is diffusion resistance to the nutrients mass transfer in the liquid layer above the gel surface. In particular, at the 220 min time from the start of the diffusion process the fuchsin penetration depth does not exceed 4 mm. Estimations based on Fig. 2 show that for this time the average relative light absorption for a test gel volume of  $10 \times 10 \times 10 \text{ mm}$  has a value lower than 0.4.

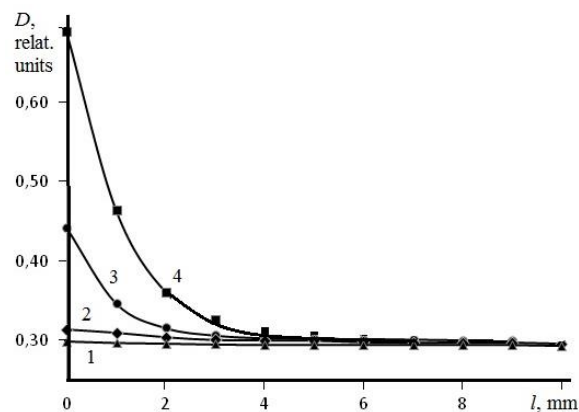


**Figure 2.** Dependence of the light absorption relative intensity  $D$  (relative units) of the gel sample on the depth  $l$  (mm) when diffusing fuchsin into its volume from the upper surface in different time moments from the start of the process, min: 1 – 0, 2 – 40, 3 – 160, 4 – 220.

When the fuchsin solution is flowing through the central rectilinear channel, its transverse diffusion into the gel volume takes place. As an example, Fig. 3 shows a photo visualizing this process for a channel with a diameter of 0.8 mm in a gel with a 0.6% agarose weight concentration. Since fuchsin absorbs light more strongly than pure gel, its diffusion appears in the photo as an increase in the channel diameter with time. It can be seen that under this supplying fuchsin method, the cuvette volume with the gel is filled much faster than when the fuchsin diffuses only from the upper boundary.

Interpretation of the data shown in Fig. 3 can be made in two ways. One can follow the approach proposed in [22] and determine the dependence of the fuchsin penetration depth from the channel into the gel volume under different time framesth. Alternatively, using computer image processing, it is possible to determine the light absorption average intensity dependence in the test gel sample volume (which will characterize the average concentration of fuchsin in its volume) on the diffusion time. The influence on the internal channel result, which

reduces less than 1.0% of the testing volume, is neglected.

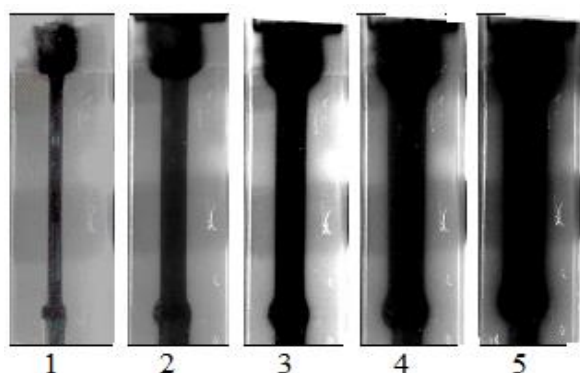


**Figure 3.** Photos visualizing the fuchsin transverse diffusion from a flow channel with a diameter of 0.8 mm into the gel volume with a weight agarose concentration of 0.6% at times from the experiment beginning, min: 1 – 0, 2 – 30, 3 – 60, 4 – 120, 5 – 200.

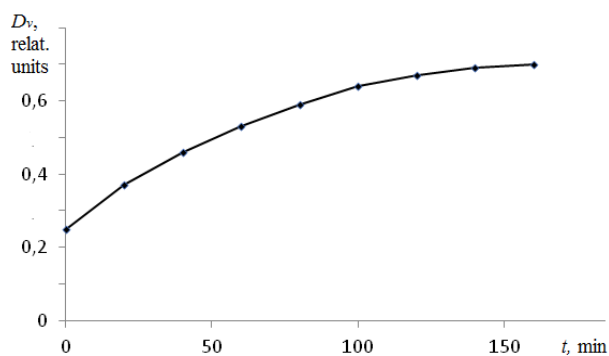


**Figure 4.** Dependence of the average volume relative light absorption intensity  $D_v$  (relative units) in the gel on the time  $t$  (min) when fuchsin diffuses into the volume from the flow channel.

Data on the temporal dynamics of the fuchsin average volumetric concentration growth in the gel volume during diffusion from the channel in the form of the volume average relative light absorption intensity  $D_v$  dependence on time  $t$  are shown in Fig. 4. In the absence of diffusion resistance to fuchsin mass transfer inside the channel due to its flow, its average volume concentration in the test volume increases. For example, the average relative light absorption for the test gel volume at 160 minutes is 0.7.

The abovementioned results confirm the simple assumption that filling the gel volume with a substance through artificial channels is more efficient than through its outer boundary. More interesting are the spectral study results of the gel sample with cells during diffusion from the channel into the gel volume of a nutrient broth that ensures cell growth and division instead of a model medium. In this case, it is possible to determine not only the temporal filling dynamics for the gel with

the nutrient medium, but also the cell concentration growth during bulk cultivation in the gel.

Further, the possibility of cultivating microorganisms (using yeast, as example) in the gel volume under feeding nutrient conditions through an artificial internal microchannel was experimentally investigated. Based on the data obtained, the increase in the yeast cells concentration as their division result was evaluated by measuring the light absorption intensity for two adjacent identical gels: with living yeast cells and without cells.

The research was carried out on the experimental equipment described above. The light absorption intensity was measured at a 540 nm light wavelength. The wavelength choice is due to the fact that it is used in microbiology to measure the yeast cells concentration by a spectrophotometric method.

An investigated gel sample with a 0.6% agarose weight concentration consists of four alternating layers: a pure gel layer, then a gel with cells layer, and so on. The studied gel system photos are shown in Fig. 5. Since the cells presence leads to high light absorption at the selected wavelength, the gel layers with cells in the photo appear darker than those without cells. An artificial channel with a 0.8 mm diameter was formed in the sample, which was filled with nutrient bouillon. It should be noted that, unlike fuchsin, the nutrient bouillon is not a high-contrast substance in relation to the gel, therefore, the presence of a channel with bouillon in the photo in Fig. 5 is almost invisible. However, the optical transmission of broth is weaker than that of water (absorption is greater). For this reason, the bouillon spread in the gel sample can be monitored by the light absorption intensity.

The measurements were carried out along the 10 mm height of the cuvette with a 0.5 mm step at time moments: 0 (immediately), 2, 15 hours after the bouillon was injected into the channel. Fig. 6 shows the absolute absorption intensity for passing through the gel sample light, depending on the depth at different microorganism's cultivation times.

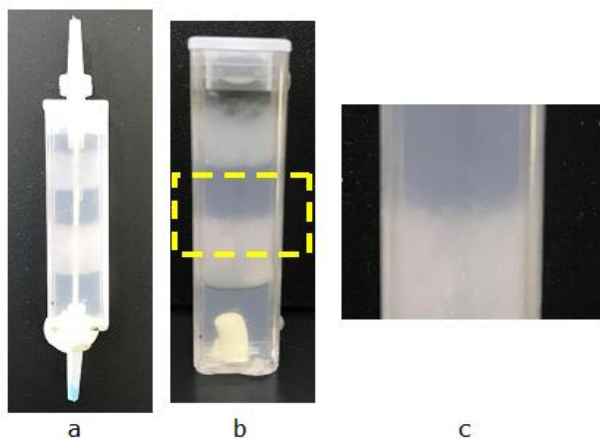


**Figure 5.** Photo of a four-layer gel sample with a 0.6% agarose weight concentration and an internal central channel of 0.8 mm diameter. Gel layers with cells and without cells alternate (darker in the photo - layers with cells). Designations under the photos: a - original sample with an empty channel; b - sample with a channel filled with nutrient broth; c - the investigated part of the layered gel sample (highlighted by a dotted line in photo 5b).

In the studied area, there was a layer of pure gel (4 mm) - on the right in the graph, the section meniscus between the layers (2 mm) - in the center and a gel layer with cells (4 mm) - on the left in the graph. Thus, as an experimental result, it is possible to see the difference in each gel layer optical density at the start of the experiment and after 15 hours with constant nutrition diffusion from the channel into the gel, which allows maintaining the cells inside the gel in an immobilized state.

As follows from Fig. 6, at the initial moment when feeding bouillon into the channel, the light absorption intensity in the layer with cells is much higher than in pure gel (curve 1). This is because the overall light absorption is due to both inside the gel and the cells. In 2 hours after the start of the experiment, the absorption intensity in both gel sample regions insignificantly increases (curve 2). This is probably due to the bouillon diffusion transfer into the gel. Moreover, in the meniscus section filled with the dispersion liquid, this difference becomes noticeable, since the bouillon mass transfer along the meniscus occurs much faster than in the gel volume.

After 15 hours of the experiment, the light absorption intensity in both sample parts significantly increases (curve 3 in Fig. 6). Moreover, in the gel area with cells, such growth is noticeably greater than in a pure gel. This is due to two reasons. Firstly, both gel samples volumes are filled with nutrient from the channel, which leads to an increase in absorption in both samples.

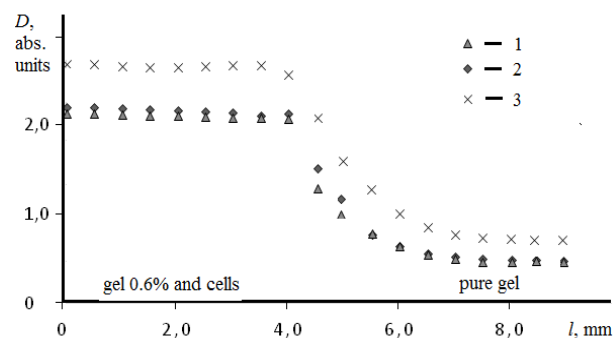


**Figure 6.** Absolute absorption intensity for light with a 540 nm wavelength passing through a gel with a 0.6% agarose weight concentration and having a central channel of 0.8 mm diameter, filled with nutrient bouillon, depending on the depth at the gel layers' junction with seeded yeast cells and without cells at different cultivation microorganisms times. To a depth of 4 mm - gel with cells, from 4 to 6 mm - section meniscus with boundary layers, under 6 mm - pure gel. The curves designations correspond to the times from the experiment beginning, h: 1 - 0; 2 - 2; 3 - 15.

Secondly, an increase in the yeast cells concentration is possible due to division, which causes an additional increase in the light absorption intensity in the area with cells in comparison with pure gel.

Suppose that the light absorption intensity is additively dependent on the magnitude of three different factors that determine the light absorption: gel, bouillon and cells. Therefore, from the measurement data in Fig. 6 it can be estimated that the increase in the microorganism's concentration during 15 hours is about 15% in relation to the initial concentration. This proves the possibility of effective bulk cells culturing in the gel volume in the microchannels presence for supplying microorganisms with nutrients. It is important to note that due to the microchannels stability in the gel, such a supply can be carried out over a long time period.

The estimates made regarding the increase in the yeast cells concentration in the gel with an artificial channel seem to be justified. Cell growth with subsequent division is possible only under conditions of sufficient supply of nutrients and oxygen. According to the abovementioned measurements this is achieved within 3-4 hours using the channel. Under optimal cultivation conditions, the selected yeast culture doubles the cell concentration within 4-6 hours. The optimum temperature for yeast cultivation is 36°C. The experiment was carried out at non-optimal temperature in the range of 23-25°C. As a result, the time for doubling the microorganisms number during growth and division increased several times.

Accordingly, the yeast concentration growth was much slower.

## CONCLUSIONS

It is shown that the mass transfer of substances into the gel volume can be carried out through an artificial microchannel system which is stable in time. In this case, the average volumetric concentration growth of the transferred substances in the gel volume occurs several times faster than in the case when it is transferred through outer boundary.

An optical method based on the light absorption intensity measurement established the cultivating microorganism's possibility (using the example of an increase in the yeast concentration) throughout the entire gel volume when nutrients and oxygen are supplied through the flow channel. With this cultivation method, the possibility of a uniform increase in the microorganism's concentration by volume, and not only near the gel sample outer boundary, was shown.

As a result, for further research and subsequent practical application, the problem of finding the optimal diameter and structure of channels for cultivation of microorganisms in a gel in a volumetric manner becomes of high importance. At the same time, it is important to understand how to create and use a branched flowing microchannels system in a gel in order to increase the efficiency and uniformity of nutrient transfer into its volume.

**Acknowledgements:** The paper was prepared in full within the state assignment of Ministry of Education and Science of the Russian Federation for 2020-2022 (project No. FZRR-2020-0027).

## REFERENCES

1. K. Schwab, N. Davis, Shaping the Fourth Industrial Revolution, Cologny, World Economic Forum, 2018.
2. V. Lee, G. Dai, *Adv. Health Care Technol.*, **1**, 23 (2015).
3. K. Kajiwara, Yo. Osada (eds.), Gels Handbook, Elsevier, 2000.
4. M. R Placzek, I.-M. Chung, H. M. Macedo, S. Ismail, T. M. Blanco, M. Lim, J. M. Cha, I. Fauzi, Yu. Kang, D. C. L. Yeo, C. Y. J. Ma, Ju. M. Polak, N. Panoskaltis, A. Mantalaris, *J. R. Soc. Interface*, **6**, 209 (2009).
5. D. Chimene, K. K. Lennox, R. R. Kaunas, A.K. Gaharwar, *Ann. Biomed. Eng.*, **44**, 2090 (2016).
6. H. Gudapati, M. Dey, I. Ozbolat, *Biomaterials*, **102**, 20 (2016).
7. H. Jian, M. Wang, S. Wang, A. Wang, S. Bai, *Bio-Des. Manuf.*, **1**, 45 (2018).
8. D. Richards, J. Jia, M. Yost, R. Markwald, Y. Mei, *Ann. Biomed. Eng.*, **45**, 132 (2017).
9. P. Sasmal, P. Datta, Y. Wu, I. T. Ozbolat, *Microphysiol. Syst.*, **2**, 9 (2018).
10. S. Wang, J. M. Lee, W. Y. Yeong, *Int. J. Bioprinting*, **1**, 3 (2015).
11. K. Jakab, C. Norotte, F. Marga, K. Murphy, G. Vunjak-Novakovic, G. Forgacs, *Biofabrication*, **2**, 20 (2010).
12. B. G. Pokusaev, S. P. Karlov, A. V. Vyazmin, D. A. Nekrasov, *Theor. Found. Chem. Eng.*, **49**(6), 617 (2015).
13. B. G. Pokusaev, D. A. Nekrasov, N. S. Zakharov, D. P. Khramtsov, S. P. Karlov, A. V. Vyazmin, *Theor. Found. Chem. Eng.*, **54**(1), 91 (2020).
14. Yu. A. Taran, A. V. Kozlov, A. L. Taran, *Fine Chem. Technol.*, **14**(2), 15 (2019).
15. B. Gao, Q. Yang, X. Zhao, G. Jin, Y. Ma, F. Xu, *Trends Biotechnol.*, **34**, 746 (2016).
16. B. Pokusaev, A. Vyazmin, N. Zakharov, S. Karlov, D. Nekrasov, V. Reznik, D. Kramtsov, *Thermal Sci.*, **24**, 347 (2020).
17. C. Norotte, F. S. Margaa, L. E. Niklason, G. Forgacs, *Biomaterials*, **30**, 5910 (2009).
18. G. R. López-Marcial, A. Y. Zeng, C. Osuna, J. Dennis, J. M. García, G. D. O'Connell, *ACS Biomater. Sci. Eng.*, **4**, 3610 (2018).
19. R. Suntornnond, J. An, C. K. Chua, *Macromol. Mater. Eng.*, **302**, 1 (2017).
20. B. G. Pokusaev, S. P. Karlov, D. A. Nekrasov, N.S. Zakharov, D. P. Khramtsov, V. V. Reznik, A.V. Vyazmin, N. V. Shumova, *Chem. Eng. Trans.*, **74**, 1171 (2019).
21. B. G. Pokusaev, A. V. Vyazmin, D. A. Nekrasov, N. S. Zakharov, D. P. Khramtsov, N. V. Shumova, D. A. Belova, *Chem. Eng. Trans.*, **79**, 13 (2020).
22. B. G. Pokusaev, A. V. Vyazmin, N. S. Zakharov, D. P. Khramtsov, D. A. Nekrasov, *Theor. Found. Chem. Eng.*, **54**(2), 277 (2020).
23. L. E. Bertassoni, M. Cecconi, V. Manoharan, M. Nikkhah, J. Hjortnaes, A. L. Cristino, G. Barabaschi, D. Demarchi, M. R. Dokmeci, Y. Yang, A. Khademhosseini, *Lap Chip*, **13**, 2202 (2014).
24. A. D. Polyenin, A. M. Kutepov, A. V. Vyazmin, D. A. Kazenin, *Hydrodynamics, Mass and Heat Transfer in Chemical Engineering*, London, Taylor & Francis, 2002.

## Liquid wall flow in counter-current column apparatuses for absorption processes with random packings

Chr. B. Boyadjiev<sup>1</sup>, D. B. Dzhonova<sup>1\*</sup>, P. G. Popova-Krumova<sup>1</sup>, K. V. Stefanova<sup>1</sup>, A. N. Pavlenko<sup>2</sup>, V. E. Zhukov<sup>2</sup>, E. Yu. Slesareva<sup>2</sup>

<sup>1</sup>*Institute of Chemical Engineering at the Bulgarian Academy of Sciences, Acad. G. Bonchev Str. Bl.103, Sofia 1113, Bulgaria,*

<sup>2</sup>*Kutateladze Institute of Thermophysics, Siberian Branch of the Russian Academy of Sciences, Lavrentyeva, 1, 630090, Novosibirsk, Russia*

Received: August 12, 2020; Accepted: August 21, 2020

Absorption processes are widely applied in chemical engineering. Important modern applications are fuel production and purification of waste gases and liquids for environment protection and production of valuable substances. Packed columns are typical apparatuses for these processes. Their efficient operation is strongly dependent on the regular distribution of the liquid and gas phase. The formation of a liquid wall flow is one of the main reasons for large-scale maldistribution in packed beds. The prediction of the liquid maldistribution is needed for evaluation of mass transfer efficiency. The present work uses a new approach to model the liquid wall flow in different types of random packings. The model results, in agreement with experimental data, show the effect of important operation parameters on the wall flow development along the column. A maldistribution parameter is calculated as a base for comparison of liquid maldistribution in packings. The present method for evaluation of the wall flow is intended for further modeling of separation efficiency in packed columns.

**Keywords:** Packed columns, absorption, random packings, liquid maldistribution, wall flow, mass transfer efficiency.

### INTRODUCTION

When designing an absorption column, the packed bed should ensure the desired absorption rate at the lowest capital and operating cost, high mass transfer efficiency and low pressure drop. The selection of packings for a desired separation process passes through calculation of the most economic geometry with smallest dimensions, which will supply the highest mass transfer conditions. Many types of packings are designed in order to achieve the desired high mass transfer efficiency of the packed bed. Random packings are classified in 4 generations [1], the modern one being represented by web-like packings with open structure. They possess high-performance characteristics which provide for good hydrodynamic conditions and intensive mass transfer. The packing height can be calculated based on Height of a Transfer Unit (HTU) and Number of Transfer Units (NTU) [2], HTU being a measure of the mass transfer efficiency of the packing for the specific separation, based on the mass transfer rate between the liquid and vapor phase. The efficiency can also be evaluated by the concept of Height Equivalent to a Theoretical Plate (HETP), which treats a packed column as a series of equivalent equilibrium stages.

The maldistribution of the phases in a packed column has a deteriorating effect on the mass

transfer efficiency. It is specified as small-scale and large-scale maldistribution. It has been shown [3] that in random and structured packings the small-scale maldistribution, in the scale of a packing element, is characterized by the deviation of the local flow rates in the main body of the packed bed. The small-scale maldistribution results from the packing geometry and structure and it cannot be eliminated. Its harmful effect on separation efficiency is expected to be partially compensated by radial mixing between phases. This maldistribution intensifies with the packing depth until reaching a stable pattern of “natural flow” [3]. The large-scale maldistribution develops along the column wall as a result of insufficient irrigation or by development of a wall flow. It cannot be easily compensated by radial mixing. The initial distribution can be improved by proper design of the liquid distributor. The wall flow can be minimized by special elements, like deflecting rings [4] or by liquid redistribution devices [5] at a certain distance along the column. Hoek *et al.* [3] showed that structured packings are characterized by much more regular liquid flow patterns and the flow equilibrium between the bulk of the column and the wall zone is established at lower depth.

The separation system can be less or more sensitive to maldistribution [6], which means that with one and the same maldistribution the effect on efficiency differs from system to system and in the even different sections of the column. It is pointed

\* To whom all correspondence should be sent:

E-mail: dzhonova@bas.bg

in [3], that maldistribution becomes relatively more detrimental for larger NTU, which has led to the industrial practice to redistribute the liquid at column height equivalent with 10-20 theoretical stages [5].

There are numerous techniques to evaluate the effect of maldistribution on the mass transfer process available in literature. The methods of parallel columns assume that liquid maldistribution results in divergences of the liquid-to-gas flow ratios and the packing can be subdivided into several (3-100) parallel bed sections (3 columns in [5] and [7]). Some “by-pass” methods are reviewed in [6]. They assume that part of the phase does not participate in the mass transfer [8], which damages the final product. There are models which obtain the flow pattern and the concentrations in each point of the packed bed, generally using CFD techniques [9, 10]. Yin [9] predicted HETP at good agreement with the experiment. His simulation tracked the effect of the loading of the phases on HETP. A widely applied approach to predict the flow pattern in the packed bed uses diffusion models [3, 11-13].

It is accepted that the large-scale maldistribution of the liquid phase is one of the main reasons for reduction in efficiency of absorption processes. The degree of maldistribution is independent of the gas flow in operation below the loading point. In order to obtain data to predict the large-scale liquid maldistribution and control the wall flow, extensive studies have been carried out. For first generation packings, ceramic Raschig rings, Farid & Gunn [14] introduced and estimated experimentally the relative permeability of the wall and bulk regions of the column. They explained the liquid maldistribution with the effect of reduced porosity in a region of one packing element diameter from the wall.

Hoek *et al.* [3] presented the following stages of development of wall flow profiles along the bed depth: 1) Non liquid-covered wall zone; 2) Migration of liquid into non liquid-covered wall zone, based on radial spreading coefficient  $D_r$ ; 3) Flow of liquid from packing to the wall, proportional to the liquid flow in the packing near the wall; 4) Flow-back of liquid from the wall into the packing, proportional to the flow rate along the wall. The growth of the wall flow reaches equilibrium at a certain packing depth. They studied the distribution of water at absence of gas flow and different heights of several random (1<sup>st</sup> and 2<sup>nd</sup> generation) and structured packings of different materials.

Yin *et al.* [15] contributed to better understanding of liquid spreading in packed columns by investigating various factors affecting wall flow formation in stainless steel Pall rings [25]. They reported that at initial maldistribution, a higher packing layer was necessary for the development of a stable “natural flow” of the packing. With the increase of liquid flow rate, the liquid relative wall flow was reduced slightly and the bed height required for the liquid to reach its equilibrium state was also reduced. In preloading regimes, the effect of gas flow rate on liquid distribution was insignificant. The liquid surface tension was found to have little or no effect on liquid distribution. The higher liquid viscosity reduces both the liquid radial spreading and the wall flow.

The aim of the present work is to demonstrate with different random packings a new approach developed theoretically in [16] for evaluation of the amount of liquid in the wall flow. The model equation suggested there is used to predict the wall flow thickness in random packings for further assessment of the effect of liquid maldistribution on mass transfer efficiency. It is used to reveal the factors affecting the relative wall flow rate and the wall flow thickness.

## METHODS

The volume of the liquid flowing on the column wall participates in the absorption process only with its outer surface. The amount of liquid entering the wall flow by-passes the core volume of intensive mixing between the phases and leads to a reduction in the mass transfer rate of the liquid phase.

As suggested in [16], the thickness of the wall layer of liquid in columns with random packings can be represented by an asymptotic function  $\delta(z)$ :

$$\delta(z) = \frac{z}{a+bz}, \quad \delta(0) = 0, \quad \delta(\infty) = \frac{1}{b} = \delta_{\max}, \quad (1)$$

where  $z$  is the axial coordinate and the parameters ( $a$ ,  $b$ ) are determined from experimental data of the flow rate of the liquid flowing along the wall of the column.

The amount of liquid by-passing the absorption process can be represented by the wall flow volume  $V$  [ $\text{m}^3\text{m}^{-1}$ ] per unit circumference of the column, which is determined by integrating (1):

$$V = \int_0^l \frac{z}{a+bz} dz = \frac{a}{b^2} \left( \frac{b}{a} l - \ln \frac{a+bl}{a} \right). \quad (3)$$

*Width of the wall flow*

In order to find the width of the wall flow  $\delta(z)$ , it is assumed that the average velocities of the liquid in the wall flow and in the bulk are:

$$\left( \frac{v_0}{2}, \frac{v_z^0 + v_0}{2} \right), \quad (4)$$

where  $v_0$  [ms<sup>-1</sup>] is the surface velocity of the wall liquid layer,  $v_z^0 = \frac{Q_L}{\varepsilon_2 \pi r_0^2}$  [ms<sup>-1</sup>] is the mean liquid velocity in the cross-section area occupied by the liquid,  $\varepsilon_2$  - liquid volume (area) fraction, and  $Q_L$  [m<sup>3</sup>s<sup>-1</sup>] - total liquid flow rate.

The flow rate of the wall flow  $Q(z)$  per unit circumference of the column ( $2\pi r_0$ ) is expressed in [16] by the average velocities of the liquid on the wall and in the bulk as a subtraction of the bulk flow rate from the total liquid flow rate in the column, resulting in a quadratic equation. Its positive root is the following relation:

$$\delta(z) = \frac{1}{2} \left\{ -r_0' + \left( r_0'^2 + \frac{8r_0 Q(z)}{v_z^0} \right)^{1/2} \right\}, \quad (5)$$

where

$$r_0' = \frac{v_z^0 \varepsilon_2 r_0 + 2Q(z) \varepsilon_2 - 2Q(z)}{v_z^0 \varepsilon_2}. \quad (6)$$

The obtained experimental values of  $\delta(z)$  by Eq. (5) allow to determine the parameters ( $a, b$ ) in Eq. (1) by minimizing the function of the least square differences between model and experimental data.

#### Maldistribution parameter

The calculation of the thickness of the wall flow in random packings enables to determine the variable radius  $r$  of the core volume of the packed column, where the absorption process takes place:

$$r = r_0 - \delta(z). \quad (7)$$

After obtaining ( $a, b$ ) and  $\delta(z)$  by Eq. (1), it is possible to calculate the equilibrium length of the

liquid layer on the wall  $l_e$ , when the layer thickness reaches 95% of its maximal value  $\delta_{\max} = b^{-1}$  [16].

$$l_e = \frac{19a}{b} \quad (8)$$

The equilibrium volume of the wall flow  $V_e$  at  $l=l_e$  is obtained directly from Eq. (3):

$$V_e = 16 \frac{a}{b^2}. \quad (9)$$

A maldistribution parameter  $E$ , suggested in [16], is used for comparison of the wall flow formation in different packings, for evaluation of their potential for separation efficiency:

$$E = V_e^{-1}. \quad (10)$$

## RESULTS AND DISCUSSION

The aforementioned calculation procedure [16] is applied to various types and sizes of random packings of different material at countercurrent gas and liquid flows of different loads, including in absence of gas flow. The experimental conditions are presented in Table 1. All experiments are carried out at a semi-industrial scale of the equipment, system air-water, uniform initial distribution of the phases, and regimes under the loading point. The constants ( $a, b$ ) in the function of the wall flow thickness, with the respective coefficients of determination  $R^2$  of the regression, and the maldistribution parameter are presented in Table 2. For the purpose of comparison, the wall flow volume and the maldistribution parameter are calculated per one-meter height of the packed bed:

$$V_e^* = V_e \cdot l_e^{-1}, \\ E^* = V_e^*^{-1}$$

**Table 1.** Operational conditions and parameters of considered cases

N	Packing [source]	Column radius $r_0$ [m]	Liquid load $L_0$ [m <sup>3</sup> m <sup>-2</sup> s <sup>-1</sup> ]	Gas load $G_0$ [m <sup>3</sup> m <sup>-2</sup> s <sup>-1</sup> ]	Maximal bed height [m]	Liquid volume fraction $\varepsilon_2$ [source]
1	Metal Raschig-Super-Ring 1.5, (RSRM) Dzhonova et al. [17]	0.235	12e-03	0	1.4	0.009 [18]
2	Metal Pall ring 25, Yin et al. [15]	0.3	2.9e-03	0.625	3	0.034 [19]
3	Metal Pall ring 25, Yin et al. [15]	0.3	6.66e-03	0.625	3	0.062 [19]
4	Plastic Pall ring 50 Kouri and Sohlo [11]	0.25	2.5e-03	0	3.5	0.022 [19]
5	Plastic Pall ring 50 Kouri and Sohlo [11]	0.25	2.5e-03	1.67	3.5	0.022 [19]
6	Plastic Pall ring 50 Kouri and Sohlo [11]	0.25	10e-03	0	3.5	0.053 [19]
7	Plastic Pall rings 50 Kouri and Sohlo [11]	0.25	10e-03	1.67	3.5	0.053 [19]

**Table 2.** Model constants for the wall flow thickness and maldistribution parameter

N	$Q_L$ [m <sup>3</sup> s <sup>-1</sup> ]	$a$	$b$ [m <sup>-1</sup> ]	$R^2$	$\delta_{\max}$ [m]	$l_e$ [m]	$V_e$ [m <sup>3</sup> m <sup>-1</sup> ]	$V_e^*$ [m <sup>3</sup> m <sup>-2</sup> ]	$E^*$ [m <sup>-3</sup> m <sup>2</sup> ]
1	0.00208	2330.80	561.23	0.99	0.0018	78.91	0.1184	0.0015	666.46
2	0.00082	415.63	384.10	0.93	0.0026	20.56	0.0451	0.0022	456.12
3	0.00188	205.78	259.08	0.89	0.0039	15.09	0.0491	0.0033	307.65
4	0.00049	222.62	318.65	0.80	0.0031	13.27	0.0351	0.0026	378.39
5	0.00049	147.39	309.05	0.84	0.0032	9.06	0.0247	0.0027	367.00
6	0.00196	40.49	251.16	0.59	0.0040	3.06	0.0103	0.0034	298.26
7	0.00196	27.79	175.23	0.73	0.0057	3.01	0.0145	0.0048	208.08

*Packing 1*

RSRM is a modern 4<sup>th</sup> generation packing of open structure. In [17] the data on liquid distribution in RSRM 1.5 are obtained at one phase flow of water by the liquid collecting method with 7 concentric annular collecting sections, at the bottom of the packed bed. The wall flow section was 5 mm wide, with an area of 4.21% of the total cross-section area. The relative wall flow rate was measured at three liquid loads, (5e-03 m<sup>3</sup>m<sup>-2</sup>s<sup>-1</sup>, 8e-03 m<sup>3</sup>m<sup>-2</sup>s<sup>-1</sup> and 12e-03 m<sup>3</sup>m<sup>-2</sup>s<sup>-1</sup>), at different packing heights 0.3-1.4 m. The initial distribution was uniform and the peripheral drip points were at a distance from the wall to prevent formation of a wall flow immediately after the distributor. The set-up and measuring procedure are reported in detail in [17, 20]. It was found that in the studied regimes, the effect of the liquid load on the liquid distribution can be accepted negligible [20]. The model function was determined for a liquid load of 12e-03 m<sup>3</sup>m<sup>-2</sup>s<sup>-1</sup>. The model data are in good agreement with the experiment, as can be seen in Fig. 1.

*Packing 2*

Metal Pall ring is a widely used well studied random packing of second generation. Yin *et al.* [15] studied a 25.4 mm stainless steel Pall ring at different water and air flow rates. They measured the liquid distribution by the liquid collecting method at different packed bed heights. The wall collecting zone was 3.12% of total column (4.7 mm wide) cross-sectional area. The set-up and measuring procedure are reported in [15]. The model data are compared to the experiment in Fig. 2. Fig. 2 demonstrates that with the increase of liquid flow rate, the liquid relative wall flow and the packing bed depth for equilibrium state are reduced, while the wall liquid layer thickness is increased.

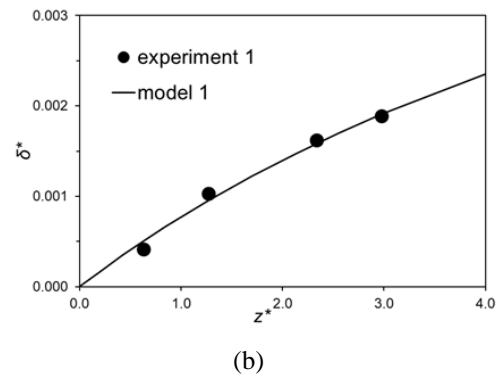
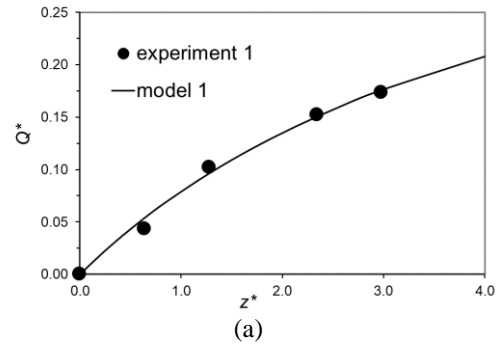


**Fig.1.** Wall flow in RSRM1.5,  $L_0=12e-03$  m<sup>3</sup>m<sup>-2</sup>s<sup>-1</sup>: a) Relative wall flow rate, b) Relative layer thickness

*Packing 3*

Plastic pall ring 50 was studied by Kouri and Sohlo [11]. The authors reported data for the liquid and gas flow patterns and the liquid wall flow in random packings, measured by the liquid collecting method with annular wall collecting section 15 mm wide with an area of 11.64% of the column cross-section. The comparison of the model to the experimental data in Fig. 3 shows good agreement. Fig. 3 demonstrates the effect of the gas phase. The presence of a countercurrent gas flow leads to an increase in the relative wall flow, the equilibrium depth, and the wall layer thickness, which implies to a local overloading. With the increase of the liquid load, the relative wall flow and its equilibrium depth is reduced, while the layer thickness is increased (in conformity with the dependencies shown in Fig. 2).

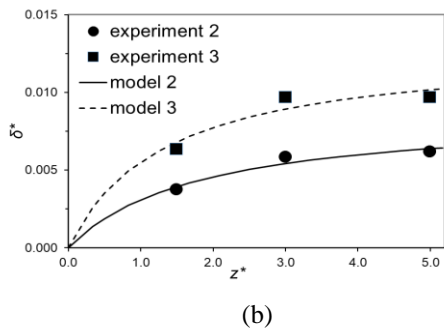
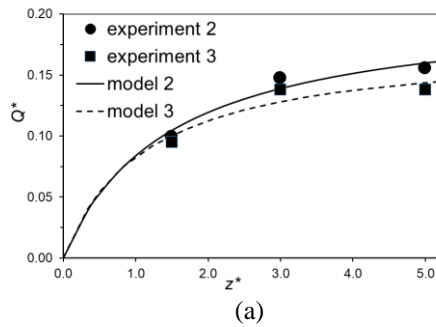


**Fig. 2.** Wall flow in a metal Pall ring 25, 2-  $L_0=2.9 \times 10^{-3} \text{ m}^3 \text{ m}^{-2} \text{ s}^{-1}$ ,  $G_0=0.625 \text{ m}^3 \text{ m}^{-2} \text{ s}^{-1}$ , 3-  $L_0=6.66 \times 10^{-3} \text{ m}^3 \text{ m}^{-2} \text{ s}^{-1}$ ,  $G_0=0.625 \text{ m}^3 \text{ m}^{-2} \text{ s}^{-1}$ : a) Relative wall flow rate, b) Relative layer thickness.

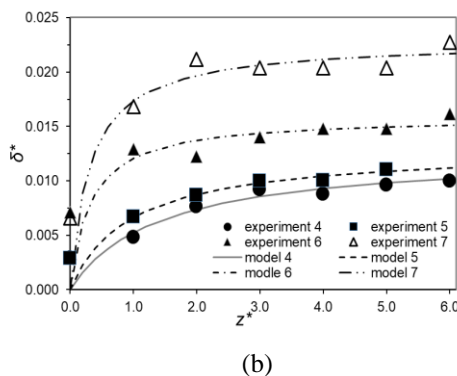
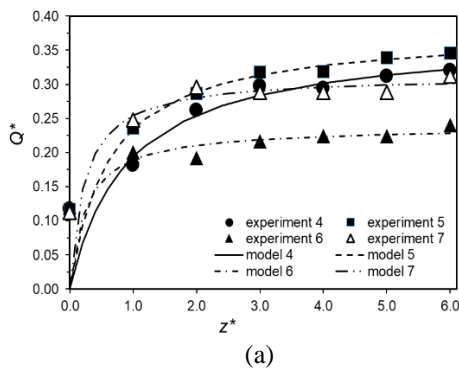


**Fig. 3.** Wall flow in a plastic Pall ring 50: 4-  $L_0=2.5 \times 10^{-3} \text{ m}^3 \text{ m}^{-2} \text{ s}^{-1}$ ,  $G_0=0 \text{ m}^3 \text{ m}^{-2} \text{ s}^{-1}$ , 5-  $L_0=2.5 \times 10^{-3} \text{ m}^3 \text{ m}^{-2} \text{ s}^{-1}$ ,  $G_0=1.67 \text{ m}^3 \text{ m}^{-2} \text{ s}^{-1}$ , 6-  $L_0=10 \times 10^{-3} \text{ m}^3 \text{ m}^{-2} \text{ s}^{-1}$ ,  $G_0=0 \text{ m}^3 \text{ m}^{-2} \text{ s}^{-1}$ ; 7-  $L_0=10 \times 10^{-3} \text{ m}^3 \text{ m}^{-2} \text{ s}^{-1}$ ,  $G_0=1.67 \text{ m}^3 \text{ m}^{-2} \text{ s}^{-1}$ : a) Relative wall flow rate, b) Relative layer thickness

Comparing the maldistribution parameter  $E^*$  (Table 2), it can be seen that it is highest for RSRM,

which speaks for a smaller wall flow and small degree of liquid maldistribution in this packing. This is in agreement with the data in [5], where a maldistribution factor was used to show a lower degree of liquid maldistribution for RSRM packing in comparison to other packings of older generations.

## CONCLUSIONS

A new model of wall flow in random packings was applied for evaluation of the liquid maldistribution. A maldistribution parameter was calculated for comparison of packings of different type, size and material for potential to develop wall flow, which is unfavorable for separation efficiency. The model was used to show the effect of liquid and gas load on wall flow build-up along the column.

The high-performance metal packing RSRM has the highest maldistribution parameter per unit height of the packed bed. It has the smallest relative wall flow and equilibrium thickness of the liquid layer on the wall, and the greatest packing depth for reaching equilibrium state.

The plastic Pall ring 50 displays the biggest relative wall flow and equilibrium layer thickness which is reached at the smallest packing depth.

The increase of the liquid load leads to a reduction in the relative wall flow and equilibrium packing depth, but to an increase in the liquid layer thickness and its equilibrium value.

In presence of a gas flow, the relative liquid wall flow and equilibrium layer thickness are increased, while the equilibrium packing depth is reduced.

The presented approach for evaluation of liquid maldistribution in random packings can be used in future development of a model for prediction of the flow pattern and separation efficiency.

**Acknowledgements:** This work was partially supported by the National Science Fund of Bulgaria, contract KP 06 RUSIA-3/27.09.2019, the Russian Foundation for Basic Research contract # 19-58-18004, and the Bulgarian Ministry of Education and Science under the National Research Programme “Low-carbon energy for transport and domestic use (EPLUS)” (approved by DCM No. 577/17.08.2018 and Grant Agreement DOI-214/28.11.2018).

## NOMENCLATURE

$a, b$  - constants in the model function (1);  
 $D_r$  - radial liquid spreading coefficient, m;  
 $E = V^l$  - maldistribution parameter,  $m \cdot m^{-3}$ ;  
 $E^* = V^{*l}$  - maldistribution parameter per one-meter height of the packed bed,  $m^2 m^{-3}$ ;  
 $G_0$  - gas load,  $m^3 m^{-2} s^{-1}$ ;  
 $L$  - packing height, m;  
 $L_0$  - liquid load,  $m^3 m^{-2} s^{-1}$ ;  
 $Q_L$  - total liquid flow rate,  $m^3 s^{-1}$ ;  
 $Q(z)$  - flow rate of the wall flow per unit circumference of the column,  $m^3 m^{-1} s^{-1}$ ;  
 $r = r_0 - \delta(z)$  - variable radius of the core volume of the packed column where the absorption process takes place, m;  
 $r_0$  - column radius, m;  
 $R^2$  - coefficients of determination;  
 $v_0$  - surface velocity of the wall liquid layer,  $ms^{-1}$ ;  
 $v_z^0$  - mean liquid velocity in the cross-section area occupied by the liquid,  $ms^{-1}$ ;  
 $V$  - wall flow volume per unit circumference of the column,  $m^3 m^{-1}$ ;  
 $V_e^* = V_e \cdot l_e^{-1}$  - wall flow volume per unit circumference per one-meter height of the packed bed,  $m^3 m^{-2}$ ;  
 $z$  - axial coordinate, m;  
 $z^* = z(2r_0)^{-1}$  - dimensionless axial coordinate;  
**Greek letters:**  
 $\delta$  - thickness of the liquid layer on the column wall, m;  
 $\delta^* = \delta r_0^{-1}$  - relative thickness of the liquid layer on the wall;  
 $\delta_{max}$  - maximal thickness of the liquid layer on the wall at equilibrium state, m;  
 $\varepsilon_2$  - liquid volume (area) fraction;  
**Subscripts:**  
 $0$  - at inlet;  
 $e$  - at equilibrium state;  
**Abbreviations:**  
 CFD - Computational Fluid Dynamics;  
 HETP - Height Equivalent to a Theoretical Plate;  
 HTU - Height of a Transfer Unit;  
 NTU - Number of Transfer Units;  
 RSSRM - metal Raschig-Super-Ring packing.

## REFERENCES

1. M. Schultes, *Trans IChemE*, **81**, Part A, 48 (2003).
2. R. Billet, M. Schultes, *Trans. IChemE*, **77**, Part A, 498 (1999).
3. P. J. Hoek, J. A. Wesselingh, F. J. Zuiderweg, *Chem. Eng. Res. Des.*, **64**(6), 431(1986).
4. N. Kolev, R. Darakchiev, Bulg. Patent No. 18018 (1972).
5. M. Schultes, *Ind. Eng. Chem. Res.*, **39**, 1381 (2000).
6. J. F. Billingham, M. J. Lockett, *Trans. IChemE*, **80**, Part A, 373 (2002).
7. M. J. Lockett, J. F. Billingham, *Trans. IChemE*, **81**, Part A, 131 (2003).
8. B. Hanley, *Separ. Purif. Technol.*, **16**, 7 (1999).
9. F. Yin, Liquid maldistribution and mass transfer efficiency in randomly packed distillation columns, PhD Thesis, Univ. Alberta, 1999.
10. Yang, CFD modeling of multiphase countercurrent flow in packed bed reactor for carbon capture, PhD Thesis, Univ. Kentucky, 2015.
11. R. Kouri, J. Sohlo, *Chem. Eng. J.*, **61**, 95 (1996).
12. V. Stanek, V. Kolar, *Collect. Czech. Chem. Commun.*, **38**, 2865 (1973).
13. T. St. Petrova, Kr. A. Semkov, D. B. Dzhonova, *Chem Eng. Trans.*, **70**, 1051 (2018).
14. M. M. Farid, D. J. Gunn, *Chem. Eng. Sci.*, **33**(9), 1221 (1978).
15. F. Yin, Z. Wang, A. Afacan, K. Nandakumar, K. T. Chuan, *Can. J. Chem. Eng.*, **78**(3), 449 (2000).
16. Chr. B. Boyadjiev, D. B. Dzhonova, K. V. Stefanova, St. P. Panyovska, P. G. Popova, A. N. Pavlenko, V. E. Zhukov, E. Yu. Slesareva, *J. of Phys. Conf. Ser.*, in press (2020).
17. D. Dzhonova-Atanasova, T. Petrova, S. Darakchiev, P. Panayotova, Sv. Nakov, R. Popov, Kr. Semkov, *Sci. Works of Univ. Food Tech.* **LXI**, 644 (2014).
18. Sv. Ts. Nakov, D. B. Dzhonova, E. N. Razkazova, *Bulg. Chem. Commun.*, **52**, Spec. Issue, in press (2020).
19. J. Mackowiak, *Fluid Dynamics of Packed Columns*, Springer, Heidelberg, 2010, p. 192.
20. D. B. Dzhonova-Atanasova, T. St. Petrova, Kr. A. Semkov, S. R. Darakchiev, K. V. Stefanova, Sv. Ts. Nakov, R. G. Popov, *Chem. Eng. Trans.*, **70**, 2077 (2018).

## New equations for gas phase pressure drop in expanded metal sheet packing (HOLPACK) for mass and heat transfer processes in packed columns

Kr. A. Semkov\*, T. St. Petrova\*

*Institute of Chemical Engineering, Bulgarian Academy of Sciences,  
Acad. G. Bonchev Str., Bl. 103, 1113, Sofia, Bulgaria*

Received: August 12, 2020; Accepted: August 21, 2020

A horizontal expanded metal sheet packing is designed and investigated for carrying out mass and heat transfer processes in column apparatuses. The packing is made of expanded metal sheet elements placed horizontally with specific orientation at certain distance from one another along the column height. This construction leads to low specific weight and creates condition for highly effective heat and mass transfer at comparatively low gas pressure drop. The packing is studied in details; mathematical models and dimensioning methodology of apparatuses are provided and tested. As a result, the packing was successfully implemented in many processes in the chemical and power industry, as well as in the environmental protection. After a careful critical analysis of the earlier models and equations for determination of the pressure drop of dry and irrigated packing, as well as of loading point gas velocity, some imperfections and, respectively, opportunities for substantial improvement were found. Subsequently, on the base of many years practical (incl. industrial) experience, three new dependences were developed, firstly presented in this work. For the new equations the same experimental data are used as in the old ones; the principal differences evolve from the more appropriate and well-founded structure of the new equations and the better estimation of the geometric dimensions. The proposed equations are derived using dimensional analysis and least squares approach regression. For each equation the main statistic parameters are given. The comparison with the experimental data is illustrated in appropriate diagrams. The accuracy of the new equations is substantially improved, offering a stable base for industrial design and further applications with best performance and energy characteristics.

**Keywords:** Packed columns; Structured packing; Horizontal expanded metal sheet (HOLPACK) packing; Gas phase pressure drop modeling – new equations; Process intensification.

### INTRODUCTION

The horizontal metal sheet packing is patented as a method for mass transfer processes [1]. It is made of expanded metal sheets, placed horizontally on a certain distance along the column height. The sheets are produced on a die by shearing with specially formed knives and subsequent sheet extension, whereupon staggered openings with inclined walls are formed. This product is standardized and is applied for many purposes; if made by thicker metal sheet it usually is used for production of stairs and platforms on different equipment. At first the packing was known as “Horizontal sheet packing”, but later for the sake of convenience was called “HOLPACK”.

The investigations carried out [1–6] confirmed its very good hydrodynamic and mass transfer characteristics. The favorable indicators of HOLPACK packing made it tempting for using in a large number of technological processes where it found industrial application.

Some of the most important hydrodynamic characteristics of the packing are the gas (vapor) flow pressure drop of the packing and the loading point velocity. They determine the productivity and

the energy consumption of the transfer process. Especially the accurate determination of the loading point velocity is of crucial importance for optimal performance of the packing. The maximum efficiency is achieved a little below of the loading point. This is considered as the upper allowed limit of the operating range. Above this gas velocity the hydrodynamic of the flows becomes instable.

After a careful critical analysis of the earlier models and equations [6, 13, 14] for determination of the pressure drop of dry and irrigated packing, as well as of loading point gas velocity, some imperfection and, respectively, opportunities for substantial improvement were found.

The aim of this article to develop more accurate equations for determination of the pressure drop characteristics in order to ensure best operation conditions, respectively, improved performance of the columns with HOLPACK packing.

### EXPERIMENTAL

#### *Packing design and main dimensions*

Amongst the known heat and mass transfer apparatuses the hollow irrigated scrubbers are distinguished by the lowest, actually near to zero pressure drop. However, they are low-effective

\* To whom all correspondence should be sent:  
E-mail: semkov@bas.bg t.petrova@iche.bas.bg

because of the non-uniform distribution of the gas across the apparatus cross section and the low values of the mass transfer coefficients. This is due to the absence of elements/structures in which liquid phase to be hit and turbulized while interchange its phase surface. A comparison between the hollow irrigated scrubbers and packed columns shows that the latter avoid the disadvantages of the hollow scrubbers at the expense of significantly increase of the apparatus pressure drop.

Consequently, the development of a hybrid apparatus combining a high mass transfer coefficient and uniform gas velocity distribution in the column with a pressure drop close to that of the hollow irrigated scrubbers appears to be an attractive task.

One convenient solution of this task is replacing the packing by horizontal perforated sheets with large free section, situated horizontally at a distance from one another of several centimeters [1, 6]. The additional pressure drop of the sheets improves the radial uniformity of the gas flow velocity profile. At the same time the hit of the liquid upon the sheets contributes to the liquid phase turbulization and surface renewal [3, 7-9]. The contradiction between the need of large free section for gas flow and low pressure drop, respectively, and the need of possibly larger sheet surface, where the irrigating liquid to be hit, can be solved through appropriate sheet profile and packing geometry optimization. Particularly suitable for design of such packing is the material known as expanded metal sheet (Figure 1-a). A good presentation of the technology of its production is given in (Technical information-mesh, 2015) [10]. It is prevalent for building of factory platforms and stairs, as well as some plate columns constructions. Its widespread use has led to its standardization (e.g. GOST 8706-78). The high productivity of the machines which manufacture expanded metal sheets, the lack of waste of material (like many new metal packings) and the significant (up to 75 %) lengthening of the sheets during its processing to expanded metal sheet determine its low cost. The expanded metal sheets are used also for the production of some corrugated structured packings, e.g. Montz packing type BSH [11, 12]. An essential advantage of this type of sheets is the directing action of the inclined lamellae forming the slits. They orientate the gas flow at an angle towards the sheet cross-section contributing to its radial redistribution. For the liquid phase this slope leads to a marked effect of liquid spreading at irrigation by multipoint

distributors. This spreading is very important for a packing because it gives an opportunity for sufficient simplification of the distributing device. To avoid the one-sided direction of the liquid by the lamellae forming each sheet, the sheets are arranged one above another by rotating of 90° in the same direction – the so called “crosswise” arrangement. Thus, at every fourth sheet the orientation of the lamellae results the same. The distance between the sheets is kept by vertical orientated distancing strips. So created packing is mounted in column sections as is illustrated by a top-view photograph in Figure 1-b. Another configuration called “opposite” arrangement with 180° rotation is also investigated, but didn’t find industrial application due to lower efficiency.

The most important hydrodynamic dimensions of the packing can be determined from its geometric sizes using the following equations - see Figure 1-a:

$$\begin{aligned} d_h &= \frac{s(B+4A)}{8X+B} ; \\ a &= \frac{8X(s_1/2+\delta)+B(s_1+\delta)}{BC(h_1+h_2)} ; \\ \varepsilon_1 &= 1 - \frac{2\delta(B/4+2X)}{BC} , \end{aligned} \quad (1)$$

where the subsidiary parameter  $X$  is determined as follows:

$$X = \frac{1}{2} \sqrt{s^2 + \left(A - \frac{B}{4}\right)^2} . \quad (1-a)$$

For comparison with other packings the HOLPACK void fraction (free packing volume) can be determined:

$$\varepsilon = \frac{\varepsilon_1 h_1 + h_2}{h_1 + h_2} . \quad (1-b)$$

According to this parameter, for example, for packing No. 1 (Table 1) with one of the lowest sheet free cross-sections  $\varepsilon_1 = 0.80$ , the void fraction is  $\varepsilon = 0.974$ . Hence, the void fraction of the HOLPACK packing is very large (mainly due to the empty volume between the sheets) which is a good precondition for low pressure drop.

The experimental investigation of the gas pressure drop of HOLPACK packing was carried out by Darakchiev and Kolev [6, 13, 14]. In the majority of experiments an air–water system was used. The main characteristics and symbols of the investigated packings are given in Table 1. The selected geometric dimensions cover practically the entire range of industrial interest.

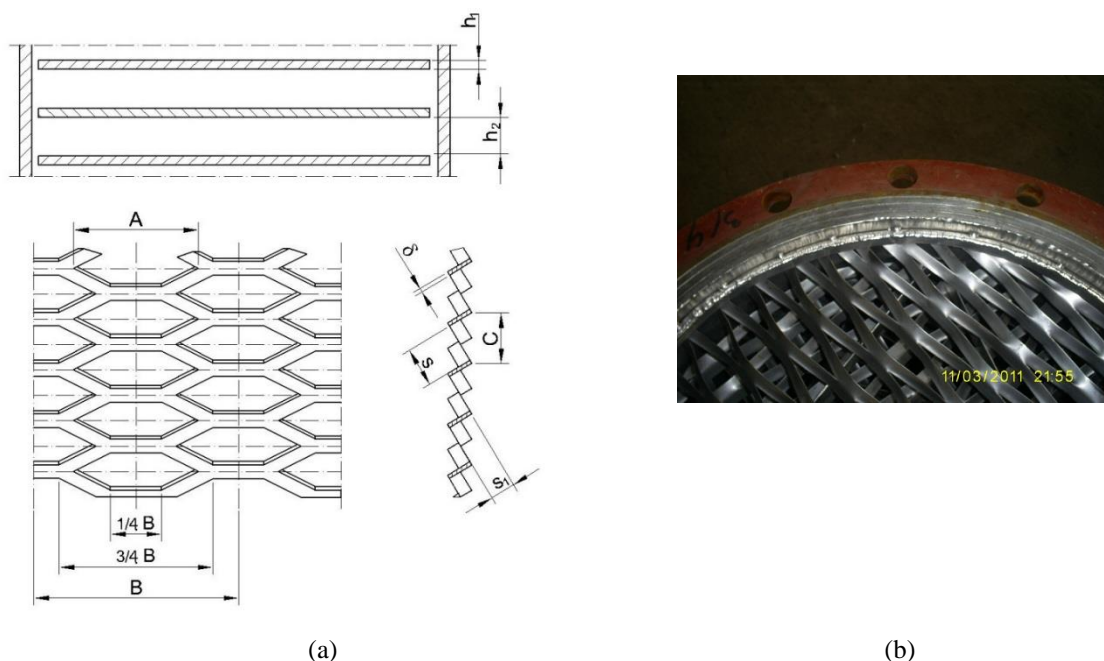


**Fig. 1.** Packing elements made of expanded metal sheet: (a) main dimensions and arrangement; (b) Overview photo of a column section.

**Table 1.** Main characteristics of Holpack packing used at the research of pressure drop

No.	Symbol	A mm	B mm	C mm	$\delta$ mm	s mm	s <sub>1</sub> mm	h <sub>1</sub> mm	h <sub>2</sub> mm	d <sub>h</sub> mm	$\varepsilon_1$ %	a m <sup>2</sup> /m <sup>3</sup>
<i>D<sub>c</sub> = 190 mm</i>												
1*	◇	22.2	30.7	6.4	1.0	4.8	4.2	3.2	20	6.2	76.6	76.6
2	□	22.2	30.7	6.4	0.8	5.0	4.0	3.0	40	6.5	81.2	37.8
3	⊕	22.2	42.7	7.7	1.0	4.5	6.2	4.6	20	6.4	86.0	63.1
<i>D<sub>c</sub> = 470 mm</i>												
4	■	85.0	114	36.0	4.0	16.0	24.0	17.5	10	20.8	83.0	61.6
5	⊙	90.0	121	27.0	1.5	13.0	16.5	13.2	50	17.1	91.6	22.1

\* The sheets are covered with polyethylene.

## RESULTS AND DISCUSSION

The new equations presented below were derived using the dimensional analysis and the least squares approach regression. The confidence intervals of the constants determined refer to 95% reliability, based on Student distribution. After each equation the main statistic parameters as the mean arithmetic error (absolute value) and the standard deviation, as well as the number of figures illustrating the comparison with the experimental data are given.

The structure of the equations is proposed striving to be closer to the real physical phenomena.

➤ Pressure drop of dry HOLPACK packing ( $\Delta P_0$ )

$$Eu = K \cdot N_1 \left( \frac{H}{d_h} \right) \left( \frac{h_1}{d_h} \right)^{n_1} Re_G^{n_2}; \quad (2)$$

Here the equation form reflects the flow pressure drop in tubes and channels. The *Euler* number (*Eu*) is defined as a ratio between the static pressure drop of the packing and the dynamic pressure (see Eq. 5). The main difference from the old equation is that the free cross-section of the packing sheet ( $\varepsilon_1$ ) is not involved as main dimensionless variable.

➤ Pressure drop of irrigated HOLPACK packing ( $\Delta P$ )

$$\frac{\Delta P}{\Delta P_0} = K \cdot Re_L^{n_1} \left( \frac{s_1}{d_h} \right)^{n_2} Re_G^{n_3}; \quad (3)$$

➤ Loading point gas velocity ( $w_{0G}$ )

$$MFr_G = K \left( \frac{s_1}{d_h} \right)^{n_1} Fr_L^{n_2}; \quad (4)$$

Here the *MFr<sub>G</sub>* is a newly introduced dimensionless number (Modified gas Froude

Number), Eq. (5), proportional to the gas flow load factor  $F = w_0 \sqrt{\rho_G}$ .

The dimensionless numbers are defined as:

$$\begin{aligned} Eu &= \frac{2\Delta P_0 \varepsilon_1^2}{w_0^2 \rho_G}; \text{Re}_G = \frac{w_0 d_h}{\nu_G \varepsilon_1}; \\ \text{Re}_L &= \frac{L_0 d_h}{\varepsilon_1 \nu_L}; \text{Fr}_L = \frac{L_0^2}{g d_h \varepsilon_1^2}; \\ M\text{Fr}_G &= \sqrt{\frac{w_{0G}^2}{\varepsilon_1^2 d_h g} \left( \frac{\rho_G}{\rho_A} \right)} \end{aligned} \quad (5)$$

It should be pointed out again that  $\varepsilon_1$  is the packing sheet free cross-section and is not equal to the packing void fraction  $\varepsilon$ .

After processing the experimental data, the constants in equations (2-4) and confidence intervals are presented in Table 2.

According to the values from Table 2 and accounting for the reliable accuracy of the constants the following final form of the equations for practical engineering is proposed:

**Table 2.** Experimental constants, their confidence intervals at 95% reliability

Constant	K	n1	n2	n3
Eq. (3)	$\left( 0.0343 + \frac{2.16}{\text{Re}_G} \right)$	2.47±0.17	0.112±0.65	
Eq. (4)	$0.884^{+0.128}_{-0.112}$	0.173±0.017	-0.253±0.067	-0.0542±0.018
Eq. (5)	$1.97^{+0.37}_{-0.31}$	0.900±0.149	-0.0112±0.021	

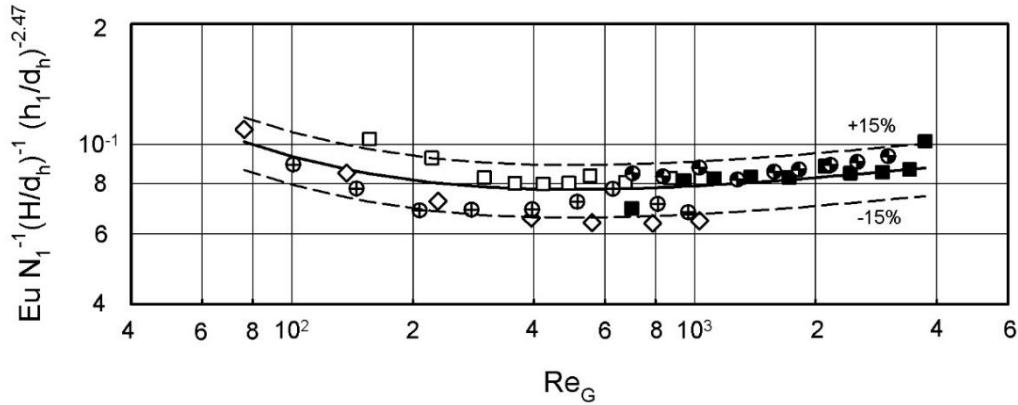


**Fig. 2.** Comparison of experimental data with the pressure drop of dry HOLPACK packing calculated by Eq. (6).

➤ Pressure drop of dry HOLPACK packing ( $\Delta P_0$ )

$$Eu = \left( 0.0343 + \frac{2.16}{\text{Re}_G} \right) N_1 \left( \frac{H}{d_h} \right) \left( \frac{h_1}{d_h} \right)^{2.47} \text{Re}_G^{0.112} \quad (6)$$

The mean relative arithmetic error is 7.88% and the standard deviation is 12.6%. The comparison with experimental data is depicted in Figure 2.

➤ Pressure drop of irrigated HOLPACK packing ( $\Delta P$ )

$$\frac{\Delta P}{\Delta P_0} = 0.884 \text{Re}_L^{0.172} \left( \frac{s_1}{d_h} \right)^{-0.25} \text{Re}_G^{-0.054}; \quad (7)$$

The mean relative arithmetic error is 5.5% and the standard deviation is 8.6%. The comparison with experimental data is depicted in Figure 3.

➤ Loading point gas velocity ( $w_{0G}$ )

$$M\text{Fr}_G = 1.97^{+0.37}_{-0.31} \left( \frac{s_1}{d_h} \right)^{-0.90} \text{Fr}_L^{-0.112}; \quad (8)$$

The mean relative arithmetic error is 4.56% and the standard deviation is 7.67%. The comparison with experimental data is depicted in Figure 4.

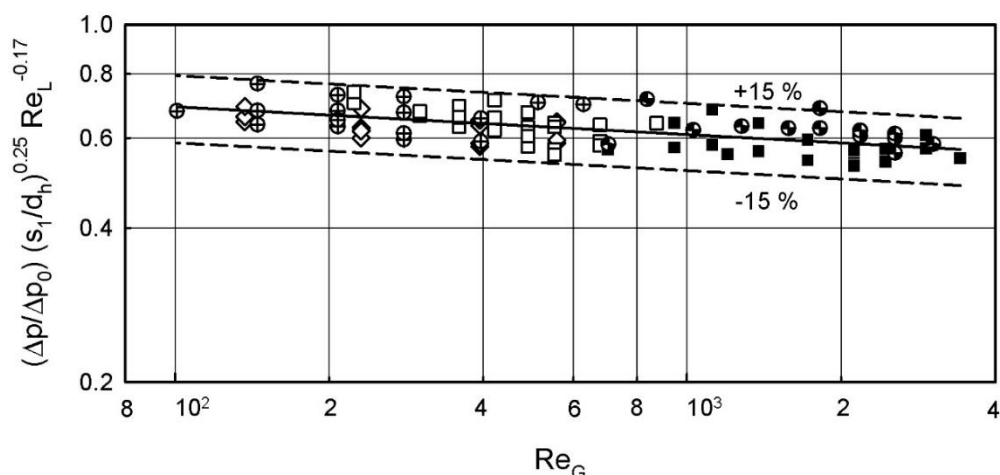


Fig. 3. Comparison of experimental data with the pressure drop of irrigated HOLPACK packing calculated by Eq. (7).

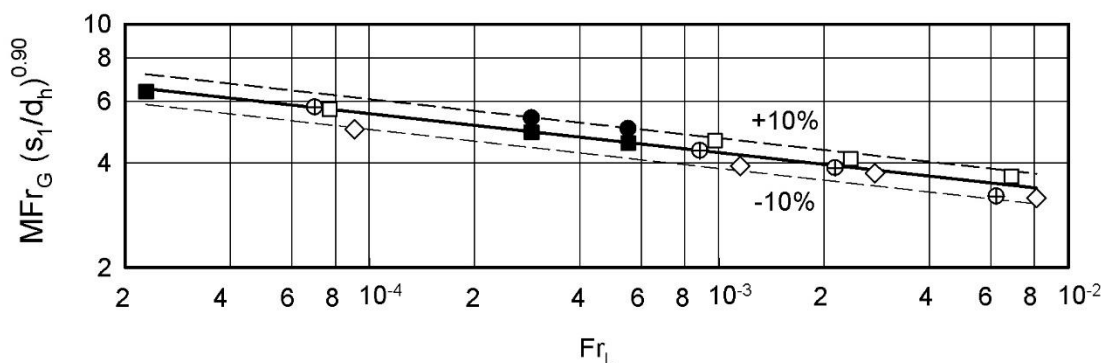


Fig. 4. Comparison of experimental data with the loading point velocity of irrigated HOLPACK packing calculated by Eq. (8).

## CONCLUSION

The HOLPACK packing is a highly effective device for gas (vapor)-liquid transfer processes.

The development of new more accurate equations for determination of the pressure drop and especially of the loading point velocity provides further opportunity for process performance improvement in a wide area of industrial applications.

**Acknowledgements:** This paper was supported by the Bulgarian Ministry of Education and Science under the National Research Programme “Low-carbon energy for transport and domestic use (EPLUS)” (approved by DCM No. 577/17.08.2018 and Grant Agreement DOI-214/28.11.2018).

## NOMENCLATURE

- $A$  - slit length of expanded metal sheet (Fig. 1-a),  $m$ ;
- $B$  - slit longitudinal (longways) step of expanded metal sheet (Fig. 1-a),  $m$ ;
- $C$  - slit transversal (breadthways) step of expanded metal sheet (Fig. 1-a),  $m$ ;
- $D_c$  - column internal diameter,  $m$ ;
- $d_h$  - hydraulic diameter of the slit,  $m$ ;
- $F = w_0 \sqrt{\rho_G}$  - gas (vapour) load factor (F-factor);
- $g$  - gravity acceleration,  $m/s^2$
- $H$  - packing height,  $m$ ;
- $h_1$  - thickness of the expanded metal sheet (Fig. 1-a),  $m$ ;
- $h_2$  - distance between the expanded metal sheets (Fig. 1-a),  $m$ ;

$L$  - liquid superficial velocity,  $m^3/(m^2 s)$ ;

$N_1$  - number of expanded metal sheets per 1 m packing height, -;

$s$  - slit width of the expanded metal sheet (Fig. 1-a),  $m$ ;

$s_1$  - lamella width of the expanded metal sheet (Fig. 1-a),  $m$ ;

$w$  - gas (vapor) velocity,  $m/s$ ;

#### Greek symbols

$\Delta P$  - pressure drop of the wet (irrigated) packing,  $Pa$ ;

$\Delta P_0$  - pressure drop of dry packing,  $Pa$ ;

$\delta$  - thickness of metal sheet (Fig. 1),  $m$ ;

$\varepsilon$  - volume void fraction of horizontal expanded metal packing, %;

$\varepsilon_1$  - free cross-section area of the expanded metal sheet, %;

$\mu$  - dynamic viscosity,  $Pa \cdot s$ ;

$\nu$  - kinematic viscosity,  $m/s^2$ ;

$\rho$  - density,  $kg/m^3$ ;

#### Subscripts

$A$  - air;

$G$  - gas phase;

$L$  - liquid phase;

$O$  - related to the overall cross-section;

$OG$  - related to the loading point.

#### REFERENCES:

1. N. Kolev, R. Darakchiev, A method for performing of mass transfer processes, Bulg. Patent No 16783/17.06.1971.
2. N. Kolev, Packed bed columns: For absorption, desorption, rectification and direct transfer, 1<sup>st</sup> edn., Elsevier, Amsterdam, 2006. <https://doi.org/10.1016/B978-0-444-52829-2.X5000-6>
3. T. K. Sherwood, R. L. Pigford, C. R. Wilke, Mass Transfer, 3<sup>rd</sup> edn., McGraw-Hill, New York, USA, 1975.
4. K. Semkov, N. Kolev, *Commun. Dept. Chem., Bulg. Acad. Sci.*, **22** (2), 329 (1989) (in Bulgarian).
5. N. Kolev, K. Semkov, *Chem. Eng. Process.*, **1991**, **29**, 83-91. [https://doi.org/10.1016/0255-2701\(91\)87017-W](https://doi.org/10.1016/0255-2701(91)87017-W)
6. N. Kolev, R. Darakchiev, *Verfahrenstechnik*, **7** (7), 214 (1973) (in German).
7. R. Higbie, *Trans. Am. Inst. Chem. Eng.*, **31**(2), 365 (1935).
8. P. V. Danckwerts, *Ind. Eng. Chem.*, **43** (6), 1460 (1951). <https://doi.org/10.1021/ie50498a055>
9. N. Kolev, K. Winkler, R. Darakchiev, E. Brosh, *Sov. Chem. Ind.*, **18**(8), 4 (1986).
10. Explaining expanded metal mesh. Available online: <http://www.nilesfence.com/files/technical-information-mesh.pdf> (Accessed Dec. 2015).
11. Z. Olujic, A. F. Seibert, J. R. Fair, *Chem. Eng. Process.*, **39**, 335 (2000). [https://doi.org/10.1016/S0255-2701\(99\)00095-1](https://doi.org/10.1016/S0255-2701(99)00095-1)
12. Rib mesh packing type BSH. High performance packing for thermal mass exchange, Available online: <http://montz.de/en/products/montz-structured-packings/rib-mesh-packing-type-bsh>, (Accessed Dec. 2015).
13. N. Kolev, R. Darakchiev, *Chem.-Ing.-Tech.*, **46** (1), 33 (1974) (in German). <https://doi.org/10.1002/cite.330460109>
14. R. Darakchiev, Hydrodynamic and mass transfer characteristics of a horizontal packing of expanded metal sheets. PhD Thesis, Bulgarian Academy of Sciences, Sofia, 1974 (in Bulgarian).

## Convective type models of co-current absorption processes in column apparatuses

B. Boyadjiev, Chr. Boyadjiev, P. Popova-Krumova\*

Institute of Chemical Engineering at the Bulgarian Academy of Sciences, Acad. G. Bonchev Str. Bl.103, Sofia 1113, Bulgaria

Received: August 12, 2020; Accepted: August 21, 2020

A new approach for the absorption processes modeling in co-current column apparatuses is presented in the cases of industrial conditions, where the models are convective type form. The use of experimental data for the average concentration at the column end, in the cases of highly soluble and lightly soluble gases, permits to obtain the model parameters related to the radial non-uniformity of the velocity in the gas and liquid phases. These experimental parameter values permit to obtain the mass transfer coefficient in the cases of physical and chemical absorption of the average-soluble gases.

**Keywords:** Mathematical modeling, column apparatuses, co-current absorption, chemical engineering processes

### INTRODUCTION

The modeling and simulation of the mass transfer processes in column apparatuses is possible using the new approach [1-3] on the basis of the physical approximations of the mechanics of continua, where the mathematical point (in the phase volume or on the surface between the phases) is equivalent to a small (elementary) physical volume, which is sufficiently small with respect to the apparatus volume, but at the same time sufficiently large with respect to the intermolecular volumes in the medium. On this base are presented [4] convection-diffusion and average-concentration type models.

The convection-diffusion type models permit the qualitative analysis of the processes. These models are the base of the average-concentration models which allow a quantitative analysis of the processes in column apparatuses.

In the industrial processes the diffusion mass transfer is negligible compared to the convective mass transfer and the models are convective type [5].

In the case of the absorption processes in the co-current columns, the effect of the radial component of velocity is not negligible and must be taken into account in the convection and average-concentration type models.

#### *Convection-diffusion model*

A theoretical analysis of the effect of the radial non-uniformity of the axial velocity components in the industrial column will be presented in the case of co-current absorption processes in a cylindrical coordinate system  $(r, z)$  [m], when the radial velocity component is not equal to zero. In the stationary case, the convection-diffusion model [3, 4] of the co-current chemical absorption process, with a pseudo-first-order chemical reaction in the liquid phase, has the form:

$$u_j \frac{\partial c_j}{\partial z} + v_j \frac{\partial c_j}{\partial r} = D_j \left( \frac{\partial^2 c_j}{\partial z^2} + \frac{1}{r} \frac{\partial c_j}{\partial r} + \frac{\partial^2 c_j}{\partial r^2} \right) + (-1)^{(2-j)} k (c_1 - \chi c_2) - (j-1) k_0 c_2;$$

$$r = 0, \quad \frac{\partial c_j}{\partial r} \equiv 0; \quad r = r_0, \quad \frac{\partial c_j}{\partial r} \equiv 0; \quad j = 1, 2; \quad (1)$$

$$z = 0, \quad c_1 \equiv c_1^0, \quad c_2 \equiv 0, \quad u_1^0 c_1^0 \equiv u_1 c_1^0 - D_1 \left( \frac{\partial c_1}{\partial z} \right)_{z=0}, \quad \left( \frac{\partial c_2}{\partial z} \right)_{z=0} = 0.$$

$$\frac{\partial u_j}{\partial z} + \frac{\partial v_j}{\partial r} + \frac{v_j}{r} = 0; \quad (2)$$

$$r = r_0, \quad v_j(r_0, z) = 0; \quad z = 0, \quad u_j = u_j(r, 0); \quad j = 1, 2.$$

\* To whom all correspondence should be sent:

E-mail: [petyabs@yahoo.com](mailto:petyabs@yahoo.com)

In (1, 2)  $u_j = u_j(r, z)$ ,  $v_j = v_j(r, z)$  [m.s<sup>-1</sup>] and  $c_j = c_j(r, z)$  [kg.mol.m<sup>-3</sup>] are the axial and radial velocity components and transferred substance concentrations in the gas ( $j = 1$ ) and liquid ( $j = 2$ ) phases,  $D_j$  [m<sup>2</sup>.s<sup>-1</sup>] are the diffusivities in the phases,  $u_j^0$  and  $v_j^0$  are the inlet velocities and the concentrations in the phases,  $k$  [s<sup>-1</sup>] is the interphase mass transfer coefficient,  $\chi$  - the Henry's number,  $k_0$  [s<sup>-1</sup>] - the chemical reaction rate constant. The concentrations of the transferred substance in the phases are presented as kg-mol of the transferred substance in 1 m<sup>3</sup> of the phase volume. The inlet velocities  $u_j^0$  ( $j = 1, 2$ ) [m.s<sup>-1</sup>] of the gas and liquid phases are equal to the average velocities  $\bar{u}_j$  ( $j = 1, 2$ ) of the phases in the column.

In (1, 2) the generalized variables can be introduced [1]:

$$\begin{aligned} r &= r_0 R, \quad z = lZ, \quad u_j(r, z) = u_j(r_0 R, lZ) = u_j^0 U_j(R, Z), \\ v_j(r, z) &= v_j(r_0 R, lZ) = v_j^0 V_j(R, Z), \quad j = 1, 2, \\ c_1(r, z) &= c_1(r_0 R, lZ) = c_1^0 C_1(R, Z), \\ c_2(r, z) &= c_2(r_0 R, lZ) = \frac{c_1^0}{\chi} C_2(R, Z) \end{aligned} \quad (3)$$

and as a result is obtained:

$$\begin{aligned} U_j \frac{\partial C_j}{\partial Z} + V_j \frac{\partial C_j}{\partial R} &= \text{Fo}_j \left( \varepsilon^2 \frac{\partial^2 C_j}{\partial Z^2} + \frac{1}{R} \frac{\partial C_j}{\partial R} + \frac{\partial^2 C_j}{\partial R^2} \right) + \\ &+ (-1)^{(2-j)} K_j (C_1 - C_2) - (j-1) \text{Da} C_j; \\ R=0, \quad \frac{\partial C_j}{\partial R} &\equiv 0; \quad R=1, \quad \frac{\partial C_j}{\partial R} \equiv 0; \quad j=1, 2; \\ Z=0, \quad C_1 &\equiv 1, \quad C_2 \equiv 0, \quad 1 \equiv U_1 - \varepsilon^2 \text{Fo}_1 \frac{\partial C_1}{\partial Z}, \quad \frac{\partial C_2}{\partial Z} \equiv 0. \end{aligned} \quad (4)$$

$$\frac{\partial U_j}{\partial Z} + \frac{\partial V_j}{\partial R} + \frac{V_j}{R} = 0; \quad R=1, \quad V_j(1, Z) = 0; \quad Z=0, \quad U_j = U_j(R, 0), \quad j=1, 2. \quad (5)$$

The parameters in (4) are

$$\begin{aligned} \text{Fo}_j &= \frac{D_j l}{u_j^0 r_0^2}, \quad j=1, 2, \quad \text{Da} = \frac{k_0 l}{u_2^0}, \quad \varepsilon^2 = \frac{r_0^2}{l^2}, \\ K_1 &= \frac{kl}{u_1^0}, \quad K_2 = \omega K_1, \quad \omega = \frac{u_1^0 \chi}{u_2^0}, \end{aligned} \quad (6)$$

where Fo and Da are the Fourier and Damkohler numbers, respectively.

In the cases of physical absorption  $\text{Da} = 0$ . In industrial conditions  $\text{Fo}_j = \frac{D_j l}{u_j^0 r_0^2} \ll 1$ ,  $j=1, 2$ ,

and the model (4) has a convective form:

$$\begin{aligned} U_j \frac{\partial C_j}{\partial Z} + V_j \frac{\partial C_j}{\partial R} &= (-1)^{(2-j)} K_j (C_1 - C_2); \quad j=1, 2; \\ R=1, \quad \frac{\partial C_j}{\partial R} &\equiv 0; \quad Z=0, \quad C_1 \equiv 1, \quad C_2 \equiv 0. \end{aligned} \quad (7)$$

#### Axial and radial velocity components

The radial non-uniformity of the gas and liquid axial velocity components in the absorption columns is a result of the fluid hydrodynamics at the column inlet and decreases along the column height as a result of the fluid viscosities. As a result radial velocity components are initiated. The theoretical analysis of the change in the radial non-uniformity of the axial velocity components (effect of the radial velocity components) in a column can be made by an appropriate hydrodynamic model, where the average velocities at the cross section of the column are constants (inlet average axial velocity components). In generalized variables [1], as an example, the following velocity distributions can be used, where the difference between the gas and liquid flows is in the average (inlet) velocities only:

$$U_j = (2 - 0.4Z) - 2(1 - 0.4Z)R^2, \quad V_j = 0.2(R - R^3), \quad j=1, 2. \quad (8)$$

The velocity components (8) satisfy the equation (5) and the average velocities are constants:

$$\bar{u}_j = \frac{2}{r_0^2} \int_0^{r_0} r u_j(r, z) dr = u_j^0, \quad \bar{V}_j = 2 \int_0^1 R U_j dR = 1, \quad j=1, 2. \quad (9)$$

#### Average-concentration model

The average values of the velocity and the concentrations at the column cross-sectional area are [3]:

$$\bar{u}_j(z) = \frac{2}{r_0^2} \int_0^{r_0} r u_j(r, z) dr, \quad \bar{c}_j(z) = \frac{2}{r_0^2} \int_0^{r_0} r c_j(r, z) dr, \quad j=1, 2. \quad (10)$$

The functions  $u_j(r, z)$ ,  $v_j(r, z)$ ,  $c_j(r, z)$ ,  $j=1, 2$  in (1, 2) can be presented with the help of the average functions (10):

$$\begin{aligned} u_j(r, z) &= \bar{u}_j U_j(R, Z), \quad v_j(r, z) = \varepsilon \bar{u}_j V_j(R, Z), \\ c_j(r, z) &= \bar{c}_j(z) \tilde{c}_j(r, z), \quad j=1, 2, \end{aligned} \quad (11)$$

where  $\tilde{c}_j(r, z)$ ,  $j=1,2$  present the radial non-uniformity of the concentrations and satisfy the following conditions:

$$\frac{2}{r_0^2} \int_0^{r_0} r \tilde{c}_j(r, z) dr = 1, \quad j=1,2. \quad (12)$$

The average concentration model may be obtained when putting (11) into (1), multiplying by  $r$  and integrating over  $r$  in the interval  $(0, r_0)$ . As a result, the following is obtained:

$$\begin{aligned} \alpha_j(z) \bar{u}_j \frac{d\bar{c}_j}{dz} + [\beta_j(z) + \varepsilon \gamma_j(z)] \bar{u}_j \bar{c}_j &= \\ = D_j \frac{d^2 \bar{c}_j}{dz^2} + (-1)^{(2-j)} k (\bar{c}_1 - \chi \bar{c}_2) - (j-1) k_0 \bar{c}_2; \\ z=0, \quad \bar{c}_j(0) &\equiv (2-j) c_j^0, \quad \frac{d\bar{c}_j}{dz} \equiv 0; \quad j=1,2. \end{aligned} \quad (13)$$

where

$$\begin{aligned} \alpha_j(z) &= \frac{2}{r_0^2} \int_0^{r_0} r U_j \tilde{c}_j dr, \quad \beta_j(z) = \frac{2}{r_0^2} \int_0^{r_0} r U_j \frac{\partial \tilde{c}_j}{\partial z} dr, \quad \gamma_j(z) = \frac{2}{r_0^2} \int_0^{r_0} r V_j \frac{\partial \tilde{c}_j}{\partial r} dr, \\ U_j &= U_j(R, Z), \quad V_j = V_j(R), \quad \tilde{c}_j(r, z) = \tilde{C}_j(R, Z), \quad j=1,2. \end{aligned} \quad (14)$$

The theoretical analysis of the model (13) will be made using the following generalized variables and functions:

$$\begin{aligned} r &= r_0 R, \quad z = lZ, \quad \bar{c}_j(z) = c_j^0 \bar{C}_j(Z), \quad c_2^0 = \frac{c_1^0}{\chi}, \\ \bar{C}_j(Z) &= 2 \int_0^1 R C_j(R, Z) dR, \quad \tilde{c}_j(r, z) = \frac{c_j(r, z)}{\bar{c}_j(z)} = \frac{C_j(R, Z)}{\bar{C}_j(Z)} = \tilde{C}_j(R, Z), \\ \alpha_j(z) &= \alpha_j(lZ) = A_j(Z) = 2 \int_0^1 R U_j(R, Z) \tilde{C}_j(R, Z) dR, \\ \beta_j(z) &= \beta_j(lZ) = B_j(Z) = 2 \int_0^1 R U_j(R, Z) \frac{\partial \tilde{C}_j}{\partial Z} dR, \\ \gamma_j(z) &= \gamma_j(lZ) = G_j(Z) = 2 \int_0^1 R V_j(R) \frac{\partial \tilde{C}_j}{\partial R} dR, \quad j=1,2. \end{aligned} \quad (15)$$

As a result, the model (13) has the form:

$$\begin{aligned} A_j(Z) \frac{d\bar{C}_j}{dZ} + [B_j(Z) + G_j(Z)] \bar{C}_j &= \\ = \varepsilon^2 \text{Fo}_j \frac{d^2 \bar{C}_j}{dZ^2} + (-1)^{(2-j)} K_j (\bar{C}_1 - \bar{C}_2) - (j-1) \text{Da} \bar{C}_j; \\ Z=0, \quad \bar{C}_1 &= 1, \quad \bar{C}_2 = 0, \quad \frac{d\bar{C}_j}{dZ} = 0; \quad j=1,2. \end{aligned} \quad (16)$$

In industrial conditions  $\text{Fo}_j \ll 1$ ,  $j=1,2$ , and the model (16) has a convective form:

$$\begin{aligned} A_j(Z) \frac{d\bar{C}_j}{dZ} + [B_j(Z) + G_j(Z)] \bar{C}_j &= (-1)^{(2-j)} K_j (\bar{C}_1 - \bar{C}_2) - (j-1) \text{Da} \bar{C}_j; \\ Z=0, \quad \bar{C}_1 &= 1, \quad \bar{C}_2 = 0; \quad j=1,2. \end{aligned} \quad (17)$$

The presented models (7, 17) permit to analyze the physical absorption ( $0 = \text{Da} \leq 10^{-2}$ ) of highly soluble ( $0 = \omega \leq 10^{-2}$ ), lightly soluble ( $0 = \omega^{-1} \leq 10^{-2}$ ) or average-soluble ( $10^{-1} < \omega < 10$ ) gases.

#### Physical absorption of highly soluble gas

In the cases of physical absorption of a highly soluble gas ( $\omega = K_2 = \text{Da} = 0$ ) and from (7, 17) follows  $C_2 = \bar{C}_2 \equiv 0$ .

$$\begin{aligned} U_1 \frac{\partial C_1}{\partial Z} + V_1 \frac{\partial C_1}{\partial R} &= -K_1 C_1; \\ R=1, \quad \frac{\partial C_1}{\partial R} &\equiv 0; \quad Z=0, \quad C_1 \equiv 1. \end{aligned} \quad (18)$$

Eq. (18) is solved (similar to [5]), using the Method of Lines [6], by discretizing it in respect to  $R_i = i/n$ ,  $i=0, \dots, n$  (transformation of the partial differential equation (18) to a system of ordinary differential equations in respect to  $Z$ ):

$$R_0 = 0, \quad R_n = 1, \quad 0 < R_i = \frac{i}{n} < 1, \quad i=1, 2, \dots, (n-1) \quad (19)$$

From (8, 18, 19) follows:

$$V_1(R_0) = V_1(R_n) = 0, \quad \left( \frac{\partial C_{1n}}{\partial R} \right)_{R=R_n} = 0. \quad (20)$$

As a result from (18) follows:

$$\begin{aligned} U_1(R_0, Z) \frac{dC_{10}}{dZ} &= -K_1 C_{10}; \\ U_1(R_i, Z) \frac{dC_{1i}}{dZ} &= -V_1(R_i) \left( \frac{\partial C_{1i}}{\partial R} \right)_{R=R_i} - K_1 C_{1i}; \\ U_1(R_n, Z) \frac{dC_{1n}}{dZ} &= -K_1 C_{1n}; \\ Z=0, \quad C_{10} &= 1, \quad C_{1i} = 1, \quad C_{1n} = 1, \quad i=1, \dots, n-1. \end{aligned} \quad (21)$$

As a result, from (21) follows the next equations system, where 2 points finite difference scheme is used:

$$U_1(R_0, Z) \frac{dC_{10}}{dZ} = -K_1 C_{10};$$

$$U_1(R_i, Z) \frac{dC_{1i}}{dZ} = -V_1(R_i) \frac{C_{1i} - C_{1(i-1)}}{R_i - R_{i-1}} - K_1 C_{1i};$$

$$U_1(R_n, Z) \frac{dC_{1n}}{dZ} = -K_1 C_{1n};$$

$$Z = 0, \quad C_0 = 1, \quad C_i = 1, \quad C_n = 1; \quad i = 1, \dots, n-1.$$
(22)

As a result:

$$C_1(R, Z) = C_{10}(0, Z), C_{11}(R_1, Z), C_{12}(R_2, Z), \dots, C_{1(n-1)}(R_{(n-1)}, Z), C_n(1, Z) = 0$$
(23)

The solution of (18) permits to obtain the concentration distribution in the gas phase  $C_1(R, Z)$ . In the case  $K_1 = 1$ , the result is presented on Fig. 1.

The concentration distribution  $C_1(R, Z)$  and (15) permit to obtain the average concentrations  $\bar{C}_1(Z_n)$  (“theoretical” values, points in Fig. 2) and functions

$A_1(Z_n), B_1(Z_n), G_1(Z_n)$  in (15), which are presented on Fig. 3 (points).

The functions  $A_1(Z), B_1(Z), G_1(Z)$  in Fig. 3 (points) can be presented as the following approximations:

$$A_1(Z) = 1 + a_{11}Z + a_{12}Z^2, \quad B_1(Z) = b_{11}Z^{b_{12}}, \quad G_1(Z) = g_{11}Z.$$
(24)

where the “theoretical” values of  $a_{11}, a_{12}, b_{11}, b_{12}, g_{11}$  are presented in Table 1.

The average-concentration model in the cases of physical absorption of highly soluble gas ( $\omega = K_2 = Da = \bar{C}_2 \equiv 0$ ) follows from (17):

$$A_1(Z) \frac{d\bar{C}_1}{dZ} + [B_1(Z) + G_1(Z)] \bar{C}_1 = -K_1 \bar{C}_1;$$
(25)

$$Z = 0, \quad \bar{C}_1 \equiv 1.$$

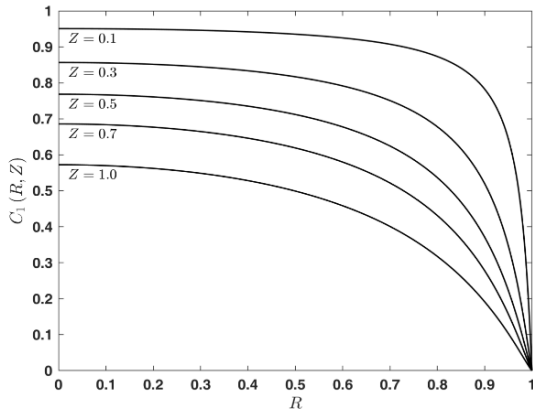


**Fig. 1.** Concentration distributions  $C_1(R, Z)$ , for different  $Z = 0.1, 0.3, 0.5, 0.7, 1.0$ .

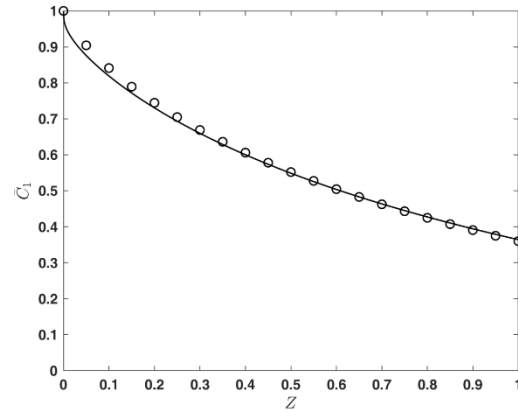


**Fig. 2.** Average concentrations  $\bar{C}_1(Z)$ : “theoretical” values (points); solution of (25), using the “experimental” parameter values  $P_1, K_1$  in Table 1 (line).

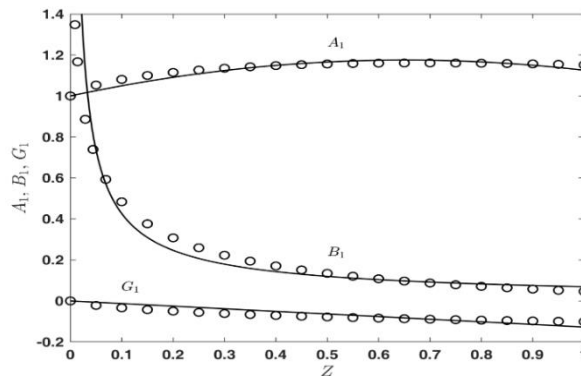


**Fig. 3.** Functions  $A_1(Z_n), B_1(Z_n), G_1(Z_n)$  (points); approximations (24) (lines).

In (25), the parameters  $P_1(a_{11}, a_{12}, b_{11}, b_{12}, g_{11})$  in the functions  $A_1(Z), B_1(Z), G_1(Z)$  and  $K_1$  must be obtained using experimental data.

The obtained values of the function  $\bar{C}_1(Z_n)$  in the cases of physical absorption of a highly soluble gas ( $\omega = K_2 = Da = 0$ ), “theoretical” value of  $K_1 = 1$  and different  $Z_n$  (Fig. 2), permit to obtain the value of  $\bar{C}_1(1)$  and the artificial experimental data (for  $j = 1$ ):

$$\bar{C}_{j\text{exp}}^m(1) = (0.95 + 0.1B_m)\bar{C}_j(1), \quad j = 1, 2, \quad m = 1, \dots, 10, \quad (26)$$

where  $0 \leq B_m \leq 1, m = 1, \dots, 10$  are obtained by a generator of random numbers. The obtained artificial experimental data (26) for  $j = 1$  are used for the parameters  $P_1, K_1$  identification in the average concentrations model (25), by the minimization of the least-squares function  $Q^{(1)}$  with respect to  $P_1, K_1$ :

$$Q^{(1)}(P_1, K_1) = \sum_{m=1}^{10} [\bar{C}_1(1, P_1, K_1) - \bar{C}_{1\text{exp}}^m(1)]^2, \quad (27)$$

where the values of  $\bar{C}_1(1, P_1, K_1)$  are obtained as solutions of (25). The obtained (after the minimization) “experimental” parameter values  $P_1, K_1$  are compared with the “theoretical” values on Table 1. They are used for the solution of (25) and the result (the line) is compared with the “theoretical” average concentration values on Fig. 2.

A comparison of (18) and (28) shows that in the case  $K_1 = K_2 = 1$  is possible to obtain  $C_1 + C_2 = 1$ , i.e. the solution of (28) is  $C_2(R, Z) = 1 - C_1(R, Z)$  and is presented on Fig. 4.

#### Physical absorption of a lightly soluble gas

In the cases of physical absorption of a lightly soluble gas ( $\omega^{-1} = K_1 = Da = 0$ ), from (7, 17) follows:  $C_1 = \bar{C}_1 \equiv 1$ .

From convection type model (7) follows:

$$U_2 \frac{\partial C_2}{\partial Z} + V_2 \frac{\partial C_2}{\partial R} = K_2(1 - C_2); \quad (28)$$

$$R = 1, \quad \frac{\partial C_2}{\partial R} \equiv 0; \quad Z = 0, \quad C_2 \equiv 0.$$

**Table 1.** Parameters  $P_j, K_j, j = 1, 2, K_1 = K, K_2 = \omega K$  (physical absorption).

Parameters	“Theoretical” values	“Experimental” values
$a_{11}$	0.537	0.578
$a_{12}$	-0.412	-0.415
$b_{11}$	0.069	0.070
$b_{12}$	-0.788	-0.680
$g_{11}$	-0.127	-0.134
$K_1 (\omega = 0)$	1	0.991
$a_{21}$	0.925	0.921
$a_{22}$	0.204	0.207
$b_2$	10.297	10.465
$g_{21}$	12.957	13.061
$g_{22}$	4.113	4.112
$K_2$	1	1.007
$K$	1	0.921

The average concentration distribution can be obtained directly  $\bar{C}_2(Z) = 1 - \bar{C}_1(Z)$  and the “theoretical” values  $\bar{C}_2(Z_n)$  are presented on Fig. 5 (points).

The obtained result for  $C_2(R, Z), \bar{C}_2(Z)$ , and (15) permit to obtain the functions  $A_2(Z_n), B_2(Z_n), G_2(Z_n)$  in (15), which are presented on Figs. 6, 7 (points).

The functions  $A_2(Z), B_2(Z), G_2(Z)$  in Figs. 6, 7 (points) can be presented as the approximations:

$$A_2(Z) = a_{21}Z^{a_{22}}, \quad B_2(Z) = \frac{1}{b_2Z}, \quad G_2(Z) = \frac{1}{g_{21}Z + g_{22}}. \quad (29)$$

where the “theoretical” values of  $a_{21}, a_{22}, b_2, g_{21}, g_{22}$  are presented in Table 1.

In the cases of physical absorption of a lightly soluble gas ( $\omega^{-1} = K_1 = Da = 0, C_1 = \bar{C}_1 \equiv 1$ ) from (16) follows:

$$A_2(Z) \frac{d\bar{C}_2}{dZ} + [B_2(Z) + G_2(Z)]\bar{C}_2 = K_2(1 - \bar{C}_2); \quad (30)$$

$$Z = 0, \quad \bar{C}_2 = 0.$$

The solution of (30) is similar to the solution of (25), where the parameters  $P_2(a_{21}, a_{22}, b_2, g_{21}, g_{22})$  in the functions  $A_2(Z), B_2(Z), G_2(Z)$  and  $K_2$  must be obtained using experimental data.

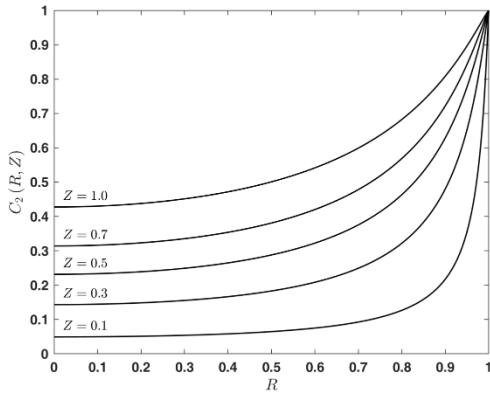


**Fig. 4.** Concentration distributions  $C_2(R, Z)$ , for different  $Z = 0.1, 0.3, 0.5, 0.7, 1.0$ .

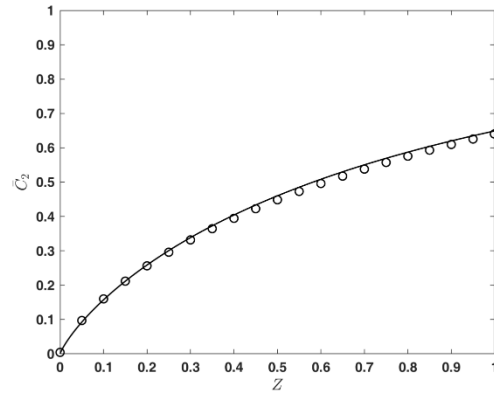


**Fig. 5.** Average concentration distributions  $\bar{C}_2(Z)$ , for different  $Z$  (points); solution of (30), using the “experimental” parameter values  $P_2, K_2$  in Table 1 (line).

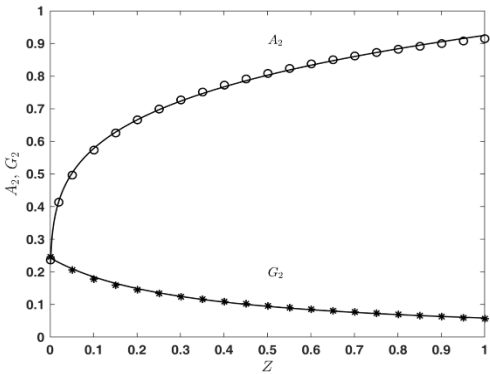


**Fig. 6.** Functions  $A_2(Z_n), G_2(Z_n)$  (points); approximations (29) (lines).

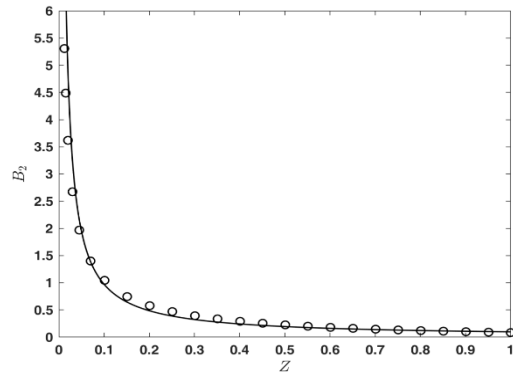


**Fig. 7.** Function  $B_2(Z_n)$  (points); approximation (29) (lines).

The obtained values of the function  $\bar{C}_2(Z_n)$  in the cases of physical absorption of lightly soluble gas ( $\omega^{-1} = K_1 = Da = 0$ ), “theoretical” value of  $K_2 = 1$  and different  $Z_n$  (Fig. 5), permit to obtain the value of  $\bar{C}_2(1)$  and the artificial experimental data (26) for  $j=2$ . They are used for the parameters  $P_2, K_2$  identification in the average concentrations model (30), by the minimization of the least-squares function  $Q^{(2)}$  with respect to  $P_2, K_2$ :

$$Q^{(2)}(P_2, K_2) = \sum_{m=1}^{10} \left[ \bar{C}_2(1, P_2, K_2) - \bar{C}_{2\text{exp}}^m(1) \right]^2, \quad (31)$$

where the values of  $\bar{C}_2(1, P_2, K_2)$  are obtained as solutions of (30). The obtained (after the minimization) “experimental” parameter values  $P_2, K_2$  are compared with the “theoretical” values on Table 1. They are used for the solution of (30)

and the result (the line) is compared with the “theoretical” average concentration values (points) on Fig. 5.

#### Physical absorption of average-soluble gas

In the cases of physical absorption of an average-soluble gas ( $\omega \sim 1, K_1 = K, K_2 = \omega K, Da = 0$ ), the convection type model can be obtained from (7):

$$\begin{aligned} U_1 \frac{\partial C_1}{\partial Z} + V_1 \frac{\partial C_1}{\partial R} &= -K(C_1 - C_2); \\ R=1, \quad \frac{\partial C_1}{\partial R} &\equiv 0, \quad Z=0, \quad C_1 \equiv 1. \\ U_2 \frac{\partial C_2}{\partial Z} + V_2 \frac{\partial C_2}{\partial R} &= \omega K(C_1 - C_2); \\ R=1, \quad \frac{\partial C_2}{\partial R} &\equiv 0; \quad Z=0, \quad C_2 \equiv 0. \end{aligned} \quad (32)$$

The problem (32) is solved using the Method of Lines [6]:

$$\begin{aligned}
 U_1(R_0, Z) \frac{dC_{10}}{dZ} &= -K(C_{10} - C_{20}); \\
 U_1(R_i, Z) \frac{dC_{1i}}{dZ} &= -V_1(R_i) \frac{C_{1i} - C_{1(i-1)}}{R_i - R_{i-1}} - K(C_{1i} - C_{2i}); \\
 U_1(R_n, Z) \frac{dC_{1n}}{dZ} &= -K(C_{1n} - C_{2n}); \\
 Z=0, \quad C_{10} &= 1, \quad C_{1i} = 1, \quad C_{1n} = 1; \quad i=1, \dots, n-1.
 \end{aligned} \tag{33}$$

$$\begin{aligned}
 U_2(R_0, Z) \frac{dC_{20}}{dZ} &= \omega K(C_{10} - C_{20}); \\
 U_2(R_i, Z) \frac{dC_{2i}}{dZ} &= -V_2(R_i) \frac{C_{2i} - C_{2(i-1)}}{R_i - R_{i-1}} + \omega K(C_{1i} - C_{2i}); \\
 U_2(R_n, Z) \frac{dC_{2n}}{dZ} &= \omega K(C_{1n} - C_{2n}); \\
 Z=0, \quad C_{20} &= 0, \quad C_{2i} = 0, \quad C_{2n} = 0; \quad i=1, \dots, n-1.
 \end{aligned} \tag{34}$$

The solution of (33, 34) permits to obtain the concentrations  $C_j(R, Z)$ ,  $j=1, 2$  in the case  $\omega=1, K=1$ , which are presented on Fig. 8 for different  $Z$  (points). This solution and (15) permit to obtain the average concentrations  $\bar{C}_j(Z_n)$ ,  $j=1, 2$  for different  $Z_n$  (Fig. 9),  $\bar{C}_j(1)$ ,  $j=1, 2$  and the artificial experimental data (26). They are used to obtain the mass transfer coefficient  $K$  by the minimization of the least-squares function  $Q$  with respect to  $K$ :

$$Q(K) = \sum_{m=1}^{10} [\bar{C}_1(1, K) - \bar{C}_{1\text{exp}}^m(1)]^2 + \sum_{m=1}^{10} [\bar{C}_2(1, K) - \bar{C}_{2\text{exp}}^m(1)]^2 \tag{35}$$

where  $\bar{C}_1(1, K), \bar{C}_2(1, K)$  are solutions of the average-concentration model:

$$\begin{aligned}
 A_1(Z) \frac{d\bar{C}_1}{dZ} + [B_1(Z) + G_1(Z)] \bar{C}_1 &= -K(\bar{C}_1 - \bar{C}_2); \quad Z=0, \quad \bar{C}_1 = 1. \\
 A_2(Z) \frac{d\bar{C}_2}{dZ} + [B_2(Z) + G_2(Z)] \bar{C}_2 &= \omega K(\bar{C}_1 - \bar{C}_2); \quad Z=0, \quad \bar{C}_2 = 0.
 \end{aligned} \tag{36}$$

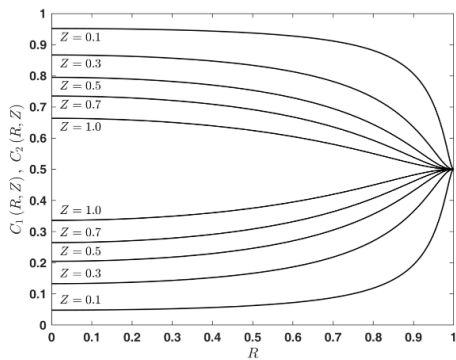


**Fig. 8.** Concentration distributions  $C_j(R, Z)$ ,  $j=1, 2$  for different  $Z=0.1, 0.3, 0.5, 0.7, 1.0$ .

The “experimental” parameter value  $K$  and the “experimental” values of the parameters  $P_1, P_2$  in Table 1 obtained (after the minimization) are used for the solution of the average-concentration model (36). The solution of (36), using the “experimental” parameter values  $P_1, P_2, K$ , is presented (lines) on Fig. 9.

### Chemical absorption

In the cases of chemical absorption of the average-soluble gas, the convection type model can be obtained from (7), where  $\omega \sim 1$ ,  $K_1 = K, K_2 = \omega K, Da \neq 0$  and  $K$  is the “experimental” value in Table 1:

$$\begin{aligned}
 U_1 \frac{\partial C_1}{\partial Z} + V_1 \frac{\partial C_1}{\partial R} &= -K(C_1 - C_2); \\
 R=1, \quad \frac{\partial C_1}{\partial R} &\equiv 0; \quad Z=0, \quad C_1 \equiv 1. \\
 U_2 \frac{\partial C_2}{\partial Z} + V_2 \frac{\partial C_2}{\partial R} &= \omega K(C_1 - C_2) - Da C_2; \\
 R=1, \quad \frac{\partial C_2}{\partial R} &\equiv 0; \quad Z=0, \quad C_2 \equiv 0.
 \end{aligned} \tag{37}$$

The solution of (37) is similar to (32), where (34) must be presented as:

$$\begin{aligned}
 U_1(R_0, Z) \frac{dC_{10}}{dZ} &= -K(C_{10} - C_{20}); \\
 U_1(R_i, Z) \frac{dC_{1i}}{dZ} &= -V_1(R_i) \frac{C_{1i} - C_{1(i-1)}}{R_i - R_{i-1}} - K(C_{1i} - C_{2i}); \\
 U_1(R_n, Z) \frac{dC_{1n}}{dZ} &= -K(C_{1n} - C_{2n}); \\
 Z=0, \quad C_{10} &= 1, \quad C_{1i} = 1, \quad C_{1n} = 1; \quad i=1, \dots, n-1.
 \end{aligned} \tag{38}$$

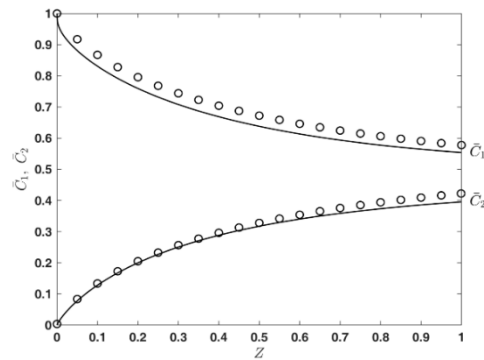


**Fig. 9.** Average concentrations  $\bar{C}_j(Z)$ ,  $j=1, 2$ : “theoretical” values (points); solution of (36) using the “experimental” parameter values  $P_1, P_2, K$  in Table 1 (line).

$$\begin{aligned}
 U_2(R_0, Z) \frac{dC_{20}}{dZ} &= \omega K(C_{10} - C_{20}) - Da C_{20}; \\
 U_2(R_i, Z) \frac{dC_{2i}}{dZ} &= -V_2(R_i) \frac{C_{2i} - C_{2(i-1)}}{R_i - R_{i-1}} + \omega K(C_{1i} - C_{2i}) - Da C_{2i}; \\
 U_2(R_n, Z) \frac{dC_{2n}}{dZ} &= \omega K(C_{1n} - C_{2n}) - Da C_{2n}; \\
 Z=0, \quad C_{20} &= 0, \quad C_{2i} = 0, \quad C_{2i} = 0; \quad i=1, \dots, n-1.
 \end{aligned}
 \tag{39}$$

The obtained concentrations  $C_j(Z)$ ,  $j=1,2$  in the case  $\omega=1, Da=1$  are presented on Figs. 10, 11. The solution of (37) and (15) permits to be obtained average concentrations  $\bar{C}_j(Z_n)$ ,  $j=1,2$  for different  $Z$ , which are presented on Fig. 12 (points).

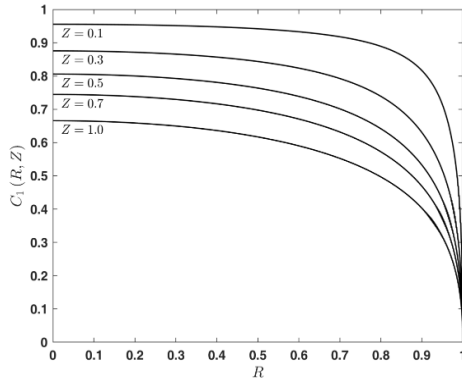


**Fig. 10.** Concentration distributions  $C_1(R, Z)$  for different  $Z=0.1, 0.3, 0.5, 0.7, 1.0$ .

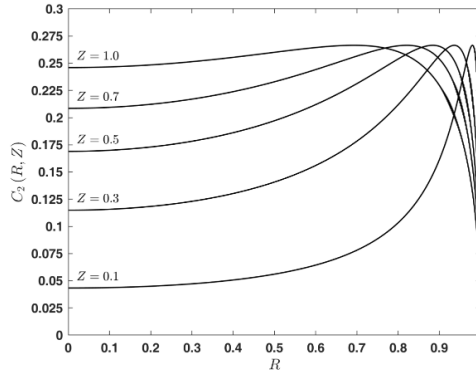


**Fig. 11.** Concentration distributions  $C_2(R, Z)$  for different  $Z=0.1, 0.3, 0.5, 0.7, 1.0$ .

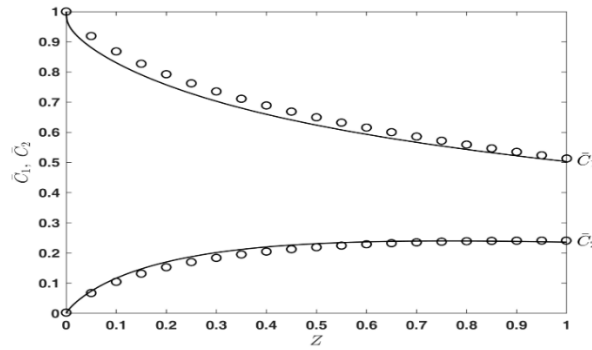


**Fig. 12.** Average concentrations  $\bar{C}_j(Z)$ ,  $j=1,2$ : “theoretical” values (points); solution of (39), using the “experimental” parameter values  $P_2, K$  in Table 1 and  $Da=1$  (line).

The obtained “experimental” values of the parameters  $P_1, P_2, K$  in Table 1 are used for the solution of the average-concentration model of the chemical absorption ( $Da \neq 0$ ) of the average-soluble gases ( $\omega \sim 1$ ), obtained from (17):

$$\begin{aligned}
 A_1(Z) \frac{d\bar{C}_1}{dZ} + [B_1(Z) + G_1(Z)] \bar{C}_1 &= -K(\bar{C}_1 - \bar{C}_2); \quad Z=0, \quad \bar{C}_1=1. \\
 A_2(Z) \frac{d\bar{C}_2}{dZ} + [B_2(Z) + G_2(Z)] \bar{C}_2 &= \omega K(\bar{C}_1 - \bar{C}_2) - Da \bar{C}_2; \quad Z=0, \quad \bar{C}_2=0.
 \end{aligned}
 \tag{40}$$

The obtained solution of (39) is presented on Fig. 12 (line).

## CONCLUSIONS

A new approach for the absorption processes modeling in co-current column apparatuses, is

presented in the cases of industrial conditions, where the models are convective type form. The use of experimental data, for the average concentration at the column end, in the cases of highly soluble and lightly soluble gases, permits to obtain the model parameters, related with the radial non-uniformity of the velocity in the gas and liquid phases. These experimental parameter values permit to obtain the mass transfer coefficient in the cases of physical and chemical absorption of the average-soluble gases.

**Acknowledgements:** This work is supported by Project of Fundamental Scientific Research 19-58-18004, conducted by RFBR and the National Science Fund of Bulgaria under contract No KP 06 RUSIA-3 from 27 Sep. 2019, “Modeling, simulation

*and experimental investigations of the interphase mass transfer and separation in distillation, absorption, adsorption and catalytic processes in industrial column apparatuses”.*

#### REFERENCES

1. Chr. Boyadjiev, *Theoretical Chemical Engineering. Modelling and simulation*, Berlin, Heidelberg, Springer-Verlag, 2010.
2. Chr. Boyadjiev, M. Doichinova, B. Boyadjiev, P. Popova-Krumova, *Modeling of Column Apparatus Processes*, Berlin, Heidelberg, Springer-Verlag, 2016.
3. Chr. Boyadjiev, M. Doichinova, B. Boyadjiev, P. Popova-Krumova, *Modeling of Column Apparatus Processes*, Second edn., Berlin, Heidelberg, Springer-Verlag, 2018.
4. B. Boyadjiev, Chr. Boyadjiev, *Bulg. Chem. Commun.*, **49**(3), 711 (2017).
5. B. Boyadjiev, Chr. Boyadjiev, *J. Eng. Thermophysics*, **29**(1), 186 (2020).
6. W. E. Schiesser, *The Numerical Method of Lines*, Academic Press, San Diego, 1991.

## Justification of the method for calculating heat transfer in film evaporators with a rotating surface

V. G. Rifert, A. S. Solomakha\*, P. A. Barabash, V. Usenko, V.V. Sereda

*Department of Theoretical and Industrial Heat Engineering, Igor Sikorsky Kyiv Polytechnic Institute, Ukraine*

Received: August 12, 2020; Accepted: August 21, 2020

The paper discusses a heat and mass transfer apparatus with a rotating surface of various shapes (disk, cone, etc.) for the treatment of liquids for which the residence time in the high-temperature region is critical (fruit juices, pharmacological preparations, etc.). In addition, such devices make it possible to create compact energy-efficient systems, including devices for microgravity conditions. Achieving the minimum dimensions and weight, the high quality of the distillate and the maximum level of concentration depends on the design of the rotation surface and on the accuracy of the calculation of heat transfer processes occurring in such devices. The paper discusses methods for calculating heat transfer during condensation and evaporation in a thin liquid film. The use of an analogy of the processes in a liquid film on a rotating surface and the gravity flow of a liquid film is justified. Experiments are performed to determine the average and local heat transfer coefficients on a rotating surface.

**Keywords:** centrifugal, film, condensation, evaporation

### NOMENCLATURE

$G$ – mass flow rate, kg/s;	<i>Greek symbols</i>
$kg/h$ ;	$\beta$ – half angle of the cone,
$G_d$ – product rate, kg/s;	measured from the
$g$ – gravity, $m/s^2$ ;	vertical, °;
$h$ – heat transfer	$\delta$ – thickness, m;
coefficient, $W/(m^2K)$ ;	$\lambda$ – thermal conductivity,
$Nu$ – Nusselt number, $Nu$	$W/(m \cdot K)$ .
$= h\lambda^{-1}(v/\omega^2R)^{1/3}$	$\mu$ – dynamic viscosity,
$n$ – rotating speed, rpm;	$kg/(m \cdot s)$ ;
$Pr$ – Prandtl number;	$\nu$ – kinematic viscosity,
$Q$ – heat flux, $W$ ;	$m^2/s$ ;
$q$ – heat flux, $W/m^2$ ;	$\rho$ – density, $kg/m^3$ ;
$R$ – radius, m;	$\tau$ – time, s;
$r$ – latent heat, $J/kg$ ;	$\omega$ – angular velocity, $s^{-1}$ ;
$Re$ – Reynolds number,	<i>Subscripts</i>
$Re = 4G/(2\pi R\mu)$ ;	$c$ – condensate;
$t$ – temperature, °C;	$d$ – diameter, disk;
$\Delta t$ – temperature	$e$ – evaporated;
difference, °C;	$exp$ – experiment;
$U$ – overall heat transfer,	$f$ – feed;
$W/(m^2K)$ ;	$i$ – counting index;
	$w$ – water.

### INTRODUCTION

The use of rotational motion to intensify heat transfer processes in liquid films was first implemented in practice at the first part of the twentieth century. The main advantage of concentrating thermolabile liquids during film flow on rotating surfaces is its short-term contact with the heating surface due to the high speed of the film flow ( $u > 10$  m/s). It also reduces the probability of formation of solid deposits on the heat transfer

surface and provides high heat transfer coefficients in such an apparatus.

There are numerous examples of successful applications of rotating surface-film evaporators. They can be used for evaporation of various aqueous solutions; they are used as distillation apparatuses in the production of fatty alcohols and acids, herbicides, etc. As a rule, these products have limited thermal stability [1].

In the food industry, where the problem of reducing the degree of thermal effect on processed products plays a primary role, there are also ample opportunities for their use: when condensing milk, concentrating fruit juices, obtaining extracts of instant coffee, tea, meat extract, for dehydration, etc. With the help of rotating film evaporators, derivatives of vitamins, a number of hormones, etc., are obtained [1]. The use of centrifugal evaporators is promising for the regeneration of water and wastewater from the life support system of astronauts in microgravity conditions [2-7].

The first description of the operation of a centrifugal apparatus was made by Hickman [8, 9]. In this apparatus, the product is distributed over the inner surface of a cone with a horizontal axis of rotation. Heating of the outer surface of the cone is carried out by steam obtained in the apparatus, which is compressed by a centrifugal compressor to create the required temperature difference (6...10 °C). For small pilot installations, the surface of revolution was chosen in the form of a disk with a diameter of 1.27 and 2.8 m.

Bromley and co-workers [10, 11] describe and study a multistage evaporator for sea water with a rotating surface in the form of a disk.

\* To whom all correspondence should be sent:  
E-mail: a.solomakha@kpi.ua

The evaporator consists of a number of evaporator plates (up to 30), located directly above one another. When sea water was desalinated, the productivity of the 29-stage device was  $G_d = 0.4$  kg/s, the heat transfer coefficient was about  $U = 8500$  W/m<sup>2</sup>K.

In [12, 13] the design of the heat exchange surface in a spinning cone column is described. It consists of a vertical succession of alternate rotating and stationary cones. Liquid flows as a film down the stationary cone, drains into the base of the rotating cone again as a film by the action of the centrifugal force. Gas flows up the column countercurrent to the flow of the liquid. Mass transfer from the liquid to the vapour phase in a spinning cone column takes place through the large surface area of the film (which may be less than 1 mm thick), and through the liquid spray in the regions between spinning and stationary cones. There may be several dozen of cone sets (stages) in a commercial column.

The Centritherm (CT) evaporator (Flavourtech, Griffith, Australia) is composed of multiple cones (1–12 depending on the evaporative capacity) that form a cone stack [14]. The centrifugal force of the rotating cones creates a thin layer and allows effective wettability of the heat-exchange surface. It is claimed that the CT evaporator is able to concentrate dairy products to concentrations unachievable with conventional designs of evaporator while maintaining product functionality. It can process viscous products at low temperature (50 °C). Moreover, the extremely short residence time, claimed to be around one second by the manufacturer, ensures very low thermal impact on the product.

In [3-6], the design and test results of a centrifugal multistage vacuum distiller (CMVD) are described for water recovery in a life-support system in microgravity. Evaporation occurs in a thin film (less than 0.02 mm) of a liquid (urine or a mixture of urine and water, etc.) inside a rotating rotor. Condensation of the produced steam occurs on the outer surface.

In all considered designs, the energy efficiency and quality of the product (distillate) in a centrifugal evaporator (distiller) depends mainly on two processes: condensation of heating steam on a rotating heat exchange surface and evaporation (sometimes boiling) of liquid. These processes take place in thin liquid films.

Heat transfer during film condensation in many works [9, 15] is calculated from the dependence obtained for the first time in work [16]:

$$\frac{h_c}{\lambda} \left( \frac{v}{\omega} \right)^{0.5} = 0,904 \cdot \left( \frac{Pr}{c_p \Delta T} \right)^{0.25} \quad (1)$$

For the case of a rotating cone, it was shown in [17] that

$$\frac{h_{cone}}{h_c} = (\sin \beta)^{1/2} \quad (2)$$

The formula (1) in empirical form is transformed into [18]:

$$Nu = \frac{h_c}{\lambda} \left( \frac{v^2}{\omega^2 R} \right)^{1/3} = 1,1 \cdot Re^{-1/3} \quad (3)$$

In this case, the local Reynolds number:

$$Re = \frac{4 \cdot G_c}{2\pi R \mu}$$

Heat transfer during evaporation of a liquid film on a rotating disc and on conical surfaces was studied in [9, 10, 15, 19, 20]. However, the authors did not measure directly the coefficient of heat transfer during evaporation ( $h_e$ ), but only the overall heat transfer coefficient  $U$ . In most papers, to calculate the heat transfer during evaporation of a liquid film on a rotating surface, a dependence based on a laminar model of liquid flow is used. But already in papers [21-23] it was shown that the nature of the influence of the liquid flow rate (Reynolds numbers) on the evaporation process cannot be described by the laminar theory

In the present study, the experimental values of the heat transfer coefficients during condensation  $h_c$  and evaporation  $h_e$  were determined. The method for calculating heat transfer using the results of numerical solutions of heat transfer in a liquid film flow (laminar and turbulent) was improved.

#### Experimental installation

In papers [21, 22] an experimental installation for studying the processes of evaporation and condensation on a rotating disk is described. The main element of this setup is shown in Fig. 1.

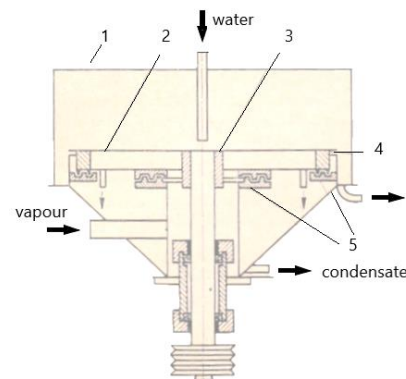


Fig. 1. Schematic diagram of the experimental installation

The centrifugal evaporator consists of a stainless steel housing 1, inside which a copper disk 2 (diameter is 300 mm and thickness is 1.5 mm) rotates on a shaft. The shaft is driven by a 0.5 kW DC motor ( $n = 0 \dots 2500$  rpm) using a V-belt transmission. The disk is rigidly connected to the flange 3 and the bronze ring 4 which is equipped with a labyrinth seal 5.

Steam was produced by boiling distilled water in a boiler and feeding it to the bottom surface of the rotating disk. The condensate was thrown by centrifugal force to the periphery of the disk and drained into the conical part of the apparatus. Then it entered the condensate measuring tank and returned to the boiler using a pump. To prevent air from entering the system, the steam pressure in the experiments was above atmospheric (about 1.1 bar) and was automatically maintained by an electronic pressure regulator, which changed the load of the electric heater in the boiler.

Water for cooling (evaporation) was supplied to the center of the disk. Its flow rate was measured with a rotameter. At the outlet of the apparatus, the condensate flow rate was determined by the volumetric method. The temperatures of steam and water were measured with mercury thermometers (graduation 0.1 °C). The vapor pressure was determined using a pressure gauge. The disk rotation speed was measured with a tachometer with an accuracy of  $\pm 10\%$ . To determine the temperature of the heat transfer surface, seven copper-constantan thermocouples with a diameter of 0.2 mm were embedded in the disk. Each thermocouple was placed in a  $0.8 \times 1.0$  mm groove, first along the circumference, and then along the radius of the disk (every 30 mm). The thermocouples were connected to the measuring device through a slip-contact current collector.

#### Heat transfer during condensation of a liquid film on a rotating disk

In the first series of experiments, the local heat transfer coefficients were measured during condensation of water vapor at a temperature of  $t_c = 99.5 \dots 99.8$  °C and at a speed of  $n = 200, 500, 1000$  and 1600 rpm. The consumption of cooling water  $G_w = 70$  kg/h; inlet water temperature  $t_w = 20$  °C; the average heat flux was constant  $q = 125$  kW/m<sup>2</sup>.

The temperature of the cooling water at the outlet of the installation and the flow rate of the condensate were measured by the volumetric method. The difference between the heat balance on the condensation side  $Q_c = G_c \cdot r$  and the water cooling side  $Q_w = G_w \cdot c_p \cdot \Delta t_w$  did not exceed 3%. Fig. 2 shows the experimental data  $t_{wall} = f(R)$  at different disk

revolutions.  $n$  – temperature of the wall. The process of calculating the local and average heat transfer coefficients  $h_c$  includes several steps.

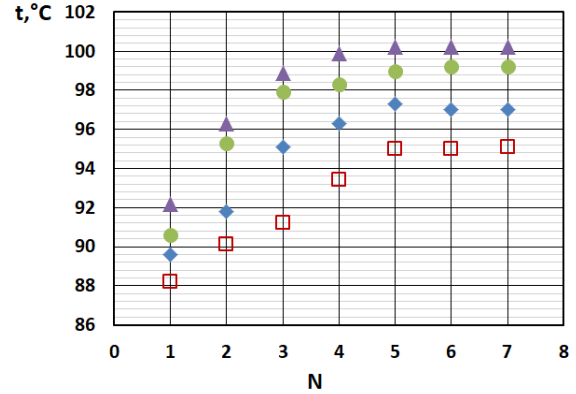


Fig. 2. Measured disk temperatures. N - thermocouple number;  $n = 200$  (□), 500 (◇), 1000 (●), 1600 (▲) rpm.

1) Calculation of the disk area corresponding to the local radius  $F_i = \pi R^2$ , and the area of the surface corresponding to the ring where the thermocouple is installed:

$$\Delta F_i = \pi R^2_N - \pi R^2_{N-1} \quad (4)$$

where  $R$  – local radius, m;  $N$  – installed thermocouple number.

2) Determination of local temperature difference

$$\Delta t_c = t_c - t_N \quad (5)$$

where  $t_c$  – condensation temperature of water vapor, °C. It is a function of the condensing pressure.

3) Determination of the calculated local heat transfer coefficient during condensation by the formula (1)

$$\sum Q_c = \sum_1^N (h_c \cdot \Delta t_c \cdot \Delta F_i) \quad (6)$$

5) Comparison of the obtained total heat flux with the amount of heat taken by the cooling water and as a result of measuring the amount of condensate obtained

$$Q_w = G_w \cdot c_p \cdot \Delta t_w \quad (7)$$

$$Q_c = G_c \cdot r \quad (8)$$

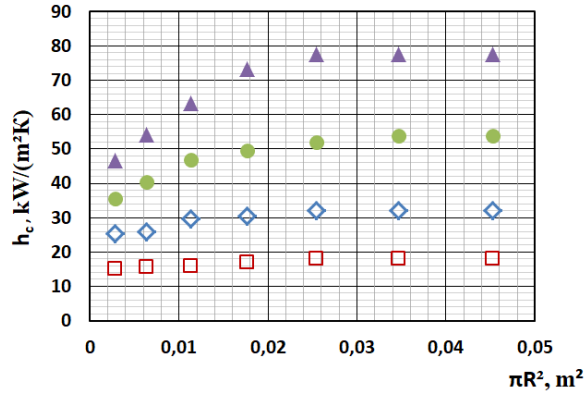
As a result of the calculations, a coincidence between the calculated and measured amounts of heat was obtained  $Q_c = Q_w$ . The maximum difference was 7%.

Fig. 3 shows the local heat transfer coefficients. Comparison with the theoretical dependence is shown in Fig. 4.

Thus, the experimental data showed once again that in the case of condensation on a rotating surface, it is possible to use the well-known dependence for the laminar flow of a liquid. The gravitational component  $g$  is replaced by a complex ( $\omega^2 R$ ). In the

performed experiments, the Reynolds number of the film did not exceed  $Re = 60$ .

In this case, it can be noted that already starting from  $Re > 40$ , a slight deviation from the laminar theory is observed. A similar effect was also noted in [34].



**Fig. 3.** Local heat transfer coefficient during vapor condensation at atmospheric pressure.  $n = 200$  ( $\square$ ),  $500$  ( $\diamond$ ),  $1000$  ( $\bullet$ ),  $1600$  ( $\blacktriangle$ ) rpm.

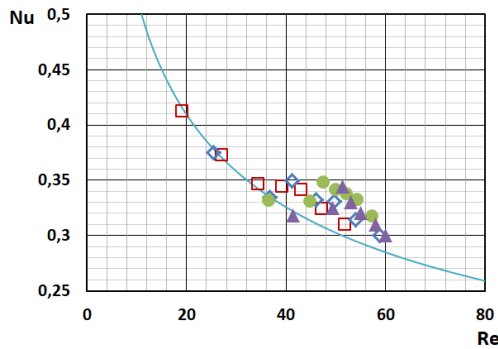


**Fig. 4.** Local Nu versus Reynolds number (condensate flow rate). Solid line - calculated by formula (1)

#### Heat transfer during evaporation from a liquid film on a rotating disk

In the second series of experiments, the local heat transfer coefficients were measured during evaporation of a liquid flowing down in the form of a film over a rotating disk surface at atmospheric pressure.

The liquid was supplied for evaporation to the center of the disk. Before being fed to the disk, the liquid was heated to boiling point. The evaporation temperature was equal to the saturation temperature and was  $t_e = 101.5$  °C. The thermal power changed as a result of a change in the heating steam flow rate, which condensed on the back side of the disk ( $d = 0.3$  m). After reaching the required temperatures, the specified disk rotation speed  $n$  and the evaporated water flow rate  $G_w$  were selected. Experiments were carried out with the following parameters: disk rotation speed  $n = 100...1900$  rpm, average heat flow

density  $q = 20 \cdot 10^3...10^5$  W/m<sup>2</sup>, feed water consumption  $G_w = 15 ... 96$  kg/h,  $\Delta t = t_e - t_{wall} = 1.3 ... 12$  °C.

The experiments were carried out in the range of variation of the heat flux density  $q < 10^5$  W/m<sup>2</sup>, when there is no nucleate boiling in the film of an evaporating liquid [24]. It was assumed that the heat transfer coefficient from the condensation side  $h_c$  is known and can be determined from dependence (1) or (3).

The local coefficient  $h_e$  is determined as follows.

1) From the known temperatures of the disk and vapor condensation, the local heat transfer coefficient  $h_c$  during condensation, local heat transferred  $q_i$  and total heat transferred  $Q$  were determined.

2) Determine the local temperature difference

$$\Delta t_e = t_e - t_i \quad (9)$$

where  $t_e$  is the temperature of evaporation, °C. It is a function of the condensing pressure.

3) Using the known local heat transferred and temperature difference, we find the local heat transfer coefficient during evaporation

$$h_e = \frac{q_i}{\Delta t_e} \quad (10)$$

4) Determine the total heat transferred

$$\sum Q_e = \sum_1^N (h_e \cdot \Delta t_e \cdot \Delta F_i) \quad (11)$$

5) Compare the obtained total heat transferred with the heat of phase transition using the formula (8) as a result of measuring the amount of obtained condensate.

As a result of the calculations, a coincidence of the calculated and measured amounts of heat was obtained  $\sum Q_e = Q_c$ . The maximum difference was 10%.

In the experiment, a weak dependence of the average and local heat transfer coefficients on the flow rate of the evaporated liquid was obtained (see Fig. 5), in contrast to the case of film condensation (see Fig. 4).

Thus, the experimental data showed that it is impossible to use the laminar theory when evaporating from a liquid film on a rotating surface. At the considered liquid flow rates, turbulization of the liquid film occurs, which leads to a change in the effect of flow rate (Re number) on the heat transfer coefficient.

#### Generalization of heat transfer during condensation and evaporation of a liquid film on a rotating disk

The processes of film condensation and surface evaporation of a liquid film heated to the saturation

temperature occur at an almost constant heat flux along the thickness of the film. Therefore, local heat transfer coefficient in both cases submits to practically the same laws. In the case of gravitational and forced flow it was investigated in many theoretical [25-27] and experimental works [28-31]. In most of such works, heat transfer coefficient is expressed as a dependence of the form  $Nu = f(Re)$ .

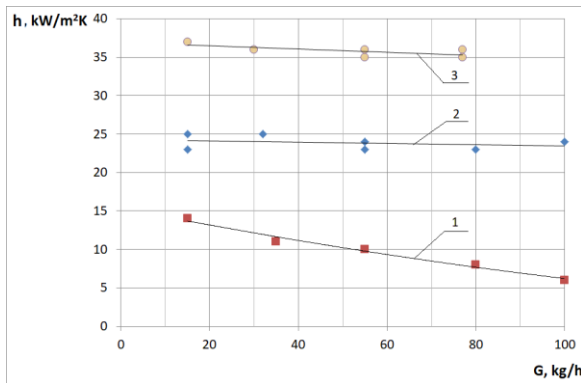


**Fig. 5.** Influence of the feedwater flow  $G$  on the heat transfer during the evaporation of the liquid film on a rotating disk at different rotation speeds  $\omega$ : 1 -  $\omega = 21$  rad/s; 2 -  $\omega = 52$  rad/s;  $q = 6,6 \cdot 10^4$  W/m<sup>2</sup>; 3 -  $\omega = 105$  rad/s;  $q = 9,6 \cdot 10^4$  W/m<sup>2</sup>.

In the case when the heat flux is the same over the entire film thickness, in the theoretical analysis of the evaporation process it is necessary to take into account the structure of the film surface (its turbulization). For this purpose, in [31], a semiempirical technique is proposed. The results of such calculation can be generalized using the following equation:

$$Nu_i = 1,1 Re^{-1/3} (1 + 0,02 Re^{0,2} + 0,0009 Re^{0,2} \cdot Pr^{0,65}) \quad (12)$$

If we drop the expression in parentheses in equation (12), then it becomes a theoretical equation for a laminar flow of a liquid film. Therefore, the expression in parentheses can be regarded as a correction factor that takes into account the increase in heat transfer during turbulization of the film flow as compared to the laminar flow.

It should be noted that Eq. (12) is valid only in those cases when the generated steam flow does not have a noticeable mechanical effect on the film.

Figure 6 shows the graphs  $Nu = f(Re)$  (solid lines) for two values  $Pr = 1.75$  and  $Pr = 2.77$  according to formula (12) [31]. The dashed line shows a graph for a strictly laminar flow of a liquid film according to formula (3).

The obtained experimental data on the evaporation and condensation on a rotating disk are shown by dots. In the range of Reynolds numbers  $Re < 60$ , heating steam condensed from the lower side

of the disk ( $t_c \approx 102$  °C;  $Pr = 1.77$ ) - see Section 1 of this paper. On the upper side of the disk, a liquid film ( $Re = 130...1100$ ) evaporated at atmospheric pressure ( $t_e \approx 100$  °C;  $Pr = 1.75$ ) - see Section 2 of this work.

The graph also shows the experimental data for the evaporation of a liquid film in a vacuum ( $t_e \approx 65$  °C;  $Pr = 2.77$ ) from paper [32].

As can be seen from Fig. 6, the theory of heat transfer is in qualitative agreement with experimental data on the evaporation and condensation of a liquid film on a rotating disk, which makes it possible to use it to calculate not only for the gravitational flow of a liquid film, but also for rotating systems, when  $(\omega^2 R) \gg g$ .

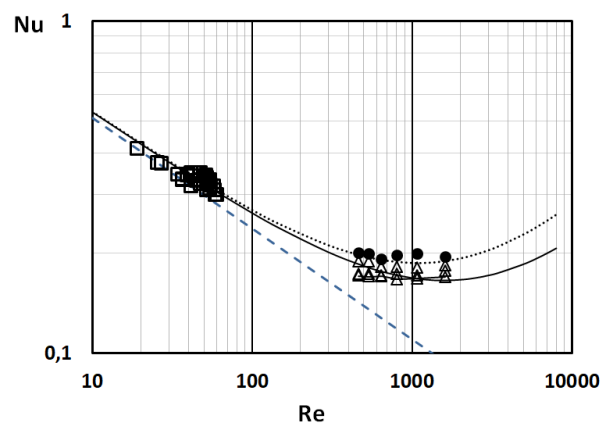


**Fig. 6.** Comparison of experimental data of the local Nusselt number with theoretical calculation: Solid line - theory ( $Pr = 1.75$ ); Line to point - theory ( $Pr = 2.77$ ); Dashed line - Nusselt's laminar theory (3); ( $\square$ ) - condensation, ( $\blacktriangle$ ) - evaporation at atmospheric pressure; ( $\bullet$ ) - evaporation in vacuum [32]

#### Comparison of experimental results with theory during evaporation

##### a) Rotating disc

One of the first works where heat transfer was measured during evaporation of water on a rotating disk, was the paper [8]. In this work, as well as in [9-11], a laminar model of liquid evaporation is used to determine  $h_c$ . According to this approach, the heat transfer coefficient depends on the flow rate of the liquid supplied to the rotating surface,  $h_c \sim G^{1/3}$ . As a result, the authors present in their works an empirical formula for calculating the heat transfer coefficient  $U$  (see, for example, formula (11) in [9]). It takes into account the deviation of the obtained data from the laminar model. The formula has a complex view, which is not very convenient for engineering calculations.

In experiments [33], the total heat transfer coefficient  $U$  was measured during water evaporation:  $t_e = 102.7...105.6$  °C and an evaporating

liquid flow rate  $G_e = 45.4 \dots 68.1$  kg/h. Total temperature difference  $\Delta t = t_c - t_e = 2.78 \dots 5.55$  °C. Rotating speed  $n = 690 \dots 1700$  rpm. The evaporating liquid was fed in the center of a copper disk  $d = 0.3$  m,  $\delta = 1.6$  mm. Analysis of the data shows that for the same  $\omega(n)$  and  $\Delta t$ , the heat transfer coefficients are the same within  $\pm 5\%$ .

Calculation of the theoretical values of  $U$  and comparison of the experimental and calculated values was carried out as follows:

1) The local values of  $Re_c$  and  $Re_e$  at different radii  $R_i = 0.03; 0.045; \dots$ , are found from the known flow rates of the condensate  $G_c$  and the evaporating liquid  $G_e$ .

2) According to Fig. 6 or according to the calculation formula (12), we find the local values of the numbers  $Nu_c$ ,  $Nu_e$  and, accordingly, local  $h_c$  and  $h_e$ .

3) Using the known area  $F_i = \pi R^2$  and the known temperature difference  $\Delta t = t_c - t_e$ , we find the local heat flux  $Q_i$ .

4) Find the total calculated heat flux through the disk  $\Sigma Q_i$  and compare it with the experimental  $Q_{exp}$ . (see Table 1).

The results of the comparison of some experimental and calculated values are presented in Table 1, from which it can be seen that the calculated values of the total heat flux are by 12...22% higher than the experimental ones. Thus, the proposed technique describes the experimental data with good accuracy.

*b) Rotating cone*

The most detailed study of heat transfer during the evaporation of various liquids in the rotating cone was studied in [15, 35-36]. In all these studies the total heat transfer coefficient  $U$  was measured.

Experimental measurements in [15, 36] of the total heat transfer coefficient were made for three liquids (water, 20% sugar solution and skim milk) at different evaporation temperatures and feed flow rate  $1.5 \dots 6.0 \cdot 10^{-5}$  m<sup>3</sup>/s.

**Table 1.** Comparison of calculated results and experimental data [33]

No	$n$ , rpm	$G_e$ , kg/h	$G_c$ , kg/h	$\Delta t$ , °C	$U_{exp}$ , kW/(m <sup>2</sup> K)	$Q_{exp}$ , kW	$R_i$ , m	$h_e$ , kW/(m <sup>2</sup> K)	$h_c$ , kW/(m <sup>2</sup> K)	$U_i$ , kW/(m <sup>2</sup> K)	$Q_i$ , W	$\Sigma Q_i$ , W	$\Delta Q$ , %
1	720	46.5	3.22	2.6	13.9	2.5	0.03	14.6	25.4	8.9	65	3.1	18
							0.045	17.4	32.7	10.9	98		
							0.06	20.0	39.3	12.6	159		
							0.075	22.4	45.3	14.1	230		
							0.09	24.6	51.0	15.6	309		
							0.105	26.8	56.3	17.0	397		
							0.12	28.8	61.4	18.2	493		
							0.135	30.8	66.3	19.4	595		
2	1010	46.4	3.58	2.4	16.6	2.9	0.03	18.3	30.8	11.0	72	3.5	19
							0.045	21.8	39.7	13.3	115		
							0.06	25.0	47.7	15.4	186		
							0.075	28.0	55.0	17.3	268		
							0.09	30.9	61.8	19.0	360		
							0.105	33.5	68.3	20.6	462		
							0.12	36.1	74.4	22.1	572		
							0.135	38.6	80.3	23.6	691		
3	1390	46.2	4.0	2.3	19.2	3.2	0.03	22.7	37.0	13.3	88	4.1	22
							0.045	27.0	47.6	16.1	133		
							0.06	31.0	57.1	18.6	214		
							0.075	34.7	65.8	20.8	308		
							0.09	38.2	73.9	22.9	414		
							0.105	41.5	81.6	24.8	530		
							0.12	44.7	89.0	26.6	656		
							0.135	47.8	96.0	28.3	791		
4	1700	46.7	4.4	2.2	24.3	3.8	0.03	25.9	41.0	14.9	93	4.3	12
							0.045	30.8	52.7	18.0	140		
							0.06	35.4	63.1	20.8	226		
							0.075	39.6	72.7	23.2	325		
							0.09	43.6	81.7	25.5	436		
							0.105	47.4	90.2	27.6	557		
							0.12	51.0	98.3	29.5	689		
							0.135	54.5	106.1	31.4	830		
							0.15	57.9	113.5	33.2	979		

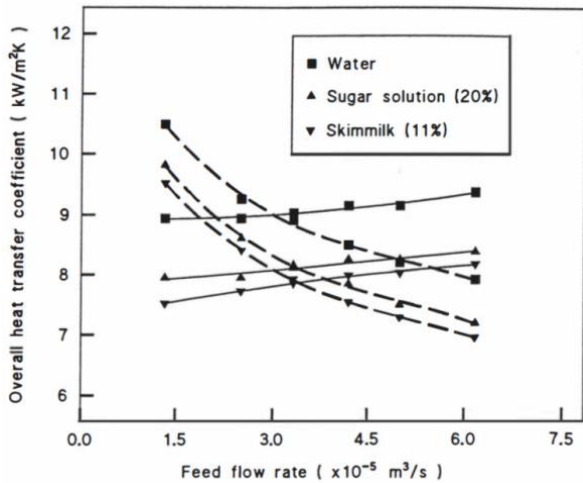


**Fig. 7.** Effect of the feed flow rate on the overall heat transfer coefficient for water, 20% sugar solution and skim milk in the Centritherm evaporator. Solid lines are experimental values while dashed lines are theoretical values. Evaporation temperature 60°C, rotating speed 146,6 rad/s, temperature difference 10K.

Fig. 7 shows a comparison of the experimental (solid lines) and heat transfer coefficients calculated by the model for the laminar flow of an evaporating liquid film (dashed lines).

In [36], an attempt was made to explain the reasons for the discrepancy between the calculated and experimental data in Fig. 7. According to this model, the authors assume (without experimental justification) that vapor bubbles are formed inside the cone and an additional temperature drop appears on the side of evaporation. As a result, the overall temperature difference will increase, which will lead to a decrease in heat transfer.

The authors of [36] provide a formula for calculating these differences and a table with some of the results. But it should be noted that the main advantage of centrifugal film evaporators is that nucleate boiling in them at  $\omega > 10^4 \text{ s}^{-1}$  occurs at a heat flux density  $q > 2 \cdot 10^5 \text{ W/m}^2$  [24, 32], which is approximately 4...5 times higher than the experimental values according to the data tests [15].

In our opinion, the influence of the liquid flow rate on the total heat transfer coefficient is associated with the characteristic of heat transfer during the evaporation. If we calculate the local Reynolds number for water at 60 °C from Fig. 7, then it will lie in the range  $Re_i = 300 \dots 2500$ . Figure 6 shows that in this range of Reynolds numbers the dependence  $Nu = f(Re)$  deviates significantly from the laminar theory and has a form similar to that in Fig. 7. The performed calculations for water according to Figs. 6 and 7, using formula (2), showed the convergence of the calculation of heat

transfer coefficient  $h_c$  within 30% without invoking additional explanations.

## CONCLUSIONS

Experimental studies of heat transfer processes during condensation and evaporation in liquid films made it possible to significantly refine the physical picture of the processes. These processes occur at an almost constant heat flux density across the film thickness; therefore, the local heat transfer in both cases obeys the same laws. At the same time, the effect of turbulization of a liquid film on the heat transfer coefficient during its flow on a rotating disk is shown for the first time. Comparison with the theory for the gravitational flow showed satisfactory agreement, which indicates a similar effect of the film flow on the heat transfer process under the action of centrifugal forces.

The considered calculation method using local heat transfer coefficients and semiempirical dependences for the gravitational flow makes it possible to accurately predict the value of the total heat transfer coefficient and to compare the experimental data of different authors obtained on disks of different diameters, including cones, when  $\beta \neq 90^\circ$ .

## REFERENCES

1. V. M. Olevskiy, V.R. Ruchinskiy, Rotary-film heat and mass exchangers, 1977.
2. V. Rifert, L. Anatyshuk, A. Solomakha, P. Barabash, V. Usenko, A. Prybyla, M. Naymark, V. Petrenko, 70th International Astronautical Congress (IAC), Washington D.C., United States, 21-25 October 2019. IAC-19-A1, IP, 11, x54316.
3. V. Rifert, P. Barabash, N. Goliyad, SAE Technical Paper 901249 (1990).
4. V. Rifert, A. Stricun, V. Usenko, SAE Technical Papers 2000-01-2387 (2000).
5. V. Rifert, V. Usenko, I.Zolotukhin, A. Lubman, A. MacKnight, Technical Papers 2003-01-2625 (2003).
6. A. Lubman, A. MacKnight, V. Rifert, P. Barabash, SAE Technical Papers 2007-01-3177 (2007).
7. V. Rifert, P. Barabash, V. Usenko, A. Solomakha et al, 68th International Astronautical Congress (IAC), Adelaide, Australia, 25-29 September 2017. IAC-17-A1.IP.25.
8. K. C. D. Hickman, *Industrial and Engineering Chemistry*, **5**, 786 (1957).
9. L. A. Bromley, *Ind. Eng. Chem.*, **50**, 233 (1958).
10. R. Clark, L. Bromley, *Chemical Engineering Progress*, **1**, 64 (1961).
11. L. A. Bromley, *Desalination*, **1**, 367 (1966).
12. T. Langrish, S. Makarytchev, D. Fletcher, R. Prince. *Chemical Engineering Research and Design*, **1**, 122 (2003).
13. S. Makarytchev, T. Langrish, D. Fletcher, *Chemical Engineering Research and Design*, **83**, 1372 (2005).

14. G. Tanguy, A. Dolivet, F. Garnier-Lambrouin, S. Mejean, D. Coffey, et al. *Journal of Food Engineering*, **166**, 356 (2015).
15. H. Chen, PhD Thesis, 1997.
16. E. M. Sparrow, J. L. Gregg, *Trans. ASME J. Heat Transfer*, **82**, 71 (1960).
17. E. M. Sparrow, J. P. Hartnett, *J. Heat Transfer*, **1** (1961).
18. S. S. Kutateladze, Fundamentals of heat transfer, 1964.
19. M. Rahman, A. Fagwri, *J. Heat Mass Transfer*, **10**, 2655 (1992).
20. J. Rice, A. Faghri, B. Cetegen, *International Journal of Heat and Mass Transfer*, **48**, 5192 (2005).
21. A. Butuzov, V. Rifert, *Heat Transfer Soviet Research*, **6**, 150 (1972).
22. A. Butuzov, V. Rifert, *Heat Transfer Soviet Research*, **1**, (1973).
23. V. Rifert, P. Barabash, A. Solomakha, V. Usenko, V. Sereda, V. Petrenko, *Bulg. Chem. Commun.*, **50** (K), 49 (2018).
24. V. Rifert, I. Pukhovoy, E. Nikitenko, Proc. 2nd European Thermal Sciences and 14th UIT National Heat Transfer Conference, 1996, 1, p. 249.
25. S. Bae, J. S. Maulbetsch, W. M. Rohsenow, Refrigerant forced-convection condensation inside horizontal tubes. Report No. DSR-79760-64. Massachusetts Institute of Technology, Cambridge, MA, 1969, p. 120.
26. D. P. Traviss, A. B. Baron, W. M. Rohsenow, Forced-convection condensation inside tubes. Report No. DSR-72591-74. Massachusetts Institute of Technology, Cambridge, MA, 1971, p. 105.
27. V. Rifert, V. Sereda, A. Solomakha, *Heat and Mass Transfer*, **11**, 3041 (2019).
28. V. Rifert, V. Sereda, V. Gorin, P. Barabash, A. Solomakha, *Energetika*, **3**, 146 (2018).
29. V. Rifert, V. Sereda, V. Gorin, P. Barabash, A. Solomakha, *Bulg. Chem. Commun.*, **50** (K), 58 (2018).
30. V. Rifert, V. Sereda, V. Gorin, P. Barabash, A. Solomakha. *Heat and Mass Transfer*, **56**, 691 (2020).
31. G. Gimbutis, Heat transfer of a falling fluid film, Monograph, Vilnius, Moklas Publishers, 1988.
32. I. I. Pukhovoy, PhD Thesis, 1974.
33. L. Bromley, R. Humphreys, W. Murray, *Journal of Heat Transfer*, February, 80 (1966).
34. T. Storch, C. Philipp, A. Doeg, U. Gross, *International Journal of Thermal Sciences*, **76**, 137 (2014).
35. H. Chen, R. S. Jebson, O. H. Campanella, *Food Bioprod. Proc. Trans. Inst. Chem. Eng.*, **75**, 17 (1997).
36. H. Chen, R. S. Jebson, O. H. Campanella, *Food Bioprod. Proc. Trans. Inst. Chem. Eng.*, **81**, 293 (2003).

### Instructions about Preparation of Manuscripts

**General remarks:** Manuscripts are submitted in English by e-mail. The text must be prepared in A4 format sheets using Times New Roman font size 11, normal character spacing. The manuscript should not exceed 15 pages (about 3500 words), including photographs, tables, drawings, formulae, etc. Authors are requested to use margins of 2 cm on all sides.

Manuscripts should be subdivided into labelled sections, e.g. INTRODUCTION, EXPERIMENTAL, RESULTS AND DISCUSSION, etc. **The title page** comprises headline, author(s)' names and affiliations, abstract and key words. Attention is drawn to the following:

a) **The title** of the manuscript should reflect concisely the purpose and findings of the work. Abbreviations, symbols, chemical formulae, references and footnotes should be avoided. If indispensable, abbreviations and formulae should be given in parentheses immediately after the respective full form.

b) **The author(s)**' first and middle name initials and family name in full should be given, followed by the address (or addresses) of the contributing laboratory (laboratories). **The affiliation** of the author(s) should be listed in detail (no abbreviations!). The author to whom correspondence and/or inquiries should be sent should be indicated by an asterisk (\*) with e-mail address.

**The abstract** should be self-explanatory and intelligible without any references to the text and containing up to 250 words. It should be followed by keywords (up to six).

**References** should be numbered sequentially in the order, in which they are cited in the text. The numbers in the text should be enclosed in brackets [2], [5, 6], [9–12], etc., set on the text line. References are to be listed in numerical order on a separate sheet. All references are to be given in Latin letters. The names of the authors are given without inversion. Titles of journals must be abbreviated according to Chemical Abstracts and given in italics, the volume is typed in bold, the initial page is given and the year in parentheses. Attention is drawn to the following conventions: a) The names of all authors of a certain publications should be given. The use of “*et al.*” in the list of references is not acceptable; b) Only the initials of the first and middle names should be given. In the manuscripts, the reference to author(s) of cited works should be made without giving initials, e.g. “Bush and Smith [7] pioneered...”. If the reference carries the names of three or more authors it should be quoted as “Bush *et al.* [7]”, if Bush is the first author, or as “Bush and co-workers [7]”, if Bush is the senior author.

**Footnotes** should be reduced to a minimum. Each footnote should be typed double-spaced at the bottom of the page, on which its subject is first mentioned. **Tables** are numbered with Arabic numerals on the left-hand top. Each table should be referred to in the text. Column headings should be as short as possible but they must define units unambiguously. The units are to be separated from the preceding symbols by a comma or brackets. Note: The following format should be used when figures, equations, etc. are referred to the text (followed by the respective numbers): Fig., Eqns., Table, Scheme.

**Schemes and figures.** Each manuscript should contain or be accompanied by the respective illustrative material, as well as by the respective figure captions in a separate file. As far as presentation of units is concerned, SI units are to be used. However, some non-SI units are also acceptable, such as °C, ml, l, etc. Avoid using more than 6 (12 for review articles) figures in the manuscript. Since most of the illustrative materials are to be presented as 8-cm wide pictures, attention should be paid that all axis titles, numerals, legend(s) and texts are legible.

**The authors are required to submit the text with a list of three individuals and their e-mail addresses that can be considered by the Editors as potential reviewers. Please note that the reviewers should be outside the authors' own institution or organization. The Editorial Board of the journal is not obliged to accept these proposals.**

The authors are asked to submit **the final text** (after the manuscript has been accepted for publication) in electronic form by e-mail. The main text, list of references, tables and figure captions should be saved in separate files (as \*.rtf or \*.doc) with clearly identifiable file names. It is essential that the name and version of the word-processing program and the format of the text files is clearly indicated. It is recommended that the pictures are presented in \*.tif, \*.jpg, \*.cdr or \*.bmp format.

The equations are written using “Equation Editor” and chemical reaction schemes are written using ISIS Draw or ChemDraw programme.

## EXAMPLES FOR PRESENTATION OF REFERENCES

### REFERENCES

1. D. S. Newsome, *Catal. Rev.–Sci. Eng.*, **21**, 275 (1980).
2. C.-H. Lin, C.-Y. Hsu, *J. Chem. Soc. Chem. Commun.*, 1479 (1992).
3. R. G. Parr, W. Yang, *Density Functional Theory of Atoms and Molecules*, Oxford Univ. Press, New York, 1989.
4. V. Ponec, G. C. Bond, *Catalysis by Metals and Alloys (Stud. Surf. Sci. Catal., vol. 95)*, Elsevier, Amsterdam, 1995.
5. G. Kadinov, S. Todorova, A. Palazov, in: *New Frontiers in Catalysis (Proc. 10th Int. Congr. Catal., Budapest (1992), L. Guczi, F. Solymosi, P. Tetenyi (eds.), Akademiai Kiado, Budapest, 1993, Part C, p. 2817.*
6. G. L. C. Maire, F. Garin, in: *Catalysis. Science and Technology*, J. R. Anderson, M. Boudart (eds.), vol. 6, Springer Verlag, Berlin, 1984, p. 161.
7. D. Pocknell, *GB Patent 2 207 355* (1949).
8. G. Angelov, PhD Thesis, UCTM, Sofia, 2001, pp. 121-126.
9. JCPDS International Center for Diffraction Data, *Power Diffraction File*, Swarthmore, PA, 1991.
10. *CA* **127**, 184 762q (1998).
11. P. Hou, H. Wise, *J. Catal.*, in press.
12. M. Sinev, private communication.
13. <http://www.chemweb.com/alchem/articles/1051611477211.html>.

***Texts with references which do not match these requirements will not be considered for publication!!!***

CONTENTS

<i>Chr. Boyadjiev</i> , Introduction in the chemical engineering processes modeling.....	5
<i>M. Z. Abdulin, O. A. Siryi, O. M. Tkachenko, A. A. Kulyk</i> , Boilers modernization due to energy-ecological improvement technology of burning.....	14
<i>B. Boyadjiev, Chr. Boyadjiev</i> , Convective type models of chemical processes in column apparatuses.....	20
<i>P. O. Kapustenko, L. L. Tovazhnyansky, O. P. Arsenyeva, S. K. Kusakov, V. V. Zorenko, O. Y. Fedorenko</i> , Computer modeling of plate heat exchanger for heat utilization from exhaust gases of drying process .....	25
<i>Sv. Ts. Nakov, D. B. Dzhonova-Atanasova, E. N. Razkazova-Velkova</i> , Dynamic hold-up of modern high-performance packings.....	32
<i>T. V. Nikulenkova, A. G. Nikulenkov</i> , Impact analysis of a transient temperature field on the service life of the high pressure rotor of K-1000-60/3000 turbine.....	36
<i>A. N. Pavlenko, V. E. Zhukov, E. Yu. Slesareva, Chr. Boyadjiev, B. Boyadjiev, D. Dzhonova-Atanasova, P. Popova-Krumova</i> , Large-scale maldistributions of local flow parameters at distillation on a structured packing.....	42
<i>V. G. Rifert, P. A. Barabash, V. P. Boianivskiy, V. V. Sereda, A. S. Solomakha</i> , The influence of heat transfer on the energy efficiency in thin film evaporators.....	47
<i>A. N. Pavlenko, V. E. Zhukov, E. Yu. Slesareva</i> , Pool boiling of refrigerant on a flat modified surface.....	54
<i>S. Stefanov, E. Razkazova-Velkova</i> , Integrated absorption-adsorption process for waste-free decontamination of gases from sulfur dioxide. Part 1. Choice of ion-exchange resin and adsorption and desorption parameters.....	57
<i>V. E. Zhukov, E. Yu. Slesareva, A. Yu. Sakhnov</i> , Autostabilization of propagation velocity of a self-sustaining evaporation front.....	64
<i>B. G. Pokusaev, A. V. Vyazmin, D. A. Nekrasov, N. S. Zakharov, D. P. Khramtsov, N. V. Shumova</i> , Approaches to mass transfer modeling in microchannels inside gel.....	68
<i>Chr. B. Boyadjiev, D. B. Dzhonova, P. G. Popova-Krumova, K. V. Stefanova, A. N. Pavlenko, V. E. Zhukov, E. Yu. Slesareva</i> , Liquid wall flow in countercurrent column apparatuses for absorption processes with random packings.....	74
<i>Kr. A. Semkov, T. St. Petrova</i> , New equations for gas phase pressure drop in expanded metal sheet packing (HOLPACK) for mass and heat transfer processes in packed columns.....	80
<i>B. Boyadjiev, Chr. Boyadjiev, P. Popova-Krumova</i> , Convective type models of co-current absorption processes in column apparatuses.....	86
<i>V. G. Rifert, A. S. Solomakha, P. A. Barabash, V. Usenko, V. V. Sereda</i> , Justification of the method for calculating heat transfer in film evaporators with a rotating surface.....	95
<i>INSTRUCTIONS TO AUTHORS</i> .....	103